POLYMER/GRAPHENE NANOCOMPOSITES FOR IMPROVED BARRIER PERFORMANCE

A thesis submitted to the University of Manchester for the degree of Doctor of Philosophy in the Faculty of Science and Engineering

2018

THOMAS P. RAINE

SCHOOL OF CHEMISTRY

TABLE OF CONTENTS

Final word count: 62542

LIST OF FIGURES

LIST OF TABLES

LIST OF EQUATIONS

LIST OF ABBREVIATIONS

11-AUDA	11-Aminoundecanoic acid
aGO	As-received graphene oxide
ATR	Attenuated total reflectance
BET	Brunauer-Emmett-Teller
bwGO	Base-washed graphene oxide
CNT	Carbon nanotube
CVD	Chemical vapour deposition
DI	Deionised
DSC	Differential scanning calorimetry
DTG	Differential thermogravimetry
EDX	Energy-dispersive X-ray spectroscopy
fGO	Functionalised graphene oxide
FT-IR	Fourier transform infrared
FWHM	Full width half maximum
GC	Gas chromatograph
GNP(s)	Graphene nanoplatelets(s)
GO	Graphene oxide
GRM(s)	Graphene related material(s)
HDPE	High density polyethylene
htGO	Heat treated graphene oxide
IPA	Isopropanol
IV	Intrinsic viscosity
MWNT	Multi-walled nanotube
OD	Oxidised debris
OTR	Oxygen transmission rate
PA11	Polyamide 11
PA12	Polyamide 12
PC	Polycondensation
PDMS	Polydimethylsiloxane
PEId	Polyetherimide
PEIn	Polyethyleneimine
PET	Polyethylene terephthalate

PMMA	Polymethyl methacrylate
PP	Polypropylene
PVDF	Polyvinylidene fluoride
SEM	Scanning electron microscopy
STP	Standard temperature and pressure (273.15 K, 1 bar)
TGA	Thermal gravimetric analysis
trGO	Thermally reduced graphene oxide
WVTR	Water vapour transmission rate
XLPE	Cross-linked polyethylene
XRD	X-ray diffraction
XRF	X-ray fluorescence

LIST OF SYMBOLS

$\boldsymbol{A}$	Area
$\boldsymbol{a}$	Penetrant activity
$\boldsymbol{b}$	Langmuir hole affinity constant
$\boldsymbol{c}$	Concentration
$\boldsymbol{C}$	Concentration
$\boldsymbol{C'_H}$	Langmuir sorption capacity
$\boldsymbol{C_D}$	Henry's Law concentration
$\boldsymbol{C_H}$	Langmuir concentration of molecules in holes
$\boldsymbol{D}$	Diffusion coefficient
$\boldsymbol{d}$	Interlayer spacing
$\boldsymbol{E_D}$	Activation energy of diffusion
$\boldsymbol{E_P}$	Activation energy of permeation
$\boldsymbol{f}$	Fugacity
$\boldsymbol{G'}$	Elastic modulus
$\boldsymbol{G''}$	Viscous modulus
$\boldsymbol{J}$	Flux
$\boldsymbol{K}$	Mark-Houwink parameter
$\boldsymbol{k_D}$	Henry's Law constant
$\boldsymbol{l}$	Thickness
$\boldsymbol{\bar{M}_v}$	Viscosity average molecular weight
$\boldsymbol{N_s}$	Number of samples
$\boldsymbol{p}$	Partial pressure
$\boldsymbol{P}$	Permeability coefficient calculated by pressure
$\boldsymbol{P_f}$	Permeability coefficient calculated by fugacity
$\boldsymbol{p_C}$	Critical pressure
$\boldsymbol{p_s}$	Saturation pressure
$\boldsymbol{Q}$	Amount
$\boldsymbol{R}$	Ideal gas constant
$\boldsymbol{S}$	Solubility coefficient
$\boldsymbol{s}$	Standard deviation
$\boldsymbol{T}$	Temperature
$\boldsymbol{t}$	Time

$T_{50wt\%}$	Temperature at 50 wt% loss
$T_{5wt\%}$	Temperature at 5 wt% loss
T_C	Critical temperature
T_c	Crystallisation temperature
T_g	Glass transition temperature
T_{m1}	First-heat melting temperature
T_{m2}	Second-heat melting temperature
T_{max}	Temperature at maximum rate of weight
t_{ps}	Flow time for polymer solution
t_{solv}	Flow time for pure solvent
$\bar{x}_s$	Mean sample value
x_s	Sample value
α	Mark-Houwink parameter
ΔH^0_m	Enthalpy of melting 100% crystalline polymer
ΔH_m	Enthalpy of melting composite
ΔH_S	Enthalpy of solvation
$\lvert\eta^*\rvert$	Complex viscosity
$[\eta]$	Intrinsic viscosity
η_r	Relative viscosity
η_{red}	Reduced viscosity
η_{sp}	Specific viscosity
Θ	Time-lag
λ	Wavelength
Π	Permeance
φ	Fugacity coefficient
ϕ_v	Volume fraction of solute
χ	Flory-Huggins penetrant-polymer interaction parameter
χ_c	Degree of crystallinity
ω	Weight fraction

ABSTRACT

The current reliance of modern society on fossil fuels, and in particular oil and gas, means that industry is forever searching for improved technologies to access and recover crude, from harder to reach and depleting reservoirs. A key innovation in the oil and gas industry is the unbonded flexible riser, a flexible pipeline designed to transfer high pressure crude mixtures from deep sea wells to floating platforms and ships. These risers consist of many concentric layers of barrier polymers, such as polyamide 11, and strengthening steel. Often, high partial pressures of 'sour' fluids, including CO_2 and H_2S, are found within the crude. Upon permeating through the polyamide 11 barrier layer, along with water, these sour fluids can corrode the steel armouring. Corrosion and subsequent weakening of the steel may lead the riser to fail and, in so doing, risks catastrophic ecological impact, economic challenges and threat to operator life. There is therefore a drive to improve the resistance of polyamide 11 to CO_2 and H_2S permeation.

The impenetrable nature of graphene was used as a starting point for increasing the barrier properties of polyamide 11. This thesis reports the first instance of testing the barrier properties of graphene and its nanocomposites to supercritical fluids of any kind. CO_2 and H_2S permeability testing was carried out in the gas, liquid and supercritical states at gauge pressures from 2 to 400 bar.

In situ polymerisations of the polyamide 11 monomer with graphene nanoplatelets and graphene oxide led to promising materials for improving the barrier properties of the polyamide.

Industrially relevant twin-screw extrusion was used to incorporate graphene related materials directly into the polyamide matrix. Extensive voiding limited the efficacy of such materials in CO_2 and H_2S barrier applications.

Chemical vapour deposition was used to synthesise large area graphene that was applied to the polyamide surface. Unavoidable tearing of the graphene led to a porous layer, which allowed unaffected transport of CO_2 and H_2S through the polyamide.

Finally, by laminating a multi-layered graphene paper between two layers of polyamide 11, extraordinary barrier performance was achieved. Compared to pure polyamide, the graphene paper laminates provided up to an order of magnitude reduction in CO_2 permeation, and reduced H_2S permeation to undetectable levels, even at gauge pressures of up to 400 bar.

DECLARATION

No portion of the work referred to in the thesis has been submitted in support of an application for another degree or qualification of this or any other university or other institute of learning.

COPYRIGHT STATEMENT

ACKNOWLEDGEMENTS

First and foremost, I would like to thank my academic supervisor, Professor Peter Budd, for his guiding hand and keen eye for detail from the start. A great many thanks also to my industrial supervisor, Doctor Bernadette Craster, TWI Ltd., who provided me with a wealth of support and countless discussions throughout the project. My thanks are also extended to my academic co-supervisor Professor Ian Kinloch for useful discussions and suggestions. I owe a great deal of gratitude to Doctor Oana Istrate, who gracefully gave up her time to aid me throughout the entire project. I'd like to extend thanks to Barnaby King for his tireless work on the permeation kit, keeping it up and running so that results were forever on their way.

Andrij Zadoroshnyj deserves a special mention for patiently training me on nearly every piece of kit that I have used, over the past three and a half years. Thanks also to Terence Hayward for designing and machining the specialist equipment required for this research. Cristina Valles, Polly Greensmith, Wayne Harrison, Jon Fellows and Heath Bagshaw are also owed thanks for their help and training.

Thank you to the EPSRC and TWI Ltd. for a CASE PhD studentship, and to TWI Ltd. for additional funding. I also acknowledge the Organic Materials Innovation Centre, the Electron Microscopy Centre, the Williamson Research Centre for Molecular Environmental Science and the Northwest Composites Centre for use of their facilities.

To the following, and in no particular order, I thank for endless hours of entertainment. Robin, Daltz, Jake, Anna, Jinesh, Daryl, Josh, Barney, Glenn, Robyn, Vaiva, Fiona, Matt, Raymundo, Bahare, Alex, Yuyoung, Seb, Kane, Ben, the LEC and DDMP. Thanks also to Derek, Emma, Sandbar, Kro, The Ducie Arms, Pancho's, the late Dirty Chippy, Umami, Tea, Coffee, Spotify, rock and roll, naughties pop and Dr Dre. Particular thanks to Stevie for his long arms, lack of stability and pies.

Last but not least, I'd like to thank my whole family. Thank you especially to my parents, Peter and Susan; my sister, Helen; and my ever tolerant fiancée, Cesca.

CHAPTER 1: INTRODUCTION

1.1 CONTRIBUTORS

This research project was an EPSRC Industrial CASE award partnership between TWI Ltd. and The University of Manchester.

1.2 BACKGROUND

Unbonded flexible risers are used extensively in the oil and gas industry. These risers are typically made up of many concentric layers of polymers and carbon steel, as shown in Figure 1.1.[1] Such pipelines are used to transport crude mixtures from subsea oil reserves to floating rigs and ships. Since the turn of the century, nearly two thirds of the flexible pipes in use contain the thermoplastic nylon 11, also known as polyamide 11 (PA11), as an internal fluid barrier (Figure 1.1).[2]

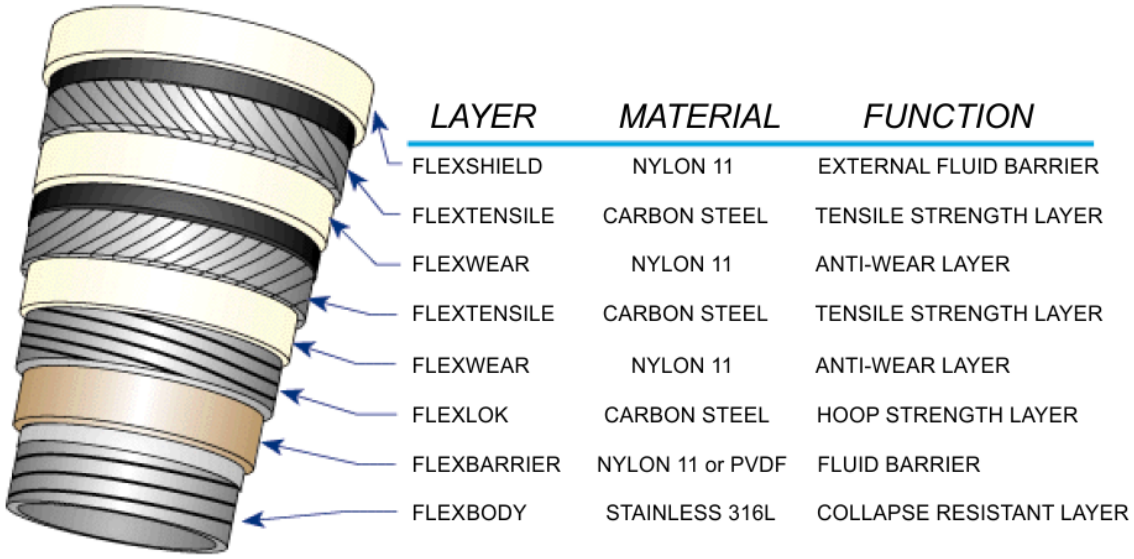

Figure 1.1. Representation of a typical unbonded flexible riser used for transport of fluids from the seafloor to floating platforms, adapted from Shen and co-workers.[1]

Along with a range of hydrocarbons, crude usually contains water and high partial pressures of 'sour' fluids including CO_2 and H_2S, typically at extreme pressures and high temperatures.[3] Flexible pipes are also used for injection of high pressure CO_2 into depleted oil wells for enhanced oil recovery, or to reduce emissions through carbon capture and storage.[4] Permeation of CO_2 and H_2S through the PA11 internal pressure sheath, in addition to water, may lead to corrosion of the steel armour layers and

subsequent failure of the riser.[5,6] Replacement of risers before failure is economically costly but necessary, in order to avoid ecological disaster and potential human casualties.[6] Increasing the safe operational lifetime of flexible risers is desirable. There is therefore great interest in improving the barrier performance of PA11, especially to CO_2 and H_2S at high temperatures and pressures.

A material that has shown extraordinary gas barrier performance on the nanoscale is graphene.[7,8] Defect-free, pristine graphene is even impermeable to helium atoms.[9,10] Since the isolation and characterisation of single and few layered graphene in 2004 by Novoselov *et al.*[7], many reviews of the properties and prospects of graphene have been carried out.[11–19] A simple search in Thompson Reuters' Web of Science for the word 'graphene', yields over 140,000 results.[20] Sorting by year yields Figure 1.2 that shows an almost exponential increase in publications, since the isolation of single layered graphene in 2004.[7] The impermeable nature of graphene makes it an ideal candidate as an additive, in order to improve the barrier performance of PA11.

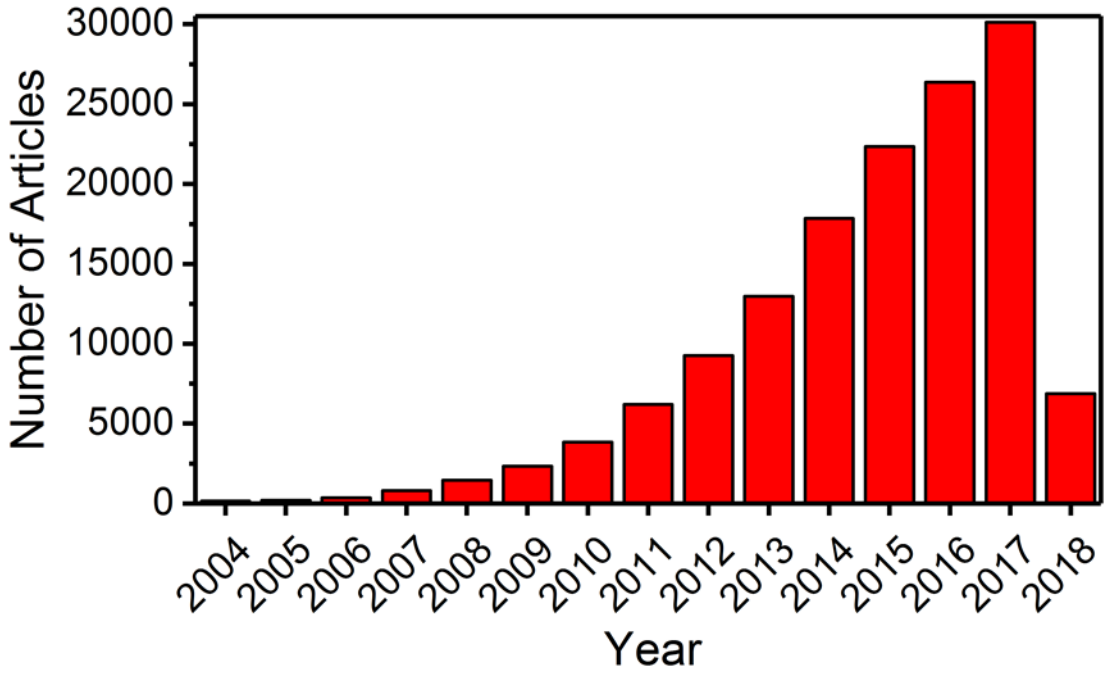

Figure 1.2. Graph of number of articles containing the topic 'graphene' found on the Web of Science as of 26/03/2018.[20]

1.3 Aims and Objectives

It is hypothesised that graphene may be incorporated with or applied to PA11 in order to improve its barrier performance. This thesis aims to examine the efficacy of graphene as such a barrier material, in order to increase the barrier properties of PA11 to high pressure (50 – 400 barg) CO_2 with 1.48% H_2S mixtures, and low pressure (2 barg) pure H_2S. The barrier properties of graphene and graphene related materials (GRMs) are examined under high pressure fluid mixtures in the supercritical regime, for the very first time. All permeability testing was carried out at TWI Ltd., Cambridge, on their specialist rig, designed specifically for high pressure testing of fluids including CO_2 and H_2S.

The aim of this work was to firstly synthesise functionalised GRMs. This was attempted by *in situ* polymerisation of PA11 monomer in the presence of graphitic materials.

Secondly, it was the aim of this work to incorporate a commercially available graphene into industrial grade PA11, with a view to creating a barrier material nanocomposite. Nanocomposite manufacture was achieved by utilising industrially relevant twin-screw extrusion. Permeability testing was carried out in order to investigate the barrier properties of the most promising nanocomposite.

The third aim of this work was to apply graphene coatings to PA11 in order to reduce the permeation of CO_2 and H_2S, while retaining the bulk properties of virgin PA11.

The fourth aim of this work was to block permeation of CO_2 and H_2S by using many layers of graphene. Sandwich structures comprising PA11 and multi-layer graphene materials were prepared and tested at pressures from 5 to 40 MPa (50 – 400 barg).

The fifth and final aim of this work was to evaluate the different methods of creating a graphene barrier, so that future research may pursue the most promising avenues of discovery.

1.4 Outline

Chapter 2 introduces PA11 and graphene, focussing on their properties. The theory of gas transport through polymer membranes is reviewed from the basics of permeation through to the measurement techniques used in this work. The barrier properties of

PA11 to sour gases, liquids and supercritical fluids are reviewed in order to create a baseline for the following chapters.

Chapter 3 investigates the synthesis of PA11 through melt polycondensation in the presence of graphene and graphene oxide to produce *in situ* polymerised functionalised GRMs. These *in situ* polymerised nanocomposites were evaluated.

Chapter 4 reports the incorporation of graphene into PA11 by twin-screw extrusion, an industrially relevant melt processing technique. Characterisation of the nanocomposites prepared through two different pre-mixing methods was carried out, and permeability testing of the most promising nanocomposite was performed at TWI.

Chapter 5 inspects the effect on fluid transport properties of applying graphene coatings onto the PA11 surface. The unusual bulk chemistry of PA11 and surface chemistry of the graphene coatings were explored, following permeability testing at TWI.

Chapter 6 investigates the incorporation of a graphene layer into a laminate structure, focussing on the barrier performance of these nanocomposites under high pressure testing at TWI.

Chapter 7 provides a discussion of the barrier performance of samples prepared for each chapter, in order to summarise the work undertaken. Conclusions are drawn and recommendations for future work proposed.

CHAPTER 2: LITERATURE REVIEW AND THEORY

2.1 INTRODUCTION

This chapter provides general background information on PA11 and graphene, which will be expanded in subsequent chapters when specific methods are utilised. The fundamentals of molecular transport are introduced along with key methodologies for the measurement of transport coefficients. The barrier performance of PA11 is examined in order to create a basis for the findings of this thesis.

2.2 POLYAMIDE 11

The semi-crystalline polymer PA11 was first synthesised by Genas in 1962 by the self-polycondensation of 11-aminoundecanoic acid (11-AUDA), shown in Figure 2.1.[21] 11-AUDA can be derived from castor oil, extracted from the castor bean. PA11 is therefore a biopolymer, with 100% renewable carbon content.[22] PA11 has a higher hydrocarbon to amide bond ratio than nylons with shorter repeat units. This means that PA11 absorbs less water than more common nylons such as nylon 6 or nylon 6-6.[23]

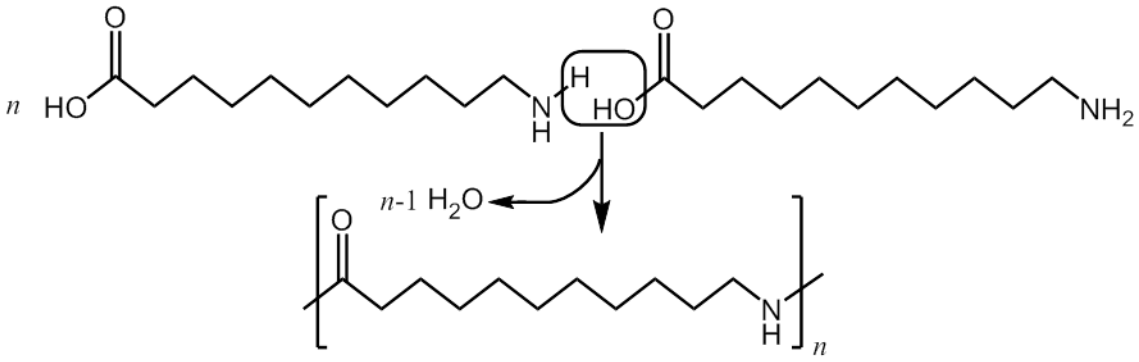

Figure 2.1. Polycondensation of *n* 11-AUDA monomers, through liberation of *n*-1 water molecules, to create PA11.

PA11 is chosen for use in the oil and gas industry due to its excellent properties, including low permeability, good resistance to aging, excellent mechanical properties and resistance to fatigue and creep.[24] Although typically used as an internal pressure

sheath, protecting against fluid permeation, PA11 can also be used in anti-wear layers as well as intermediate and external sheaths, as shown in Figure 1.1.[1]

A number of other polymers may be used as internal pressure sheaths, including high density polyethylene (HDPE), cross-linked polyethylene (XLPE), polyamide 12 (PA12) and polyvinylidene fluoride (PVDF).[25] The choice of polymer depends very much on the conditions expected for each particular application, and the polymer cost. The temperature classification of a few commonly used polymers is shown in Figure 2.2.[26] HDPE is used at low to moderate temperatures and is susceptible to plasticisation by the hydrocarbons found in crude mixtures. Cross-linking leads to some resistance to the absorption of hydrocarbons as well as greater thermal stability and thus, XLPE may be used at slightly higher temperatures, for example 60 – 90 °C. PA11 and PA12, although more stable to hydrolysis than shorter chained nylons, are still susceptible to hydrolysis at elevated temperatures. A lifetime of 20 years can be expected for a PA11 pipe exposed to an acidic, humid oil flow at 60 °C, although use at up to 100 °C is possible.[26] In extreme cases, PVDF can be used at temperatures up to 130 °C, however, it is very expensive (15 times more expensive per unit mass than HDPE).[27]

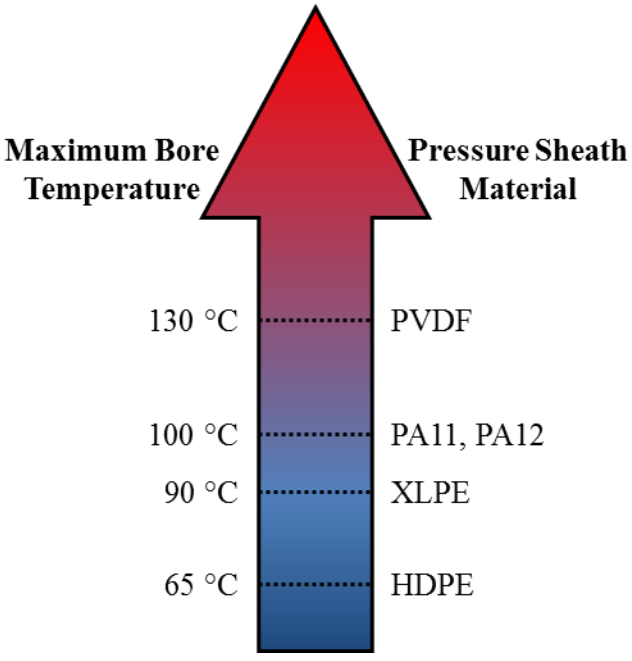

Figure 2.2. Schematic of polymer classification according to bore fluid temperature, redrawn from Taravel-Condat and Epsztein.[26]

Generally, oilfield fluids are found at temperatures less than 100 °C, however, pressures can reach over 100 MPa.[3] Currently, PA11 is the most commonly used polymer, with over two thirds of flexible oil risers utilising the material as an internal pressure barrier sheath.[2]

2.3 Graphene and Graphene Related Materials

2.3.1 Graphene

A graphene layer is, according to IUPAC:[28] "a single carbon layer of the graphite structure, describing its nature by analogy to a polycyclic aromatic hydrocarbon of quasi infinite size". A schematic of a single graphene layer, displaying the hexagonal connectivity between the carbon atoms, is shown in Figure 2.3.

First isolated and characterised in 2004,[7] graphene has a range of properties that make it suitable for myriad applications. One particularly interesting aspect of graphene is its complete impermeability to gases – modelling studies show that even defective graphene is impenetrable.[9,10,29] The perfect barrier performance of graphene on the nanoscale is limited by the size of the graphene flake. Such studies therefore provide a rationale for using graphene as a barrier material; however, they do not address scalability beyond single graphene flakes, towards the macroscale.

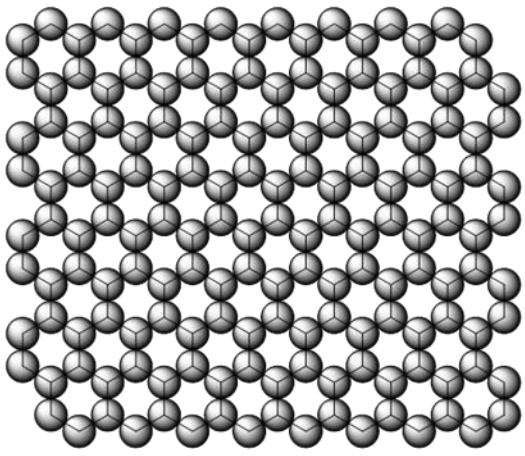

Figure 2.3. Schematic of a single graphene layer showing the linked hexagonal arrangement of carbon atoms.

There are four main ways to produce pristine graphene as outlined by Zhu *et al.*[15] and Park and Ruoff,[30] which can be separated into two groups – bottom-up or top-

down.[14,15,18,31] The bottom-up methods include epitaxial growth on metal surfaces using chemical vapour deposition (CVD) as well as epitaxial growth on SiC.[32] One top-down method is micromechanical exfoliation, for example, the 'scotch tape' method, employed by Novoselov and co-workers.[7,8] The second is solvent-aided exfoliation using mechanical shear, sonication, electrochemistry or intercalation to create suspensions of graphene from bulk graphite.[18,33,34] In practice, there may be many or few-layered graphene flakes in these suspensions. Thus the definition of 'graphene' has expanded to include a wide range of materials. Recently developed graphene nanoplatelets (GNPs) are an example of the new forms of graphene that have been made available. Produced by acid intercalation followed by thermal expansion,[35,36] GNPs have a typical thickness of 6 – 8 nm (approximately 20 graphene layers) and a range of lateral sizes.[37]

2.3.2 Graphene Oxide

Most graphene oxide (GO) syntheses rely on the oxidation of graphite in strong acids and oxidants to yield graphite oxide,[38–40] followed by exfoliation in highly polar organic solvents or, typically, water to yield GO.[41]

Unlike graphene, the structure of GO is poorly understood. It is typically considered to be a chemically functionalised graphene, containing a range of oxygen moieties at edges and on the basal plane – represented by the Lerf-Klinowski model, Figure 2.4.[42,43] These oxygen functionalities provide a range of positions for further chemical modifications, as reviewed by Dreyer and co-workers.[44,45] An alternative to the Lerf-Klinowski model has been proposed by Rourke *et al.*[41] where GO is suggested to consist of partially oxidised graphene like platelets onto which highly oxidised debris (OD) is strongly, yet non-covalently, bound. The rationale for this hypothesis is the ability to remove the OD through base washing of the as-produced GO (aGO). The subsequent isolation of both the graphene like material, that is, base-washed (bwGO), and the OD is possible at 64 ± 2% and 30 ± 9% of mass with respect to aGO, respectively.

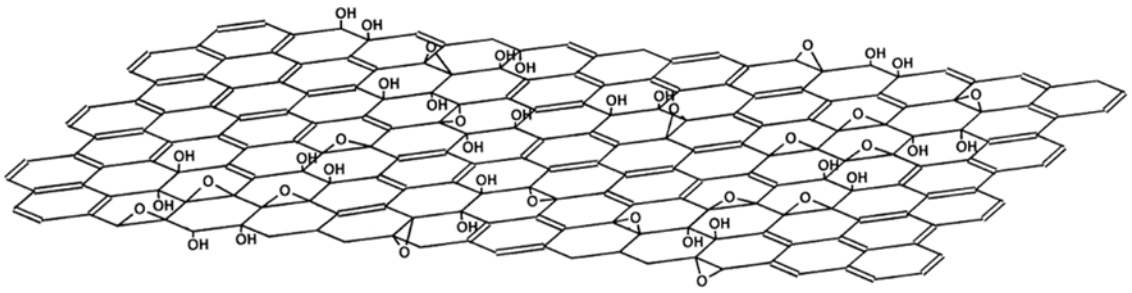

Figure 2.4. Structure of GO according to the Lerf-Klinowski model, reproduced from He and co-workers.[43]

Thermogravimetric analysis (TGA) of aGO, bwGO and OD can be seen in Figure 2.5. For aGO, the TGA showed a two stage degradation process starting at 200 °C, corresponding to degradation of oxygen containing groups, followed by a step at 600 °C, attributed to the decomposition of graphene like regions. The bwGO showed no weight loss at 200 °C, only a loss at 600 °C; whereas the OD displayed a loss at 200 °C, without a weight loss at 600 °C. These observations suggested that no oxygen functionalities were present in the bwGO, and that no graphitic regions were present in the OD. This comparison methodology was extended to Fourier Transform Infrared (FT-IR) spectroscopy, where the aGO spectrum was effectively a combination of the bwGO and OD spectra. This allowed the group to suggest that instead of the covalently functionalised model of GO that is usually reported, in fact the GO is made up of slightly oxidised graphitic sheets, non-covalently functionalised by the OD. The proposed GO structure is shown in Figure 2.6 and is similar to the Lerf-Klinowski model (Figure 2.4) with the addition of small highly oxidised molecules covering the lightly functionalised GO sheet.

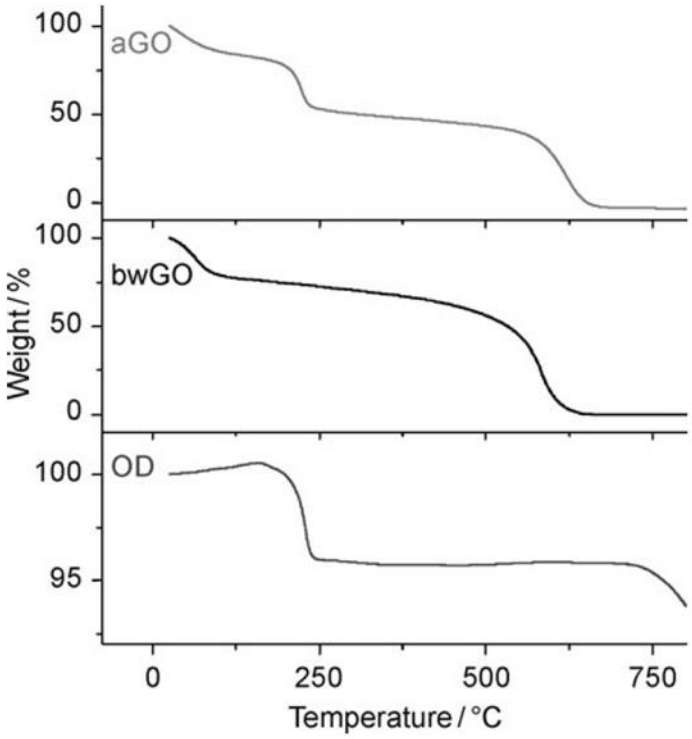

Figure 2.5. TGA degradation profile of the aGO, bwGO and OD showing that aGO is a combination of bwGO and OD. Extracted from Rourke and co-workers.[41]

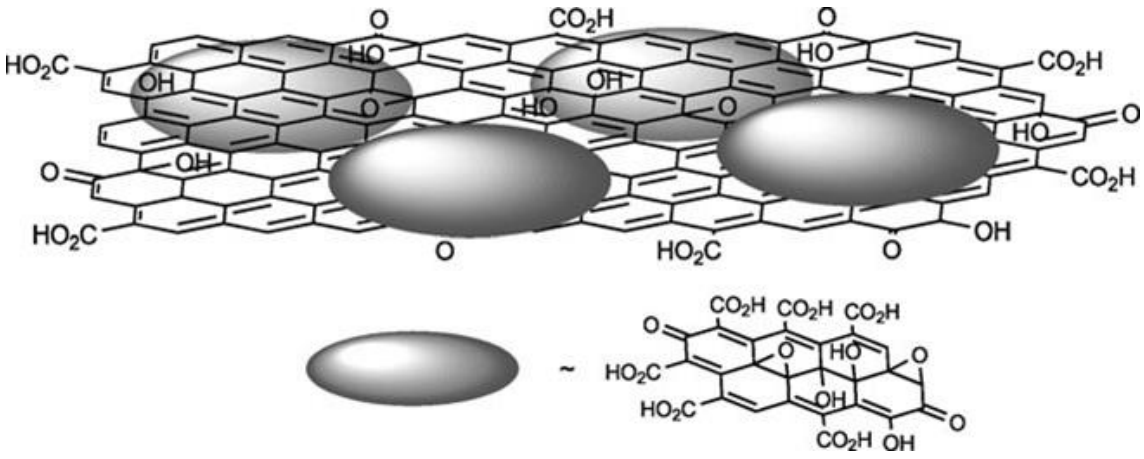

Figure 2.6. Schematic of the proposed aGO structure, showing a lightly functionalised graphitic sheet and stabilising OD. Reproduced from Rourke and co-workers.[41]

2.4 MOLECULAR TRANSPORT

2.4.1 SOLUTION-DIFFUSION MODEL

The solution-diffusion model describes the transport of ideal gas molecules through a non-porous membrane, based on the seminal work of Graham,[46,47] Mitchell,[48] and Fick,[49] in the early to mid-19th century. In 1829, Graham observed the inflation of a non-porous rubber bladder in an atmosphere of CO_2. Initially he postulated that water filled capillaries acted as canals for the transport of the CO_2 from the external atmosphere, through the membrane to the interior.[46] Mitchell then published a paper in 1830,[48] where he heavily criticised Graham on failing to examine the evidence effectively: "the failure, on the part of that intelligent and ingenious chemist, to pursue, in the only true spirit of science, the investigation of a principle, one of the most striking manifestations of which had thus been placed conspicuously before him". Mitchell suggested that the permeation of a gas through rubber was the same regardless of the water content, that is, the non-porous membrane had an intrinsic permeability. These observations led Fick in 1855,[49] to establish, by analogy to heat transfer by conduction, the mathematical representation of the solution-diffusion model, albeit for salts diffusing through a solvent. Although 'Fick's laws of diffusion' are quoted for the solution-diffusion model, Graham's paper in 1866 is regarded as the basis for membrane transport by the solution-diffusion model.[50] In this paper, Graham reported the following: "The first absorption of the gas by the rubber must depend upon a kind of chemical affinity subsisting between the material of the gas and the substance of rubber…" and "The rubber being *wetted through* by the liquefied gas, the latter comes to evaporate into the vacuum, and reappears as gas on the other side of the membrane. Now it is known that such evaporation is the same into the vacuum and into another gas, being equally gas-diffusion in both circumstances". These sentences contain the essence of the solution-diffusion model: firstly, gas absorption by the polymer at the high pressure side; secondly, gas diffusion through the polymer matrix; and finally, gas desorption from the low pressure side.

The mathematical description of the solution-diffusion model may be laid out as follows. Firstly, the flux across a membrane, *J*, can be defined as shown in Equation 2.1.[51] Where *Q* is the quantity of gas diffusing, *A* is the active membrane area, and *t* is time.

$$J = \frac{Q}{A.t}$$ Equation 2.1

The flux is governed by Fick's first law of diffusion as defined below.[49] The flux, *J*, is related to the concentration gradient, ∇C across the film in all directions at the steady state and the average diffusion coefficient, *D*, of the membrane material. This is schematically shown in Figure 2.7.

$$J = -D\nabla C$$ Equation 2.2

In the case of unidirectional diffusion in direction *x*, through a thin membrane, Equation 2.2 reduces to Equation 2.3 which includes the partial derivative of the concentration in only the *x* direction.[52]

$$J_x = -D\frac{\partial C}{\partial x}$$ Equation 2.3

Again, assuming unidirectional diffusion through a membrane of thickness, *l*, integration of Equation 2.2 leads to the relation shown in Equation 2.4. C_1 and C_2 are the upstream and downstream gas concentrations, respectively, as shown in Figure 2.7.[51]

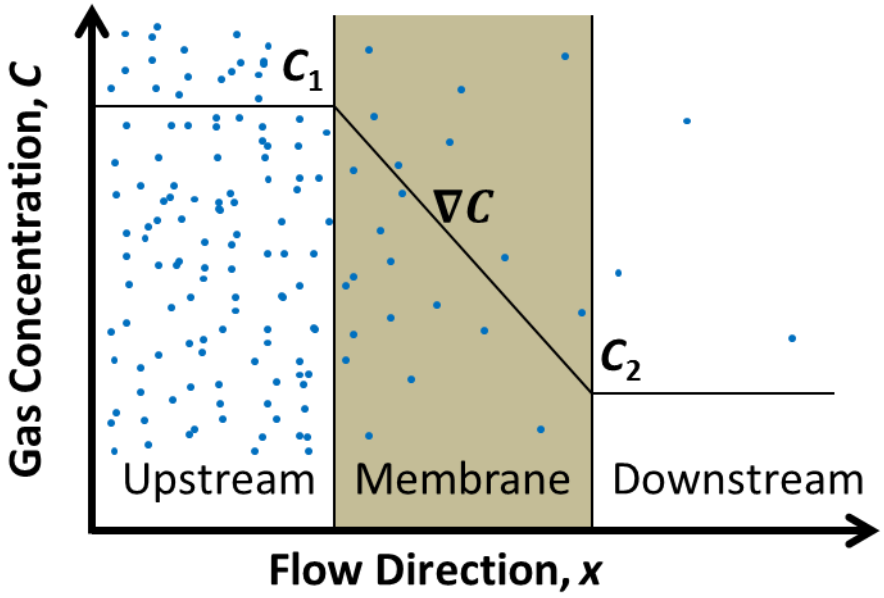

Figure 2.7. Schematic showing the relationship between the upstream and downstream concentrations and the concentration gradient across the membrane.

$$J\int_0^l \mathrm{d}x = -D\int_{C_1}^{C_2} \mathrm{d}C \qquad \text{Equation 2.4}$$

The result of the integration in Equation 2.4 leads to Equation 2.5:[51]

$$J = \frac{D(C_1 - C_2)}{l} \qquad \text{Equation 2.5}$$

Equation 2.6 shows how concentration is related to the partial pressure, *p*, according to Henry's law, where *S* is the average solubility coefficient.[51] Henry's law can be used assuming a linear relationship between concentration and partial pressure at the membrane surface.

$$C_n = S.p_n \qquad \text{Equation 2.6}$$

Through substitution of Equation 2.6 for C_n in Equation 2.5, the relation in Equation 2.7 can be derived[51]:

$$J = \frac{D.S(p_1 - p_2)}{l} \qquad \text{Equation 2.7}$$

In most cases, the upstream partial pressure (p_1) is much greater than the downstream partial pressure (p_2). In such a case, Equation 2.7 can be simplified to Equation 2.8, where p_1 is the partial pressure of the gas in the feed.[53]

$$J = \frac{D.S.p_1}{l} \qquad \text{Equation 2.8}$$

The terms *D* and *S* can be combined, producing the total permeability coefficient, *P*, where Equation 2.9 may be defined.

$$P = D.S \qquad \text{Equation 2.9}$$

As defined, the permeability coefficient depends on two competing factors. *D* is a kinetic term that describes the mobility of molecules through the polymer matrix. *S* is a thermodynamic term that describes the number of molecules that are sorbed into the polymer. Large permeability coefficients can therefore be due to a large *D* term, a large *S* term, or both – dependent upon specific polymer-penetrant interactions. Typically, *S* is large for heavy molecules that interact well with the polymer, for example CO_2, however, *D* is usually reduced due to these strong interactions. Conversely, *S* tends to be small for light, weakly interacting molecules such as He and H_2, however, *D* is high

for these molecules.[53] In the case of PA11, for example, the relative permeability, diffusion and solubility coefficients for a range of gases are ranked as follows:[54]

$P(\mathrm{He}) > P(\mathrm{CO_2}) > P(\mathrm{Ar}) > P(\mathrm{CH_4}) > P(\mathrm{N_2})$

$D(\mathrm{He}) >>> D(\mathrm{CO_2}) \approx D(\mathrm{Ar}) > D(\mathrm{N_2}) \approx D(\mathrm{CH_4})$

$S(\mathrm{CO_2}) >> S(\mathrm{CH_4}) \approx S(\mathrm{Ar}) > S(\mathrm{N_2}) > S(\mathrm{He})$

Note how the permeability values do not directly follow either the diffusion or solubility coefficients, and are rather a combination of the two.

Through combining Equation 2.8 and Equation 2.9 and equating to Equation 2.1, one may generate Equation 2.10.[54]

$$P = \frac{Q.l}{A.t.p_1} \qquad \text{Equation 2.10}$$

Comparing Equation 2.1 to Equation 2.10, *P* may be thought of as the pressure and thickness corrected flux, as shown in Equation 2.11. *P* is therefore a material property, rather than the specific membrane property.

$$P = \frac{J.l}{p_1} \qquad \text{Equation 2.11}$$

The permeability coefficient, *P*, is not to be confused with the permeance, *Π*, a term typically used in engineering that is membrane specific (Equation 2.12).[55] Comparing Equation 2.1 to Equation 2.12, one can see that the permeance is the flux corrected for the partial pressure or, through comparing Equation 2.10 and Equation 2.12, is the ratio of permeability to thickness.

$$\Pi = \frac{Q}{A.t.p_1} \qquad \text{Equation 2.12}$$

Permeance is a useful quantity for selecting a specific membrane for a specific application; whereas permeability allows for the selection of a promising material for a general application.

2.4.2 Modes of Sorption

There are a number of sorption modes that help to describe the way a polymer-penetrant system behaves. The simplest observed modes are Henry's Law sorption, Langmuir

mode sorption, and Flory-Huggins sorption, shown schematically in Figure 2.8a, b and c, respectively. Henry's Law (Equation 2.13) is applicable in cases of low concentration (and feed pressure) of solute in the polymer matrix.[56] Equation 2.13 shows a linear relationship between dissolved concentration (C_D) and pressure (p), scaling with Henry's Law parameter, k_D. For such sorption to be observed, the polymer-polymer interactions must be stronger than the polymer-penetrant and penetrant-penetrant interactions. It is therefore usually observed for weakly interacting, non-condensable gases, for example: He, H_2, N_2, O_2 and CH_4 in polymers above their glass transition temperature ($T > T_g$).[53]

$$C_D = k_D . p \qquad \text{Equation 2.13}$$

If polymer-penetrant interactions dominate, then Langmuir mode sorption (Figure 2.8b) can be used to describe the system behaviour.[52] This mode is typical for glassy polymers ($T < T_g$) where penetrant molecules occupy the free volume (micro-voids or frozen-in holes) between polymer chains and around fillers. Equation 2.14 shows how the concentration of solute adsorbed in holes (C_H) varies with pressure. The Langmuir sorption capacity constant (C'_H) characterises the excess volume present in the polymer in the glassy state. The Langmuir affinity constant, b, describes the polymer-penetrant interactions and can be correlated to the condensability of the penetrant in the polymer.[53]

$$C_H = \frac{C'_H . b . p}{1 + b . p} \qquad \text{Equation 2.14}$$

Flory-Huggins behaviour (Figure 2.8c) is typical for sorption within a polymer where $T > T_g$. Described by Equation 2.15, Flory-Huggins sorption occurs when penetrant-penetrant interactions are stronger than penetrant-polymer and polymer-polymer interactions.[52] This results in either: clustering of penetrants within the polymer matrix; or plasticisation of the polymer.

$$\ln a = \ln(p/p_s) = \ln \phi_v + (1 - \phi_v) + \chi(1 - \phi_v)^2 \qquad \text{Equation 2.15}$$

The vapour phase penetrant activity, a, is equal to the quotient of the feed pressure, p, to the saturation pressure, p_s, the pressure at which the vapour phase and dissolved gas within the polymer is at equilibrium. ϕ_v is the volume fraction of solute within the matrix and χ is the Flory-Huggins penetrant-polymer interaction parameter.

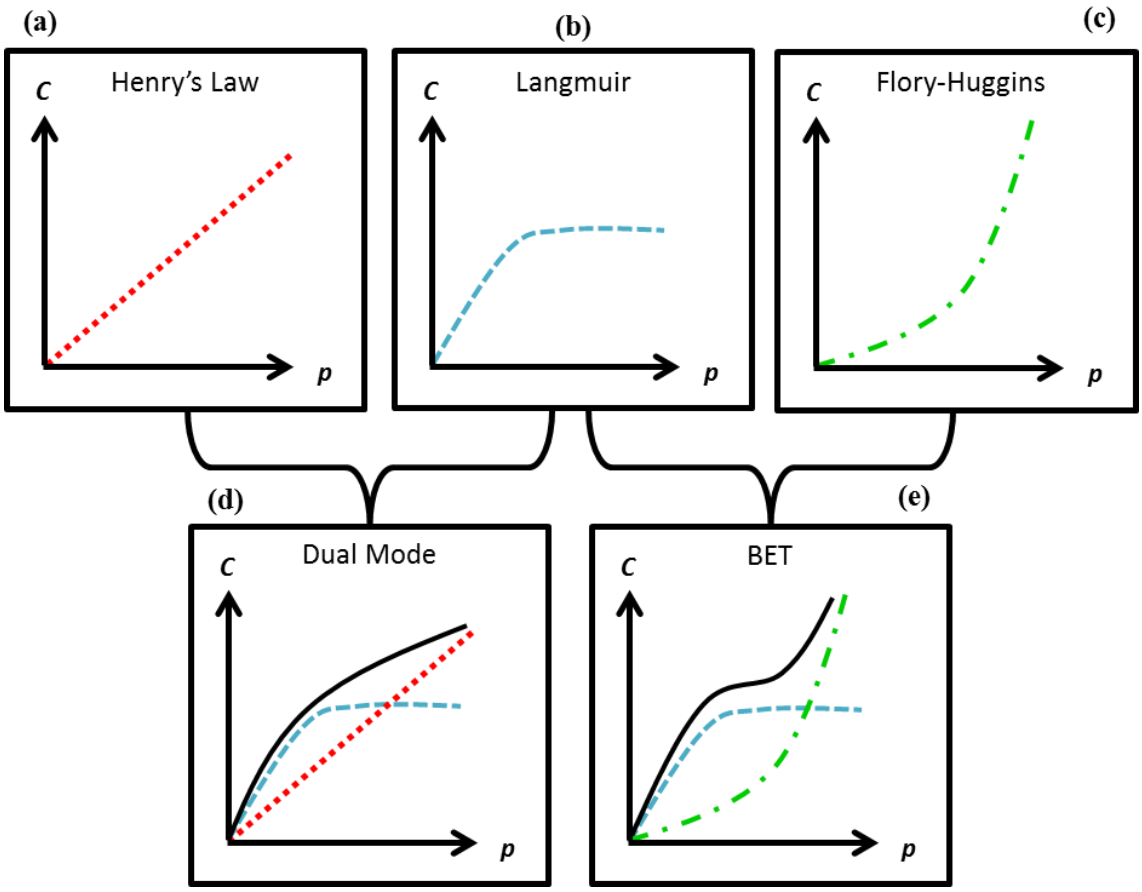

Figure 2.8. Schematics of common sorption modes. (a) Henry's Law sorption; (b) Langmuir sorption; (c) Flory-Huggins sorption; (d) Dual Mode sorption; and (e) BET sorption.

Not all real-world sorption isotherms correlate to the simple isotherms in Figure 2.8a, b and c. Dual mode sorption (Figure 2.8d) can be fitted to data that exhibits a deviation from Henry's Law linearity, empirically derived by Barrer *et al.*[57] in 1958. Mathematically, it is simply the sum of Henry's Law (Equation 2.13) and Langmuir mode sorption (Equation 2.14) as shown in Equation 2.16. Dual mode sorption allows for both classical diffusion of dissolved molecules as well as diffusion of penetrants that jump between micro-voids. The populations of molecules in each state are in local equilibrium with one another.

$$C = C_{\mathrm{D}} + C_{\mathrm{H}} = k_{\mathrm{D}}.p + \frac{C'_{\mathrm{H}}.b.p}{1 + b.p} \qquad \text{Equation 2.16}$$

Substituting for C through Equation 2.6 gives Equation 2.17 which shows the inverse dependence of S upon p.[52]

$$S = k_{\mathrm{D}} + \frac{C'_{\mathrm{H}}.b}{1 + b.p}$$ Equation 2.17

Diffusivity may also be affected by increasing feed pressure. Increases in free volume through plasticisation due to strong penetrant-polymer interactions lead to greater chain mobility and so faster diffusion rates. Alternatively, strong penetrant-penetrant interactions may lead to a reduced diffusion coefficient as large penetrant clusters have a reduced diffusivity.[53]

The effect of pressure upon the permeability coefficient depends on the effect of *p* upon *D* and *S*. Should plasticisation occur, the diffusion term increases the permeability of the system, as pressure increases. The permeability of a system can also decrease with increasing pressure, as has been observed for some glassy polymers.[53]

Through combination of the two non-linear modes – Langmuir and Flory-Huggins sorption – Brunauer-Emmett-Teller (BET) mode sorption can be modelled (Figure 2.8e). This is indicative of strong sorption of molecules to sites within a polymer at low pressure, followed by clustering of molecules at higher pressure.[52] Table 2.1 summarises the sorption modes described in this chapter, along with the dominant interactions associated with each.

Table 2.1. Summary of sorption modes and the dominating physical interactions for each system.[52]

Sorption mode	Dominating interactions
Henry's	Polymer-polymer
Langmuir	Penetrant-polymer
Flory-Huggins	Penetrant-penetrant
Dual Mode	Combination of Henry's and Langmuir modes
BET	Combination of Langmuir and Flory-Huggins modes

2.4.3 Time-Lag Method

First developed by Daynes in 1920,[58] the time-lag method follows the transport of molecules through a membrane with time. Within the time-lag method, there are two separate experimental techniques that can be used: the manometric technique; and the continuous flow technique. The manometric technique measures the change in pressure with time of a constant volume which can be either upstream or downstream of the

membrane. The continuous flow technique monitors the transport of molecules into a flow stream on the downstream side of the membrane, that goes on to be analysed by gas chromatography. One of the main advantages of the continuous flow method over the manometric technique, is that the chemical make-up of the permeate can be evaluated, and so mixed gas systems can be investigated. Additionally, detection to sub ppm levels means that the continuous flow method has greater sensitivity than that achieved by pressure transducers. The theory for both methods is the same. Firstly, a period of transient flux is observed where the flux alters with time, until eventually a steady state is reached and the flux is constant. At time, *t*, the quantity of gas diffusing, *Q*, for membrane thickness, *l*, is defined in Equation 2.18.[59] Where C_0 is the concentration of permeating gas initially in the membrane, C_1 and C_2 are upstream and downstream concentrations, respectively. In this work, the sweep gas removes the permeate immediately, thus $C_2 = 0$.

$$Q = \int_0^t -D\left(\frac{\partial C}{\partial x}\right)_{x=l} \mathrm{d}t$$

$$= D(C_1 - C_2)\frac{t}{l} + \frac{2l}{\pi^2}\sum_{n=1}^{\infty}\frac{C_1.\cos n\pi - C_2}{n^2}\left\{1 - \exp\left(-\frac{Dn^2\pi^2 t}{l^2}\right)\right\} \qquad \text{Equation 2.18}$$

$$+ \frac{4l.C_0}{\pi^2}\sum_{m=0}^{\infty}\frac{1}{(2m+1)^2}\left\{1 - \exp\left(-\frac{D(2m+1)^2\pi^2 t}{l^2}\right)\right\}$$

In instances where $C_0 = C_2 = 0$, that is, if the membrane and downstream contain no molecules of interest, Equation 2.18 reduces to that shown in Equation 2.19. Comparing Equation 2.18 to Equation 2.19, it can be seen that the final term for C_0 corrects the measured diffusion coefficient for a system already with a concentration of penetrants in the membrane.

$$Q = \frac{D.t.C_1}{l} - \frac{l.C_1}{6} - \frac{2l.C_1}{\pi^2}\sum_{n=1}^{\infty}\frac{(-1)^n}{n^2}\exp\left(-\frac{D.n^2.\pi^2.t}{l^2}\right) \qquad \text{Equation 2.19}$$

At the steady state, *t*, tends to be very large, so the exponential term approaches zero and so Equation 2.19 reduces to the linear Equation 2.20.

$$Q = \frac{D.C_1}{l}\left(t - \frac{l^2}{6D}\right)$$ Equation 2.20

The point at which the linear equation from the steady state crosses the time axis, that is, when $Q = 0$, is defined as the time-lag, Θ, as shown in Equation 2.21.

$$\Theta = \frac{l^2}{6D}$$ Equation 2.21

Through simple rearrangement of Equation 2.21, the value of the D can be calculated. The gradient of the linear equation at the steady state, that is, the value of Q at time t can be used to calculate P according to Equation 2.10. S may then be deduced as the ratio of P over D as a rearrangement of Equation 2.9 shows.

If $C_0 > 0$ and $C_2 = 0$ then Equation 2.18 may be solved as $t \rightarrow \infty$ to yield:

$$Q = \frac{D.C_1}{l}\left(t - \frac{l^2}{6D} + \frac{l^2 C_0}{2DC_1}\right)$$ Equation 2.22

Equation 2.22 contains the correction term for calculating the diffusion coefficient when there are already molecules of interest within the membrane. As for Equation 2.20, Equation 2.22 may be equated to zero, to yield the time-lag, Θ:

$$\Theta = \frac{l^2}{D}\left(\frac{1}{6} - \frac{C_0}{2C_1}\right)$$ Equation 2.23

The correction term $C_0/2C_1$ tends to zero when the concentration of permeants in the membrane is far smaller than the feed concentration, a case that is typical in high pressure testing. For the derivation of Equation 2.23 from Equation 2.18 and an estimation of the effect of C_0 on the measured diffusion coefficient, see Appendix A.

2.5 Transport Properties of Polyamide 11

2.5.1 Barrier Properties

Only a handful of publications have investigated the barrier performance of PA11 to sour gases and fluids.[3,24,54,60,61] The CO_2 permeability results in the literature are displayed in Table 2.2. Table 2.2 shows that there is a wide range of different permeability coefficients for CO_2 within the literature.[3,24,54,60,61]

Many of the differences between the values may be due to the use of different PA11 grades or different plasticiser loadings. Plasticisers are small molecules that are added to polymers in order to improve various properties ranging from processability to flexibility.[62] Typically, plasticisers increase the permeability of a polymer by disrupting chain packing and increasing the free volume within the polymer matrix. Flaconnèche *et al.* investigated the effect of plasticiser loading on the permeability of PA11.[54] As can be seen in Table 2.3, the CO_2 permeability coefficient is increased by a factor of five from the value at 0 wt% plasticiser loading to the value at 29.5 wt% loading.

Despite this, the CO_2 results in Table 2.2 show a large disparity between the results of Andersen *et al.*[61] and the supplier's data and the other publications.[3,24,54,60] Of course, direct comparison between the results is difficult due to the differences in temperature and pressures applied during testing. There does seem to be, however, an order of magnitude disparity between the Andersen *et al.*[61] results and the other results.[3,24,54,60] For example: the permeability of CO_2 at 10 MPa and 70 °C is 343×10^{-16} mol m^{-1} s^{-1} Pa^{-1} from Andersen *et al.*[61] whereas the supplier data under the same conditions is over an order of magnitude lower at 22×10^{-16} mol m^{-1} s^{-1} Pa^{-1}. The supplier data is more in line with the results of Dawans *et al.*[3] measured at 10 MPa and 75 °C of 23×10^{-16} mol m^{-1} s^{-1} Pa^{-1}. The permeability values at 50 °C for Ash *et al.*[60] and Dawans *et al.*[3] are almost identical to within a factor of two of one another, as are the results at 60 °C for Ash *et al.*[60] and the Rilsan® handbook.[24] The permeability values found by Flaconnèche *et al.*[54] are also comparable to the values in the Rilsan® handbook at 4 MPa and 61 – 71 °C.[24] These differences are well within the factor of five difference due to different loading plasticisers in the PA11, as shown by the data in Table 2.3.[54] For a consistent pressure, the effect of increasing temperature is to increase the permeability of CO_2. Increasing the pressure under an isotherm also increases the permeability, according to the data of Andersen *et al.*[61].

Table 2.2. Variation of the permeability of PA11 to CO_2 found within the literature.

T (°C)	p (MPa)	P_{CO2} (10^{-16} mol m^{-1} s^{-1} Pa^{-1})	Publication
40	0.02*	3.4	Ash *et al.*[60]
50	0.02*	4.8	
60	0.02*	7.2	
71	4.2	10	Flaconnèche *et al.*[54]
101	4.3	24	
121	3.8	44	
131	4.0	53	
70	2.5	101	Andersen *et al.*[61]
70	5.0	255	
70	7.5	343	
70	10	343	
70	10	22†	
25	10	3.7‡	Dawans *et al*.[3]
50	10	10‡	
75	10	23‡	
100	10	45‡	
41	4.1	6.6	Rilsan® handbook[24]
60	3.9	20	
61	3.9	19	
79	4.0	44	
80	3.9	41	

*Test pressure range difference to evacuated side 0.004 – 0.02 MPa, maximum pressure difference quoted.[60]
†Supplier data from Andersen paper.[61]
‡Extracted using https://automeris.io/WebPlotDigitizer/ from plot in the Dawans and co-workers paper.[3]

Table 2.3. Effect of plasticiser (n-butyl-benzene-sulfonamide) loading on the permeability of CO_2 through PA11, measured at 120 °C and 4 MPa.[54]

Plasticiser Loading (wt%)	P_{CO2} (10^{-16} mol m^{-1} s^{-1} Pa^{-1})
0	47
7.5	100
12.5	160
19	160
29.5	230

Table 2.4 contains permeability coefficients for H_2S through PA11 found in the literature.[3,24] If plasticisers affect the permeation of H_2S to the same extent as CO_2, then the values at 75 °C and 10 MPa for Dawans *et al.*[3] and 80 °C and 10 MPa for the Rilsan® handbook are well within a factor of five.[24] Under an 80 °C isotherm, the permeation of H_2S through PA11 is increased, with increasing pressure, according to

the data from Rilsan® handbook.[24] This suggests that high concentrations of H_2S strongly plasticise PA11, leading to an increase in permeation.

Table 2.4. Variation of the permeability of PA11 to H_2S found within the literature.

T (°C)	p (MPa)	P_{H2S} (10^{-16} mol m^{-1} s^{-1} Pa^{-1})	Publication
25	10	19*	Dawans *et al.*[3]
50	10	50*	
75	10	110*	
100	10	220*	
80	3.9	170	Rilsan® PA11 in Oil & Gas[24]
80	4.0	200	
80	4.1	190	
80	9.2	340	
80	10	290	
80	10	300	

*Extracted from plot in Dawans *et al.*[3]

2.5.2 Calculation of Activation Energies

In rubbery and glassy polymers, the transport of penetrants through the polymer is thermally activated and governed by the Arrhenius-van't Hoff equations below:[53,63–65]

$$P(T) = P_0 \exp\left(-\frac{E_P}{RT}\right) \quad \text{Equation 2.24}$$

$$D(T) = D_0 \exp\left(-\frac{E_D}{RT}\right) \quad \text{Equation 2.25}$$

$$S(T) = S_0 \exp\left(-\frac{\Delta H_S}{RT}\right) \quad \text{Equation 2.26}$$

Where $P(T)$, $D(T)$ and $S(T)$ are the permeability, diffusion and solubility coefficients at temperature, T. P_0, D_0 and S_0 all represent the transport coefficients at infinite molecular movement, that is, as $T \rightarrow \infty$. R is the ideal gas constant = 8.314 J K^{-1} mol^{-1}. The activation energy of permeation E_P is the sum of the activation energy of diffusion, E_D, and the heat of solution, ΔH_S:[52]

$$E_P = E_D + \Delta H_S$$ Equation 2.27

By plotting the natural logarithm of *P*, *D* and *S* against 1/*T*, the exponential terms in Equation 2.24, Equation 2.25 and Equation 2.26 may be found. Example plots and results, from the literature are shown in Figure 2.9 and Table 2.5.[54,60]

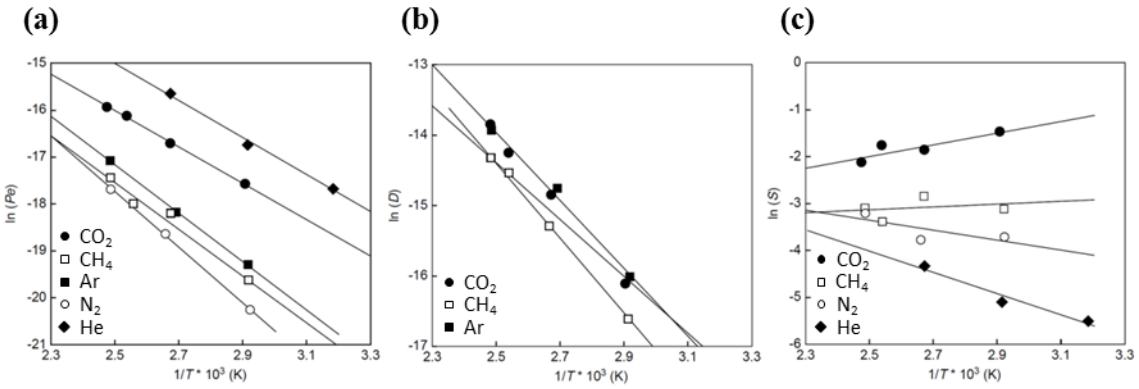

Figure 2.9. Plots extracted from Flaconnèche *et al.* for PA11 of the natural logarithm of (a) permeability coefficient; (b) diffusion coefficient; and (c) solubility coefficient, *versus* 1/*T*.[54]

Table 2.5. Activation energies for permeability, diffusion and heats of solution in PA11.[54,60]

Gas	$E_P^{\dagger}$ (kJ mol^{-1})	$E_P^{\ddagger}$ (kJ mol^{-1})	$E_D^{\dagger}$ (kJ mol^{-1})	$E_D^{\ddagger}$ (kJ mol^{-1})	$\Delta H_S^{\dagger}$ (kJ mol^{-1})	$\Delta H_S^{\ddagger}$ (kJ mol^{-1})
He	28	28	13	22	16	5
Ar	43	42	41	41	-2	-3 – -1
N_2	42	N/A*	45	N/A*	-3	N/A*
CH_4	42	N/A*	46	N/A*	-4	N/A*
CO_2	35	34	40	52	-10 – -4	-18 – -13

*Not determined
†Flaconnèche *et al.*[54]
‡Ash *et al.*[60]

2.6 Polyamide 11 Crystallinity

The crystallinity of any polymeric barrier material is important as permeation is assumed to be limited, almost exclusively, to the amorphous regions of the polymer. In fact, it may be that the crystalline regions of a polymer actually act as impermeable

barriers to permeation, increasing the tortuosity of diffusion, much like a heterogeneous filler. It is therefore important to introduce crystallinity within this literature review.

The nomenclature used for describing the crystal structures in PA11 is rather confusing, with many groups erroneously using terms interchangeably. Yu *et al.*[66] define a range of crystallinities in 1998 from the early work done on PA11: α crystallinity is the result of annealing a quenched polymer (at temperatures below the melt point) or solution casting from *m*-cresol. α' crystallinity results from slow cooling from the melt. δ crystallinity is the high temperature version of α' crystallinity, found above the Brill transition. δ' crystallinity is the result of fast quenching the melt (for example, with iced water). Casting from trifluoroacetic acid results in γ crystallinity. Regardless of this, a number of publications erroneously label crystals resulting from cooling from the melt as α crystals,[67–75] despite systematic differences between these crystals and those cast from *m*-cresol.[76] This may stem from the nomenclature for PA6 in which α crystallinity does, indeed occur when cooling from the melt.[77] A few papers do recognise the difference between α and α' crystallinity,[77–80] the study by Pepin *et al.*[77] is particularly rigorous and is detailed below.

Pepin *et al.*[77] prepared three different PA11 samples: PA11-α, cast from *m*-cresol; PA11-α', cooled slowly from the melt; and PA11-δ', quenched from the melt. Figure 2.10 shows X-ray diffraction (XRD) diffractograms of the PA11-α and PA11-α' heating and cooling runs to below the melt point. As can be seen in Figure 2.10a α crystallinity retains its double peak appearance whereas the α' transforms reversibly into δ crystallinity at around 95 °C, the so-called Brill transition. The Brill transition effectively allows rearrangement of the hydrogen bonding in the crystalline phases; in PA11, the triclinic α' crystals are transformed into pseudo-hexagonal δ crystals. They also noted a bimodal melting peak in the differential scanning calorimetry (DSC) data for α', whereas α displayed a single melting peak. The double melt peak suggested that upon heating the δ crystals (high temperature α'), α' crystals that had not enough time to rearrange into δ crystals melted first, followed by the more stable δ crystals at high temperature. This means that bimodal melting peaks are likely to occur when α' crystallinity is observed at room temperature, rather than α or δ'.

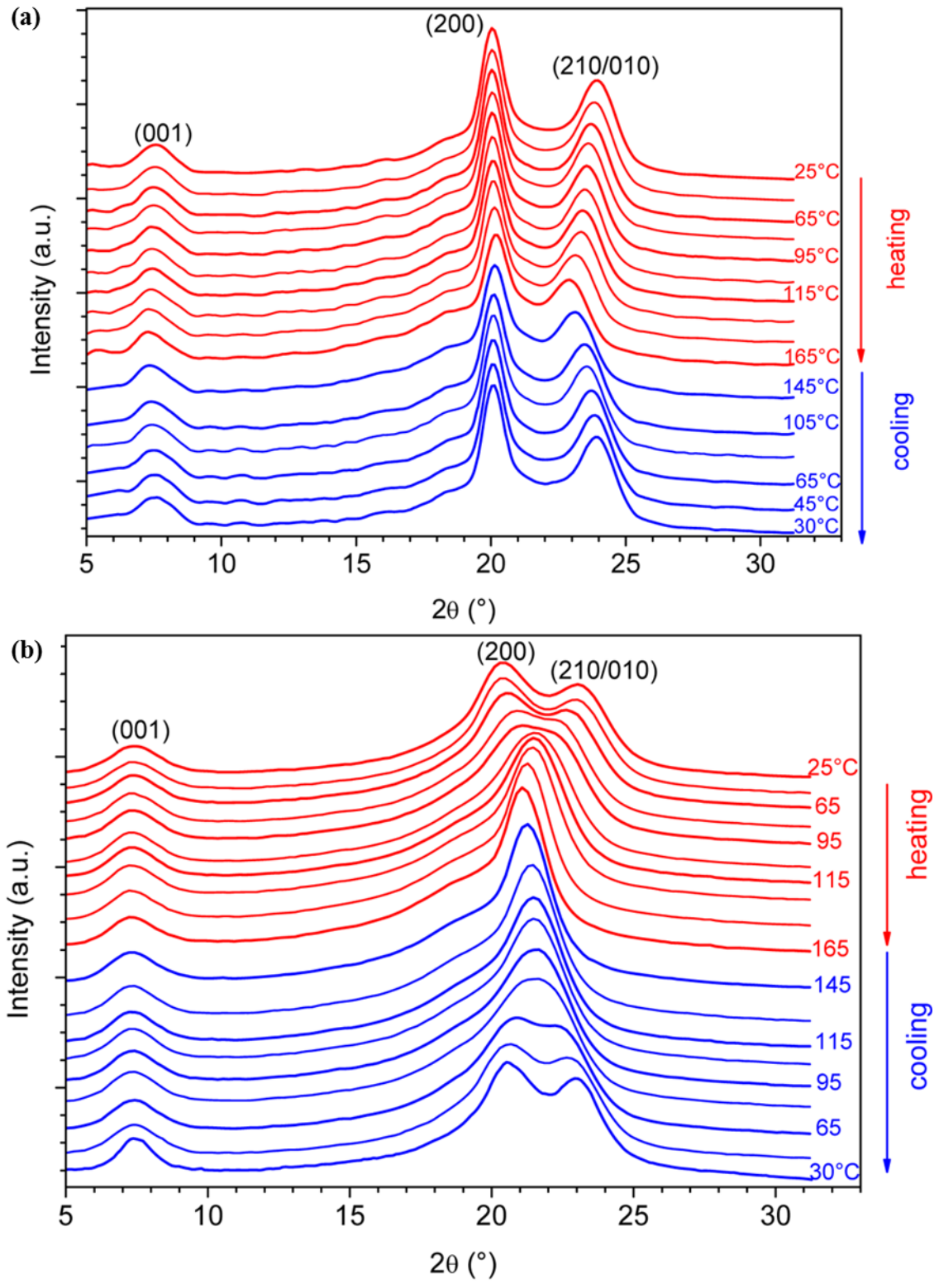

Figure 2.10. Change in the wide angle XRD diffractograms as (a) PA11-α and (b) PA11-α' is heated and cooled through the Brill transition, extracted from Pepin *et al.*[77].

2.7 RAMAN SPECTROSCOPY

Raman spectroscopy is an important characterisation method used to characterise graphene and GRMs.[81] Raman spectroscopy allows information regarding the number of layers, defects, chemical modification, strain and edges to be elucidated.[82] Graphene, or rather, 'non-pristine' graphene is characterised by the D, G and 2D peaks (Figure 2.11). The D band at ≈ 1350 cm^{-1} gives a measure of defects or functionality. The G band at ≈ 1600 cm^{-1} provides a measure of non-defective sp^2 regions. A ratio of the intensities of the D and G band, $I(D)/I(G)$, gives an indication of the amount of defects present, with large values for many defects and low values for few defects.[83] Typically, increasing the defects or degree of oxidation leads to an increase in the $I(D)/I(G)$ ratio, whereas thermal or chemical reduction leads to a decreased $I(D)/I(G)$ ratio.[84] The 2D band shifts its shape, position and intensity depending on the number of layers present.[82] For example, the 2D peak of single layer graphene has a full width half maximum (FWHM) of typically < 30 cm^{-1}, AB stacked bilayer graphene has FWHM ≈ 50 cm^{-1} and twisted bilayer graphene has FWHM ≈ 70 cm^{-1}.

Although Raman spectroscopy is possibly the most important diagnostic tool for graphene, Raman spectroscopy is simply one method used to characterise GO.[85] Raman spectroscopy gives an indication of the defects present in GO, however, cannot distinguish oxygen defects from permanent structural defects. With this in mind, there is often only a small difference in Raman spectra of GO and thermally reduced GO (trGO). Often the 2D band is reduced or not observed for GO due to disruption of the stacking order during the oxidation reaction.[84]

Figure 2.12 shows the stretching modes that yield the peaks observed in graphene.[86] The A_{1g} symmetric breathing mode of the D peak is shown in Figure 2.12a. The D peak mode is forbidden in perfect graphene and requires defects or edges to be present in order to activate it. According to Malard *et al.*[87], the activation of the D band arises from inelastic electron-phonon scattering followed by elastic defect scattering. The G peak is indicative of graphitic regions and is due to all sp^2 carbon atom pairs stretching in-plane (Figure 2.12b). This anisotropic stretch is Raman active and so is seen regardless of defects. The 2D peak occurs due to the inelastic scattering of an electron with two phonos.[87]

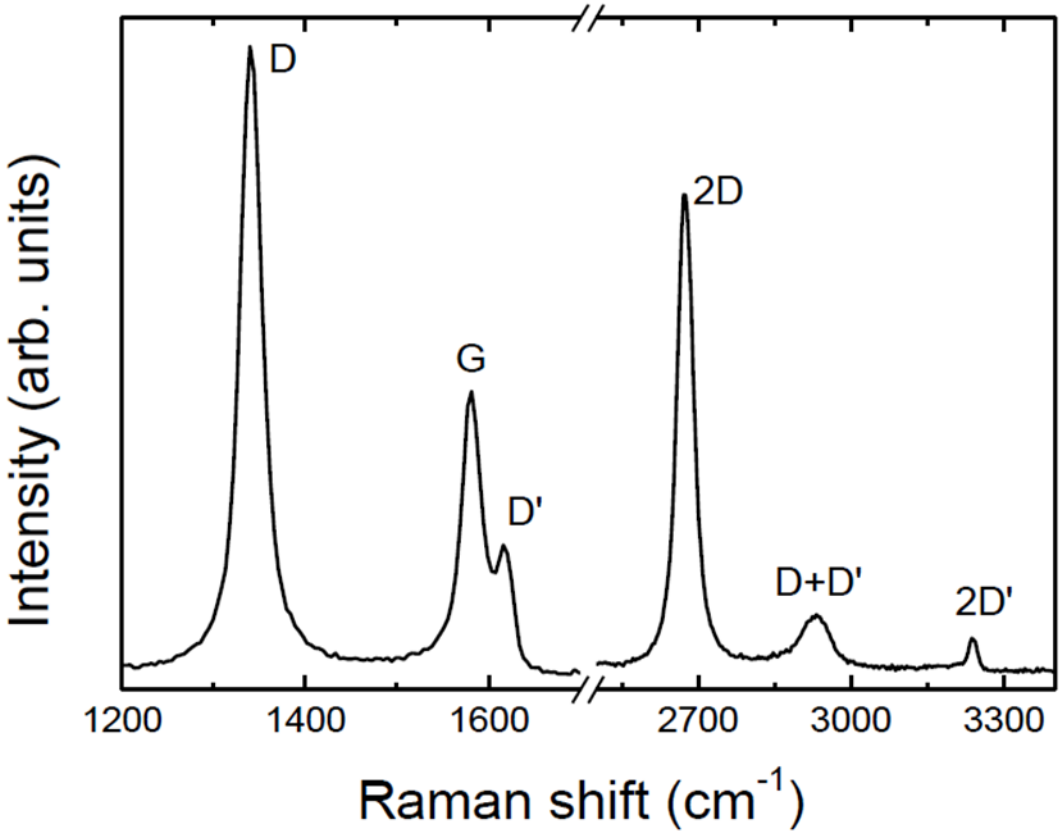

Figure 2.11. Plot showing the indicative D, G and 2D peaks found in graphene. Extracted from Eckmann.[82]

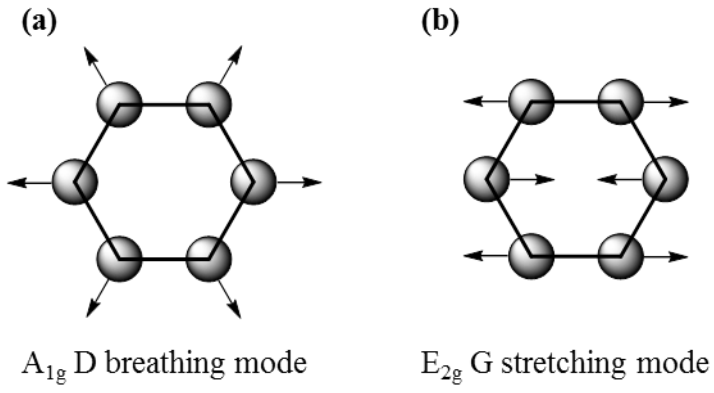

Figure 2.12. Schematics of the D band and G band vibrations, redrawn from Ferrari and Robertson.[86]

2.8 PROPERTIES OF GASES AND GAS MIXTURES

2.8.1 PHASE CHANGES OF CO_2

As noted in the section 1.3, the permeability of CO_2 and H_2S is very important in the present work. CO_2 with 1.48% H_2S at 60 °C was used for the majority of the permeation studies under a range of pressures. At standard temperature and pressure (STP), CO_2 is in the gas phase; however, as shown in its phase diagram (Figure 2.13), CO_2 also exists in solid, liquid and supercritical phases dependent upon conditions.[88] At 60 °C, and pressures up to the critical pressure, p_C (7.39 MPa), CO_2 is in the gaseous phase. At 60 °C and pressures greater than p_C, CO_2 is in the supercritical phase. Note that at pressures that are far higher than p_C, the solid phase returns, as shown in Figure 2.13.

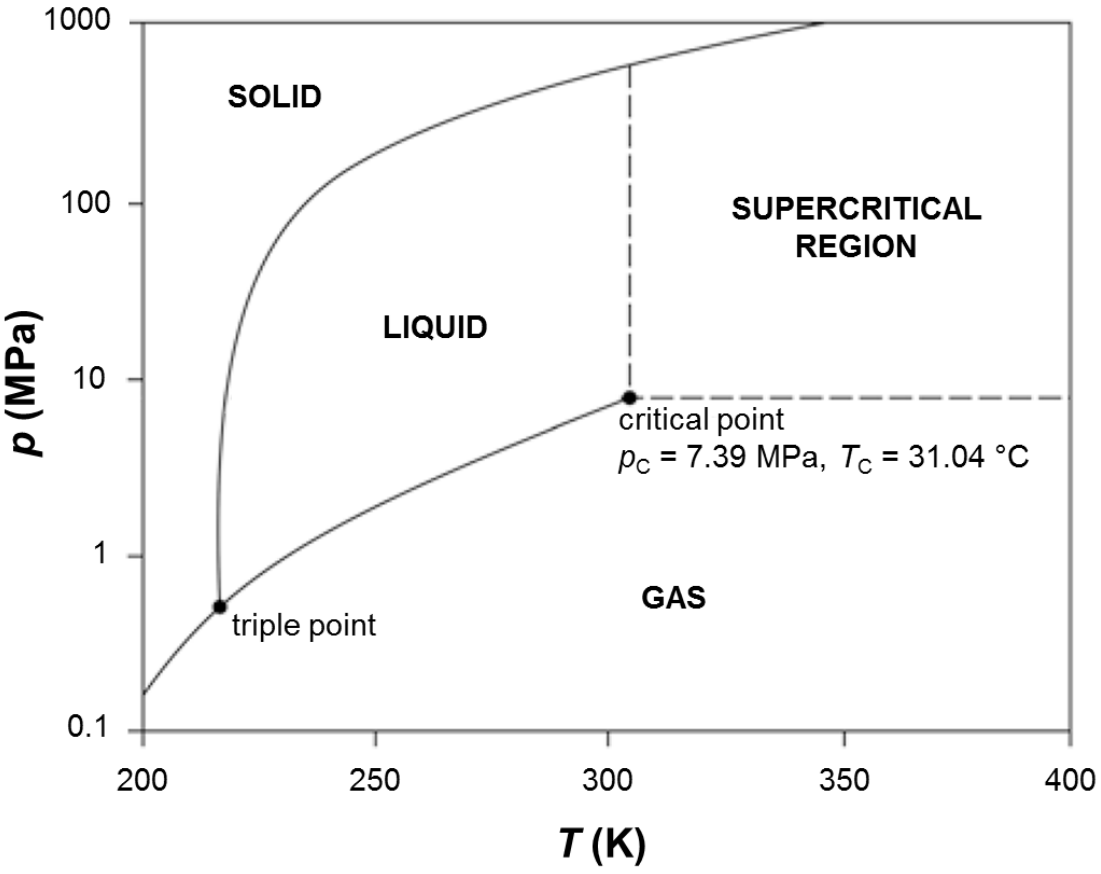

Figure 2.13. CO_2 phase diagram taken from "Advances in Carbon Dioxide Compression and Pipeline Transportation Processes" and modified.[88] Note the log scale pressure axis.

A supercritical fluid is defined as "… a compound, mixture or element above its critical pressure and critical temperature".[89] Supercritical fluids have a number of characteristics that make them both liquid-like and gas-like.[90] For example, they have

densities and solvating power comparable to liquids; however, they usually have viscosities at least an order of magnitude lower than liquids. Supercritical fluids also expand to fill their containers, like gases. Some relative properties for liquids, gases and supercritical fluids are shown in Table 2.6.[26] Supercritical CO_2, due to its relatively ambient critical point is suitable for a range of applications including chemical extractions and chemical reactions.[90,91]

Table 2.6. Approximate relative properties of liquids, supercritical fluids and gases, adapted to Taravel-Condat and Epsztein.[26]

Properties	**Units**	**Liquid**	**Supercritical fluid**	**Gas**
Density	$g\ cm^{-3}$	1	0.1 – 0.5	0.001
Self-Diffusivity	$cm^2\ s^{-1}$	0.00001	0.001	0.1
Viscosity	Pa s	0.001	0.00001	0.000001

2.8.2 Phase Behaviour of CO_2 and H_2S Mixtures

The critical point may change in the CO_2 phase diagram upon the addition of a small amount of contaminant.[88] Sobocinski and Kurata investigated the change in phase behaviour of CO_2 and H_2S mixtures at temperatures and pressures near the critical point.[92] As the mole fraction of H_2S increased, the critical point increased in temperature and pressure (Figure 2.14). Mixture G contained the lowest loading of H_2S (9.05%), which is greater than the 1.48% H_2S used in this work. With 9.05% H_2S in CO_2, the location of the critical point is similar to that of pure CO_2, as indicated by the intersecting dotted red lines.

These data suggest that the CO_2 with 1.48% H_2S mixture used in this work behaves very similarly to pure CO_2. Therefore, at 60 °C and 5 MPa, the CO_2 and 1.48% H_2S mixture is gaseous, and at 10 MPa and above, the mix is supercritical.

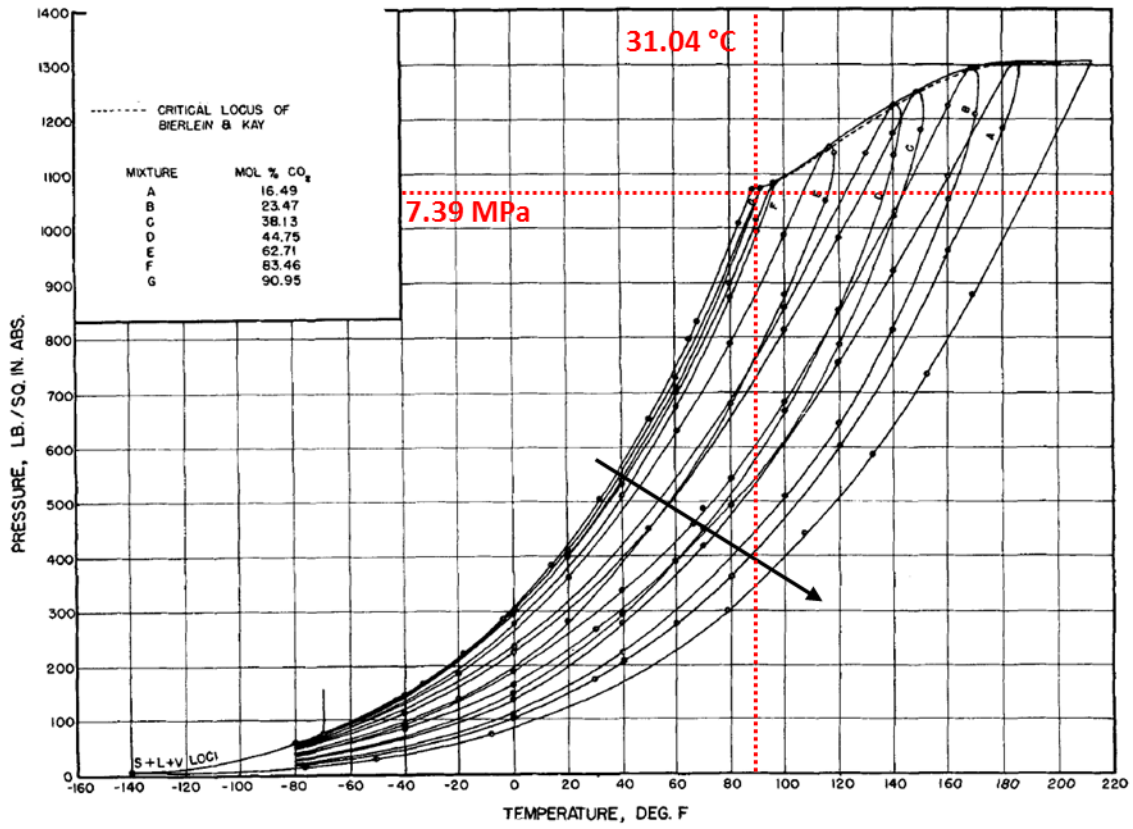

Figure 2.14. Pressure-temperature plot for CO_2 and H_2S mixtures adapted from Sobocinski and Kurata.[92] The critical points are shown by a black dotted line at the top of the plot. The amount of H_2S increases in the direction of the arrow. The critical point of pure CO_2 is marked by red dotted lines.

2.8.3 NONIDEALITY

In section 2.4, molecular transport assuming ideality was described. Ideal gases are defined by obeying the equation of state in Equation 2.28.[28]

$$pV = nRT \qquad \text{Equation 2.28}$$

CO_2 and H_2S, however, are far from ideal gases due to their intermolecular interactions, particle volume and intermolecular inelastic collisions. These effects are important at high pressures and/or low temperatures, and particularly when in the supercritical state.[26] In order to account for this nonideal behaviour, the empirically derived fugacity, *f*, of the gas may be used. The fugacity describes the chemical activity of the gas and is essentially the effective partial pressure acting as a driving force, defined by Equation 2.29.[93]

$$f = \varphi . p$$ Equation 2.29

where φ is the fugacity coefficient which tends to decrease as the pressure increases, as shown in Figure 2.15.

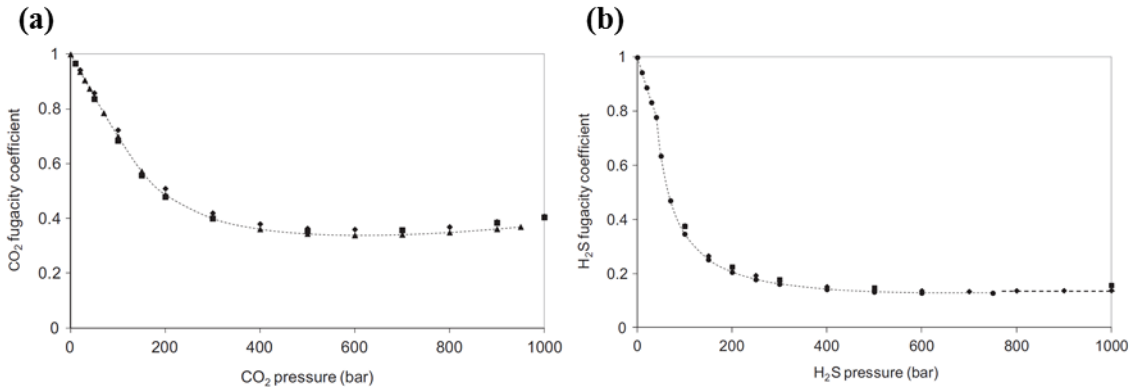

Figure 2.15. Plots displaying the variation of fugacity coefficient against total pure gas pressure for (a) CO_2 and (b) H_2S. Adapted from Sarrasin *et al.*[93].

Substituting for pressure with fugacity in Equation 2.10 yields:

$$P_f = \frac{Q.l}{A.t.f_1} = \frac{Q.l}{A.t.\varphi.p_1}$$ Equation 2.30

As shown in Equation 2.30, the use of fugacity instead of partial pressure for calculation of P_f effectively increases the magnitude of P. Fugacity may be thought of as a truer representation of the driving force for permeation of high pressure fluids than simply the hydrostatic pressure.

CHAPTER 3: *IN SITU* POLYMERISED NANOCOMPOSITES

3.1 INTRODUCTION

This section of work was carried out to produce *in situ* polymerised PA11 nanocomposites through grafting PA11 monomer to GNPs and GO. *In situ* polymerisation is perhaps the most fundamental method of producing nanocomposites, by grafting directly to or polymerising around fillers.

3.2 LITERATURE REVIEW

3.2.1 IN SITU POLYMERISATION

Many investigations into chemical functionalisation of GO have been made, utilising oxygen functionalities as grafting points.[43,44,94,95] A publication by Yuan *et al.*[96] describes the preparation of a very tough PA11/GO nanocomposite through an *in situ* polymerisation technique. 11-AUDA is polymerised in the presence of GO, with the intention that the PA11 binds directly to the GO surface functionalities during the polycondensation. The 11-AUDA powder and GO-water dispersion were mixed to form a uniform paste which was then filtered and dried in vacuo at 80 °C for 12 h. The mixture was then heated over 1 h to 190 °C under nitrogen before being evacuated. The evacuated vessel was then heated to 240 °C at 10 °C h^{-1} and polymerised for 6 h. Wide angle XRD showed evidence of the pseudo hexagonal δ' form in the *in situ* polymerised PA11/GO nanocomposites while pure PA11 displayed only α morphology. The group attributed the toughening effect observed in the nanocomposites to the δ' form crystal rather than the intrinsic properties of the GO. Similar toughening effects were observed in the melt blending work of Jacobs *et al.*[97] and Jin *et al.*[98], however, these effects were attributed to the intrinsic properties of graphene and GO, respectively.

Similar polymerisation methods were used by Chen *et al.*[99–101], however, the polymerisation times were altered slightly to 4 or 8 h. Sisti *et al.*[102] have very recently published a paper investigating the thermal and mechanical properties of *in situ* polymerised PA11/graphene nanocomposites.

3.2.2 Graphene Oxide Synthesis

Graphite oxide may be synthesised by the chemical oxidation of natural graphite in mixtures of strong acids and oxidants.[38–40] Graphite oxide is then typically exfoliated in water to yield GO.[44,103] In 1859, Brodie used potassium chlorate ($KClO_3$) and fuming nitric acid (HNO_3) in a four day reaction to produce graphite oxide.[38] Staudenmaier modified the Brodie method, adding sulphuric acid (H_2SO_4) for increased acidity, whilst adding the $KClO_3$ gradually in a four day reaction.[39] Hummers used potassium permanganate ($KMnO_4$), sodium nitrate ($NaNO_3$) and H_2SO_4 in a fast one hour reaction.[40]

The Hummers method has been adapted over recent years and a so called 'modified' Hummers method is generally used to produce graphite oxide from graphite. One such method involved the pre-treatment of graphite powder with H_2SO_4, phosphorous pentoxide (P_2O_5) and potassium persulphate ($K_2S_2O_8$) to begin the oxidation procedure, before subsequent full oxidation according to the Hummers method.[104] Phosphoric acid (H_3PO_4) and H_2SO_4 used in a 1:9 ratio was found to achieve more complete graphite oxidation.[105] Additionally, perturbation of the GO basal plane was reportedly less than for the traditional Hummers method. A different modification was made by increasing the intercalation time from just a few hours, to seven days, thus allowing greater exfoliation later in the preparation.[41,106,107]

3.3 Aims and Objectives

The aim of this work was to synthesise and characterise PA11, PA11/GNP and PA11/GO nanocomposites by *in situ* polymerisation for possible use in barrier materials. To current knowledge, there appears to be no direct comparisons made between *in situ* polymerised PA11 nanocomposites produced from GNPs compared to oxidised GNPs (GO).

Firstly, GO25 was synthesised from 25 μm GNPs and both GO25 and GNPs were characterised.

Nanocomposites containing GNPs and GO25 were then synthesised, and the effect of filler type and loading on the PA11 was investigated. The FT-IR and Raman spectra of the nanocomposites were compared to the pure polymer and starting materials. Thermal

degradation studies were undertaken and the crystallinity was probed by DSC and XRD. The morphologies of the samples were investigated by scanning electron microscopy (SEM) in order to observe the compatibility between the fillers and the polymer.

3.4 Materials and Methods

3.4.1 11-Aminoundecanoic Acid

11-AUDA was sourced from Sigma Aldrich Co., UK and purified prior to use as follows:[96] powdered 11-AUDA (30 g) was dispersed in deionised (DI) water (150 mL) under a N_2 purge. The slurry was stirred and heated to 95 °C for 2 h before being filtered and washed with warm DI water. The white filter cake was then dried under vacuum at 50 °C for at least 24 h prior to use.

3.4.2 Polyamide 11

PA11 was sourced from Arkema Inc., Colombes, France, provided by NCC Ltd., Ireland, under the Rilsan® trade name. Rilsan® PA11 G BESVO A FDA was provided. The additive-free, food and medically approved extrusion grade was provided in pellet form. The BESVO (manufacturer's code) was used for comparative purposes to the *in situ* polymerised neat PA11.

3.4.3 Graphene Nanoplatelets

GNPs were sourced from XG Sciences Inc., Lansing, Michigan (USA). xGnP Grade M 25 µm nanoplatelets were chosen for the study. According to the datasheet,[37] the GNPs had an average lateral size of 25 µm with surface areas of 120 – 150 m^2 g^{-1} and average thickness of 6 – 8 nm.

3.4.4 Graphene Oxide

GO25 was synthesised following the modified Hummers method according to Rourke *et al.*[41], derived from the method by Hirata and co-workers.[107] All reagents were supplied by Sigma Aldrich Co., UK and used as received.

25 µm diameter GNPs (5.0 g) were placed in a round bottomed flask (1 L) equipped with a stirrer bar and immersed in ice. To this, $NaNO_3$ (4.5 g) and 95 – 98% H_2SO_4 (170 mL) was added, and stirred for 2 h. To this was slowly added $KMnO_4$ (22.5 g) over 40 min keeping $T < 10$ °C, the suspension turned dark green over time. Following complete

addition, the mixture was allowed to warm to room temperature, covered and stirred. The mixture became thicker over time and stirring was not possible after a few hours.

After seven days, a pre-mixed solution of DI water (500 mL) and 95 – 98% H_2SO_4 (14 mL) was added drop wise to the flask with vigorous shaking, heat was produced and care was taken to keep the flask $T < 100$ °C. Once addition was complete, the dispersion was stirred at room temperature for 3 h. Then 30% H_2O_2 (10 mL) was added dropwise, with care to avoid extreme effervescence. The dark grey/black dispersion was stirred for 2 h and turned into a yellow/brown glittery suspension. The dispersion was then poured into a 'wash solution' comprising DI water (500 mL), 95 – 98% H_2SO_4 (8 mL) and 30% H_2O_2 (2 mL) and stirred overnight.

The dispersion was centrifuged (Sorvall Legend XTR) at 11000 rpm for 30 min, discarding the clear supernatant, keeping the yellow/brown viscous gel. More wash solution was added, the gel was shaken to re-disperse and centrifugation was repeated. The washing and centrifugation was repeated approximately six times, until all glittery particles were removed and the gel became darker. The dark brown viscous liquid was then dispersed in DI water and centrifuged at 11000 rpm for 1 h. This was repeated until the supernatant approached pH 7 (approximately six rounds). The brown viscous liquid had a concentration of 7.5 mg mL^{-1}, calculated by drying 5 mL of GO25 dispersion *in vacuo* at 50 °C and measuring the remaining mass.

In order to evaluate the GO25 following *in situ* polymerisation, thermal reduction of the GO25 was carried out according to the polymerisation protocol, outlined shortly. Firstly, GO25 was filtered through Anodisk™ ceramic filters (0.2 µm pore size) prior to placing into a glass petri dish. The petri dish was placed in a furnace and purged thoroughly with dry nitrogen before heating as outlined in section 3.4.6 for PA11 synthesis.

3.4.5 POLYCONDENSATION KIT

Following attempts at PA11 synthesis in round bottomed flasks, it became clear that purpose-built equipment was required. The polycondensation (PC) kit (Figure 3.1 and Figure 3.2) consisted of a cylindrical aluminium block encased in a heating jacket. The aluminium block had a central hollow cavity into which a test tube could be snugly placed. Thermocouples were placed in a neighbouring cavity equidistant between the test tube and the heating jacket. Test tubes with ground glass joints were specially made

and a purpose-made paddle stirrer could be inserted into the tube. A gas/vacuum inlet/outlet was then slid down over the paddle stirrer to fit the ground glass joint of the test tube. The space between the paddle stirrer shaft and gas inlet walls could be sealed during evacuation and left open when a positive pressure of N_2 was applied. The paddle stirrer was attached to a high torque Stuart SS30 overhead stirrer.

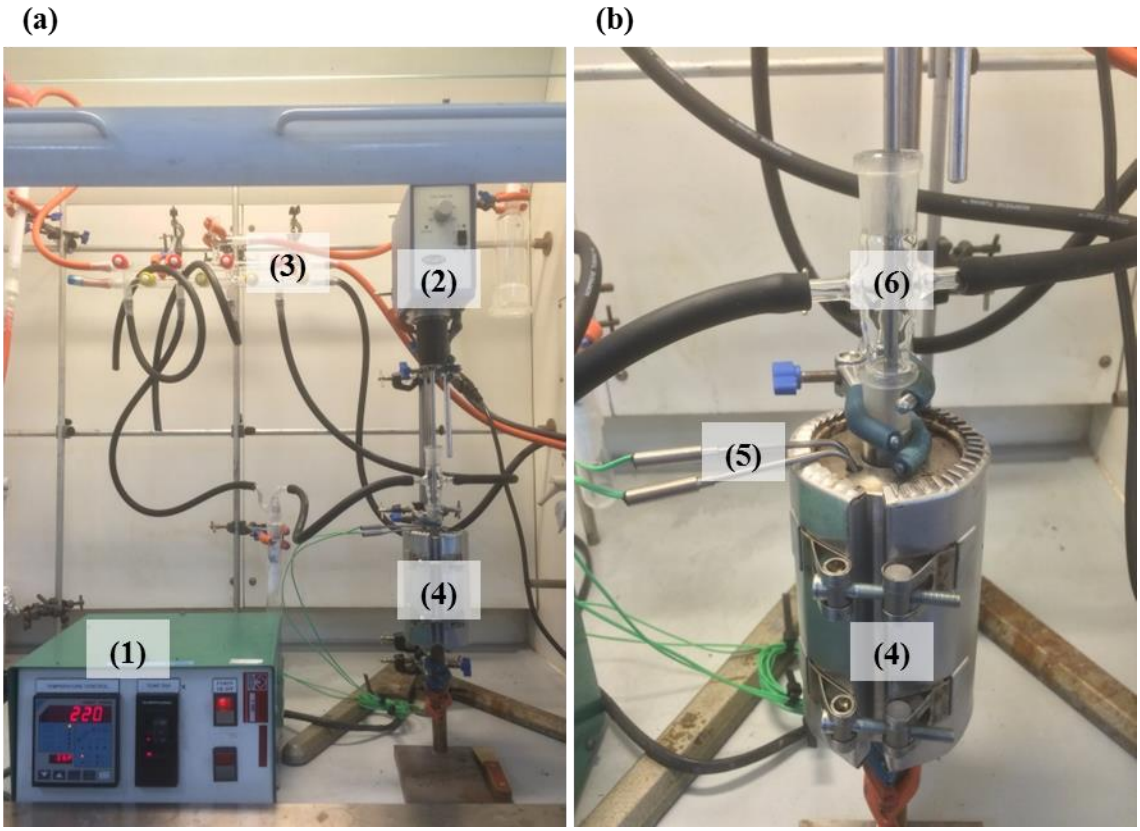

Figure 3.1. Photographs of (a) fume cupboard and (b) PC kit close-up: (1) temperature control box; (2) overhead stirrer; (3) N_2/vacuum line; (4) aluminium block and heating jacket; (5) thermocouples to temperature control box; (6) glass test tube with inlet/outlet fitting.

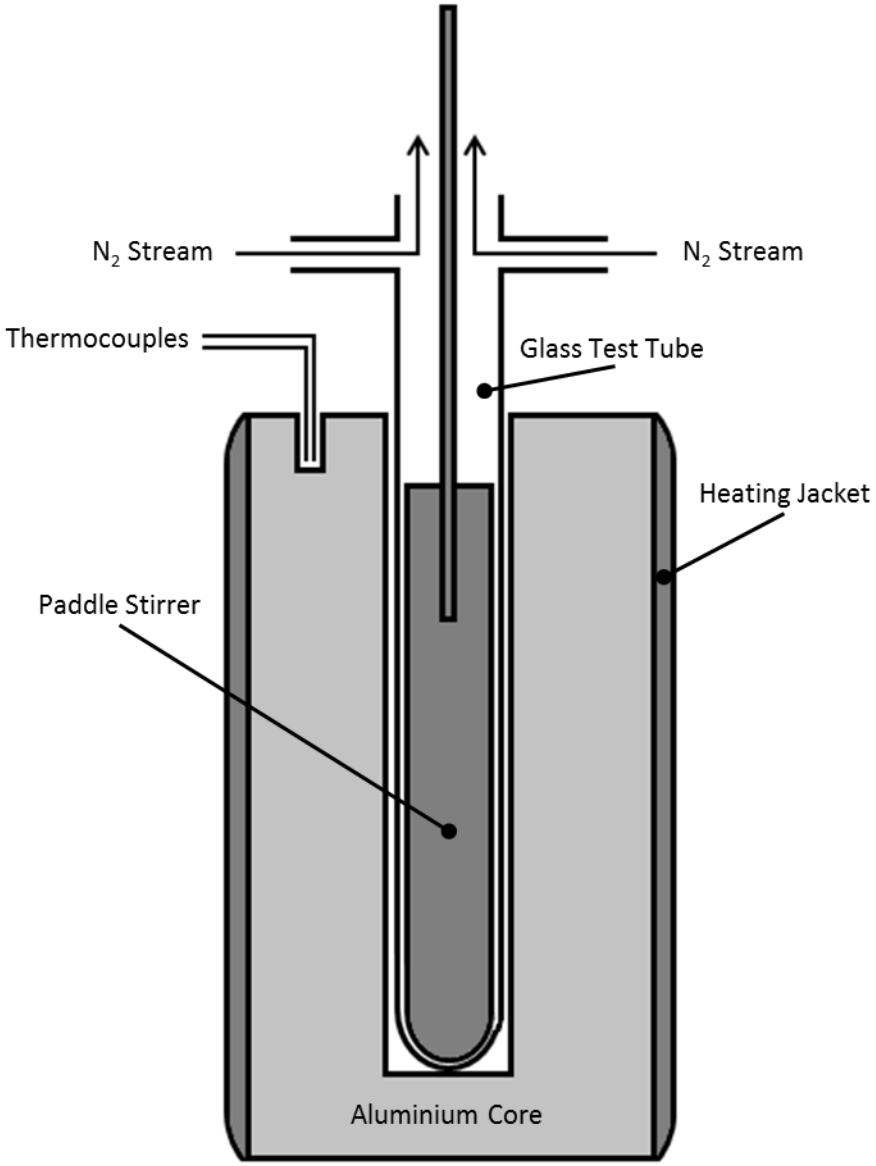

Figure 3.2. PC kit cross-sectional schematic showing the setup used to synthesise PA11/GNP and PA11/GO25 nanocomposites.

3.4.6 POLYAMIDE 11 SYNTHESIS

Purified 11-AUDA (10 g) was loaded into a test tube in the PC kit described above and heated to 80 °C under vacuum for at least 16 h. The tube was degassed by five rounds of pressurisation with dry N_2 followed by evacuation. The tube was then heated to 190 °C at a rate of 2 °C min^{-1} and left for 1 h under a positive pressure of N_2. After this time, the stirrer was started and the temperature was raised at 1 °C min^{-1} to 220 °C. Once at 220 °C, the tube contents were stirred for 5 h. Following polymerisation, the stirrer was removed and scraped clean with a brass scraper to yield polymer at an approximately 50% yield. Around 50% of the polymer remained coated to the inside of the test tube

and could not be collected. The control polymer was opaque and just off colourless (Figure 3.3). Nanocomposites were synthesised of varying GNP and GO25 loadings with respect to the final PA11 mass, assuming complete conversion of 11-AUDA to PA11. The loadings are shown in Table 3.1. *In situ* PA11/GNP (IS*n*XG25) nanocomposites were produced by mixing GNP powder with the 11-AUDA powder until homogeneous, prior to loading into the PC kit. *In situ* PA11/GO25 (IS*n*GO25) nanocomposites were produced by mixing 11-AUDA with an appropriate volume of pre-sonicated (10 min) GO25 dispersion. The slurry was then dried *in vacuo* at 80 °C to create dry grey cake. The cake was then ground into a homogeneous powder in a pestle and mortar, before being loaded into the PC kit. IS*n*XG25 and IS*n*GO25 nanocomposites were opaque and black in colour (Figure 3.4). As can be seen in Figure 3.4, the 1 and 5 wt% (a and d, b and e, respectively) nanocomposites are quite glossy in appearance; however, the 10 wt% nanocomposites (c and f) have a matt appearance.

Figure 3.3. Photograph of IS0 PA11 with off-white opaque colouration.

Table 3.1. Loadings of GNP and GO25 used in this work for IS*n*XG25 and IS*n*GO25 composites with amount of 11-AUDA required to produce PA11 composites of the correct loading.

Composite	Loading (wt%)	GNP/GO25 loading (g)	PA11 (g)	11-AUDA (g)
IS0	0	0.000	4.998	5.489
IS1XG25	1	0.050	4.975	5.463
IS5XG25	5	0.257	4.879	5.358
IS10XG25	10	0.528	4.753	5.220
IS0	0	0.000	4.998	5.489
IS1GO25	1	0.050	4.975	5.463
IS5GO25	5	0.257	4.879	5.358
IS10GO25	10	0.528	4.753	5.220

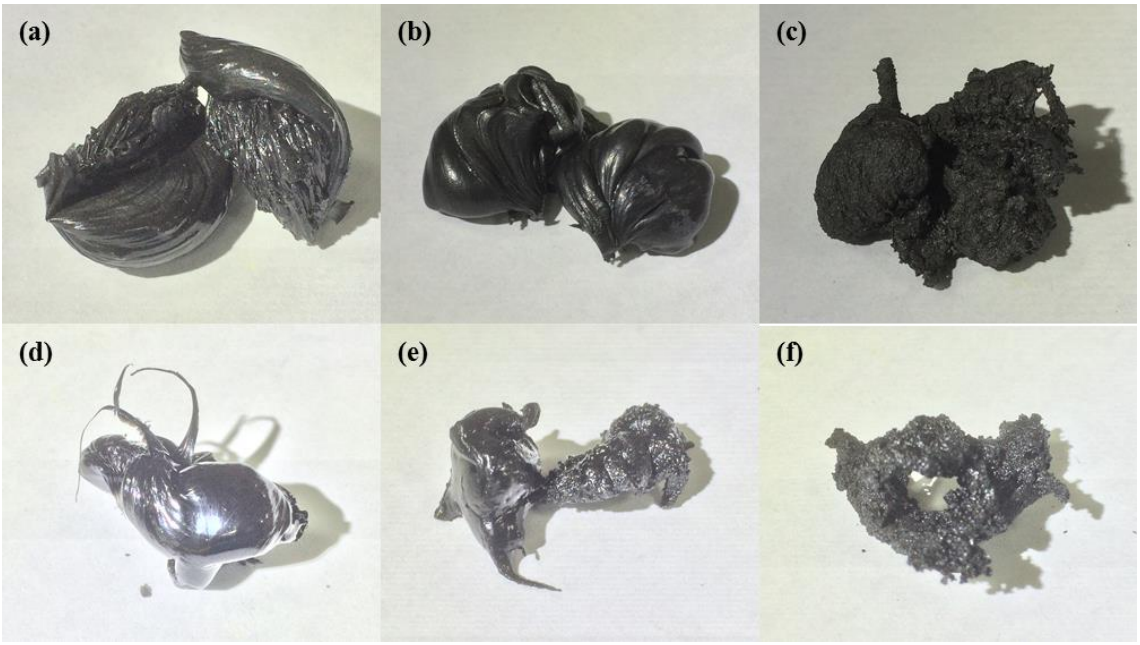

Figure 3.4. Photographs of the *in situ* polymerised GNP and GO25 samples: (a) IS1XG25, (b) IS5XG25, (c) IS10XG25, (d) IS1GO25, (e) IS5GO25, and (f) IS10GO25.

3.5 Characterisation Methods

3.5.1 Intrinsic Viscosity and Molecular Weight

An Ubbelohde viscometer was used to calculate the intrinsic viscosity (IV), [η], of PA11 in *m*-cresol at 30 °C. The Mark-Houwink equation (Equation 3.1) was used to calculate an estimated viscosity average molecular weight, $\bar{M}_v$.[108,109]

$$[\eta] = K.\bar{M}_v{}^{\alpha}$$ Equation 3.1

The Mark-Houwink parameters, K = 0.091 cm^3 g^{-1} and α = 0.69 were extracted from Terán *et al.*[110] for PA11 in *m*-cresol at 30 °C.

In order to calculate [η], dilute solutions of PA11 in *m*-cresol were prepared and their average flow times through the Ubbelohde capillary were recorded. The relative viscosity, η_r, was calculated using the flow time of polymer solution, t_{ps}, over the flow time for pure solvent, t_{solv}, according to Equation 3.2.[109]

$$\eta_r = \frac{t_{ps}}{t_{solv}}$$ Equation 3.2

The specific viscosity, η_{sp}, was calculated according to:[109]

$$\eta_{sp} = \eta_r - 1$$ Equation 3.3

The reduced viscosity, η_{red}, was calculated as shown in Equation 3.4, by dividing by concentration of polymer in solvent, c.[109]

$$\eta_{red} = \frac{\eta_{sp}}{c}$$ Equation 3.4

A plot of η_{red} against c was then used to evaluate [η] as the *y*-intercept, that is, [η] was provided in the limit of very low concentration, as shown in Equation 3.5.

$$[\eta] = \lim_{c \to 0} \eta_{red}$$ Equation 3.5

3.5.2 Infrared Spectroscopy

Attenuated total reflectance (ATR) FT-IR spectroscopy was performed on a ThermoScientific Nicolet iS5 spectrometer with iD5 ATR diamond stage. The signal was averaged over 32 scans for both the background and sample spectra at a resolution of 4 cm^{-1}. The diamond was cleaned with isopropanol (IPA) between each acquisition and allowed to dry thoroughly.

3.5.3 Raman Spectroscopy

Raman spectroscopy was carried out on a Renishaw inVia Raman Microscope equipped with a HeNe 633 nm laser at a power suitable to sample stability. Spectra were collected through Leica N Plan EPI 50× objectives.

3.5.4 *Thermal Gravimetric Analysis*

TGA was carried out on three samples with masses between 5 and 20 mg under nitrogen from room temperature to 800 °C at a heating rate of 10 °C min^{-1}. Similar methods may be found in papers regarding PA11/graphene and PA11/carbon nanotube (CNT) nanocomposites.[111–113]

3.5.5 *Differential Scanning Calorimetry*

DSC analysis was carried out on a TA Instruments Q100 DSC on three to five repeat samples weighing 6 – 10 mg, accurately weighed, with the following method:

- Cool to – 50 °C and hold for 1 min.
- Heat to + 300 °C at 10 °C min^{-1} and hold for 1 min.
- Cool to – 50 °C at 10 °C min^{-1} and hold for 1 min.
- Reheat to + 300 °C at 10 °C min^{-1} and hold for 1 min.

Data analysis was carried out on TA Instruments Universal Analysis 2000 software. The first-heat melting temperature (T_{m1}), cooling crystallisation temperature (T_c), and second-heat melting temperature (T_{m2}) were all measured to the greatest height of the peak, with a baseline from 100 °C to 200 °C. The glass transition temperature (T_g) was measured between 0 °C and 100 °C on the second-heat and measured as the centre of an inflection point. The enthalpy of crystallisation (ΔH_m) was measured as the area under the T_{m2} peak with a baseline from 100 °C to 200 °C. χ_c was calculated, manually, according to:[114]

$$\chi_c = \frac{\Delta H_m}{\Delta H_m^0 . \omega} . 100 \qquad \text{Equation 3.6}$$

where ΔH_m^0 = 189.05 g mol^{-1} for 100% pure crystalline PA11, and ω is the weight fraction of polymer in the composite.[115,116]

3.5.6 *X-ray Diffraction*

XRD was carried out on a Bruker D8 Advance Powder diffractometer using a Cu K_α radiation source (λ = 0.15418 nm), at ambient temperature. The samples were rotated throughout measurement to obtain a sample average, regardless of orientation. Fitting of XRD data has been carried out in the literature,[74] in this case, Lorentzian curves were fitted to the data.

3.5.7 *Scanning Electron Microscopy*

SEM in this chapter was carried out on a Quanta 250 ESEM in high vacuum mode at 10 kV. Samples were cryogenically fractured, mounted onto an aluminium stub with carbon tape and Au/Pd coated.

3.5.8 *Calculation of Standard Deviation*

All values for the standard deviation, *s*, were calculated using Equation 3.7 shown below:

$$s = \sqrt{\frac{\sum(x_s - \bar{x_s})^2}{N_s - 1}}$$ Equation 3.7

where N_s is the number of samples, x_s is the sample value and $\bar{x_s}$ is the mean value.

3.6 Results and Discussion

3.6.1 *Characterisation of Graphene Nanoplatelets and Graphene Oxide*

Before discussion of the nanocomposites, it is important to characterise the GNP and GO25 fillers. The GNPs had low levels of oxygen functionality, assumed to be found mostly on the flake edges, according to the material data sheet.[117]

3.6.1.1 *FT-IR Spectroscopy*

The ATR FT-IR spectra of GNP powder, GO25 (Hummers method oxidised GNPs) and trGO25 (GO25 thermally reduced according to *in situ* polymerisation protocol) films are shown in Figure 3.5. The GNP spectrum shows very few peaks, other than artefacts due to the ATR crystal. FT-IR spectra in the literature for GNPs from XG Sciences do, however, appear to show some functionality, associated with carboxylic acid (COOH), phenolic or alcoholic OH, C=O and C-O, as shown in Figure 3.6.[118,119]

The ATR artefact can also be seen in the GO25 spectrum; however, the signals due to absorbing functionality have a greater magnitude than for GNPs. The broad peak at 3700 cm^{-1} – 3000 cm^{-1} representing phenolic OH, COOH and water, may be identified in the spectrum of GO25, but is removed in the trGO25 spectrum.[41] The additional peak at 1720 cm^{-1} may be attributed to carboxylic acid carbonyls;[120] the 1620 cm^{-1} peak may be attributed to ketone,[120] or C=C species,[121] respectively. The peak at 1030 cm^{-1} is

indicative of C-O of COOH groups or epoxides and 850 cm^{-1} could indicate C=C groups in the graphitic planes.[121,122] The region between 1500 cm^{-1} and 800 cm^{-1} encompasses a range of signals for various species including: phenols, epoxides, hydroxyl, carboxylic and ketone groups.[41,120] Thermal reduction does not remove all functionality from GO25. The trGO25 spectrum shows that at least some carbonyl functionality remains at 1720 – 1620 cm^{-1}, possibly in the form of anhydrides,[123] as well as possible epoxide functionality at 1040 cm^{-1}.[122]

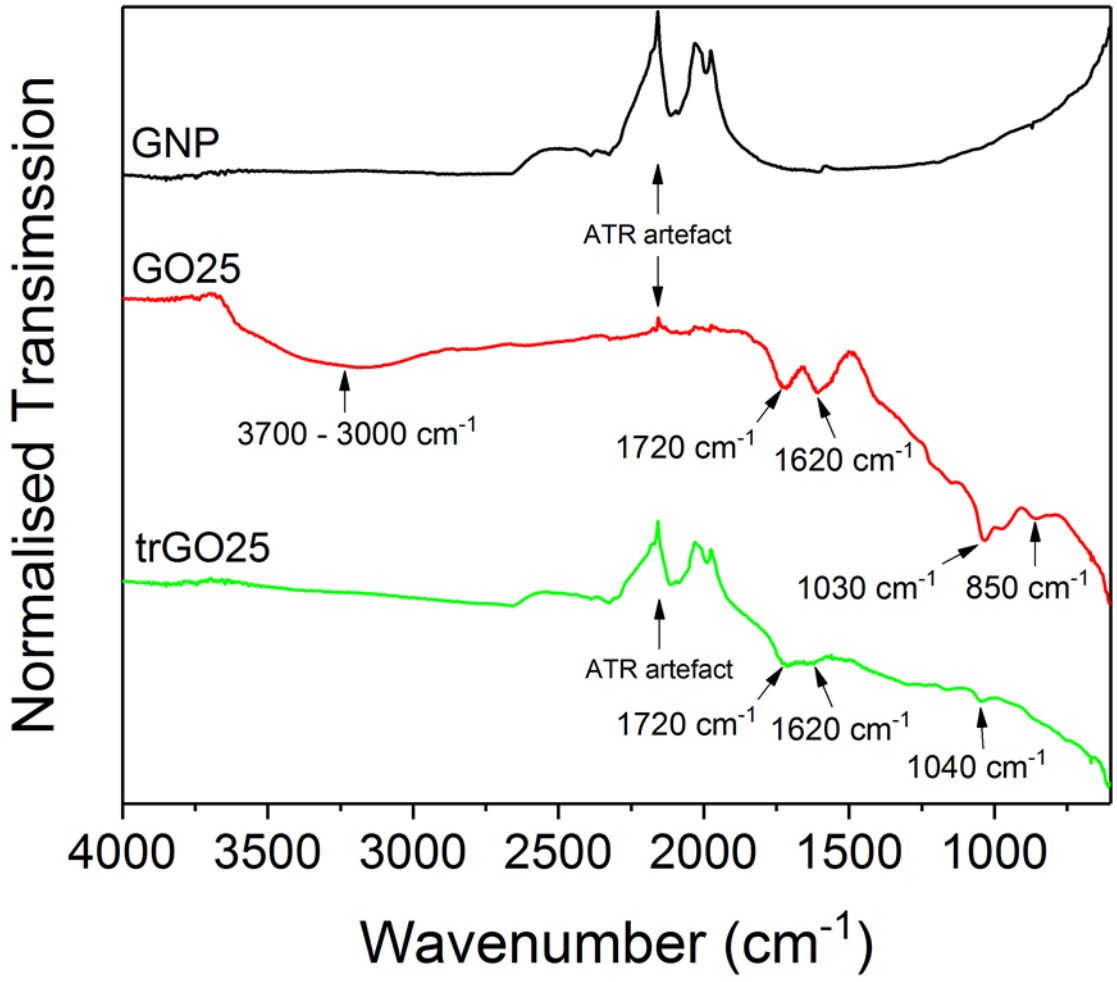

Figure 3.5. ATR FT-IR spectra of GNPs, GO25 and trGO25 materials with peaks of interest labelled. The reflection artefact due to the ATR diamond is labelled.

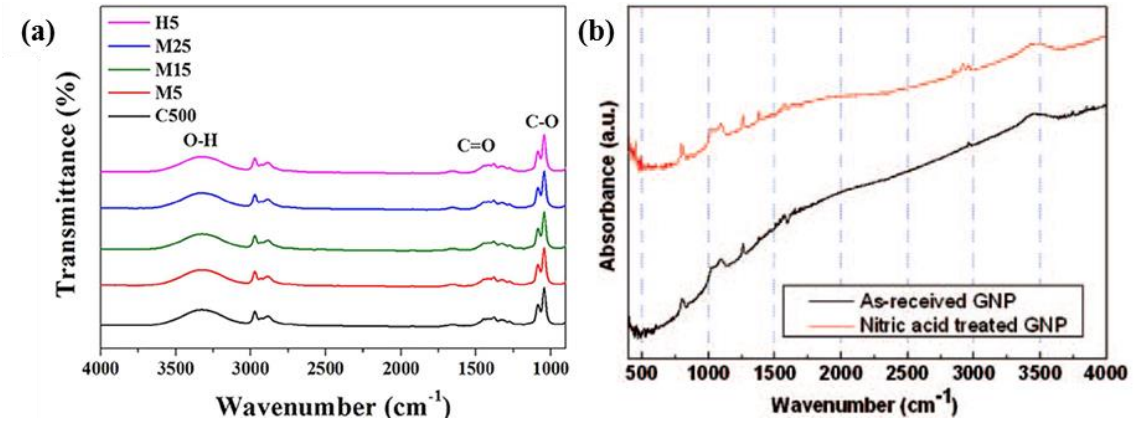

Figure 3.6. FT-IR spectra of GNPs supplied by XG Sciences from (a) H. S. Kim *et al.*[118] and (b) H. C. Kim and co-workers.[119]

3.6.1.2 Raman Spectroscopy

Typical Raman spectra of the GNP powder, GO25 and trGO25 reduced under the same conditions as used in the *in situ* polymerisations are shown in Figure 3.7.

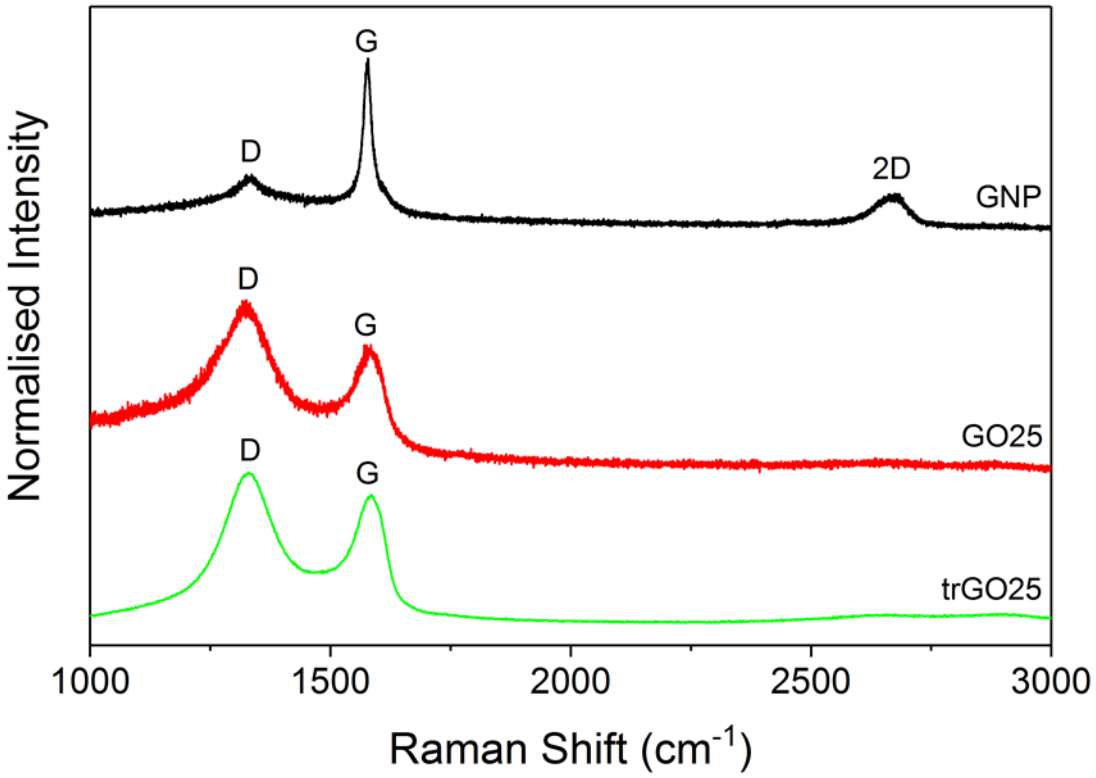

Figure 3.7. Typical Raman spectra of GNPs, GO25 and trGO25. The D, G and 2D peaks are labelled.

The GNP powder has some defective regions, as shown by the small D peak and the GO25 has a very large D peak, in comparison to the G peak. The trGO25 also has a large D peak, but compared to GO25 appeared to have a slightly larger G peak relative to the D peak, which would be consistent with partial regeneration of graphitic regions or removal of functionality. The $I(D)/I(G)$ ratios are 0.3, 1.5 and 1.2 for GNPs, GO25 and trGO25, respectively. In single layer graphene, the intensity of the 2D peak is approximately four times the G peak intensity.[83] The 2D peak for GNPs is roughly a quarter of the G peak intensity, which is closer to the 2D peak intensity of bulk graphite.[83]

3.6.1.3 Thermal Stability

The TGA and differential thermogravimetry (DTG) profiles for GNPs and GO25 are shown in Figure 3.8. As can be seen, GNPs exhibit a single small degradation step at 550 – 800 °C. GO25 shows characteristic two-step degradation at around 150 – 250 °C and then 700 – 800 °C. The first step corresponds to evaporation of tightly bound water and degradation of labile oxygen-containing functional groups, yielding CO_2, CO and water.[124–126] The continuation of degradation suggests that more tightly bound functional groups are slowly removed between 250 and 700 °C. The final degradation step may be attributed to the sublimation of the defective graphitic carbon backbone. The GNP clearly shows a greater thermal stability than the GO25, providing further evidence that the GNPs have far less functionality than the highly oxidised GO. The GNPs show a small mass loss at 100 – 550 °C, which may be due to the removal of small amounts of oxygen functionality. The final degradation step at 550 – 800 °C may be due to the degradation of tightly bound functionality or impurities.[127]

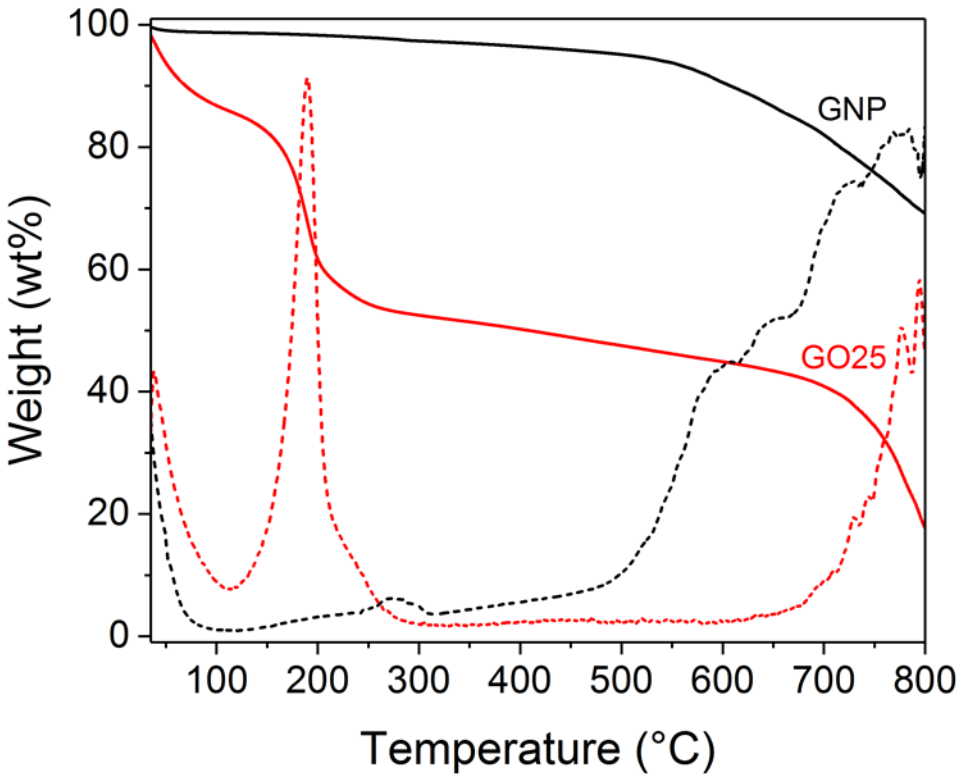

Figure 3.8. Nitrogen sweep degradation profiles (solid lines) and differential thermograms (dotted lines) for GNP powder (black) and GO25 (red), filtered from GO25 dispersion.

The degradation profile of neat GO25 associated with the *in situ* polymerisation method outlined in the experimental section is shown in Figure 3.9. Note that the GO25 was held at 100 °C under nitrogen flow for 2 h for the initial drying step, rather than at 80 °C under vacuum overnight, as used in the synthesis method. As can be seen, around 15 wt% loss may be attributed to water evaporation during drying. Upon heating at 2 °C min^{-1} to 190 °C, there is a further weight loss of around 25 wt%. At 190 °C, 11-AUDA would be molten in the *in situ* polymerisation and a small amount of grafting may begin, so stabilising the GO25. In the case of neat GO25, however, there is then a further weight loss of around 3 wt% upon heating to 220 °C at 1 °C min^{-1} and holding for 5 h. The remaining mass of GO25 at the end of the mimicked polymerisation is around 57 wt% of the loaded mass. As the degradation profile levels off when holding at 220 °C, it would appear that the graphitic regions of the GO25 that degrade at higher temperatures (Figure 3.8) are unlikely to be changed.

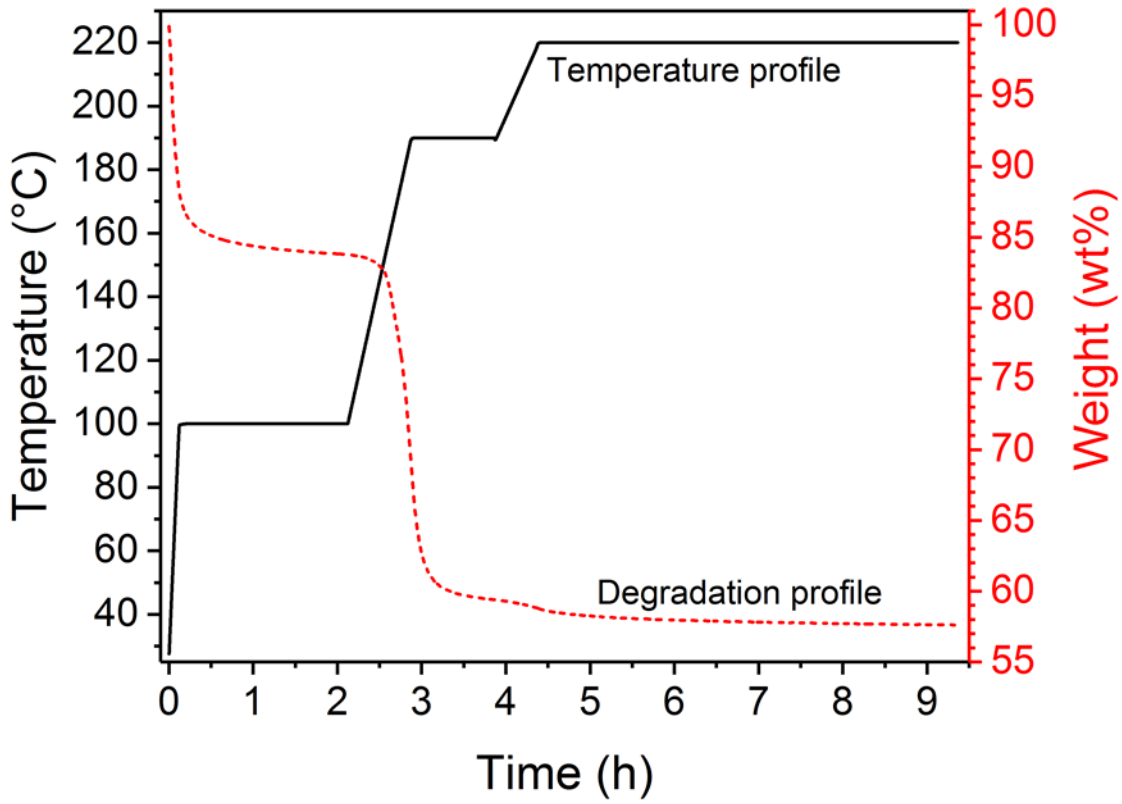

Figure 3.9. Plot showing an *in situ* polymerisation mimic performed on a TGA instrument in order to investigate the thermal behaviour of pure GO25 under nitrogen.

3.6.1.4 X-ray Diffraction

XRD diffractograms for GNP, GO25 and trGO25 are shown in Figure 3.10. Following Lorentzian curve fitting, the interlayer spacings according to Bragg's Law (Equation 3.8) were calculated and are presented in Table 3.2.[128]

$$d = \frac{\lambda}{2 \sin \theta} \qquad \text{Equation 3.8}$$

Where d is the interlayer spacing, λ is the Cu K_α X-ray wavelength (0.15418 nm) and Θ is the angle of incidence of parallel X-rays with a value of half of 2Θ.[128]

As can be seen in Table 3.2, the curve fitting of the GNP (002)[129] peak (a) in Figure 3.10 provides a graphite interlayer spacing of 0.34 nm, in good agreement with literature values for graphite.[130,131] The 0.80 nm interlayer spacing associated with peak (b) in the GO25 diffractogram (Figure 3.10), is also in good agreement with literature values for dry GO.[129,132–134] The expansion of the GO interlayer distance is due to the myriad functional groups on the edges and basal planes of the GO flakes.[131] The wide

peak (c) in the GO25 diffractogram (Figure 3.10), has been observed in a number of publications but not necessarily characterised.[135,136] One publication labelled peak (c) as the (002) reflection,[137] although the broad nature of the curve in the current work suggests that the (002) reflection may also be convoluted with peaks due to restacked graphene-like GO basal planes. Interestingly, upon thermal reduction, GO25 loses the peak at 2Θ = 11.1 ° (peak (b) in Figure 3.10) and develops a broader peak in the regions marked (d) and (e). Peak (d) in Figure 3.10 has the same interlayer spacing as peak (c). This suggests that upon thermal reduction, the stacked graphene-like GO25 basal planes are not substantially modified. There may be some further reduction as demonstrated by the shoulder peak labelled (e) in Figure 3.10. The broad peak suggests that a range of interlayer distances are present, although the thermal reduction does not return all interlayer spacing to that of the starting material.

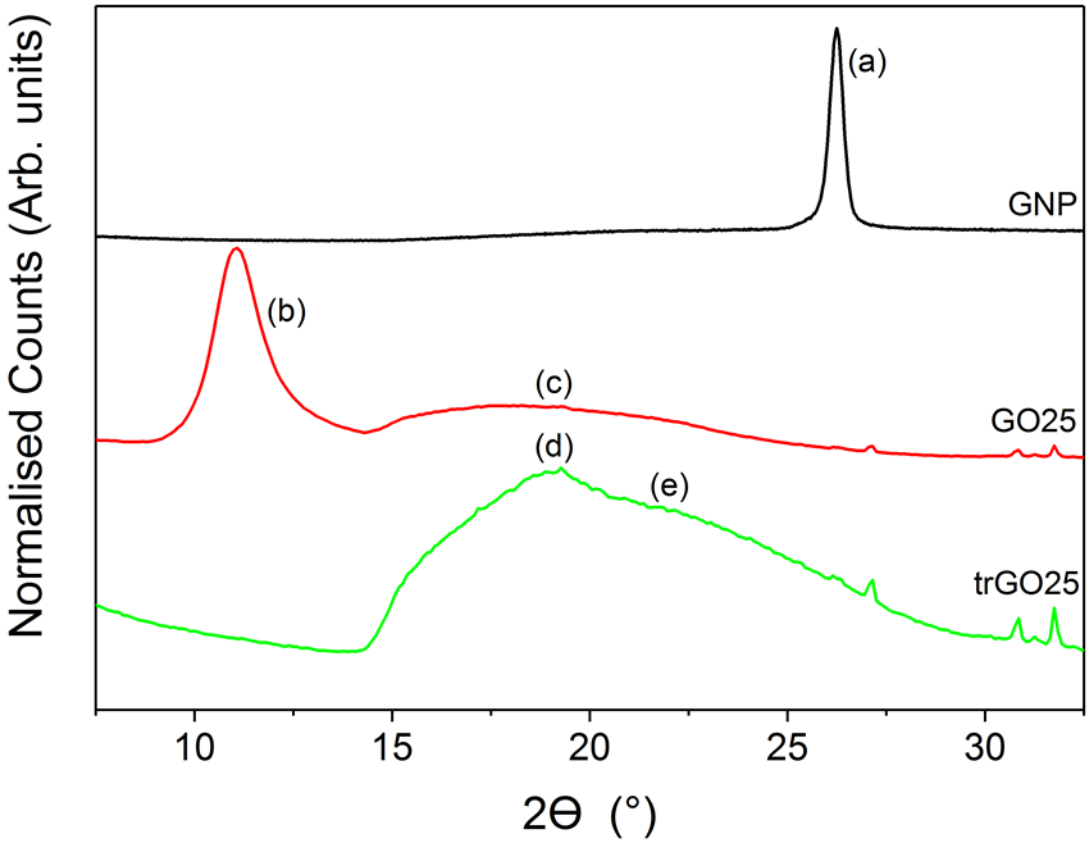

Figure 3.10. XRD diffractograms for GNP, GO25 and trGO25. GNP and GO25 filtered from suspensions, trGO25 was thermally reduced under nitrogen according to the IS*n*XG25 synthesis method. (a) – (e) peaks fitted with Lorentzian curves.

Table 3.2. Peak properties for labelled peaks in Figure 3.10 following Lorentzian curve fitting.

Peak	**2Θ (°)**	***d* (nm)**
a	26.2	0.34
b	11.1	0.80
c	18.5	0.48
d	18.5	0.48
e	22.9	0.39

3.6.1.5 Scanning Electron Microscopy

SEM was performed on 25 µm GNPs drop cast from NMP dispersion (2 mg mL^{-1}) onto a hot SEM stub and coated with Au/Pd. Representative images are shown in Figure 3.11. The images show thin GNP flakes, highlighted by yellow arrows along with thicker stacks, highlighted by red rings. As can be seen, the GNPs range in size from approximately 5 to 40 µm and display wrinkles and folds.

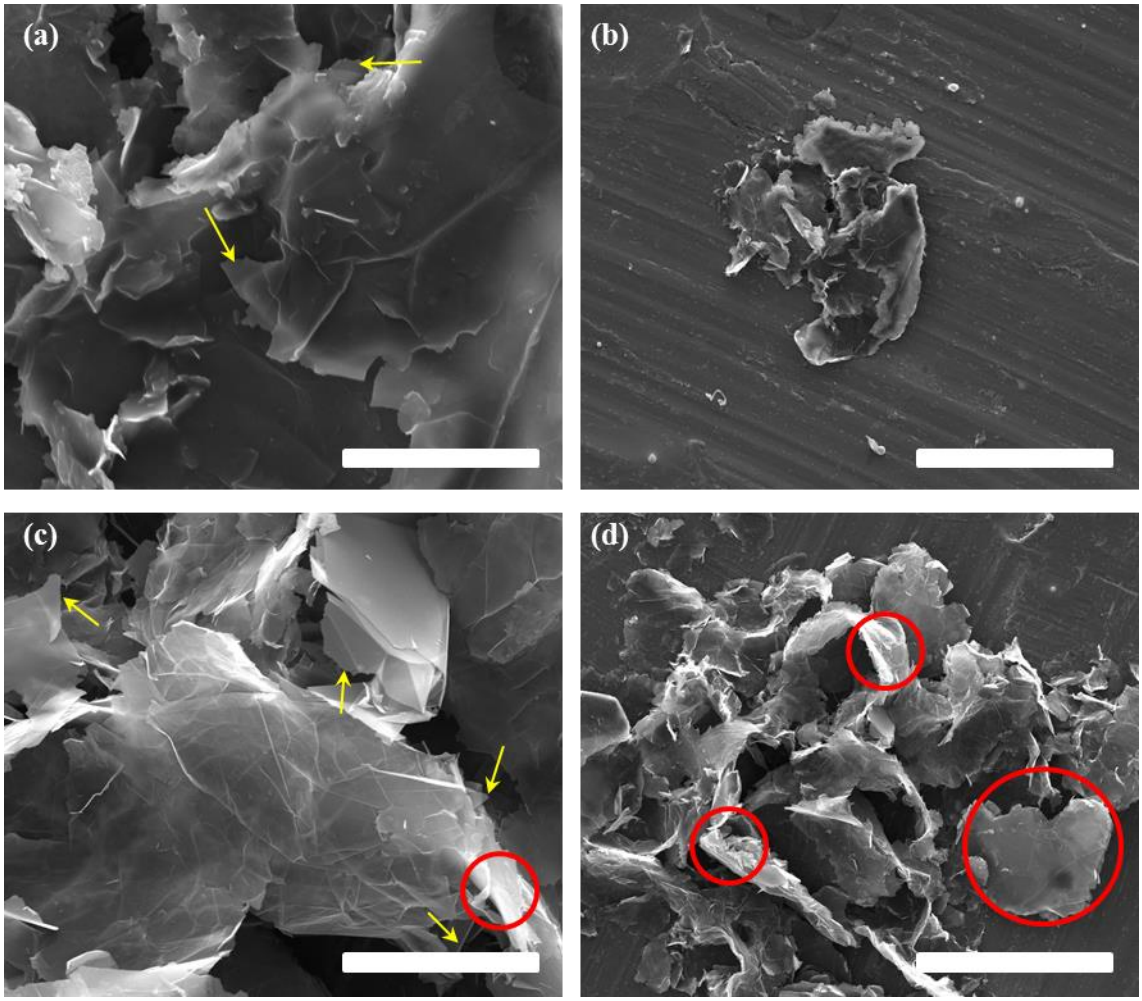

Figure 3.11. SEM images of Au/Pd coated GNPs (a) and (b) are of one agglomerate and (c) and (d) are of a second agglomerate. Scale bar is 10 µm in (a) and (c) and 50 µm in (b) and (d).

3.6.2 Characterisation of In Situ Polymerised Nanocomposites

Synthesis of PA11 nanocomposites was chosen as a starting point to gain an understanding of the interactions between PA11 and GNP or GO fillers.

3.6.2.1 Viscosity Average Molecular Weight and Solubility Experiments

The IV, $[\eta]$, of the neat *in situ* polymerised PA11 was determined by a plot of the reduced viscosity against the concentration of PA11 in *m*-cresol at 30 °C as shown in Figure 3.12. The calculated values of $[\eta]$ and $\overline{M}_v$ are shown in Table 3.3.

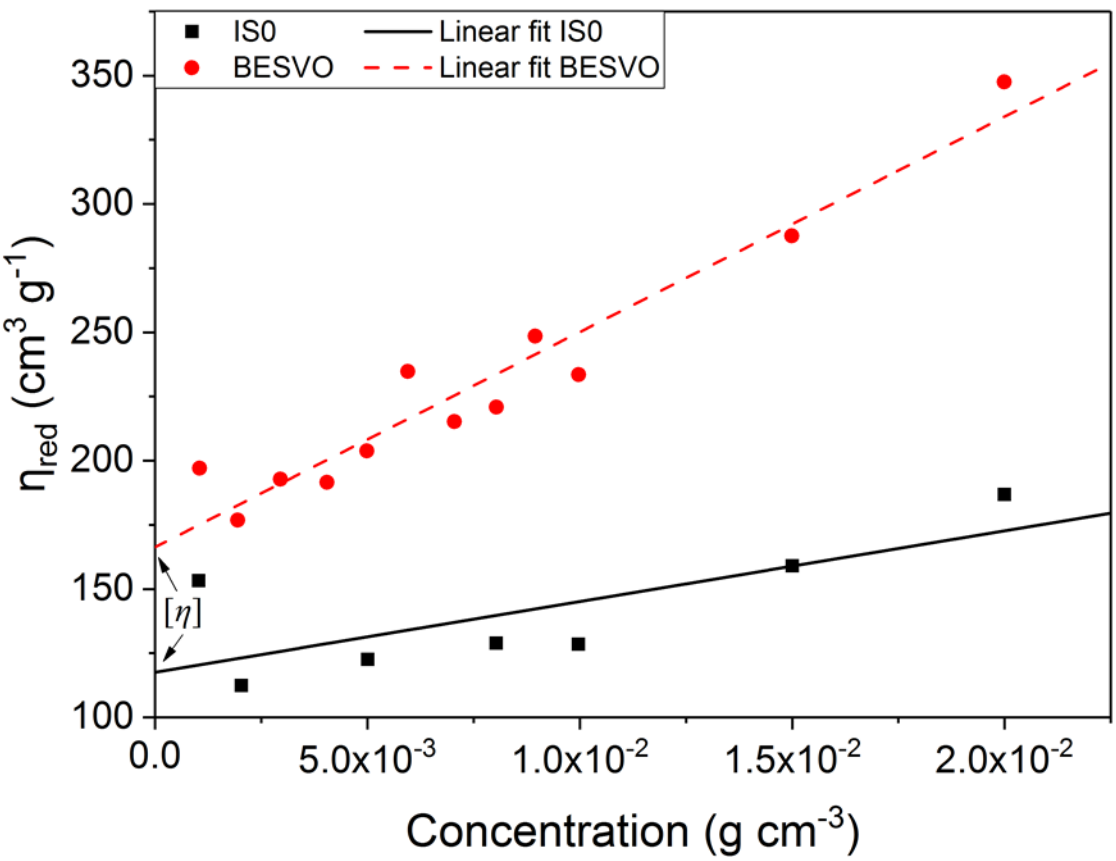

Figure 3.12. Plot of reduced viscosity against concentration of IS0 PA11 in *m*-cresol, the industrial BESVO PA11 is included as a comparison.

Table 3.3. Extracted values of [η] and the calculated $\bar{M}_v$ values according to Equation 3.1.

Sample	**[η] (cm^3 g^{-1})**	**$\bar{M}_v$ (g mol^{-1})**
IS0	118	32000*
BESVO	166	53000*

*Quoted to nearest 1000 g mol^{-1}.

Table 3.3 shows that the IS0, neat PA11, was synthesised with a viscosity average molecular weight of 32000 g mol^{-1}, which is lower than the 53000 g mol^{-1} calculated for the industrially synthesised PA11. 32000 g mol^{-1} is not an unreasonable viscosity average molecular weight and is comparable to literature values for weight average molecular weight of nylons.[109,138,139]

IV measurements were not performed on the *in situ* polymerised GNP and GO25 nanocomposites due to their relative poor solubility. However, solubility experiments were carried out in order to evaluate the degree of polymerisation (Figure 3.13).

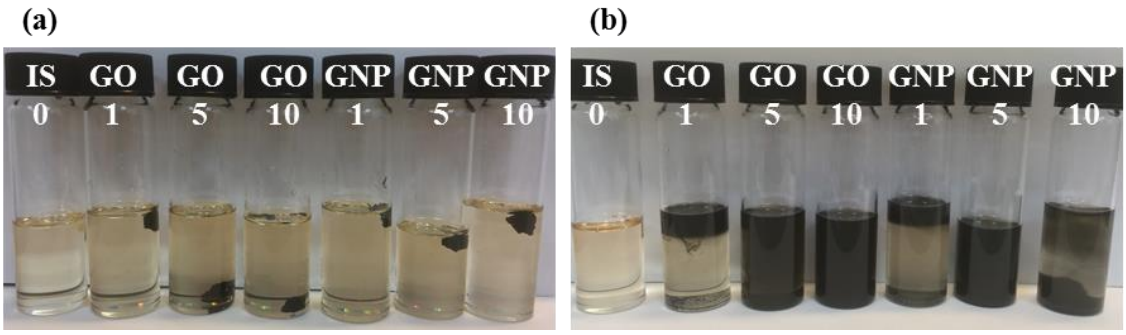

Figure 3.13. Solubility experiments for the *in situ* polymerised nanocomposites containing GO25 and GNPs. Filler and loading (wt%) is annotated for each nanocomposite. (a) Initial sample appearance and (b) samples after one week without agitation.

50 – 70 mg, accurately weighed, of each sample was taken and *m*-cresol added to make the concentration 10 mg mL^{-1}. The IS0 PA11 was found to dissolve fully in 24 h without agitation in *m*-cresol. The IS1XG25 and IS1GO25 nanocomposites were found to swell over the same time-frame, before eventually forming a low-viscosity gel that was less dense than the pure *m*-cresol (Figure 3.13b). The 5 and 10 wt% nanocomposites also swelled but appeared to dissolve more readily than the 1 wt% nanocomposites. This suggests that the low loadings of filler were polymerised with the PA11 while allowing substantial free chain molecular weights to be achieved. The higher loadings may have restricted PA11 chain lengths by providing too many functional group sites for reaction, or by forming physical barriers between adjacent chains. This is supported by the qualitative differences in toughness. Generally, the polymers were quite tough; however, the 5 and 10 wt% loadings were typically more brittle than the 0 and 1 wt% samples. In particular, the IS5GO25 and IS10GO25 were more brittle than their GNP counterparts, implying that these polymers had a lower molecular weight than their GNP analogues. A decreased molecular weight reduces the degree of chain entanglement meaning that brittle, rather than ductile behaviour may be expected.

3.6.2.2 Spectroscopic Characterisation

Table 3.4 shows the assignments of PA11 FT-IR spectra from the literature,[140] alongside those found in this work (Figure 3.14). Figure 3.14 shows the modification in the FT-IR spectrum on going from 11-AUDA starting material to IS0 polymerised PA11, with industrial BESVO PA11 as a comparison.

Table 3.4 FT-IR spectra assignments from this work and the literature.[140]

Absorption (cm^{-1})	**Literature value (cm^{-1})***	**Assignment**
3310	3305	N-H bond
3080	3087	N-H Fermi resonance
2920	2920	CH_2 asymmetric stretch
2850	2850	CH_2 symmetric stretch
1645	1634	Amide I C=O stretch
1535	1537	Amide II -NH-CO- group
1465	1468	C=O bend
940	935	Amide IV (CONH)
720	718	CH_2 rocking
685	683	Amide V CONH out of plane deformation

*Taken from Domingos *et al.*[140]

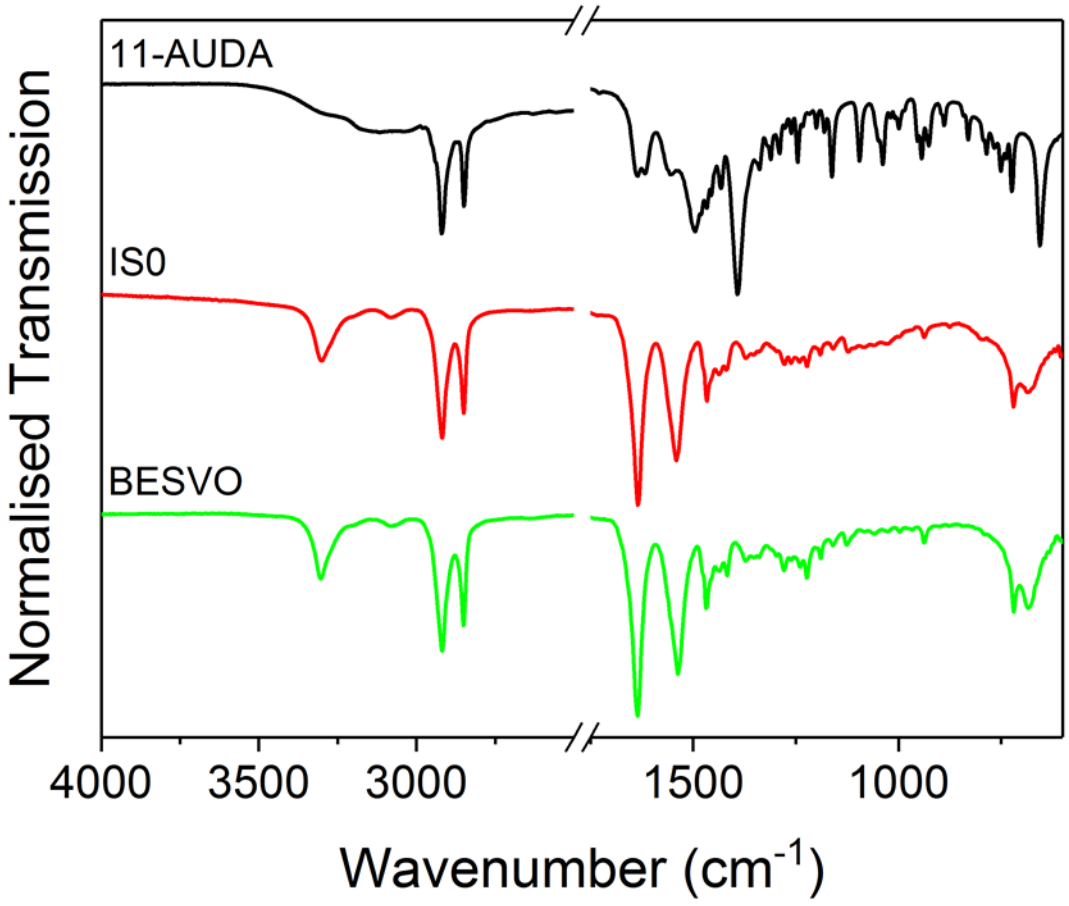

Figure 3.14. FT-IR spectra of 11-AUDA, IS0 and BESVO PA11.

The functionality identified on GO25 by FT-IR spectroscopy in Figure 3.5 was expected to be used as a grafting site during the *in situ* polymerisation reaction. The FT-IR spectra of IS*n*XG25 and IS*n*GO25 are shown in Figure 3.15a and b, respectively. As can be seen in Figure 3.15a, upon the *in situ* polymerisation of GNP powder with 11-AUDA, a number of new bands could be observed at 2960, 1260, 1000 – 1100, and 850 cm^{-1}. It can also be seen that the amide II band at 1540 cm^{-1} seems to decrease in intensity with increasing GNP loading. In comparison to IS*n*XG25 spectra, the IS*n*GO25 spectra in Figure 3.15b do not show any new bands upon polymerisation of 11-AUDA in the presence of GO25, although the background at lower wavenumbers appears to increase slightly with GO25 loading.

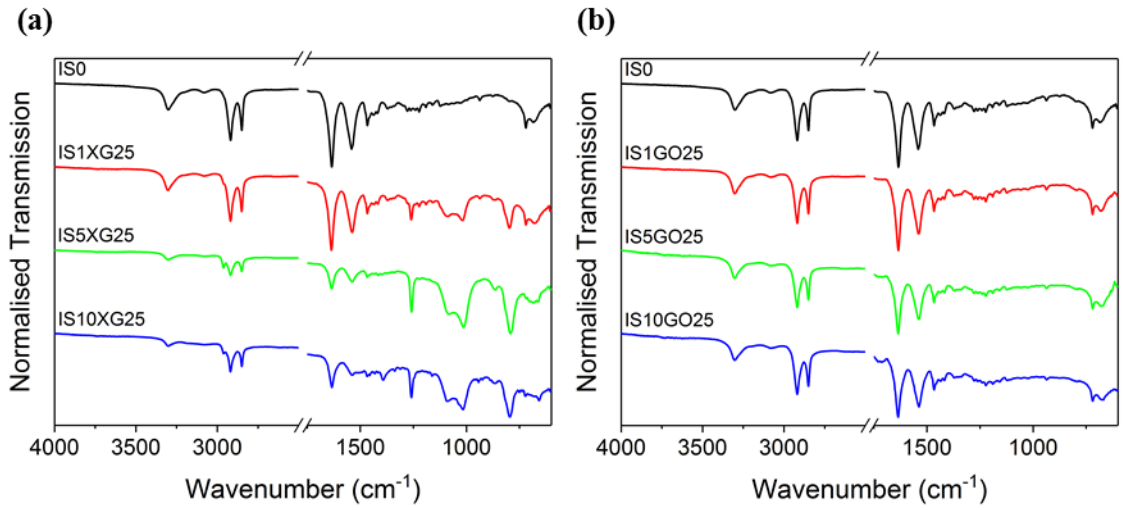

Figure 3.15. FT-IR spectra of (a) neat polymerised PA11 along with IS*n*XG25 at 1, 5 and 10 wt% loading and; (b) neat polymerised PA11 along with IS*n*GO25 at 1, 5 and 10 wt% loading.

These were surprising results. Initially, the new bands in Figure 3.15a were attributed to impurities present within the GNP powder, possibly left over from the acidic treatment prior to thermal expansion.[35] In order to test this, a PA11/graphite nanocomposite was synthesised *in situ* (Figure 3.16). The FT-IR spectrum of IS10Graphite shows no evidence of new bands which suggests that the bands in the IS*n*XG25 samples did come from impurities. The GNP powder was therefore washed by refluxing in water for 24 h; however, upon *in situ* polymerisation of the washed GNPs, the new bands were still observed. It was therefore deduced that the new bands came from tightly bound functionality on the GNPs, rather than impurities. Indeed, the bands observed in the literature (Figure 3.6) do appear to correlate with those observed in the IS*n*XG25 composites.[118,119] The *in situ* polymerisation may amplify the bands which have been shown to be present in GNPs in Figure 3.6a at 2960, 1260 and 1000 – 1100 cm^{-1} and Figure 3.6b at 850 cm^{-1}.[118,119] This may be through grafting reactions linking the PA11 to the low levels of functionality purportedly present on the GNP edges.[35]

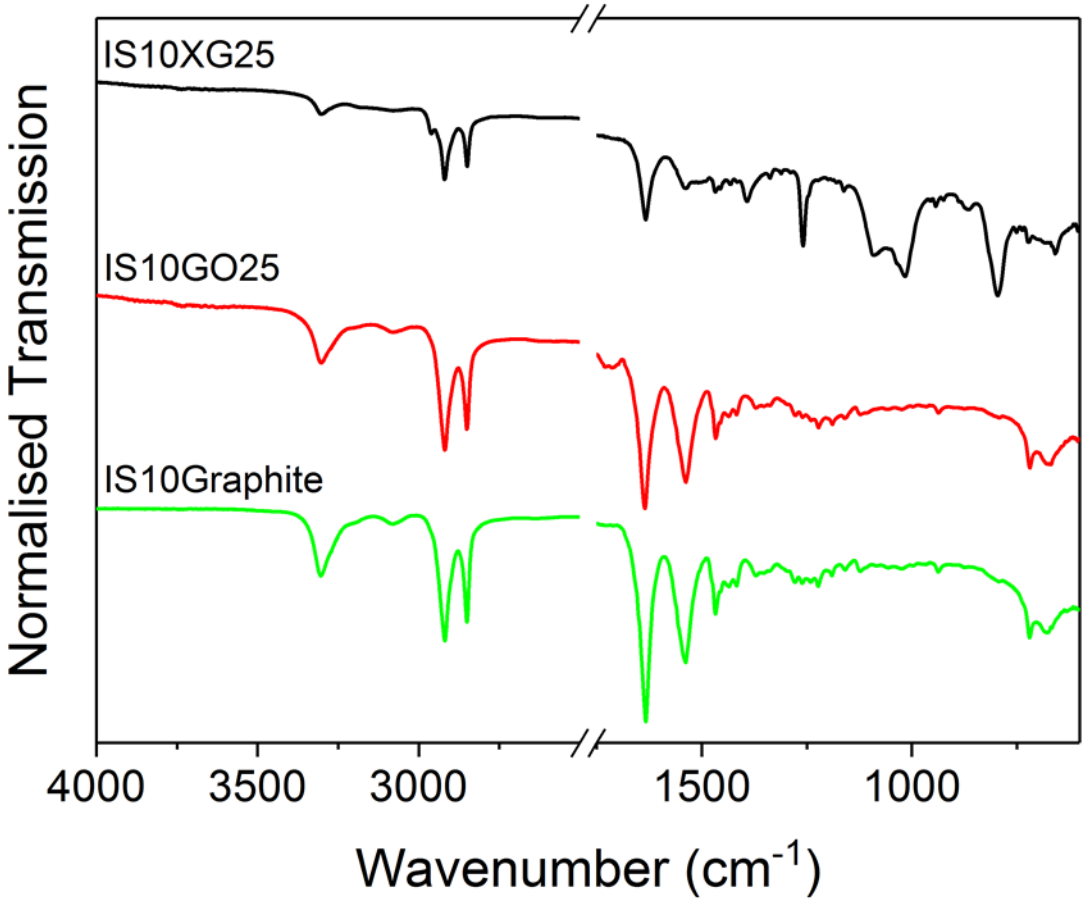

Figure 3.16. Comparison of FT-IR spectra for 10 wt% loaded *in situ* synthesised nanocomposites.

Raman spectroscopy of the *in situ* polymerised IS*n*XG25 and IS*n*GO25 samples are shown in Figure 3.17a and b, respectively. The graphitic 2D peak at around 2700 cm^{-1} can be observed in each GNP-containing nanocomposite, growing stronger with increased loading. The D and G peaks at approximately 1300 and 1600 cm^{-1}, respectively, are masked by PA11 peaks in the IS1XG25 spectrum. The IS5XG25 and IS10XG25 display clear D, G and 2D peaks with diminishing PA11 peaks visible at 2900 cm^{-1}. As can be seen through comparing Figure 3.7 and Figure 3.17a, the profiles of the D, G and 2D peaks are similar. The Raman spectra of IS*n*GO25 in Figure 3.17b show similar D and G peaks, with growing intensity relative to the PA11 peaks. As can be seen, the signal to noise ratio decreased with increased loading. This was due to a large background fluorescence, which led to smaller relative D and G peaks, compared to noise. Comparing the pure trGO25 Raman spectrum in Figure 3.7 to the spectra in

Figure 3.17b, it may be seen that the D and G peaks do not change markedly upon polymerisation. For neat GO25 the I(D)/I(G) = 1.5, whereas the 1, 5 and 10 wt% loaded samples had I(D)/I(G) ratios of 1.3, 1.3 and 1.2, respectively, which is similar to the value for trGO25 I(D)/I(G) = 1.2. The reduced I(D)/I(G) ratio suggests that there was a small amount of thermochemical reduction upon *in situ* polymerisation of GO25 at 220 °C. This may be due to a slight restoration of the sp^2 regions on the GO basal planes or removal of functionality.[94] The perpetuation of the high I(D)/I(G) ratio in the *in situ* polymerised samples means that the GO25 is not completely reduced to graphene-like platelets.[95]

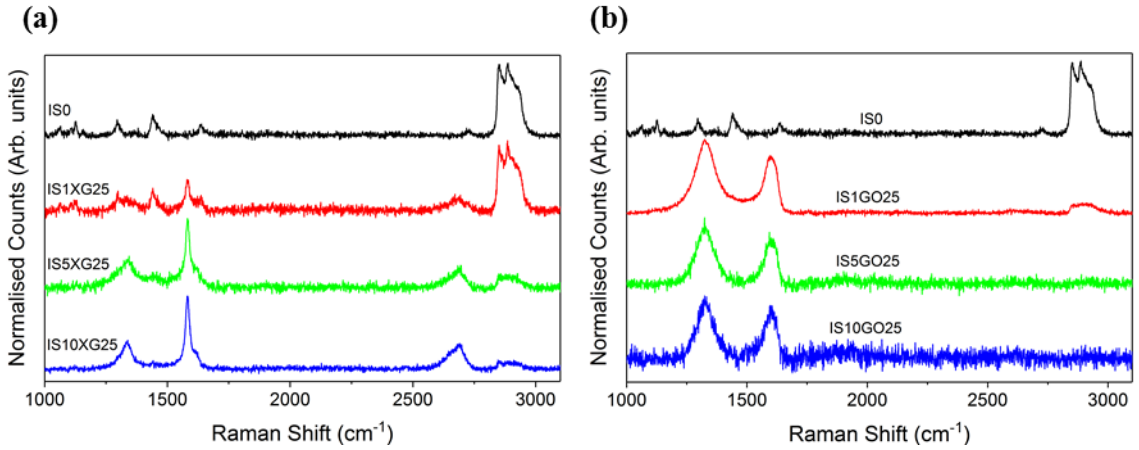

Figure 3.17. Raman spectra for (a) IS*n*XG25 and (b) IS*n*GO25.

3.6.2.3 Thermal Stability

TGA plots for the IS*n*XG25 and IS*n*GO25 nanocomposites are shown in Figure 3.18a and b, respectively. As can be seen in Figure 3.18a, the single degradation step for GNP-containing *in situ* polymers shifted to higher temperatures, with a later onset at higher GNP loadings. GO25-containing polymers (Figure 3.18b) also displayed a single degradation step but did not provide such an increase in thermal stability. Indeed, the degradation onset occurred earlier as the GO25 loading increased. There was no obvious weight loss at 200 – 300 °C due to free GO25 (Figure 3.8); providing further evidence for successful grafting of PA11 to the GO25.[141] Residues are indicated by dotted lines and the residue values at 500 °C are displayed in Table 3.5. From the plots, it was possible to extract the following degradation values: the temperature at which a loss of 5 wt% was observed ($T_{5wt\%}$);[142] the temperature at which the rate of mass loss

was a maximum – maximum in the DTG, example shown in Figure 3.8 (T_{max});[143] the temperature at which 50 wt% loss occurred ($T_{50wt\%}$);[142] and the residue at 500 °C.

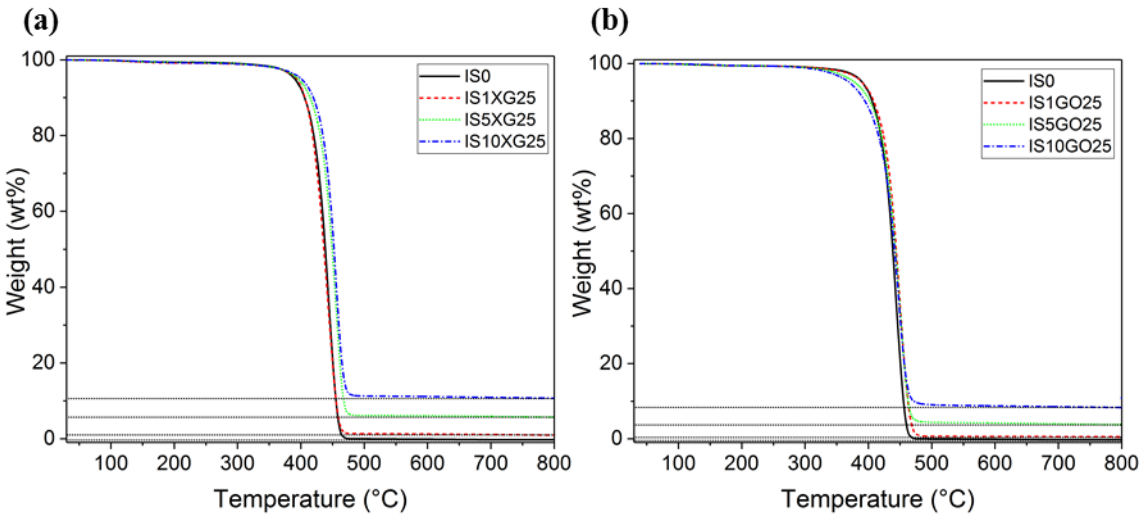

Figure 3.18. Typical TGA curves taken under a dry nitrogen stream, the horizontal dotted lines signify residue values. (a) IS*n*XG25 and (b) IS*n*GO25.

Table 3.5. Intended loadings displayed with TGA residue at 500 °C and the actual loading calculated by subtracting the residue for IS0 nanocomposite.

Composite	Intended loading (wt%)	Residue remaining at 500 °C (wt%)	Actual loading (wt%)
IS0	0	1.9	0
IS1XG25	1	2.6	0.75
IS5XG25	5	6.8	4.9
IS10XG25	10	10.9	9.0
IS0	0	1.9	0
IS1GO25	1	2.2	0.27
IS5GO25	5	5.7	3.8
IS10GO25	10	11.3	9.4

Plots comparing the $T_{5wt\%}$, T_{max} and $T_{50wt\%}$ of the GNP and GO25 *in situ* polymers are shown in Figure 3.19, Figure 3.20 and Figure 3.21, respectively. The standard deviations of the three repeats are displayed as error bars. It can be seen in Figure 3.19 that the temperature at which a 5 wt% loss was observed, increased with the addition of GNPs, and decreased with the addition of GO25. The enhancement of the initial degradation temperature due to GNPs may be explained by the GNPs providing a

barrier to the diffusion of degradation products out of the polymer matrix.[142,144] The earlier onset of thermal degradation for IS*n*GO25 nanocomposites with increasing GO25 loading is evident in Figure 3.19. This may be attributed to the reduction in polymer chain lengths due to the high levels of functionality available for grafting on the GO25. Low molecular weight polymers typically have a reduced thermal stability,[145] however, confirmation of molecular weight was not possible for the *in situ* polymerised samples.

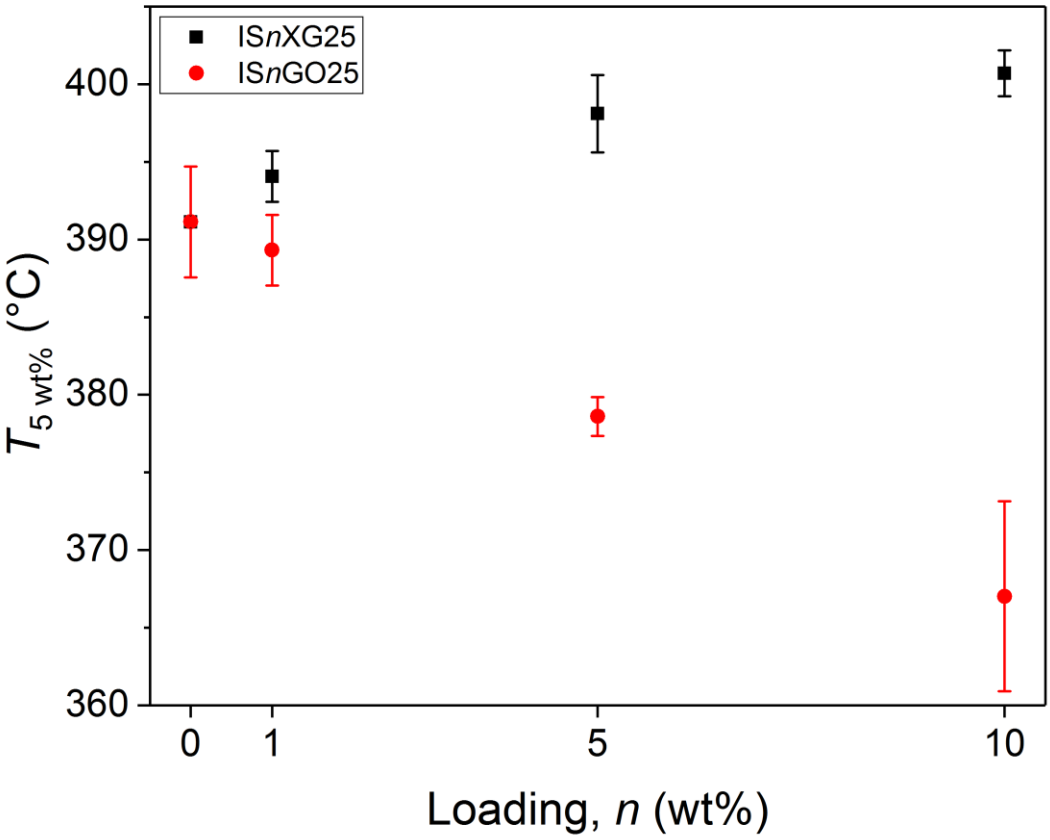

Figure 3.19. $T_{5wt\%}$ against GNP or GO25 loading.

As shown in Figure 3.20 and Figure 3.21, 1 wt% loading of GNPs did not appear to improve the T_{max} or $T_{50wt\%}$. At 5 and 10 wt% GNP loadings, the degradation temperatures were greater than for equivalent GO25 nanocomposites and the neat PA11. This change in behaviour with GNP loading demonstrated the presence of two different degradation mechanisms: the GNPs acted as both a mass barrier and a heat conductor.[142,146] At 1 wt% loading, the improved thermal conduction of the GNPs led to faster heating and subsequent degradation, but the low concentration of GNPs meant that the mass barrier effect was minimal.[146] At higher loadings, the mass barrier effect

of the GNPs dominated over the improved heat conduction, thus, the thermal stability was improved.[142,146]

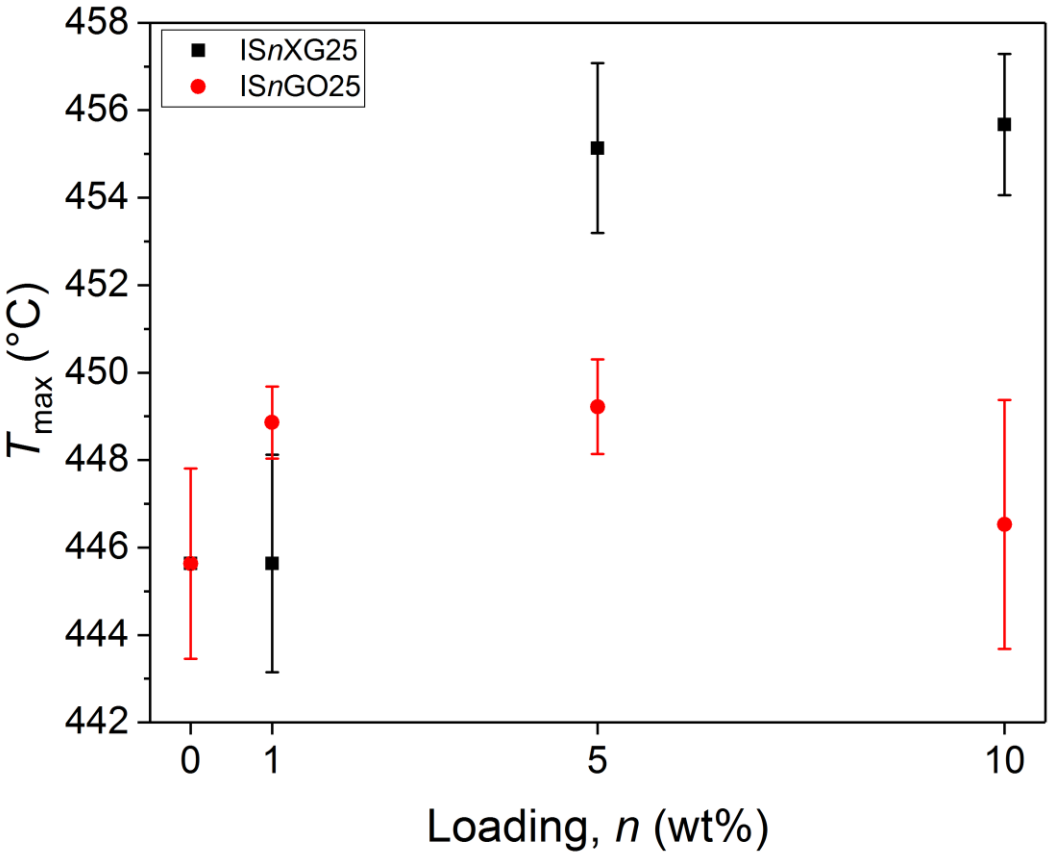

Figure 3.20. T_{max} against GNP or GO25 loading.

Although the onset of degradation occurred earlier for IS*n*GO25 samples (Figure 3.18b and Figure 3.19), GO25 had some stabilising effect at higher temperatures, as shown in Figure 3.20 and Figure 3.21. The GO25 stabilising effect outperformed GNPs at 1 wt% loading; however, GNPs outperformed GO25 at 5 and 10 wt% loading. At 1 wt% loading of GO25, there was likely an excess of monomer compared to the GO25 oxygen moieties, thus, long polymer chains were likely to be synthesised, grafted to at least one GO25 platelet. At higher GO25 loadings, the available GO25 functionality for grafting to monomer increased greatly, thus polymer chains were likely to be shorter. There may, therefore, be two competing mechanisms for GO25 *in situ* polymerised nanocomposite stability: initially, at low GO25 loading, crosslinking of long polymer chains led to an increased thermal stability; and then the shortening of polymer chains

due to the availability of a higher number of grafting sites led to poorer thermal stability. There may also be an aspect of mass barrier behaviour for the GO25 platelets.[142,146] As the temperature increased, the graphitic nature of the GO25 should be increased due to thermal reduction; therefore, at higher temperatures (T_{max} and $T_{50wt\%}$) the diffusion of degradation species through the matrix may have been harder than at lower temperatures ($T_{5wt\%}$).

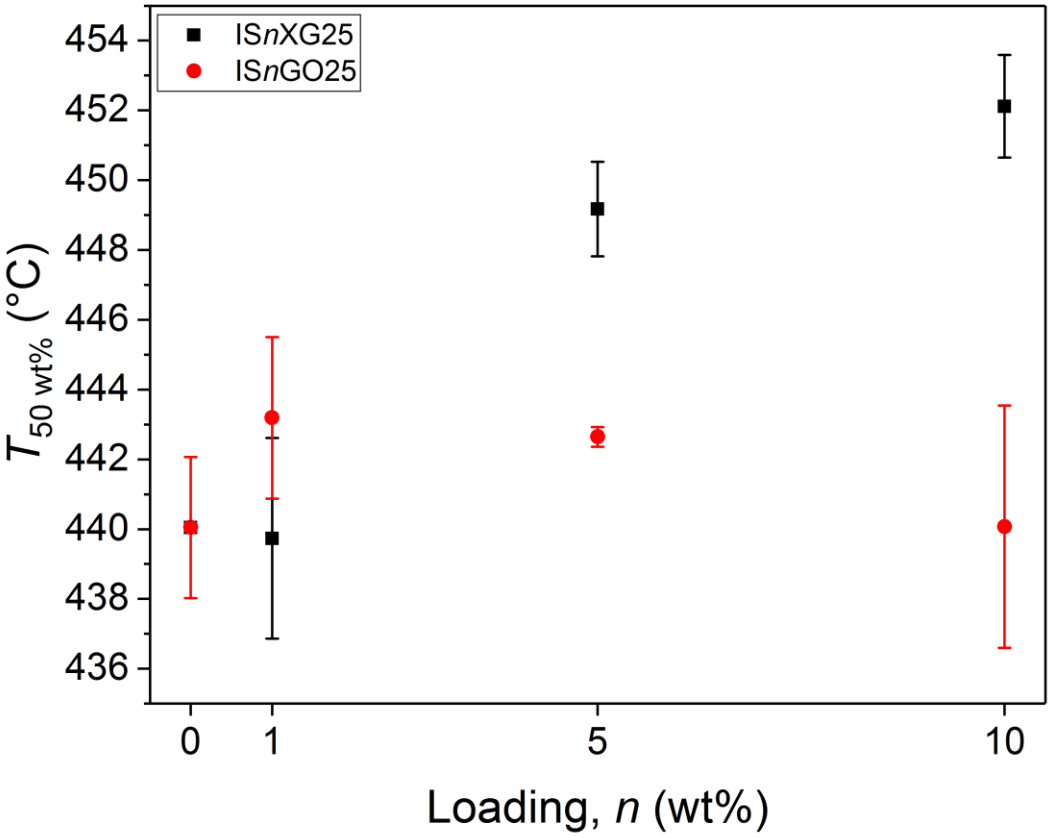

Figure 3.21. $T_{50wt\%}$ against GNP or GO25 loading.

3.6.2.4 Crystallisation

The crystallisation behaviour of IS*n*XG25 and IS*n*GO25 was monitored by DSC and the results are shown in Table 3.6. As can be seen, there was no remarkable change in T_g, T_{m1} or T_{m2} with GNP or GO25 loading, apart from for IS5GO25 and IS10GO25. The low T_{m1} and T_{m2} for IS5GO25 and IS10GO25 may be due to the very high loading of GO25 which provided too many grafting functionalities, thus limiting molecular weight of the resultant PA11.[147]

An increase in T_c with nano-filler loading is expected as the filler may act as a nucleating surface for crystallisation.[148–152] The value of T_c generally increased with GNP loading, however, it showed less of an increase at the highest loading. This may have been due to the agglomeration of GNPs at higher loadings, meaning that the net effect was a reduction in possible nucleating sites. The increased T_c for IS*n*GO25 with loading was possibly due to the GO25 initially acting as a good nucleating agent. However, the subsequent decrease may have been because of the reduced PA11 molecular weight, again due to increased grafting opportunity. An increase in T_c has been observed with increased GO loading for PA11/GO composites.[98] However, the loadings were limited to less than 3 wt%, so the threshold for substantial reduction in molecular weight may not have been reached.

The decrease in ΔH_m with filler loading can be explained by the decrease in the weight fraction of PA11 for each sample as the GRM loading increases. This effect is taken into account by Equation 3.6. χ_c varied slightly with GNP loading, however it varied dramatically with GO25 loading. The degree of crystallinity increased at 1 wt% GO25 loading, which corresponded to a very high T_c value. This suggested that 1 wt% loading of GO25 allowed for grafting between GO25 flakes, encouraging crystallisation at a higher temperature and to a greater extent. The degree of crystallinity was greatly reduced at higher GO25 loadings; this may be due to interactions between the polar amide groups of the PA11 with oxygen functionalities on the GO, preventing rearrangement of the polymer chains into crystals.[153]

Table 3.6. DSC results for IS0 control PA11, IS*n*XG25 and IS*n*GO25 nanocomposites. The standard deviation is calculated from three measurements.

Composite	T_g (°C)	T_{m1} (°C)	T_c (°C)	T_{m2} (°C)	ΔH (J g^{-1})	χ_c (%)
IS0	38 ± 1	188.4 ± 0.6	163.5 ± 0.5	188.82 ± 0.09	65.8 ± 0.7	34.8 ± 0.4
IS1XG25	39.4 ± 0.4	190.0 ± 0.9	166.8 ± 0.1	188.3 ± 0.2	61.3 ± 0.2	32.4 ± 0.1
IS5XG25	39.9 ± 0.7	189 ± 1	170.5 ± 0.7	188.4 ± 0.2	63 ± 2	33 ± 1
IS10XG25	40.2 ± 0.2	189 ± 1	167.3 ± 0.6	189.5 ± 0.4	56 ± 4	30 ± 2
IS0	38 ± 1	188.4 ± 0.6	163.5 ± 0.5	188.82 ± 0.09	65.8 ± 0.7	34.8 ± 0.4
IS1GO25	38 ± 2	188.4 ± 0.9	173 ± 1	188.2 ± 0.3	72.3 ± 0.3	38.3 ± 0.1
IS5GO25	37.1 ± 0.5	184.6 ± 0.3	167.3 ± 0.6	184.6 ± 0.6	62 ± 1	32.6 ± 0.7
IS10GO25	34 ± 2	180.2 ± 0.6	158 ± 2	180 ± 1	55 ± 1	29.1 ± 0.7

Representative DSC curves for the *in situ* polymers are shown in Figure 3.22, Figure 3.23 and Figure 3.24 for T_{m1}, T_{m2} and T_c, respectively. As outlined in section 2.6, the nomenclature surrounding PA11 crystallisation is confusing, with some groups using terms erroneously. As can be seen in Figure 3.22 and Figure 3.23, the melting endotherm for the neat IS0 PA11 has a different shape to the samples loaded with GNPs or GO25.

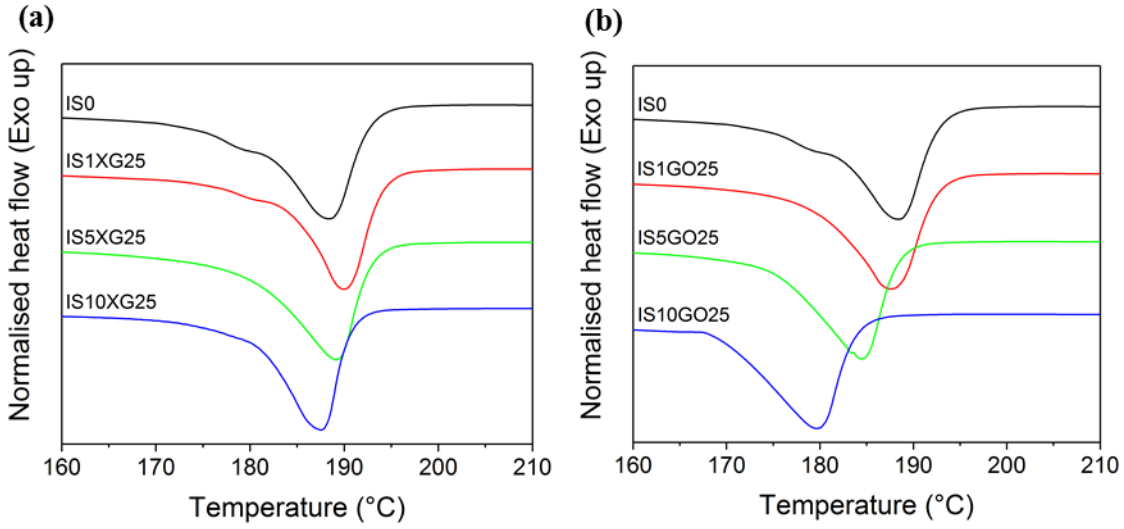

Figure 3.22. T_{m1} endotherms for: (a) IS*n*XG25; and (b) IS*n*GO25.

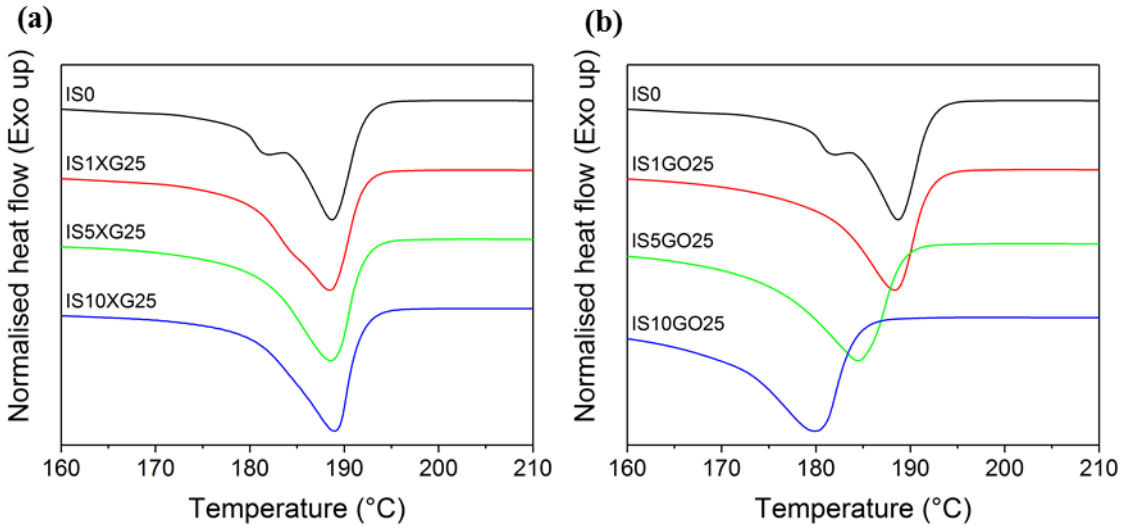

Figure 3.23. T_{m2} endotherms for: (a) IS*n*XG25; and (b) IS*n*GO25.

The difference in T_{m2} is particularly marked in Figure 3.23, with the IS0 control displaying two different endotherms, possibly representing two different crystallinities or melt recrystallisation.[71,154] The lower temperature peak of the double melting peak of PA11 has been attributed to the melting of δ (high temperature α' phase) crystals.[69] The higher temperature peak, however, has been assigned to the melting of δ' crystals.[69] Melt recrystallisation has been observed for PA11 in previous studies and is due to either the crystallisation of amorphous regions or partial melting of imperfect crystals and subsequent recrystallisation.[70,155] The low temperature peak has been assigned as original α' crystals melting and the high temperature peak assigned to δ (stable high temperature α' analogue) phase melting.[77] α' crystallinity has been reported to display such melting behaviour previously, while other PA11 crystallinity displayed no such low temperature peak.[77]

The IS1XG25 T_{m2} endotherm shows the presence of a shoulder, which may also be due to α' crystals melting followed by δ crystal melting.[77] All GO25 T_{m2} peaks display a single endotherm which shows that the grafted GO25 platelets limit the melt recrystallisation behaviour of PA11. The variation of melting peak shapes has also been followed with *in situ* polymerised PA11 with GO loading by Yuan *et al.* at 0, 0.125, 0.25 and 0.5 wt%.[96] They found that all samples displayed a double melt peak; however, the GO loadings in this work start at 1 wt%. This may suggest that at low

loadings, double melt peaks are seen, but at loadings of 1 wt% and above, only single endotherms are observed.

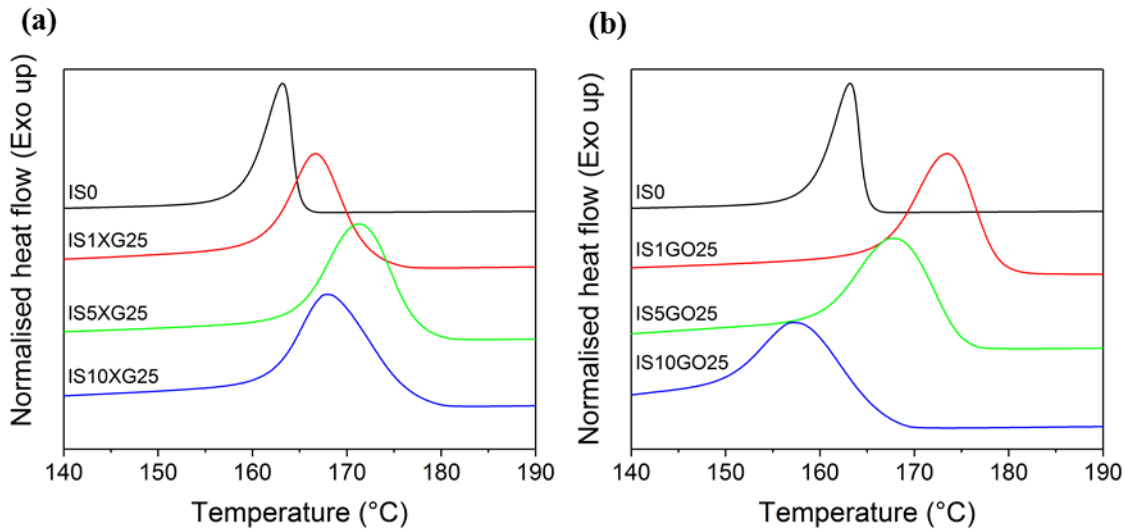

Figure 3.24. T_c exotherms for: (a) IS*n*XG25; and (b) IS*n*GO25.

XRD was carried out on compression moulded samples that were slow cooled from 240 °C to room temperature at around 0.5 °C min^{-1}, in order to investigate the native crystallinity of the *in situ* polymerised nanocomposites. Figure 3.25a and Figure 3.25b show XRD diffractograms for IS*n*XG25 and IS*n*GO25 nanocomposites, respectively. Lorentzian peak fitting of the IS*n*GO25 reflections yielded Figure 3.25c. The 2Θ values shown in Table 3.7 were obtained by this Lorentzian curve fitting. As shown in Figure 3.25 and Table 3.7 all samples, regardless of filler content, show reflections indicative of α' crystallinity with (100) and (110)/(010) reflections at 2Θ around 20 and 23 ° respectively.[67,78,79,156] Figure 3.25a also shows graphitic reflections at approximately 26 ° for the GNP loaded nanocomposites. No GNP reflection is visible in the IS*n*GO25 samples, which is unsurprising, given that trGO25 shows no graphitic peaks (Figure 3.10). Interestingly, the GO25 loaded nanocomposites appear to have a larger (110)/(010) peak, however, this may be due to coupling of the reflections observed in the trGO25 diffractogram (Figure 3.10). The curve fitting shown in Figure 3.25c shows that the IS1GO25, IS5GO25 and IS10GO25 XRD diffractograms could be fitted with three curves, centred at 20, 22 and 23 °. The peak at 22 ° could be attributed to a combination of peaks visible in the diffractogram of trGO25 (peaks (d) and (e) in Figure

3.10). Assuming this treatment is appropriate; the trGO25 peak (Figure 3.25c, green curve) appeared to increase in relative height as the GO25 loading increases.

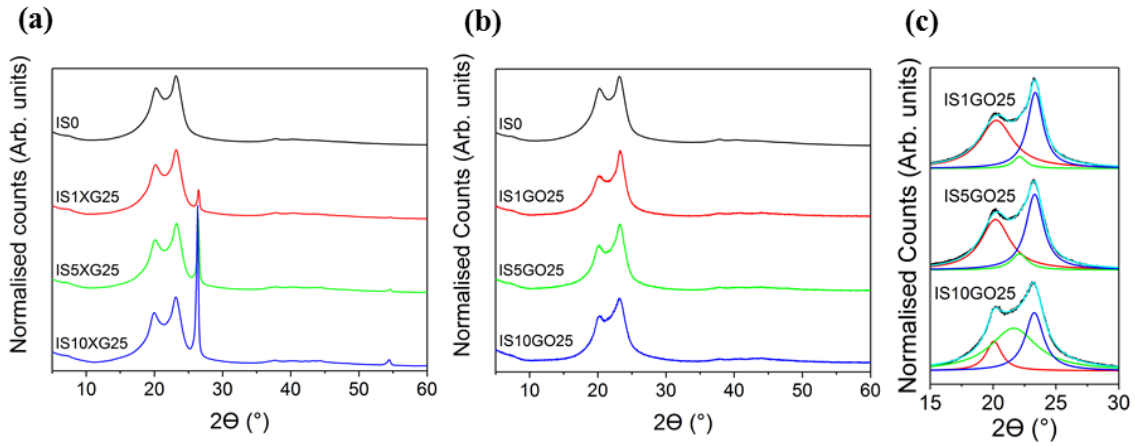

Figure 3.25. XRD diffractograms for (a) IS*n*XG25 and (b) IS*n*GO25 samples (c) curve fitting 1, 5 and 10 wt% GO25 loaded nanocomposites, loadings increasing from top to bottom.

As the XRD confirmed native α' crystallinity, the melting behaviour of the IS0 and IS1XG25 nanocomposite may be attributed to the double melting behaviour of imperfect α' crystals and then δ crystals at higher temperature.[77]

Table 3.7. Table of 2Θ values for the centre of Lorentzian curves fitted to the PA11 peaks in Figure 3.25.

Composite	**2Θ α'$_{100}$ (°)**	**2Θ α'$_{110/010}$ (°)**	**2Θ GNP / trGO25 (°)**
IS0	20.4	23.2	N/A
IS1XG25	20.3	23.2	26.5
IS5XG25	20.3	23.3	26.4
IS10XG25	20.1	23.2	26.3
IS0	20.4	23.2	N/A
IS1GO25	20.3	23.4	22.1
IS5GO25	20.2	23.3	22.1
IS10GO25	20.1	23.3	21.6

3.6.2.5 Morphology

The morphology of the *in situ* polymerised nanocomposites was investigated by SEM and secondary electron images are shown in Figure 3.26 – Figure 3.32. The characteristics of the hydrophobic GNPs and hydrophilic GO25 appeared to have a marked effect upon the observed morphologies.

The morphology of IS0 is shown in Figure 3.26. The detailed morphologies in Figure 3.26a (IS0), Figure 3.27a (IS1XG25) and Figure 3.28a (IS1GO25) all have similar appearances, although a few GNP flakes are visible in Figure 3.27a (yellow arrows).

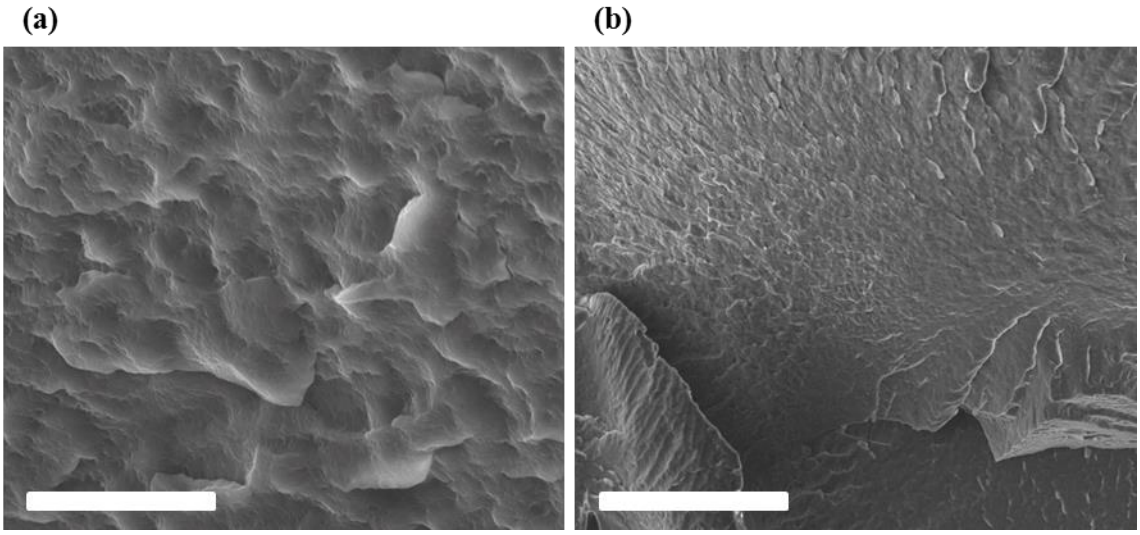

Figure 3.26. SEM images of IS0 nanocomposites: (a) 10 µm scalebar; (b) 100 µm scalebar.

As can be seen by comparing IS1XG25 and IS1GO25, the GNP flakes can be seen protruding at the fracture surface (Figure 3.27a) whereas no GO25 flakes are visible (Figure 3.28a). The macroscopic morphologies (Figure 3.27b and Figure 3.28b) also appear to differ as IS1XG25 displayed a crazed surface, and the IS1GO25 had a more ordered structure, closer to that of IS0 (Figure 3.26b).

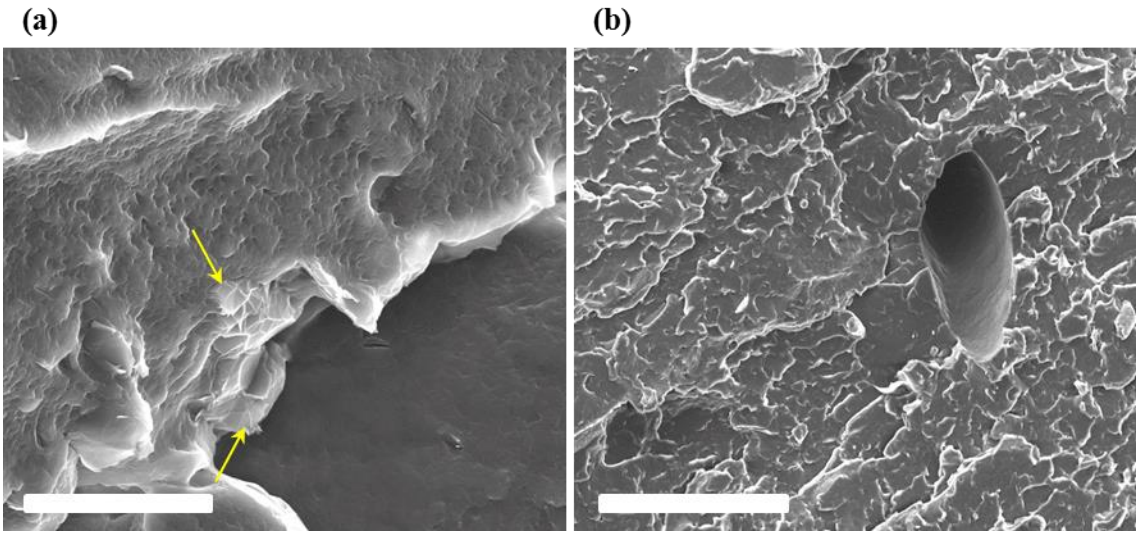

Figure 3.27. SEM images of IS1XG25 nanocomposites: (a) 10 µm scalebar; (b) 100 µm scalebar.

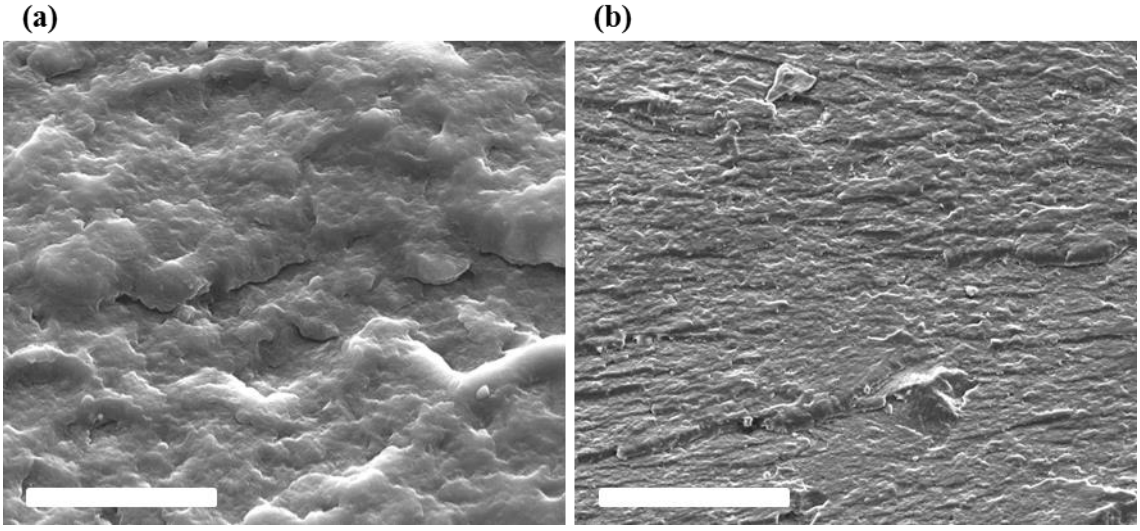

Figure 3.28. SEM images of IS1GO25 nanocomposites: (a) 10 µm scalebar; (b) 100 µm scalebar.

As the loadings of GNP and GO25 increase from 1 wt% to 5 wt%, the differences in morphology start to become more obvious. GNP flakes are clearly visible (yellow arrows) in Figure 3.29a and b, whereas the GO25 flakes appear to have a coating of polymer, and are completely imbedded within the polymer matrix (Figure 3.30a). As no free flakes were visible, it appeared that the GO25 had better compatibility with the PA11. This is probably due to the hydrophilic oxygen functionalities that interact with

the amide bonds within the PA11 as well as the grafting of some polymer chains to the GO itself during the polymerisation. Again, the macroscopic morphologies show interesting differences. As can be seen in Figure 3.29b (IS5XG25), the fracture surface has a rough topology whereas that of IS5GO25 in Figure 3.30b, has morphology closer to that of IS0 (Figure 3.26b).

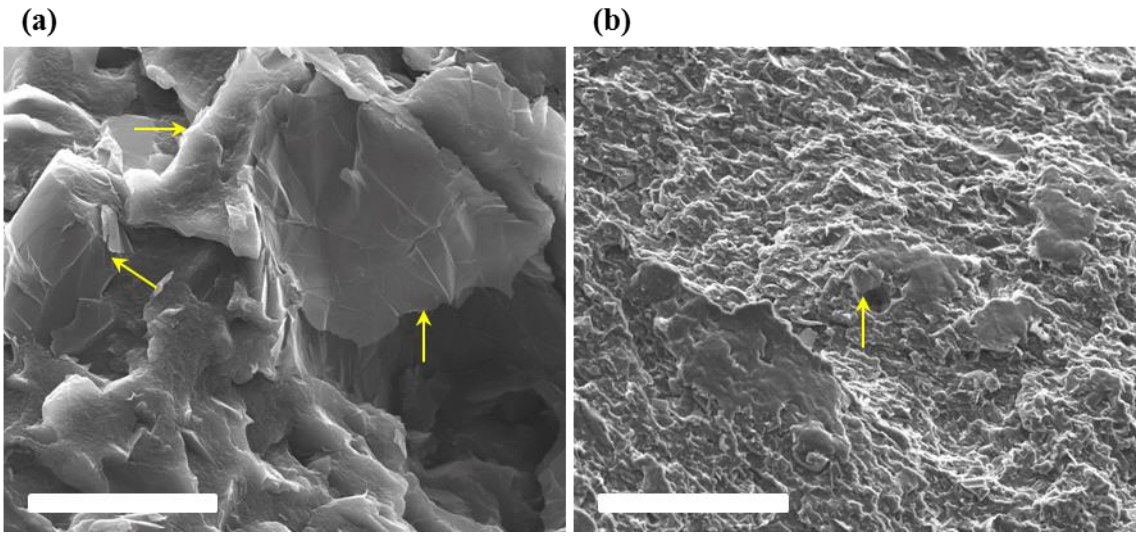

Figure 3.29. SEM images of IS5XG25 nanocomposites: (a) 10 µm scalebar; (b) 100 µm scalebar.

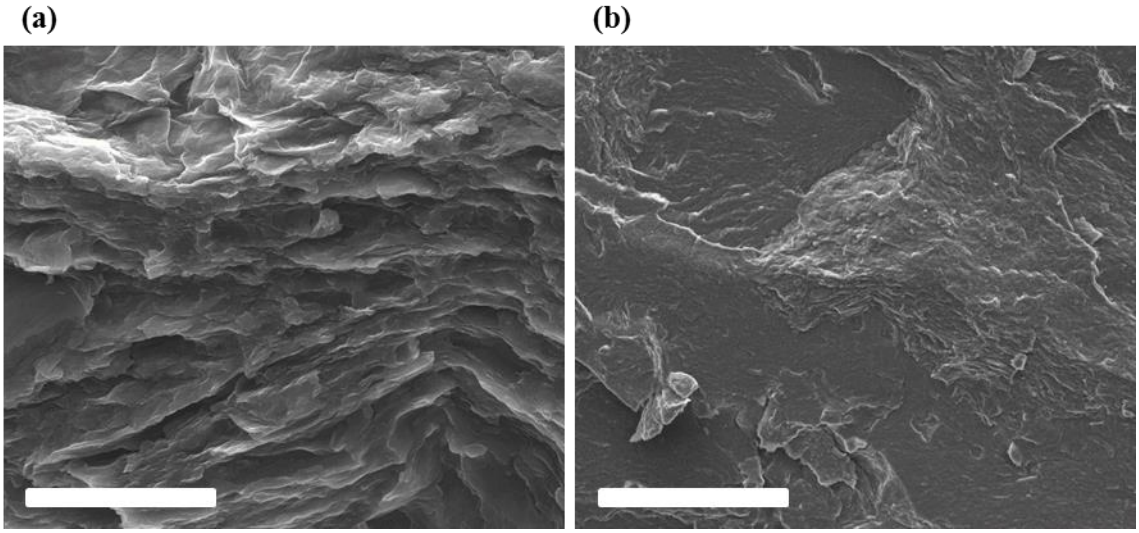

Figure 3.30. SEM images of IS5GO25 nanocomposites: (a) 10 µm scalebar; (b) 100 µm scalebar.

Again, as the loading increases to 10 wt% filler; GNPs can be clearly seen in Figure 3.31a and b whereas 10 wt% GO25 composite (Figure 3.32) shows no appreciable change in morphology compared to the IS0 composite (Figure 3.26).

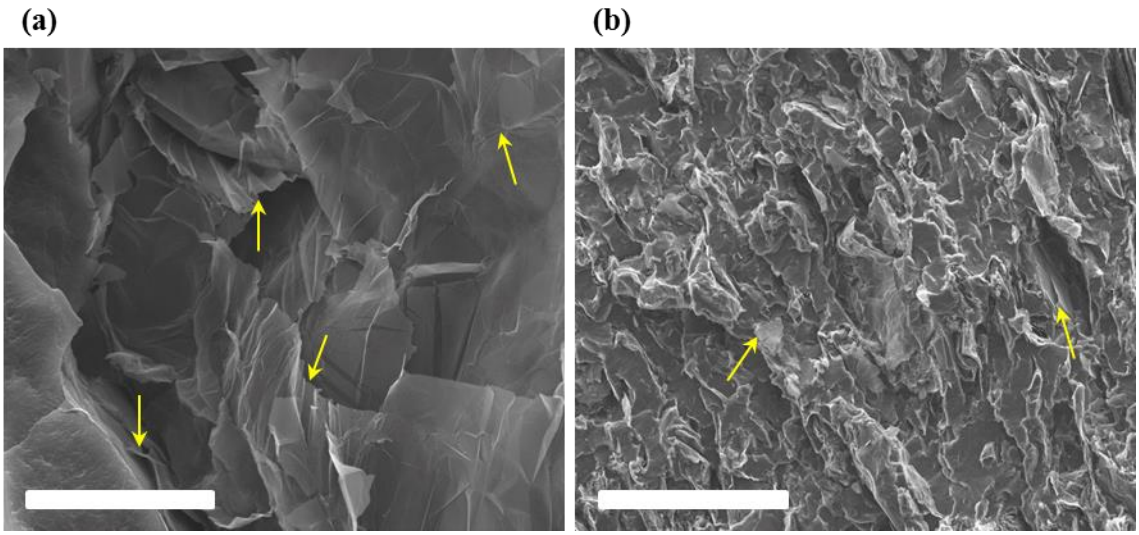

Figure 3.31. SEM images of IS10XG25 nanocomposites: (a) 10 µm scalebar; (b) 100 µm scalebar.

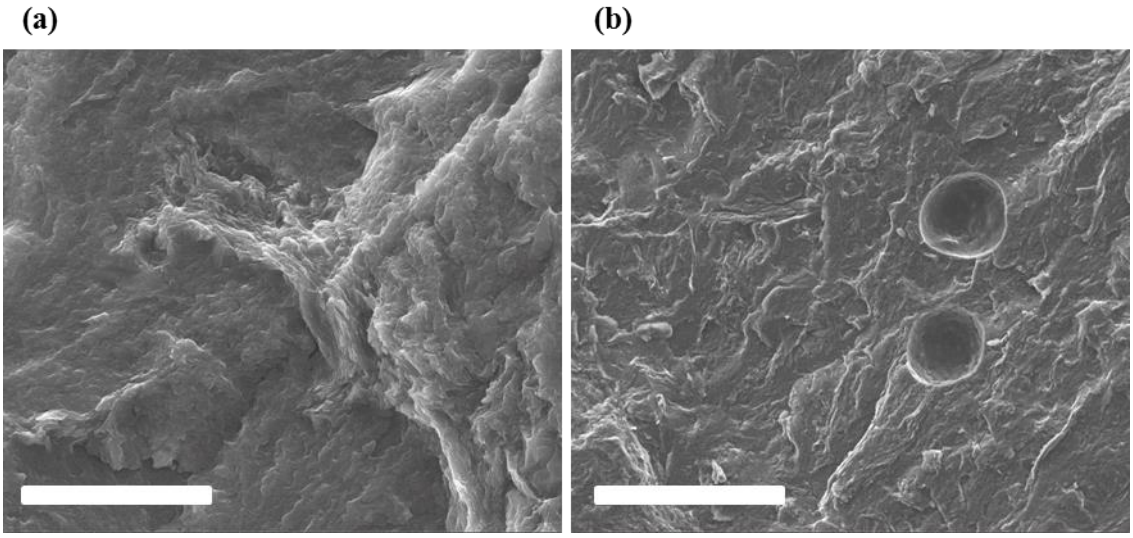

Figure 3.32. SEM images of IS10GO25 nanocomposites: (a) 10 µm scalebar; (b) 100 µm scalebar.

The similarities in the detailed and macroscopic morphologies of IS0 and IS*n*GO25 nanocomposites suggested that the PA11 grafts well to the GO25 and that the GO25 was compatible with the PA11. The GNPs on the other hand appear to delaminate more easily at the fracture surface and can be easily seen at even the lowest loading (Figure

3.27). These observations suggest that the interfacial interactions between GNPs and PA11 are very poor in comparison to the PA11/GO25 interactions. This was not unlikely, considering the largely hydrophobic, graphitic nature of the GNPs and the hydrophilic and aliphatic nature of the polyamide. GO25, with its hydrophilic nature and myriad of grafting sites provided better compatibility and subsequent polymerisation with PA11.

3.7 CONCLUSIONS

In situ polymerisations provide a good starting point for the thesis and the results are compared with melt blending techniques in Chapter 4. Although permeability testing was not carried out, the characterisation provided interesting information that allowed effective comparisons to be drawn, particularly for the melt blending studies to follow.

GO25 and trGO25 were synthesised from GNP starting material and characterised. *In situ* polymerised nanocomposites were produced with GNP and GO25 loadings up to 10 wt%.

A combination of solubility experiments, FT-IR spectroscopy, TGA, DSC and SEM supplied evidence that grafting of PA11 to GNPs and GO25 was successful.

It was found by FT-IR spectroscopy that the thermal reduction of GO25 at 220 °C leaves some functionality available for reaction during *in situ* polymerisation. No functionality on GNPs could be identified by FT-IR spectroscopy in this work, however, upon *in situ* polymerisation, new peaks were observed that could be correlated with GNP spectra found in the literature. *In situ* polymerisation of GO25 resulted in no substantial modification of the FT-IR spectra.

Raman spectroscopy provided additional information on the functionality of the GNPs, GO25 and trGO25 – showing that there was a small amount of functionality on GNPs and substantial functionality or defects remaining on trGO25 following reduction. Applying Raman spectroscopy to the *in situ* polymerised GO25 nanocomposites suggested that there was some thermochemical reduction during polymerisation.

XRD allowed the calculation of interlayer spacing for GNPs, GO25 and trGO25 materials. XRD of the *in situ* nanocomposites provided information on the crystal

structure of the nanocomposites. It was concluded that α' crystallinity was the main crystallinity yielded, which resulted in a double melting peak in the DSC traces due to imperfect α' crystal melting, followed by their high temperature form, δ crystal melting. DSC data showed that the addition of GNPs and GO25 did not affect the T_{m1} or T_{m2} greatly, although there was a change from bimodal to single melting peaks with increased filler loading. The T_c was increased for all nanocomposites compared to the neat PA11, except for nanocomposites with high loadings of GO25. No appreciable change in T_g was observed but the χ_c decreased with increased filler loading.

The morphologies of the two *in situ* polymerised nanocomposites were markedly different. GNP containing nanocomposites appeared to delaminate easily, probably due to poor compatibility between the hydrophobic, graphitic basal planes of the GNPs and polar, aliphatic polyamide. GO25 on the other hand, appeared to have a coating of PA11, masking the flakes so that they were not clearly observable. This suggests that grafting to GO25 was successful and that PA11/GO25 interactions were favourable in comparison to PA11/GNP interactions.

CHAPTER 4: MELT BLENDED NANOCOMPOSITES

4.1 INTRODUCTION

Following on from *in situ* polymerisations, industrially important, solvent-free melt processing was investigated. In this chapter, the work carried out on melt blended nanocomposites comprised of PA11 and GNPs is described. First, though, the state of the art for creating nanocomposites of polymers with graphene through melt blending is reviewed, with focus particularly on polymers for improved barrier performance.

4.2 LITERATURE REVIEW

4.2.1 POLYMER/GRAPHENE NANOCOMPOSITES

Section 4.2.2 reviews PA11/graphene nanocomposites in detail. First, the literature is reviewed of other polymer/graphene nanocomposites specifically for improved barrier performance.

The petrochemical fuel and oxygen barrier properties of HDPE/GNP nanocomposites, prepared through twin-screw extrusion, were evaluated by Honaker and co-workers.[157] It was found that GNPs dramatically reduced the permeation of oxygen up to GNP loadings of 7.5 wt%. After this loading, the oxygen permeability reduction became less stark, before eventually increasing at loadings higher than 20 wt%. Fuel permeation initially followed a similar trend, although continued to slowly drop up to the highest GNP loading tested (40 wt%). A maximum reduction in oxygen transport of 77% was achieved at 20 wt% loading and a reduction in fuel transport of approximately 80% was achieved at 40 wt% loading. Melt compounded polycarbonate/GNP composites were produced by Müller and co-workers.[158] They compared GNPs to a range of carbon materials and found that GNPs provided the best barrier performance, providing a 41% reduction in oxygen permeability at 3 wt% loading. Al-Jabareen *et al.* found that polyethylene terephthalate (PET)/GNP nanocomposites reduced oxygen transmission rate (OTR) by over 99% at 1.5 wt% loading.[159] They found that a reduction in OTR correlated with the increasing crystallinity of the system, afforded by increased GNP

loading. GNPs also provided a 20% reduction in oxygen transport for polypropylene (PP) at 6.7 wt% (3 vol%) loading.[160]

4.2.2 Polyamide 11/Graphene Nanocomposites

Relatively few publications have focussed on the addition of GNPs to PA11. Chen *et al.*[111] used powder-powder mixing of PA11 with GNPs in an acoustic mixer and rotary mixer, before compression moulding. Jacobs *et al.*[97] also incorporated GNPs into powdered PA11 through compression moulding. They first pre-mixed the PA11 and GNPs in an IPA paste to encourage good dispersion of the GNPs prior to drying and pressing into thin films. Gaikwad *et al.*[161] added 1 – 7 wt% GNPs on an industrial pilot scale twin-screw extruder for selective laser sintering without pre-mixing. Recently, Rashmi *et al.*[162] created 15 wt% masterbatches of GNPs in PA11 which were then diluted with PA11 to supply 0.5 – 5 wt% PA11/GNP nanocomposites. The work to date has focussed on mechanical, rheological, and thermal properties of the PA11/GNP nanocomposites.

In some cases, GO, instead of graphene, has been used in combination with PA11. Pan *et al.*[163] added functionalised GO to PA11 powder in ethanol, applying the suspension as a spray coating for steel before heating to 230 °C in order to plasticise the PA11 powder. Melt compounding on a lab-scale twin-screw extruder was utilised by Jin *et al.*, in order to combine GO with PA11 and PA12.[98] The samples were tested for barrier performance to water and oxygen at atmospheric pressure. They observed a maximum reduction in water permeability of 49% at 0.1 wt% loading and a maximum reduction in OTR of 47% at 0.3 wt% loading for PA11. The reduction in water and oxygen transport tended to be greatest for the PA11 composites compared to the PA12 composites, as shown in Table 4.1.

Table 4.1. Summary of the percentage reduction in water permeability and OTR of melt blended nanocomposites compared to virgin polymer.[98]

FG loading	Water permeability reduction (%)		OTR reduction (%)	
(wt%)	PA11	PA12	PA11	PA12
0	0	0	0	0
0.1	49	33	38	26
0.3	39	34	47	30
0.6	35	38	42	32
1.0	31	27	35	27
3.0*	N/A	N/A	22	11

*PA12 nanocomposite only

4.3 AIMS AND OBJECTIVES

It was the aim of this section of work to manufacture PA11/GNP nanocomposites and test their permeability under high pressure CO_2 with H_2S.

Firstly, two different methods of nanocomposite production were investigated, both using twin-screw extrusion, however, one had a pre-mixing step.

The nanocomposites were characterised in order to evaluate the effect of GNP content on the behaviour of the PA11, as well as enabling comparison between the two methods of manufacture. In particular, the morphological analysis using SEM provided key evidence for the behaviour of the nanocomposites produced.

Finally, the most promising nanocomposite was permeation tested under high pressure conditions and the effect of GNP addition was discussed.

4.4 MATERIALS AND METHODS

4.4.1 POLYAMIDE 11

The PA11 used was described in section 3.4.2. A portion of the polymer was cryogenically milled at Queen's University, Belfast. The size distribution achieved is displayed in Figure 4.1 and shows that the majority of the PA11 powder was less than 150 µm in length. The polymer had an IV of 170 $cm^3\ g^{-1}$ and $\bar{M}_v$ = 53000 g mol^{-1}, as measured through Ubebelohde viscometry (section 3.5.1).

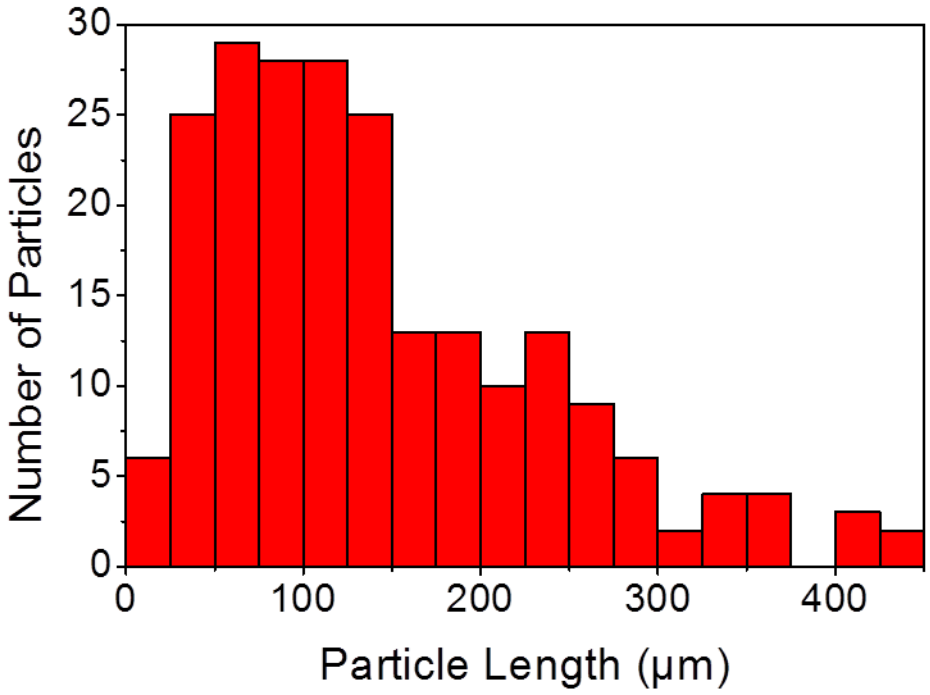

Figure 4.1. Particle size distribution of a microscope image of cryogenically milled PA11, measured using ImageJ.

4.4.2 Graphene Nanoplatelets

GNPs were sourced from XG Sciences Inc., Lansing, Michigan (USA). xGnP Grade M 25 µm nanoplatelets were chosen for the study. According to the datasheet,[37] the GNPs had an average lateral size of 25 µm with surface areas of 120 – 150 m^2 g^{-1} and average thickness of 6 – 8 nm.

4.4.3 Nanocomposite Production

Nanocomposites were produced on a benchtop Haake Minilab Twin-Screw Extruder (Figure 4.2a and b) with co-rotating screws at 215 °C, 50 rpm with 10 min cycling (red arrows) before extrusion (blue dotted arrow).

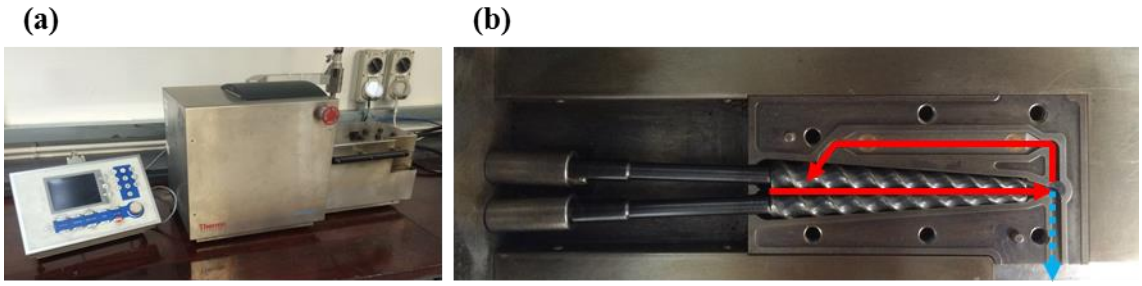

Figure 4.2. Photographs of Haake Minilab Twin-Screw Extruder: (a) on the bench top; (b) inside the barrel, red arrows show direction of flow during cycling and a blue dotted arrow shows extrusion direction.

The yield from the extruder was approximately 2 g of lace for an input mass of around 5 g (approximately 7 cm^3 capacity). After the extruder was fully loaded, the molten polymer was cycled for 10 min. The polymer lace was extruded and collected before being chopped into pellets. The extruder was cleaned thoroughly following each batch before the next batch was processed.

4.4.4 Melt Blending Techniques

The loadings used in this work were 0, 1, 5, 10 and 20 wt% GNPs in BESVO PA11, denoted PA0XG25, PA1XG25, PA5XG25, PA10XG25 and PA20XG25, respectively as shown in Table 4.2.

Table 4.2. GNP loadings of the nanocomposites produced in this work per 5 g capacity of the Haake Minilab.

Composite	Loading (wt%)	Loading (vol%)	Mass GNP (g)	Mass PA11 (g)
PA0XG25-C	0	0.00	0.000	4.998
PA1XG25-C	1	0.50	0.050	4.975
PA5XG25-C	5	2.40	0.257	4.879
PA10XG25-C	10	4.90	0.528	4.753
PA20XG25-C	20	10.4	1.120	4.479
PA0XG25-P	0	0.00	0.000	4.998
PA1XG25-P	1	0.50	0.050	4.975
PA5XG25-P	5	2.40	0.257	4.879
PA10XG25-P	10	4.90	0.528	4.753
PA20XG25-P	20	10.4	1.120	4.479

For each loading, two different melt blending methods were investigated: the ‘chip’ method – repeated sequential addition of PA11 pellets (chip) followed by GNP powder; and the ‘powder’ method – simultaneous addition of pre-mixed PA11 powder and GNP

powder. The nanocomposites produced by the chip method are named PA*n*XG25-C and those produced by the powder method are named PA*n*XG25-P (Table 4.2), where *n* is the loading in wt%. Photographs of the samples following extrusion and chopping are shown in Figure 4.3. The size distribution of PA11 used in the powder method is shown in Figure 4.1. The chip process relied on pressing PA11 pellets into the extruder until melted, GNP powder was then fed onto the melt and the cycle was repeated, as shown in Figure 4.4. The powder method allowed for both PA11 powder and GNPs to be added at the same time in an effort to achieve better GNP dispersion (Figure 4.4).

It is worth noting that the addition of GNPs into the PA11 matrix made the nanocomposites, qualitatively, very brittle, an effect that was exacerbated at higher GNP loadings. For the 20 wt% nanocomposites, the viscosity was qualitatively very high, leading to difficult melt mixing and subsequent extrusion.

No attempt was made to incorporate GO25 into PA11 by melt blending due to thermal degradation of the GO at the processing temperature (215 °C). For GO25 to have been incorporated safely, the GO25 would require thermal reduction prior to extrusion.

Figure 4.3. Photographs of melt processed PA11/GNP nanocomposites following extrusion and chopping, labelled appropriately.

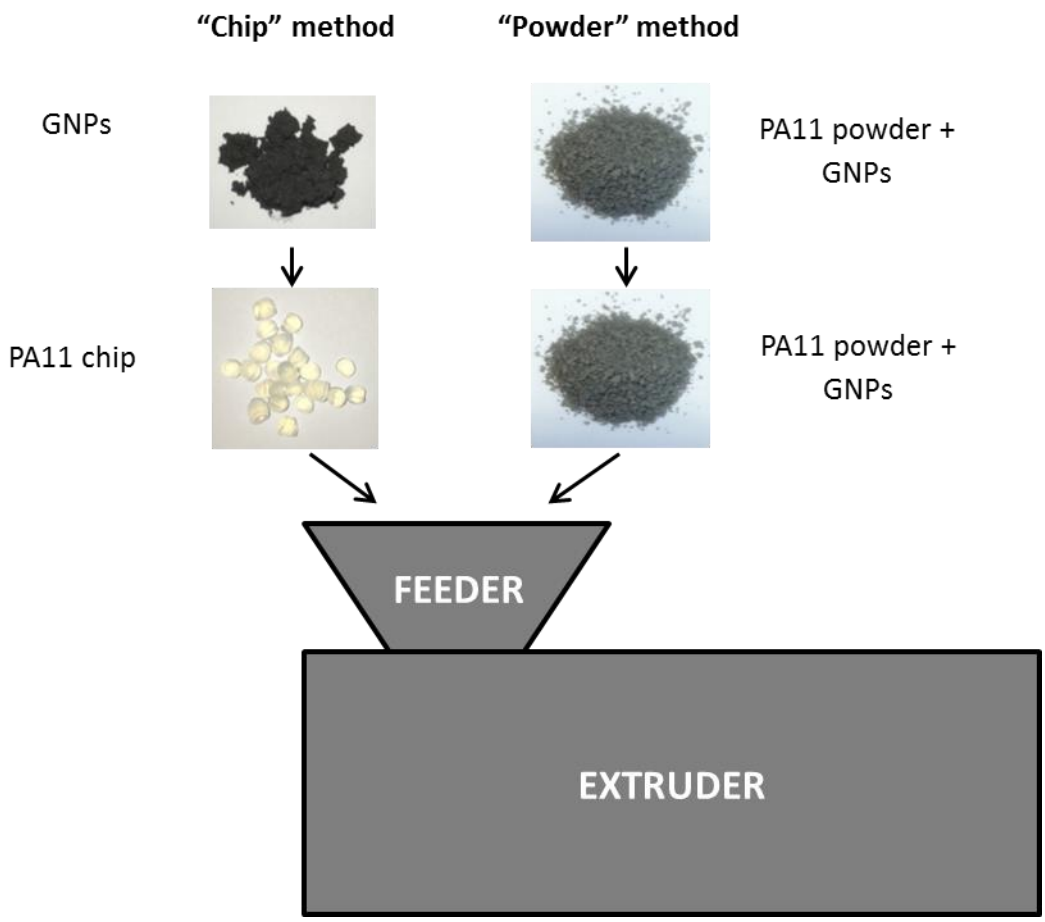

Figure 4.4. Schematic of nanocomposite production by the two different methods employed for GNP incorporation into PA11.

4.4.5 Compression Moulding

Compression moulding was carried out on a LOSCA hot press with a 4 inch (10.16 cm) diameter ram. The samples were prepared as follows (Figure 4.5): a steel plate was covered by DuPont™ Kapton® polyimide film to aid release; the mould was then placed on top and loaded with material (dried at 50 °C under vacuum for at least 16 h); a second DuPont™ Kapton® polyimide film was placed on top before the top steel plate was applied. The two platens of the hot press were each set to 240 °C and allowed to reach temperature before the loaded mould was inserted.

The compression moulding regime employed was as follows: the lower platen was raised until just touching (0 MPa) for 4 min and then raised to a pressure of 1.2 MPa for a further 4 min. Following this, the pressure was increased to 2.5 MPa for 2 min and 8.6 MPa for 30 s. The platens were then cooled to 30 °C at approximately 10 °C min^{-1} while

maintaining the final ram pressure. The samples were obtained by peeling away the DuPont™ Kapton® polyimide film and releasing from the mould with the use of a scalpel. It is worth noting that the total applied pressure would be applied to the metal mould, not to the polymer directly.

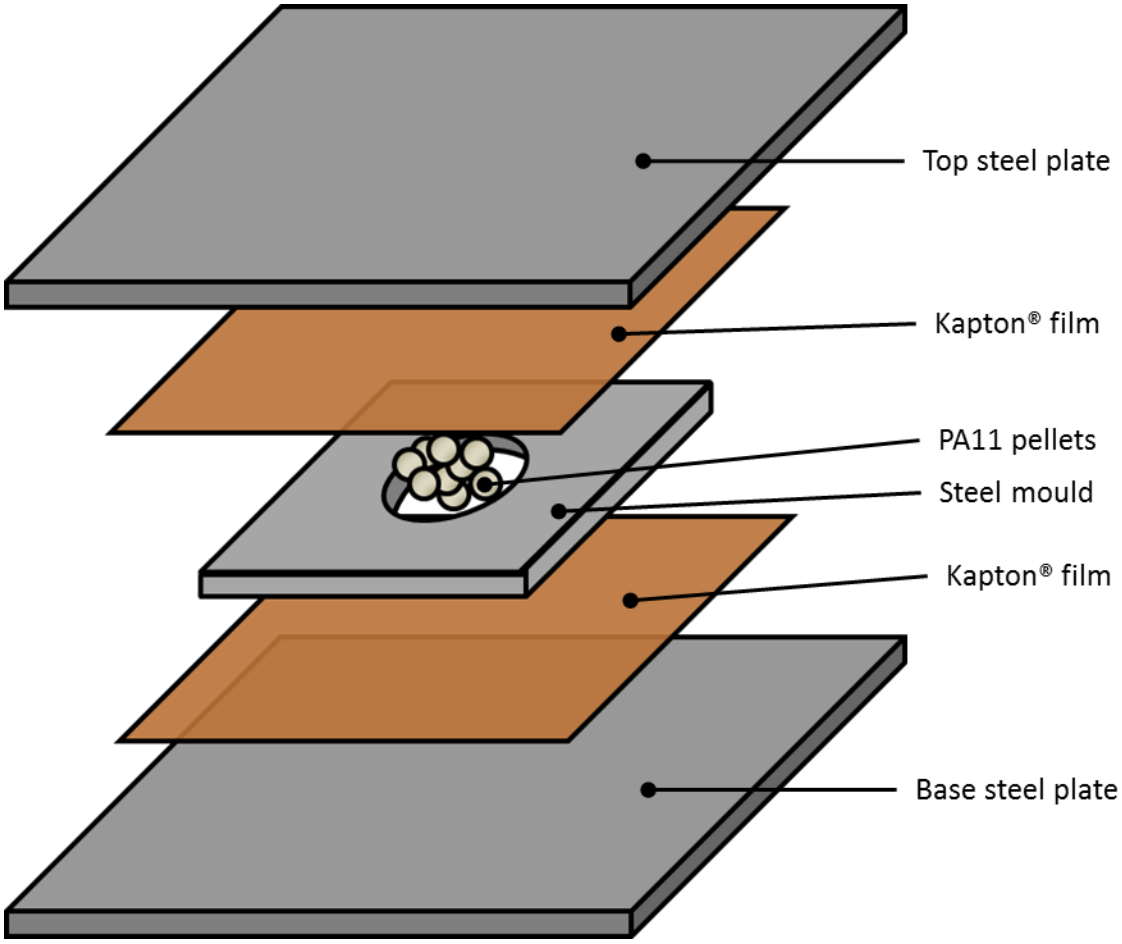

Figure 4.5. Mould arrangement employed for compression moulding, adapted from Raine *et al.* Supporting Information.[164]

4.4.6 Permeation Sample Preparation

Four permeation specimens were prepared, two containing PA0XG25-C and two containing PA1XG25-C nanocomposite. Firstly, the 0 wt% and 1 wt% nanocomposites were dried and pressed as above into 0.5 mm disks. These disks were then compression moulded between 0.5 mm and 1 mm PA11 BESVO disks to create a sandwich structure (Figure 4.6). This was done to ensure that the brittle PA1XG25-C sample did not crack when tested in the permeability rig at high pressure.

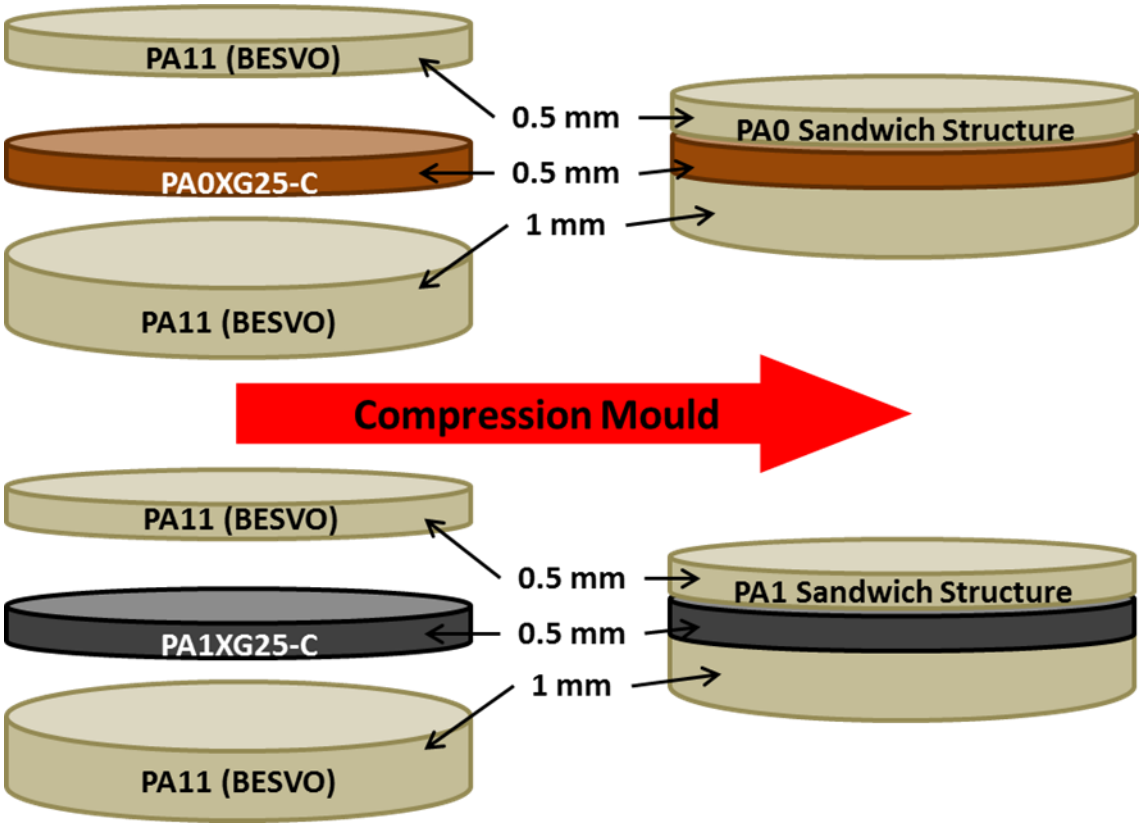

Figure 4.6. Schematic of the make-up of the sandwich structures that were permeability tested.

4.5 Characterisation Methods

4.5.1 Previously Outlined Methods

FT-IR spectroscopy, Raman spectroscopy, TGA, DSC and XRD methods have been outlined previously (section 3.5). All standard deviations were calculated according to Equation 3.7.

4.5.2 Scanning Electron Microscopy

SEM in this chapter was carried out on a Zeiss EVO60 Extended Pressure SEM in high vacuum mode at 10 kV. Samples were cryogenically fractured, mounted onto an aluminium stub with carbon tape and Au/Pd coated.

4.5.3 Rheology

Rheology was performed on an AR-G2 Rheometer with TA Instruments TRIOS v4.1.1.33073 software. The samples were compression moulded into 25 mm diameter, 1 mm thick disks, according to section 4.4.4. The disks were dried for at least 16 h at 50

°C, under vacuum. The samples were then placed onto preheated rheometer EHP 25 mm diameter aluminium parallel plates at 215 °C and the gap closed to 950 µm, trimming the excess from the sides. The gap was closed to 900 µm and an oscillatory frequency sweep from 0.1 to 300 rad s^{-1} at 1% strain was performed. Data was collected at five points per decade after an initial 60 s soak time. Points ran with 3 s conditioning time and 3 s sampling time.

4.5.4 Permeability Testing Method

Permeability testing was carried out at TWI Ltd., Cambridge, on a purpose built permeability rig, capable of testing polymer samples at high temperature and high pressure, under a range of feed gases. Raw permeation data is included in Appendix B. The time-lag method, introduced in section 2.4.3 was used to calculate the permeability, diffusion and solubility coefficients. Examples of a time-lag plot and cell schematic are shown in Figure 4.7.[164]

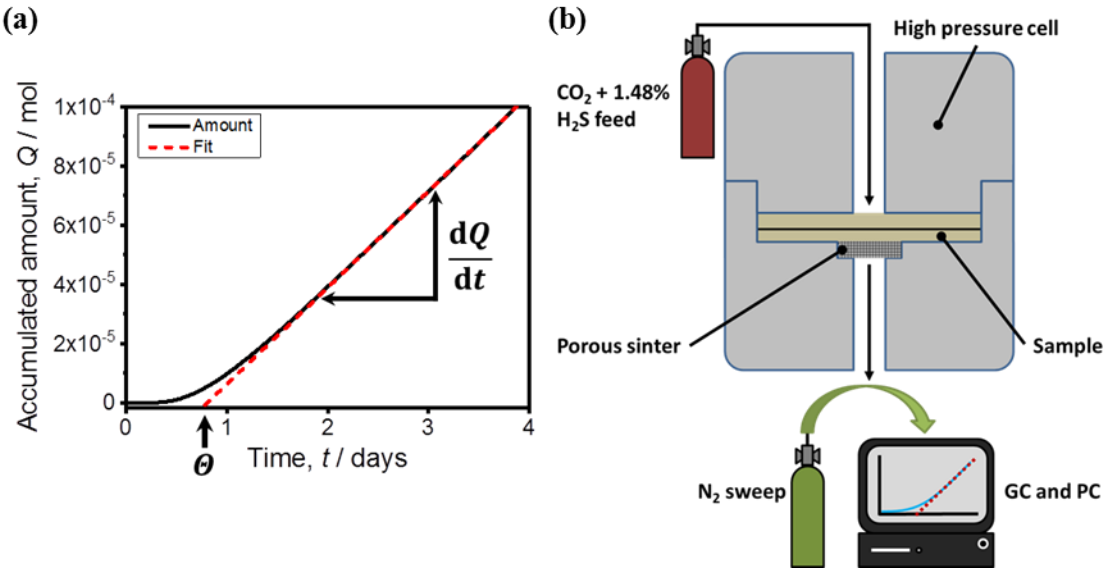

Figure 4.7. (a) An example of a time-lag plot with the time-lag, Θ, and gradient of the steady state, $\frac{dQ}{dt}$, labelled. (b) Continuous flow test cell schematic.[164]

Modification of Equation 2.10 for the gradient of the time-lag plot yields Equation 4.1 which allows calculation of the apparent permeability coefficient, P. The permeability coefficient as a function of fugacity may also be calculated by replacing partial pressure, p_1, with fugacity of the mixture component, f_1.

$$P = \frac{\mathrm{d}Q}{\mathrm{d}t}\frac{l}{A.p_1}$$ Equation 4.1

The apparent diffusion coefficient, *D*, may be calculated by rearrangement of Equation 2.21, repeated below:

$$\Theta = \frac{l^2}{6D}$$ Equation 2.21

With the measured values of *P* and *D*, the value of the apparent solubility coefficient, *S*, may be calculated by the quotient of *P* and *D*, according to Equation 2.9.

The continuous flow method (Figure 4.7b) relies on the diffusion of permeated molecules into an inert sweep gas. The sweep gas-permeate mix then flows to a switchable gas chromatograph (GC) that detects sub ppm levels of permeate. A total of four test cells could be run in parallel. The advantage of using this setup over traditional manometric techniques is that the amount of each gas permeate from a gas mixture can be detected.[165] The effect of sweeping away permeated gas means that the downstream concentration (C_2, and thus p_2) approaches zero.

In most cases, a CO_2 with 1.48% H_2S feed gas mix was used, which allowed the transport properties of both CO_2 and H_2S to be acquired at gauge pressures from 5 to 40 MPa (50 to 400 barg) and at a temperature of 60 °C. The other gas used was 100% H_2S at gauge pressure of 0.2 MPa (2 barg). Transport coefficients for H_2S will be quoted with the test method clearly stated. All CO_2 transport coefficients were calculated from the CO_2 with 1.48% H_2S method. Measurement of the sample thickness, *l*, was performed prior to permeability testing and was an average of three to five measurements using callipers. It is assumed that the thickness is not altered during the experiments, so that calculation of transport coefficients may be carried out. The area used for the calculation of permeability coefficients was that downstream of the membrane, in contact with the supporting sinter (2.259 cm^2).

Testing typically took two weeks for a test at a single pressure but could last up to two months for more complex testing, for example when pressures were incrementally increased, or temperatures altered. Typically samples were allowed to maintain steady state flux for around one week under particular conditions before either the conditions were changed, or the test was terminated. Testing at higher pressure resulted in higher

fluxes, so the steady state was often maintained for less time compared to lower pressure testing.

4.5.5 Chapter Specific Permeability Testing

Two samples containing PA1XG25-C and two samples containing PA0XG25-C (preparation in section 4.4.6) were sealed into the cells with the 0.5 mm PA11 side facing upstream. The cells were then placed into an oven at 60 °C and allowed to equilibrate. The samples were exposed to CO_2 with 1.48% H_2S at 5 MPa at 60 °C (gas) and reached the steady state which was maintained for twelve days. The temperature was then reduced to 35 °C (gas) and the flux was allowed to reach a steady state which was maintained for nine days. One sample each of PA1XG25-C and PA0XG25-C containing nanocomposites were removed. The remaining samples were reheated to 60 °C and exposed to 10 MPa CO_2 with 1.48% H_2S (supercritical), the steady state was reached and maintained for five days. The diffusion coefficients were calculated for each increase in pressure, that is, from t = 0 for 5 MPa. For 10 MPa, the diffusion coefficient was calculated from the time at which the pressure was first increased from 5 MPa. Testing ran for seven weeks in total.

4.5.6 Calculation of Fugacity Values

Fugacity was introduced in section 2.8.3 and describes the nonideality of gas systems. The fugacity values for the CO_2 with 1.48% H_2S mix used in this work were calculated using NIST REFPROP software. For an unknown reason, the NIST REFPROP software did not yield a fugacity coefficient for 10 MPa, so the value was interpolated by using a straight line of best fit for the linear region around 10 MPa, as shown in Figure 4.8.

Figure 4.9a shows the values of the fugacity coefficient, φ, for CO_2 and H_2S against the total feed pressure. Figure 4.9b shows the variation of the fugacity coefficients against the partial pressures of CO_2 and H_2S in the mix. In both cases, the 10 MPa fugacity values interpolated from Figure 4.8 are included. For an ideal gas, φ = 1, by definition, regardless of pressure. This highlights the deviation from ideality observed for CO_2 and H_2S in Figure 4.9.

Values for P and S calculated with fugacity as the driving force are noted in the captions for figures presenting pressure-derived transport coefficients. The values are also tabulated in Appendix C.

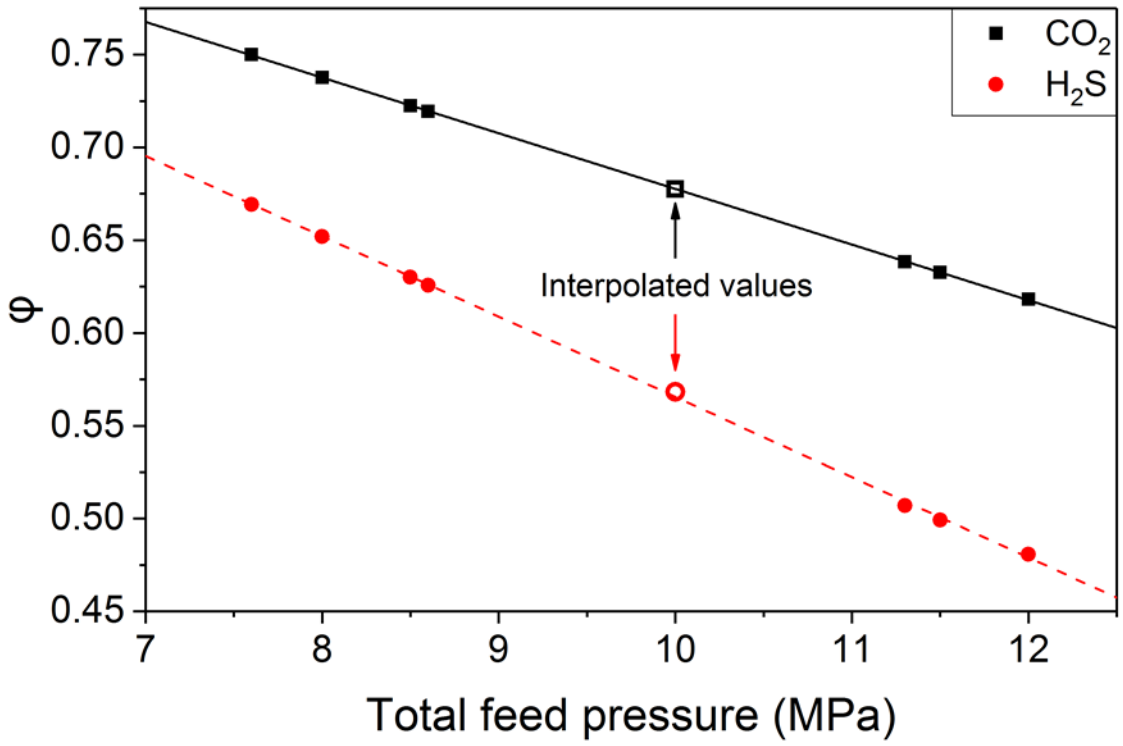

Figure 4.8. Line of best fit for straight line region of fugacity coefficient variation with 10 MPa value marked.

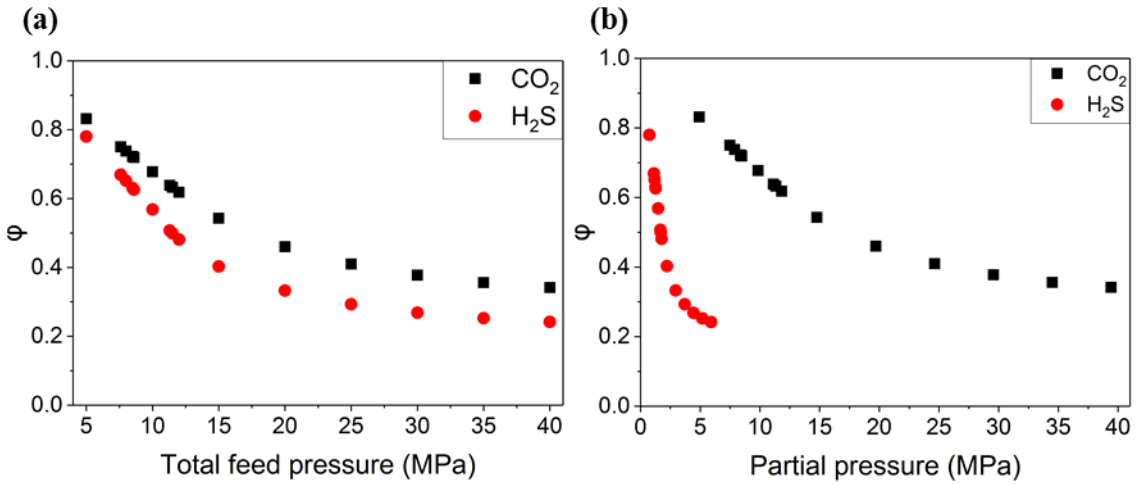

Figure 4.9. Variation of CO_2 and H_2S fugacity coefficients with (a) total feed pressure and (b) partial pressure of CO_2 and 1.48% H_2S in the mix.

4.6 Results and Discussion

4.6.1 Spectroscopic Characterisation

As evidenced in Figure 4.10a and b, the FT-IR spectra of the chip and powder processed nanocomposites are very similar. It can be seen that with increased GNP loading that the PA11 fingerprint region became masked and the baseline decreased in transmission. No obvious GNP signals appeared, unlike for the *in situ* polymerised samples in Figure 3.15. This suggested that polymerisation to the GNP functionality is required to evolve the new peaks observed, whereas melt blending leads only to incorporation of the GNPs into the PA11.

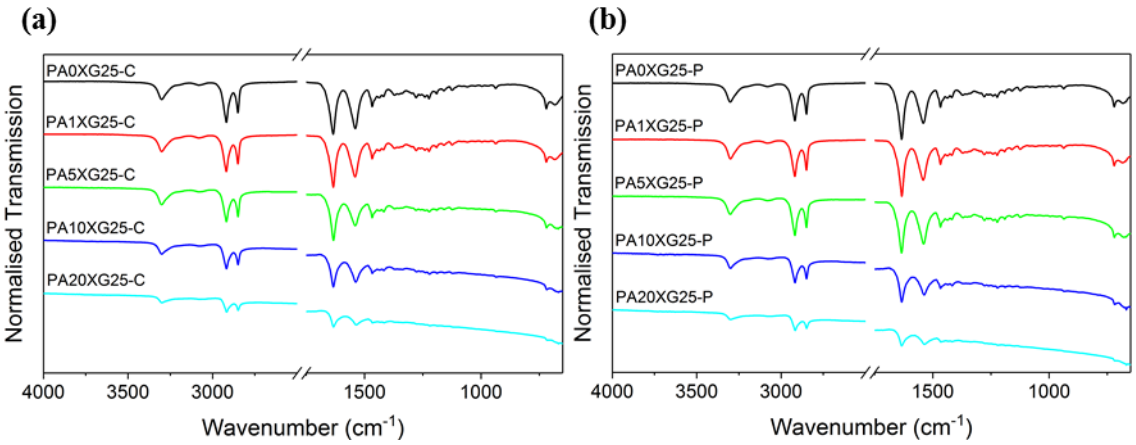

Figure 4.10. FT-IR spectra of (a) PA*n*XG25-C nanocomposites and (b) PA*n*XG25-P nanocomposites.

The Raman spectra in Figure 4.11a and b are for the chip and powder nanocomposites, respectively. Fluorescence was observed for the lowest loadings, and was removed as a background. As the GNP loading increased, the relative size of the PA11 peaks at around 2900 cm^{-1} and around the D peak of the GNPs reduced. At loadings of 5 wt% and above, the GNP spectra dominated over the PA11 spectra. There was very little difference in the Raman responses for chip processed samples compared to powder processed samples. The Raman spectra for the melt blended samples are very similar to those for the *in situ* polymerised GNP samples, displayed in Figure 3.17a, and to unprocessed GNPs in Figure 3.7. This suggests that the GNPs were not substantially altered during the melt blending technique.

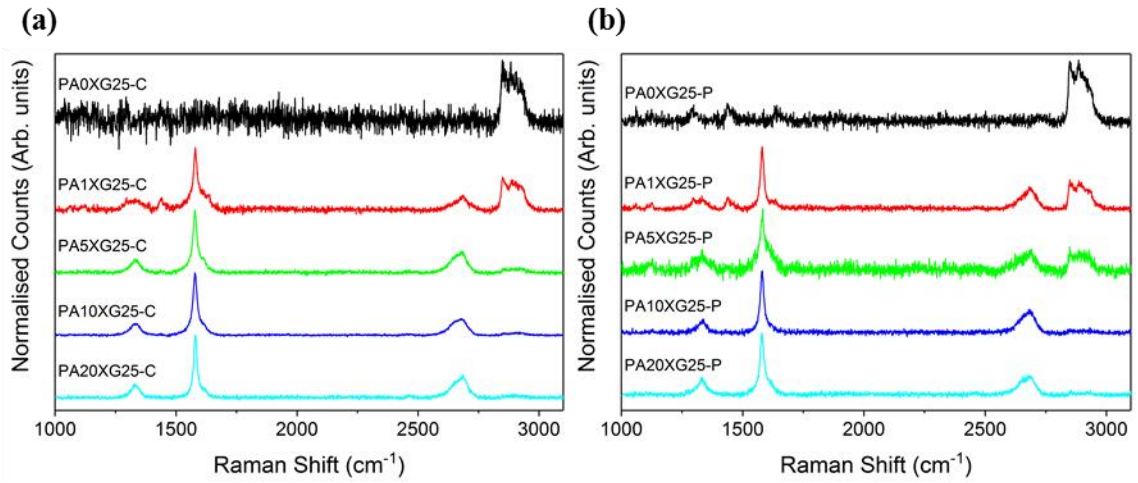

Figure 4.11. Raman spectra of (a) PA*n*XG25-C nanocomposites and (b) PA*n*XG25-P nanocomposites.

4.6.2 THERMAL STABILITY

Figure 4.12a and b show typical nitrogen atmosphere TGA degradation profiles for the PA*n*XG25-C and PA*n*XG25-P nanocomposites, respectively. It can be seen that both PA*n*XG25-C and PA*n*XG25-P displayed single step degradation with apparently similar onset temperatures. The general trend in both data sets was for the degradation step to shift to higher temperatures with increasing GNP loading, as expected.[142,144,166–169] This is probably due to the mass barrier effect of the GNPs blocking the diffusion of degradation species from the polymer matrix.[142,144]

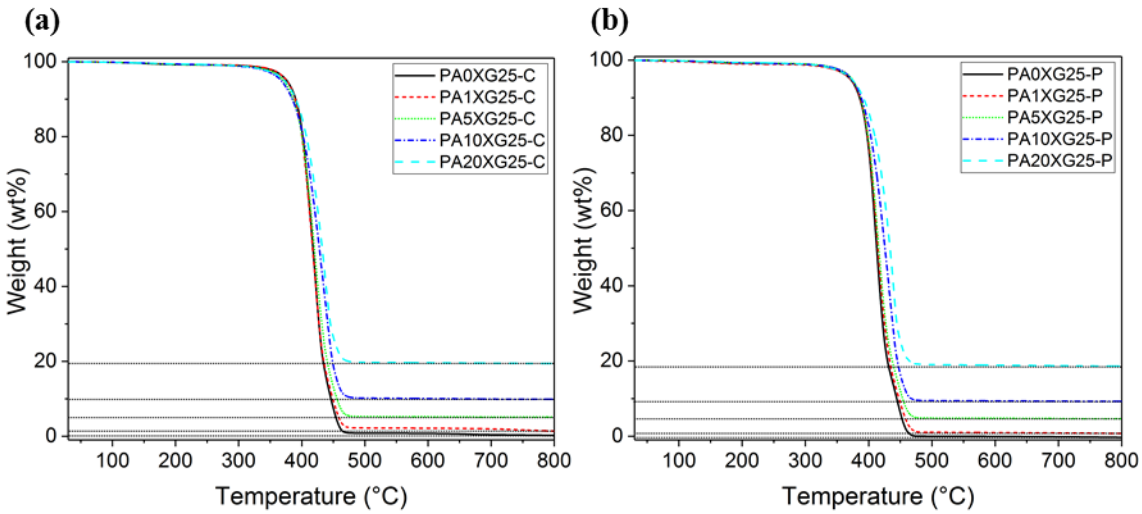

Figure 4.12. TGA decomposition profiles for nanocomposites under a dry nitrogen atmosphere, the horizontal dotted lines signify residue values. (a) PA*n*XG25-C and (b) PA*n*XG25-P.

Residues are indicated by the dotted lines which were used to calculate the actual loadings in the nanocomposite, as displayed in Table 4.3. The actual loadings were close to the intended loadings, suggesting that GNP losses were low for both experimental methods.

Table 4.3. Intended loadings displayed with TGA residue at 500 °C and the actual loading calculated by subtracting the residue for 0 wt% loaded nanocomposite.

Composite	Intended loading (wt%)	Residue remaining at 500 °C (wt%)	Actual loading (wt%)
PA0XG25-C	0	1.1	0
PA1XG25-C	1	1.8	0.70
PA5XG25-C	5	5.1	4.0
PA10XG25-C	10	10.4	9.3
PA20XG25-C	20	21.2	20.1
PA0XG25-P	0	0.0	0
PA1XG25-P	1	1.1	1.1
PA5XG25-P	5	4.9	4.9
PA10XG25-P	10	9.5	9.5
PA20XG25-P	20	19.0	19.0

Figure 4.13, Figure 4.14 and Figure 4.15 show the $T_{5wt\%}$, T_{max} and $T_{50wt\%}$, respectively, calculated as outlined previously (section 3.6.2.3).

The values of $T_{5wt\%}$, in Figure 4.13, show a large standard deviation and large scatter. Since $T_{5wt\%}$ is calculated so early on in the degradation, it may be that small changes between samples are exaggerated. As can be seen, there was no variation of $T_{5wt\%}$ with GNP loading, to within experimental error. The degradation behaviour at higher temperatures appears to be more consistent, as shown in Figure 4.14 and Figure 4.15. It is interesting, however, that the thermal stability of the chip processed control sample displays a much higher $T_{5wt\%}$ than the powder processed sample.

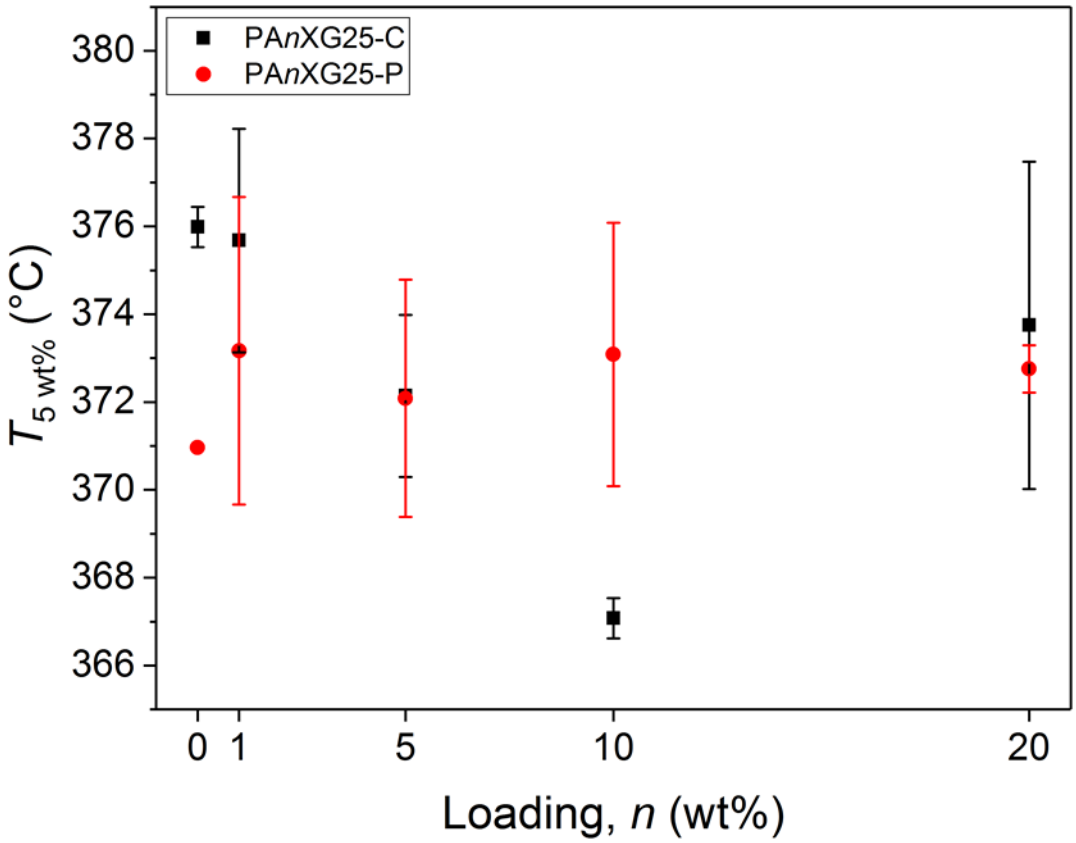

Figure 4.13. $T_{5wt\%}$ against GNP loading for PA*n*XG25-C and PA*n*XG25-P nanocomposites.

Figure 4.14 shows the variation of T_{max} with sample loading and sample preparation method. The general trend was for an increase in thermal stability with GNP loading, similar to the trend for the *in situ* polymerised GNP nanocomposites. This effect was probably due to the mass barrier afforded by the GNPs, retarding the diffusion of degradation products from the PA11 matrix.[142,144]

There did appear to be a variation in the thermal stability with processing method. As can be seen, particularly at the lower loadings, n < 10 wt%, the chip processed samples displayed better thermal stability than the powder processed samples. This pattern of superior thermal stability is repeated for values of $T_{50wt\%}$, as shown in Figure 4.15. The 0 wt% nanocomposites also show a difference in thermal stability depending upon processing method. The reason for this is unknown; however, it could be due to faster melting of the powdered samples, leading to more thermal degradation because of the longer lifetime in the extruder.

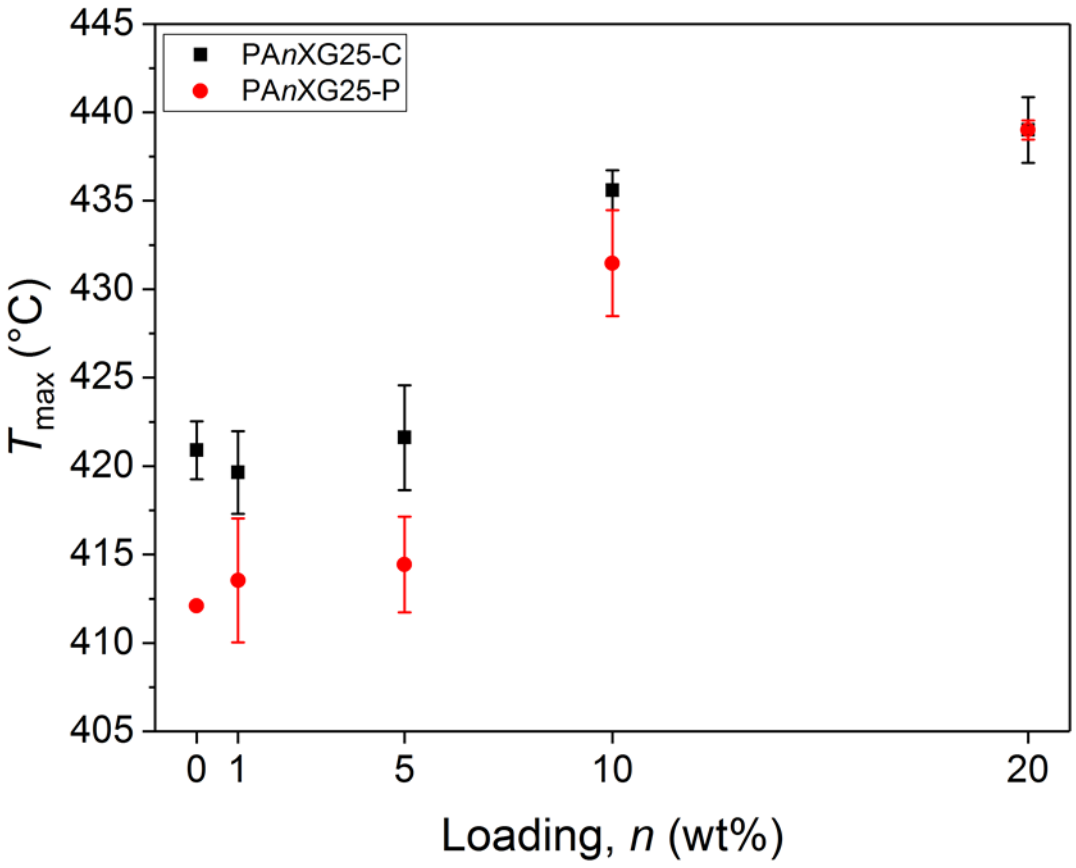

Figure 4.14. T_{max} against GNP loading for PA*n*XG25-C and PA*n*XG25-P nanocomposites.

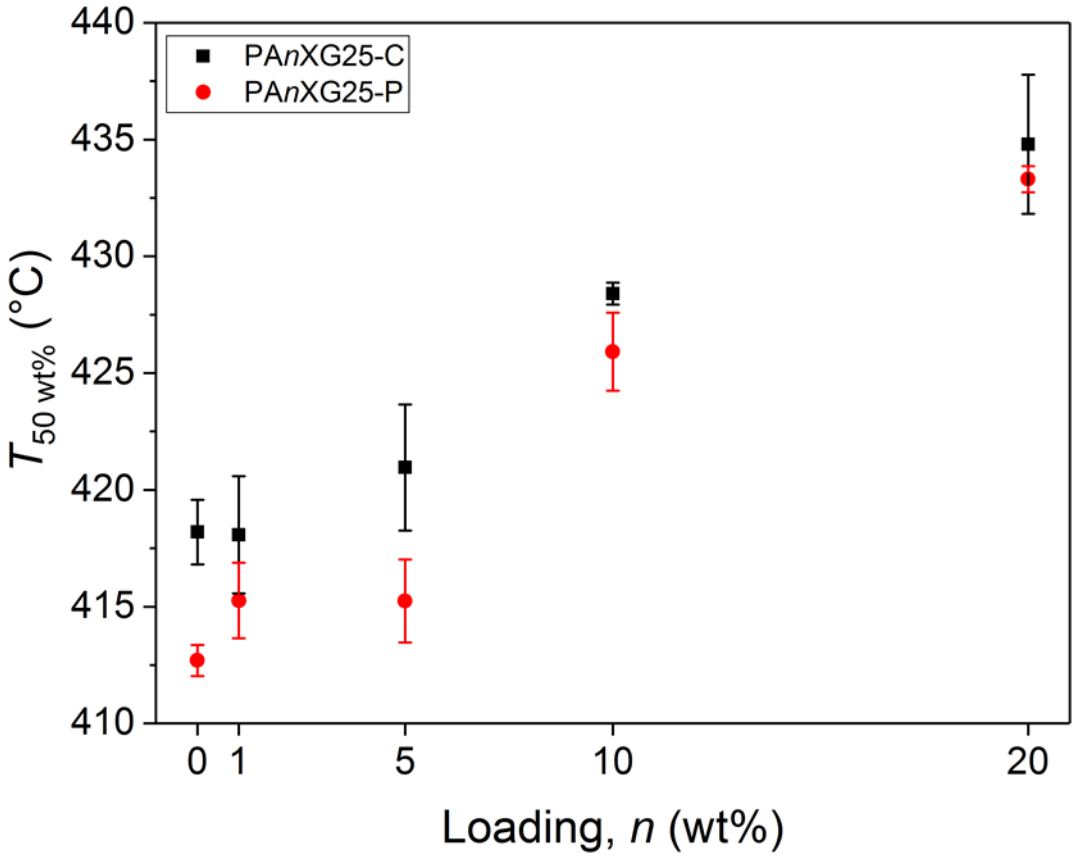

Figure 4.15. $T_{50wt\%}$ against GNP loading for PA*n*XG25-C and PA*n*XG25-P nanocomposites.

Comparing the degradation behaviour of the *in situ* polymerised samples (Figure 3.19 – Figure 3.21) to the melt blended samples (Figure 4.13 – Figure 4.15), it can be seen that the $T_{5wt\%}$, T_{max} and $T_{50wt\%}$, are approximately 20 °C higher for the *in situ* samples. This suggests that *in situ* polymerisation improves the interactions between filler and polymer. Even 0 wt% loaded IS0 had an improved thermal stability compared to PA0XG25-C and PA0XG25-P. This suggests that degradation during melt mixing plays a role in the relatively poor thermal stability of the melt blended samples.

4.6.3 Crystallisation

DSC results for the chip and powder processed nanocomposites are displayed in Table 4.4. There appears to be no change in T_g, T_{m1}, T_{m2}, and χ_c with GNP loading, that is, changes in the values are within a single standard deviation of the samples. The decrease in ΔH_m with GNP loading can be explained by the decrease in the weight fraction of PA11 for each sample as the GNP loading increases. ΔH_m is therefore measured to be lower than expected, as the mass of polymer is actually lower than the

mass of composite investigated. χ_c takes the decreasing PA11 weight fraction into account as shown in Equation 3.6.

T_{m1} and T_{m2} have often been found to remain constant with carbon filler loading,[97,98,148,149,162] although some small changes have been observed for PA11/CNT composites.[150] χ_c did not increase with GNP loading which is in agreement with some papers,[96,148,150] but also contrasts with the findings of others.[98,149,162] In addition, the T_g did not alter, which is different to the results of a couple of publications.[97,162] There did seem to be a large change in T_c with increasing GNP loading for both PA*n*XG25-C and PA*n*XG25-P. An increase in T_c with increased filler loading has been observed previously in this work (section 3.6.2.4) and for other PA11/GNP nanocomposites,[97,162] PA11/GO composites,[98] PA11/CNT nanocomposites,[148–151] and PA11/WS_2 inorganic nanotube nanocomposites.[152] The reason for the increase in T_c with increasing GNP loading can be explained by the GNPs acting as heterogeneous nucleating agents, meaning that crystallisation can occur at a higher temperature.[148–152] A couple of papers attribute an increase in T_c with increased filler loading to a rise in activation energy for crystallisation.[98,162]

Table 4.4. DSC results for nanocomposites produced through the chip and powder methods. The standard deviation from five measurements is given.

Composite	T_g (°C)	T_{m1} (°C)	T_c (°C)	T_{m2} (°C)	ΔH_m (J g^{-1})	χ_c (%)
PA0XG25-C	39 ± 4	190.3 ± 0.6	164 ± 1	188 ± 1	64 ± 3	34 ± 2
PA1XG25-C	40 ± 1	191 ± 1	167 ± 1	188 ± 1	63 ± 1	34 ± 1
PA5XG25-C	40 ± 1	189.8 ± 0.5	172.8 ± 0.2	188.5 ± 0.1	62 ± 1	34 ± 1
PA10XG25-C	42 ± 2	189 ± 1	173 ± 1	188.4 ± 0.2	60 ± 3	35 ± 1
PA20XG25-C	42 ± 1	189 ± 1	174.7 ± 0.5	189.4 ± 0.3	50 ± 4	33 ± 2
PA0XG25-P	39 ± 1	191 ± 1	165 ± 1	188.9 ± 0.4	62 ± 2	33 ± 1
PA1XG25-P	40 ± 1	190 ± 1	167 ± 1	188.8 ± 0.2	62 ± 1	33 ± 1
PA5XG25-P	40 ± 1	191 ± 1	170 ± 1	188.7 ± 0.4	61 ± 3	33 ± 1
PA10XG25-P	40 ± 1	189.6 ± 0.5	173.3 ± 0.4	189.0 ± 0.2	61 ± 1	35 ± 1
PA20XG25-P	42 ± 2	189 ± 1	174.7 ± 0.4	189.7 ± 0.3	61 ± 2	35 ± 1

Figure 4.16, Figure 4.17, and Figure 4.18 show representative thermograms of the first-heating T_{m1}, second-heat T_{m2}, and cooling T_c peaks. As can be seen in Figure 4.16a and b, the T_{m1} peak shape changes from a bimodal peak, or shouldered peak, to a single peak with increasing GNP loading. This may be due to polymorphism,[150] that is, there being two different crystalline regions present in the 0 and 1 wt% loaded samples – in a

similar fashion to the IS*n*XG25 and IS*n*GO25 samples discussed in section 3.6.2.4. At loadings of 5, 10 and 20 wt%, it would appear that only one crystal type is present. A similar effect can be seen in the second-heat T_{m2} peaks in Figure 4.17a and b. Such an effect was observed for PA11/GNP nanocomposites by Rashmi *et al.*[162], however, the authors didn't comment on the disappearance of the second peak (or shoulder) with increased GNP loading. Yuan *et al.*[96] observed double melting peaks for all of their *in situ* polymerised PA11/GO composites, which they attributed to two different crystalline regions being present, however their loadings stopped at 0.5 wt%. As the melting peak consistently appears as a single melt peak for 5, 10 and 20 wt% loading, regardless of the processing method, it would suggest that the GNPs limit the crystallisation to a single crystal form. Stoclet *et al.*[70] suggested that the double melting peak is simply due to melt recrystallising imperfect crystallites, rather than the presence of two different crystal types. Pepin *et al.*[77] argued that α' crystals that did not have time to rearrange into the more stable high temperature δ phase, melted first, and then the highly stable δ crystals melted at higher temperature. The lack of a double melting peak at higher GNP loadings therefore suggests that the GNPs favour single crystal formation of either unstable α' or stable δ phases. High temperature XRD would be required to confirm such behaviour.[77]

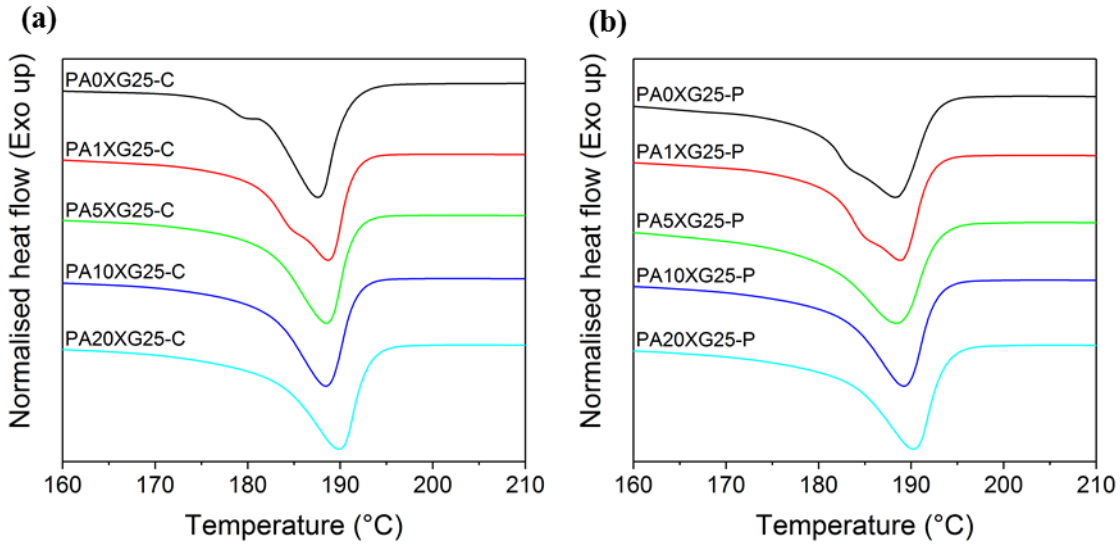

Figure 4.16. T_{m1} endotherms for: (a) PAnXG25-C; and (b) PAnXG25-P.

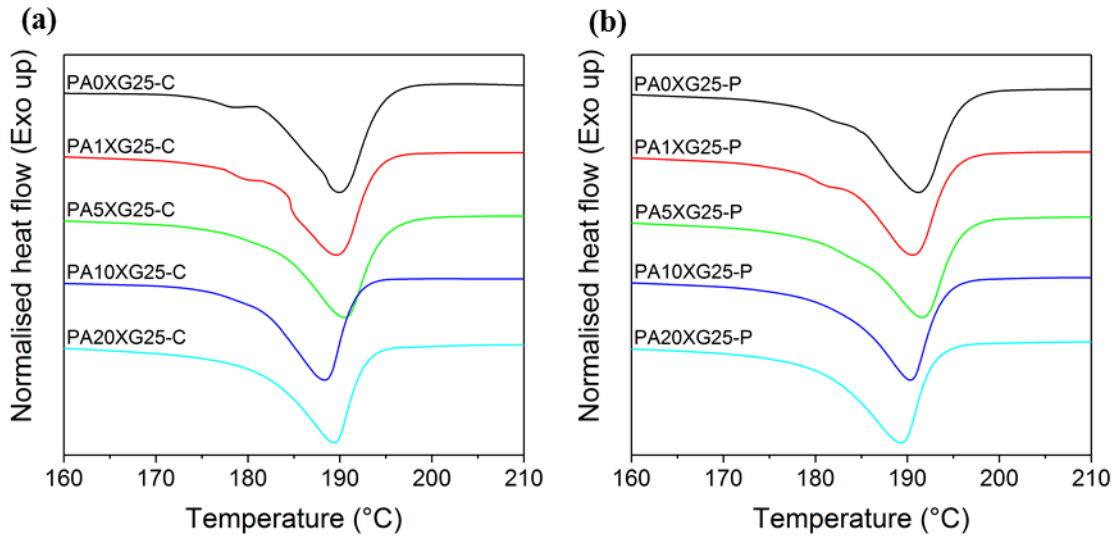

Figure 4.17. T_{m2} endotherms for: (a) PAnXG25-C; and (b) PAnXG25-P.

The T_c exotherms displayed in Figure 4.18 show the general increase in peak value of T_c with GNP loading, as described earlier. The slopes at the onset (high temperature side) appear to get less steep, qualitatively, which is contrary to the effect observed by Jacobs *et al.*[97], as they observed an increase in the slope to the T_c, with GNP loading in PA11. They suggested that the increasing slope observed could mean that the crystallisation rate was faster for GNP containing nanocomposites; by reversal of this argument, it could be suggested that the crystallisation observed in this work occurs more slowly with increasing GNP loading.

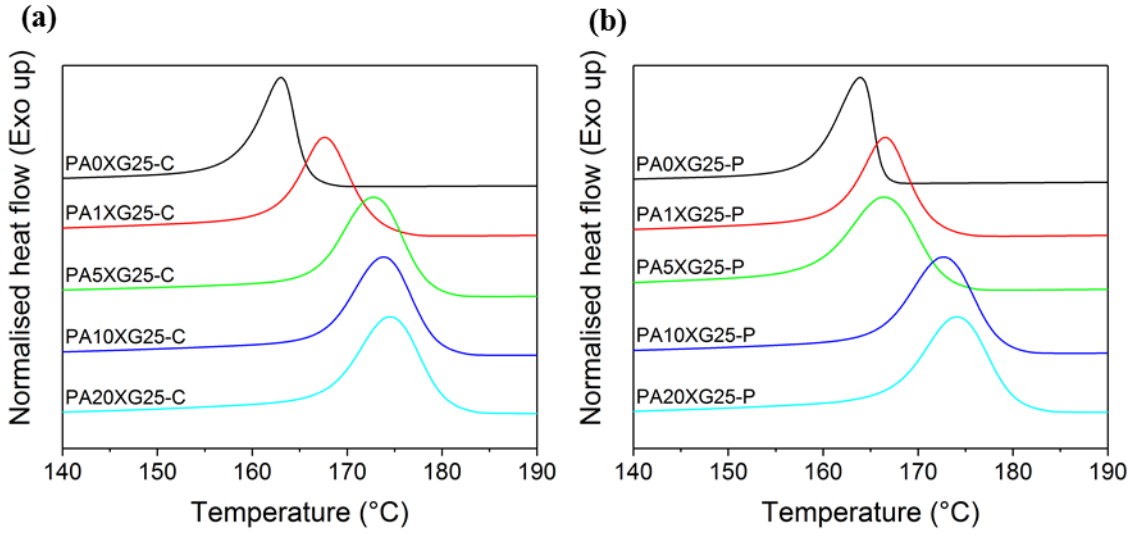

Figure 4.18. T_c exotherms for: (a) PAnXG25-C; and (b) PAnXG25-P.

In order to probe the crystallisation of the PAnXG25-C and PAnXG25-P nanocomposites further, XRD was performed on compression moulded disks, slow cooled in order to allow full crystallisation to occur. As shown in Figure 4.19, regardless of processing method and GNP loading, all PA11 nanocomposites display α' crystallinity due to the (100) and (110)/(010) reflections at 20 and 23 °, respectively.[67,78,79,156] Table 4.5 shows the 2Θ values as fitted by Lorentzian peaks and shows the consistency between the different samples.

The presence of only α' crystallinity at room temperature suggested that the bimodal melting peak in the DSC data was due to the melting of imperfect δ crystals, that is unrearranged α' crystals at low temperature, followed by stable δ crystals at high temperaure.[70,77] This was also observed earlier in the *in situ* polymerised nanocomposites (section 3.6.2.4). The bimodal melting peak reduced to a single melting peak with increasing GNP loading, implying that the GNPs encourage the formation of stable δ crystals, at high temperature.

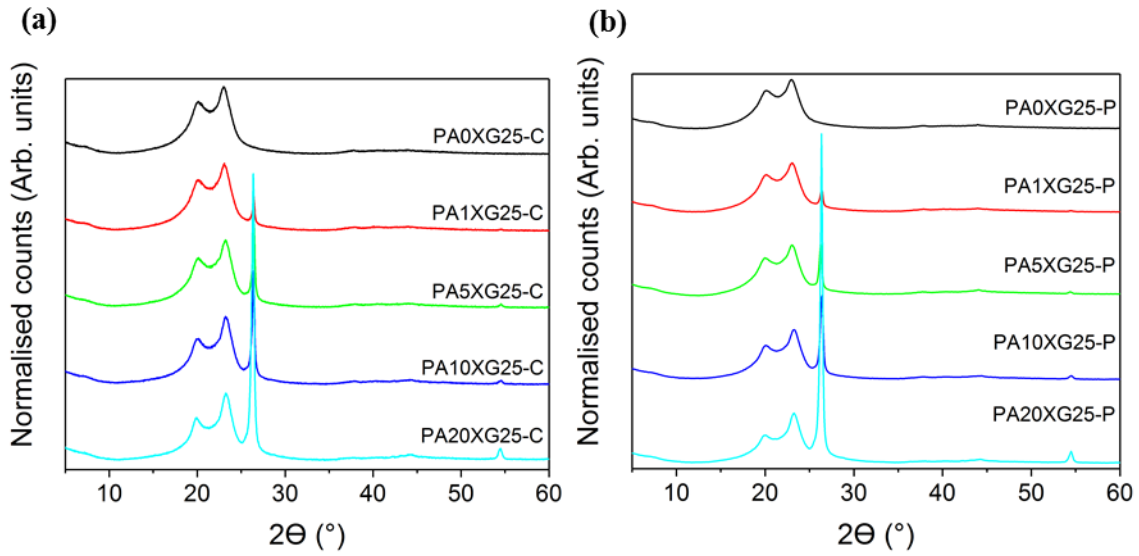

Figure 4.19. XRD diffractograms for (a) PA*n*XG25-C and (b) PA*n*XG25-P samples, loadings increasing from top to bottom.

Table 4.5. Table of 2Θ values for the centre of Lorentzian curves fitted to the PA11 and GNP peaks in Figure 4.19.

Composite	2Θ α'_{100} (°)	2Θ $\alpha'_{110/010}$ (°)	2Θ GNP (°)
PA0XG25-C	20.2	23.1	N/A
PA1XG25-C	20.2	23.1	26.4
PA5XG25-C	20.3	23.2	26.4
PA10XG25-C	20.2	23.3	26.4
PA20XG25-C	20.2	23.3	26.3
PA0XG25-P	20.2	23.0	N/A
PA1XG25-P	20.2	23.1	26.4
PA5XG25-P	20.1	23.0	26.3
PA10XG25-P	20.3	23.3	26.4
PA20XG25-P	20.2	23.3	26.4

4.6.4 MORPHOLOGY

SEM was performed in order to investigate the morphology of the PA11/GNP nanocomposites. Two images of each PA*n*XG25-C and PA*n*XG25-P composites are shown in Figure 4.20 – Figure 4.29 where the scale bar is 10 µm and 100 µm in a and b, respectively.

Comparing PA0XG25-C to PA0XG25-P fracture surfaces in Figure 4.20 and Figure 4.21, respectively; it can be seen that the morphology is not altered greatly with processing method.

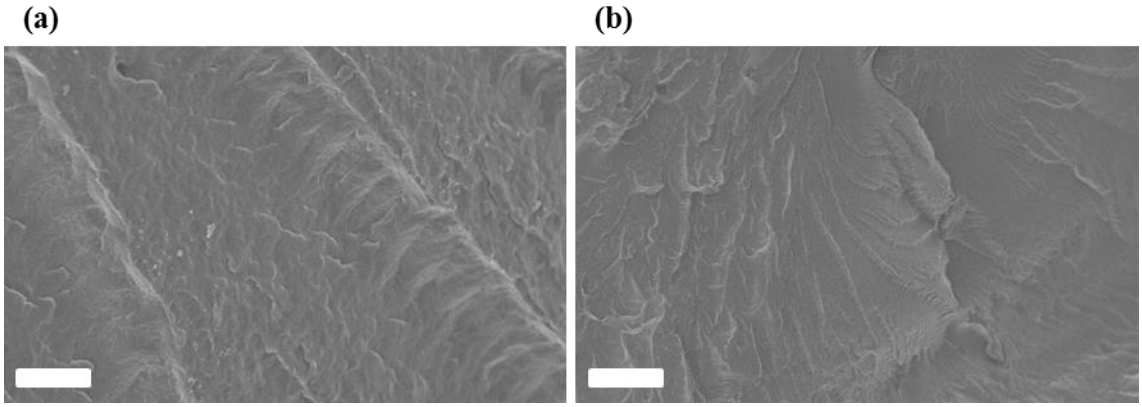

Figure 4.20. SEM images of PA0XG25-C nanocomposites: (a) 10 µm scalebar; (b) 100 µm scalebar.

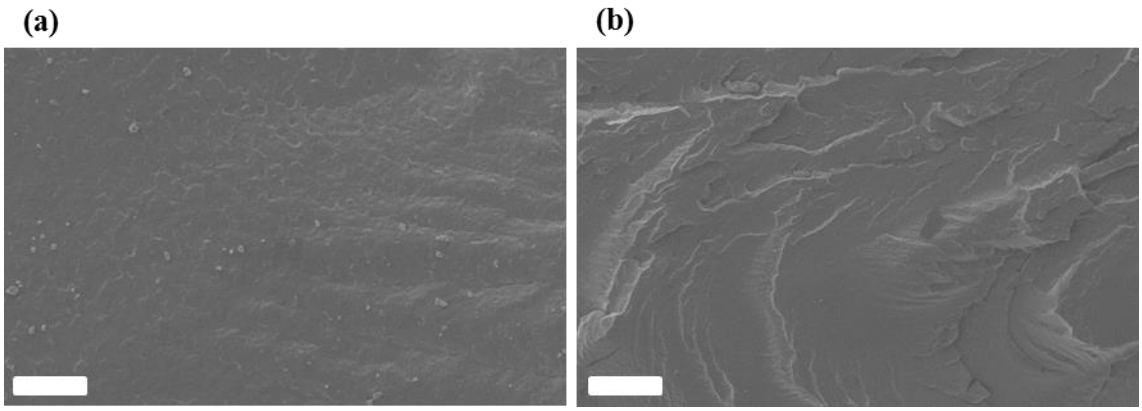

Figure 4.21. SEM images of PA0XG25-P nanocomposites: (a) 10 µm scalebar; (b) 100 µm scalebar.

PA1XG25-C and PA1XG25-P are shown in Figure 4.22 and Figure 4.23, respectively. As can be seen, through comparison of Figure 4.22a and Figure 4.23a with Figure 4.20a and Figure 4.21a, the addition of 1 wt% GNP has changed the microstructure slightly. Some flakes are visible, in Figure 4.22a and Figure 4.23a, which are highlighted by yellow arrows, however, they appear to be well dispersed, with minimal aggregation. At 1 wt% loading, there appears to be little difference between the chip and powder methods, as the morphology appears to be very similar.

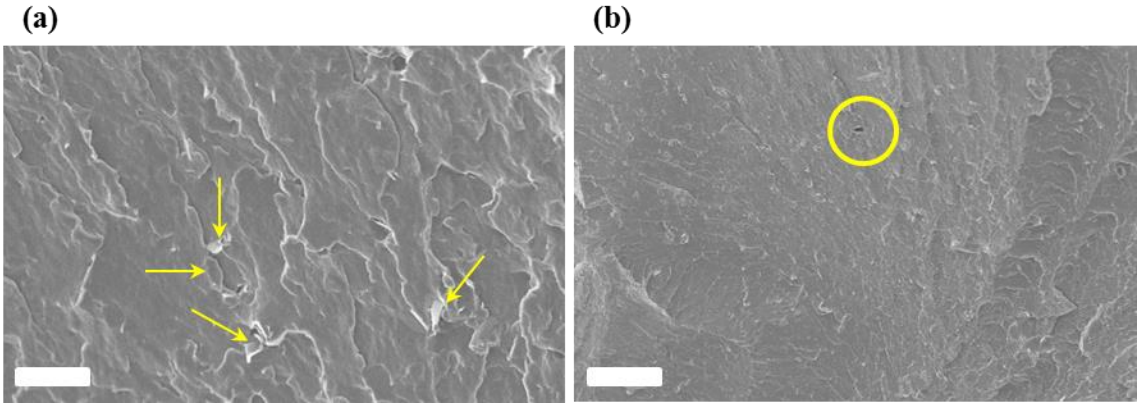

Figure 4.22. SEM images of PA1XG25-C nanocomposites: (a) 10 µm scalebar; (b) 100 µm scalebar. Yellow arrows highlight visible flakes and yellow circle highlights a void.

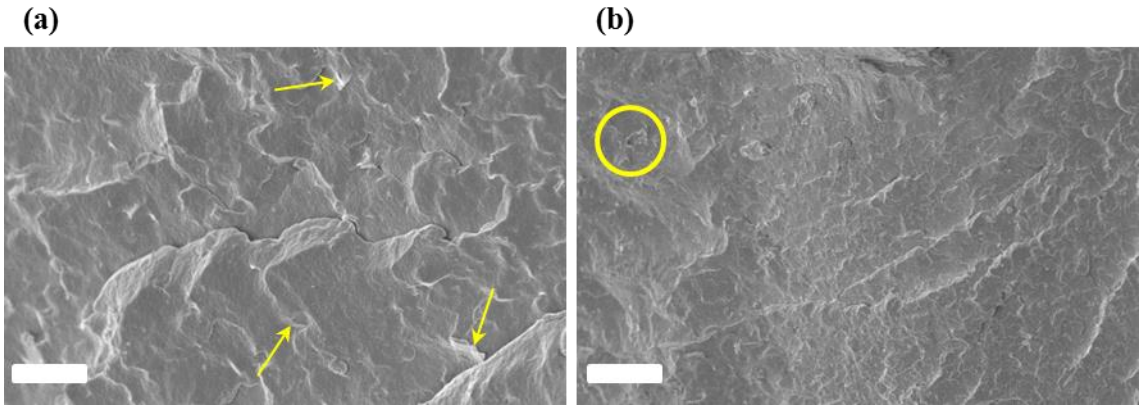

Figure 4.23. SEM images of PA1XG25-P nanocomposites: (a) 10 µm scalebar; (b) 100 µm scalebar. Yellow arrows highlight visible flakes and yellow circle highlights a void.

PA5XG25-C and PA5XG25-P SEM images are shown in Figure 4.24 and Figure 4.25, respectively. The morphologies shown in Figure 4.24 and Figure 4.25 are markedly different. PA5XG25-C, in Figure 4.24a has far more GNP-like character compared to the homogeneous polymer-like PA5XG25-P in Figure 4.25a, interspersed with well distributed GNP flakes (highlighted by yellow arrows). This suggests that the PA5XG25-C sample was taken from a GNP rich region of the lace, which shows that GNP distribution through the polymer is poor. The morphology in Figure 4.24a also shows plastic deformation,[162] which shows that the sample may not have been cooled in liquid nitrogen sufficiently before fracturing. In addition, there appear to be a number of large (approximately 30 µm diameter) voids, highlighted by circles in Figure 4.24b, whereas Figure 4.25b shows less voiding. These observations suggest that incorporating GNPs with powdered PA11 instead of sequentially with pellet PA11 leads to better mixing and incorporation of less air. The incorporation of air may be due to the open nature of the extruder, so allowing air ingress during cycling of the melt. Upon extrusion and cooling, the voids became frozen in the polymer matrix.

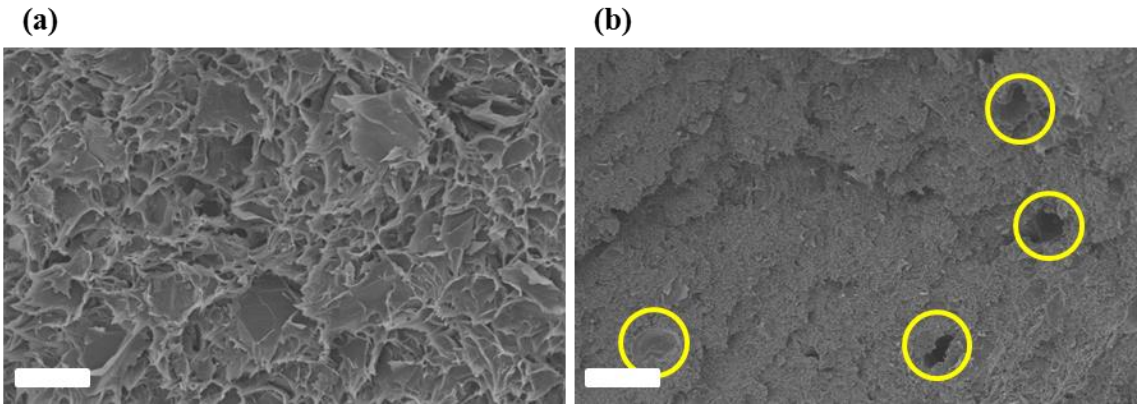

Figure 4.24. SEM images of PA5XG25-C nanocomposites: (a) 10 µm scalebar; (b) 100 µm scalebar. Yellow circles highlight voids.

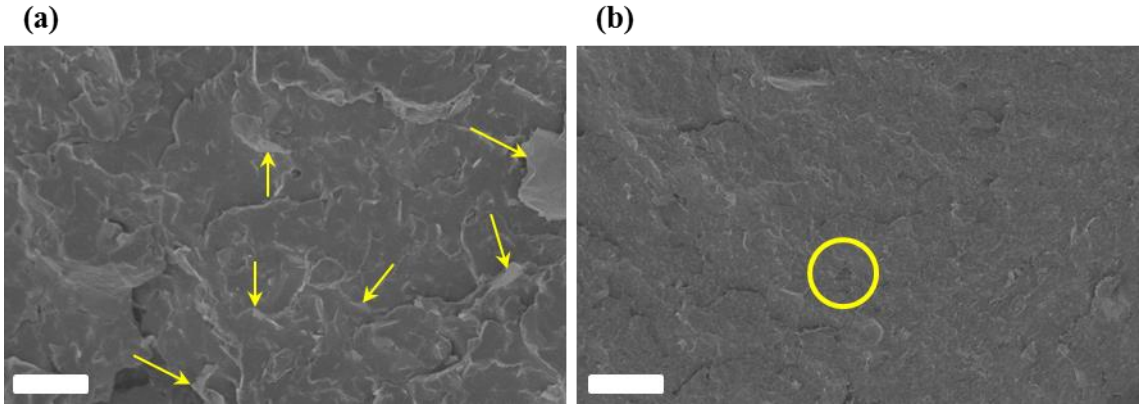

Figure 4.25. SEM images of PA5XG25-P nanocomposites: (a) 10 µm scalebar; (b) 100 µm scalebar. Yellow arrows highlight visible flakes and yellow circle highlights a void.

The voiding behaviour of the PA*n*XG25-C composites continues as the loading increases to 10 and 20 wt%; the PA*n*XG25-P samples also begin to show greater voiding behaviour as the loadings increase. PA10XG25-C and PA10XG25-P are shown in Figure 4.26 and Figure 4.27, respectively. Agglomerated GNP stacks are observable in the PA10XG25-C sample, highlighted by yellow arrows in Figure 4.26a. A number of voids are highlighted in Figure 4.26b. Agglomeration may also be inferred in the PA10XG25-P (Figure 4.27a) from regions where delamination between graphene flakes during fracturing is visible, again highlighted by yellow arrows. Figure 4.27b shows the first evidence of excessive voiding for powder processed nanocomposites, at 10 wt%; however, extensive voiding for chip processed nanocomposites began at 5 wt% loading. Therefore, by utilising the pre-mixing powder-powder method, the loading of GNPs may be doubled before voiding becomes extensive.

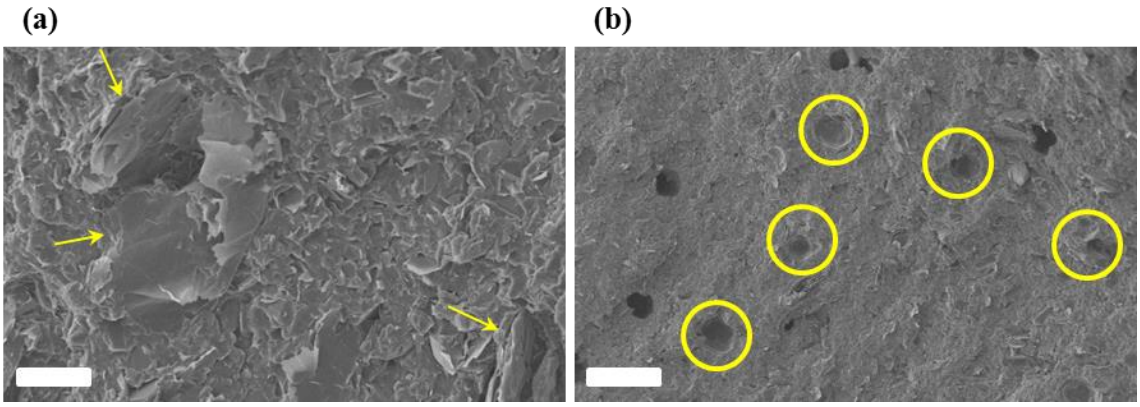

Figure 4.26. SEM images of PA10XG25-C nanocomposites: (a) 10 µm scalebar; (b) 100 µm scalebar. Yellow arrows highlight visible flakes and yellow circles highlight voids.

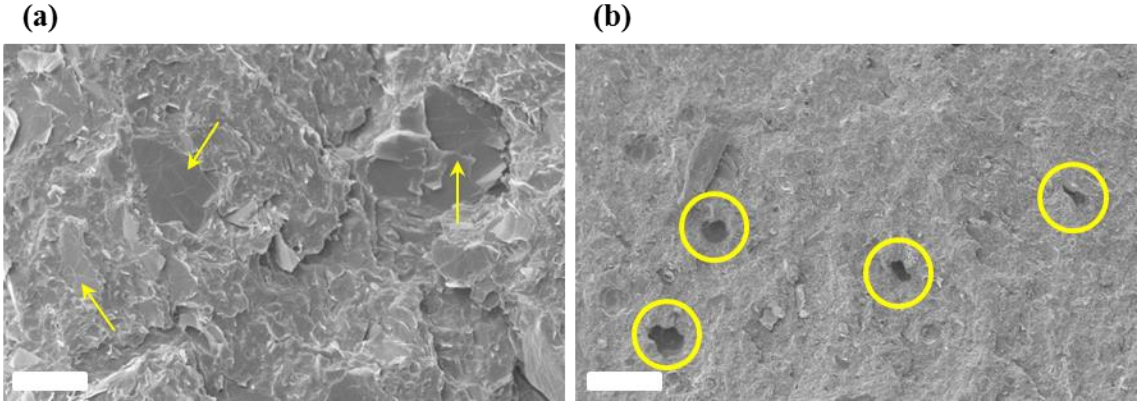

Figure 4.27. SEM images of PA10XG25-P nanocomposites: (a) 10 µm scalebar; (b) 100 µm scalebar. Yellow arrows highlight visible flakes and yellow circles highlight voids.

Figure 4.28 and Figure 4.29 show SEM images for PA20XG25-C and PA20XG25-P, respectively. Agglomeration (yellow arrows) can be seen in Figure 4.28a and Figure 4.29a, as well as single layer graphene flakes (circled in red). As can be seen in Figure 4.28b, the PA20XG25-C appears to have a semi-porous morphology, with a number of voids (circled) linking together. PA20XG25-P (Figure 4.29) also has voids (circled); however, the voids are not linked to the same extent and have a more similar appearance to PA10XG25-C (Figure 4.26b). Table 4.6 shows number of voids measured per mm^2 of cross sectional surface area. The values were calculated by counting the number of voids in SEM images similar to those in Figure 4.20b – Figure 4.29b with an area of approximately 0.4 mm^2 and scaling the values accordingly. Table 4.6 summarises how voiding markedly increases with GNP loading and is especially evident in the chip

processed samples. The semi-quantification of the voids displayed in Table 4.6 was carried out for a single sample of each nanocomposite in an area representative of the particular sample. A more rigorous approach would have been to investigate a number of different samples for each nanocomposite; however, as a tool to indicate the broad differences between the two melt blending techniques, the estimates in Table 4.6 are appropriate.

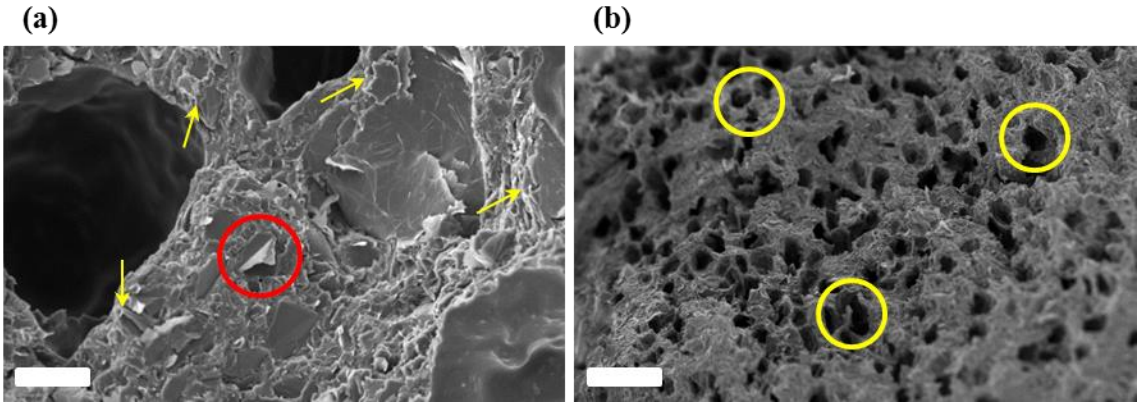

Figure 4.28. SEM images of PA20XG25-C nanocomposites: (a) 10 µm scalebar; (b) 100 µm scalebar. Yellow arrows highlight visible flakes, yellow circles highlight voids. The red circle highlights a folded monolayer graphene flake.

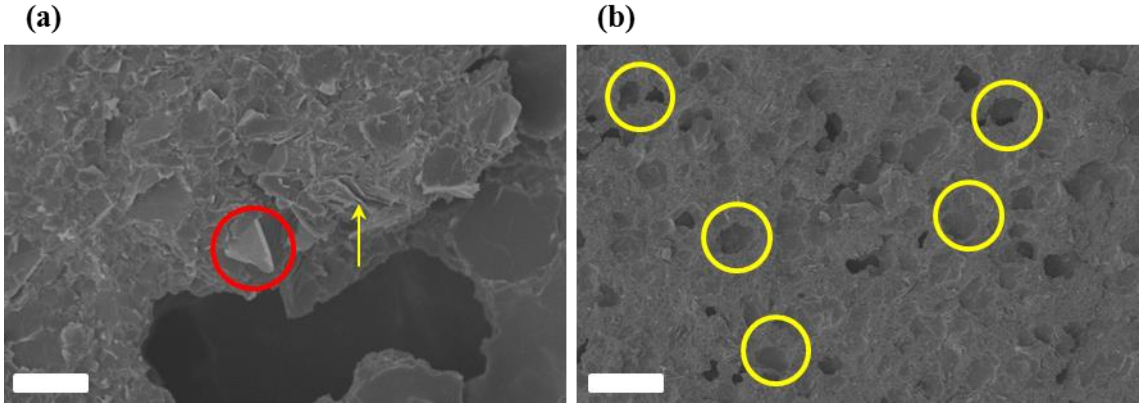

Figure 4.29. SEM images of PA20XG25-P nanocomposites: (a) 10 µm scalebar; (b) 100 µm scalebar. Yellow arrows highlight visible flakes, yellow circles highlight voids. The red circle highlights a folded monolayer graphene flake.

Table 4.6. Average number of voids per 1 mm^2 surface area of cryogenically fractured cross-section for chip and powder processed nanocomposites. Scaled from area of 0.4 mm^2 measured.

Loading (wt%)	0	1	5	10	20
Chip	0	2	20	50	430
Powder	0	2	5	10	200

Voiding has been observed before for polymer/carbon nanocomposites.[127,162,170–173] Recently, Rashmi *et al.*[162] also observed voiding with increasing loading of GNPs in PA11 using an industrial scale extruder. This suggests that there is an inherent compatibility problem between the GNPs and PA11 matrix which leads to substantial voiding. Magniez *et al.*[170] attributed the 'cavities' to carbon fibre (CF) pull-out in their PA11/CF composites, although conceded that the cavities found in local aggregation could have been induced during injection moulding of the samples. Bidsorkhi *et al.*[171] found a reversal of the effect observed in this work for solution processed PVDF/GNP composites, with increasing GNP loading leading to fewer voids. Similar to current work, Nadiv *et al.*[172] found that voiding occurred for 9 – 35 wt% loading of GNP in epoxy resin, but not for lower loadings. Nadiv *et al.*[173] also found the same effect in epoxy/CNT nanocomposites made in a similar way. Damari *et al.*[127] observed air entrapment in samples of 3 wt% GNP loading and above in polyurethane, such bubbles resulted in an increase in water vapour transmission at higher loadings, compared to loadings < 3 wt%.

Interestingly, the voiding observed in the melt blending work of this chapter far exceeded the voiding observed the *in situ* polymerised nanocomposites (Figure 3.26 – Figure 3.32). This suggests that the grafting of PA11 to the fillers improves the general compatibility of the filler and matrix, and therefore may be a better route for producing barrier materials.

With the quantities of voiding observed in the current work, it seemed unlikely that an improvement in barrier properties would be observed. The 1 wt% loading of GNP in PA11 yielded the lowest voiding levels, so was chosen for permeability testing, which will be discussed in a later section.

4.6.5 RHEOLOGICAL PROPERTIES

Rheological studies are an important method for the characterisation of polymers, particularly for nanocomposites produced through methods of industrial importance.

Plots of the complex viscosity with angular frequency for PA*n*XG25-C and PA*n*XG25-P at 215 °C are displayed in Figure 4.30a and b, respectively. The complex viscosity is found by applying an oscillatory shear stress on a viscoelastic fluid and is made up of the in-phase dynamic viscosity and the out-of-phase imaginary viscosity. As can be seen, the nanocomposites are more viscous than neat PA11 at both low and high angular frequencies, a trend that is observed in other polyamide/GNP studies.[162,174,175] The opposite behaviour has been observed in *in situ* polymerised PA6/functionalised GO (fGO) composites, attributed to fewer entanglements between shorter grafted chains as fGO loading increases, leading to lower viscosity.[141] In the current work, the viscosity increases with increasing GNP loading although it appears that the 20 wt% nanocomposite shear thins significantly compared to the lower loaded nanocomposites. This effect was also observed for 2 wt% multi-walled nanotubes (MWNTs) in PA11 and was attributed to single MWNTs and bundles (analogous to single GNPs and GNP agglomerates in this work, respectively) orienting preferentially under the strong shear force, so disrupting the polymer chain entanglement, leading to strong shear thinning behaviour.[112] Shear thinning of 10 wt% GNP loaded PA6 nanocomposites was also observed in flow sweep measurements – the highest GNP loadings had the highest viscosity at low shear rates but the pattern reversed at high shear rates and the highest GNP loadings displayed the lowest viscosity.[175] The neat PA11, 1 and 5 wt% nanocomposites all display a flat region at low angular frequency. This means that the nanocomposites behave as Newtonian fluids, that is, the viscosity does not depend on the angular frequency (or shear rate). On the other hand the 10 wt% and 20 wt% nanocomposites, exhibit shear thinning behaviour from the outset, the effect is particularly obvious for the 20 wt% nanocomposites.

Comparing Figure 4.30a to b, it can be seen that generally, the chip processed nanocomposites have a lower viscosity than the powder processed nanocomposites. This may be due to superior GNP exfoliation and dispersion in the powder processed samples, leading to greater PA11/GNP interactions. Greater MWNT content displayed a similar effect on the viscosity of PA11/MWNT composites, although at an order of magnitude lower MWNT loading.[112] Even the PA0XG25-P has a marginally higher

viscosity than PA0XG25-C, possibly due to faster melting and mixing of powdered PA11 compared to the chip samples. The 20 wt% powder processed nanocomposite shear thins more rapidly than the 20 wt% chip processed sample. This may be due to greater exfoliation of the GNPs in powder processing, leading to more disruption of chain entanglement. Interestingly, the PA20XG25-P nanocomposite shear thins to such an extent that it approaches the viscosity of the neat PA11, whereas PA20XG25-C retains a much higher viscosity.

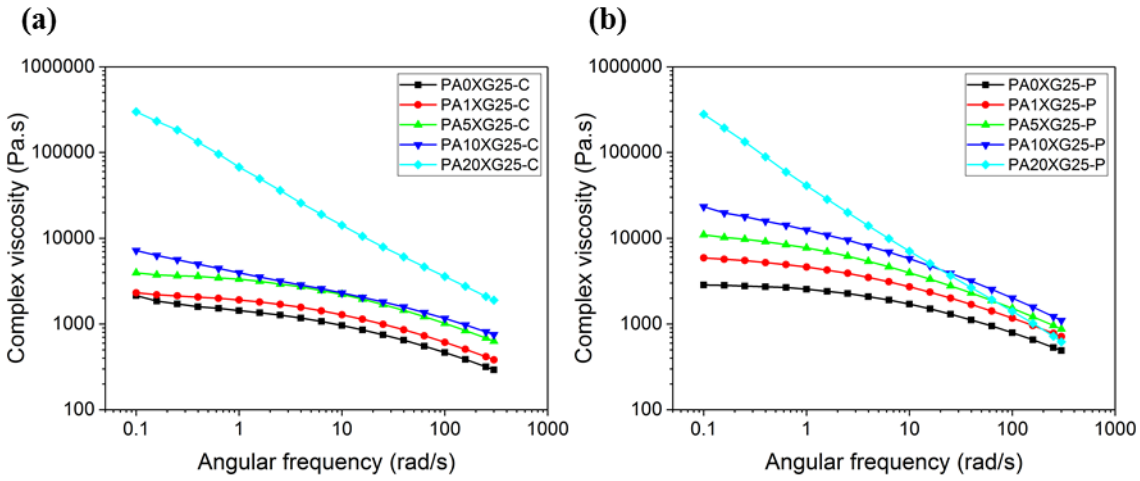

Figure 4.30. Complex viscosity ($|\eta^*|$) measurements for (a) PA*n*XG25-C and (b) PA*n*XG25-P at 215 °C.

The relationship between complex viscosity and GNP loading for the two blending methods over a range of oscillation frequencies is shown in Figure 4.31. As can be seen, each set of samples shear thins, that is, the higher the shear rate, the lower the viscosity. Interestingly, the difference in viscosities between the nanocomposites produced by the two processing methods can easily be seen in this plot. For the chip processed nanocomposites, there is a moderate increase in viscosity up to 10 wt% before a large increase in viscosity for the 20 wt% sample. A similar trend occurs for the powder processed samples up to 10 wt%; however, the 20 wt% nanocomposite shear thins dramatically to a value approaching the 0 wt% nanocomposite at high shear rates. This suggests that the addition of 20 wt% GNP affects the powder nanocomposite viscosity less than the chip processed samples. This may be due to the already relatively high viscosities of the 0, 1, 5 and 10 wt% powder samples compared to the chip nanocomposites. The measured complex viscosity profiles remained much flatter and

had a lower magnitude at higher shear rates, demonstrating shear thinning. Shear thinning was also observed at high frequencies by Rashmi *et al.*[162] for PA11/GNP nanocomposites as well as similar viscosity increases with increased GNP loading.

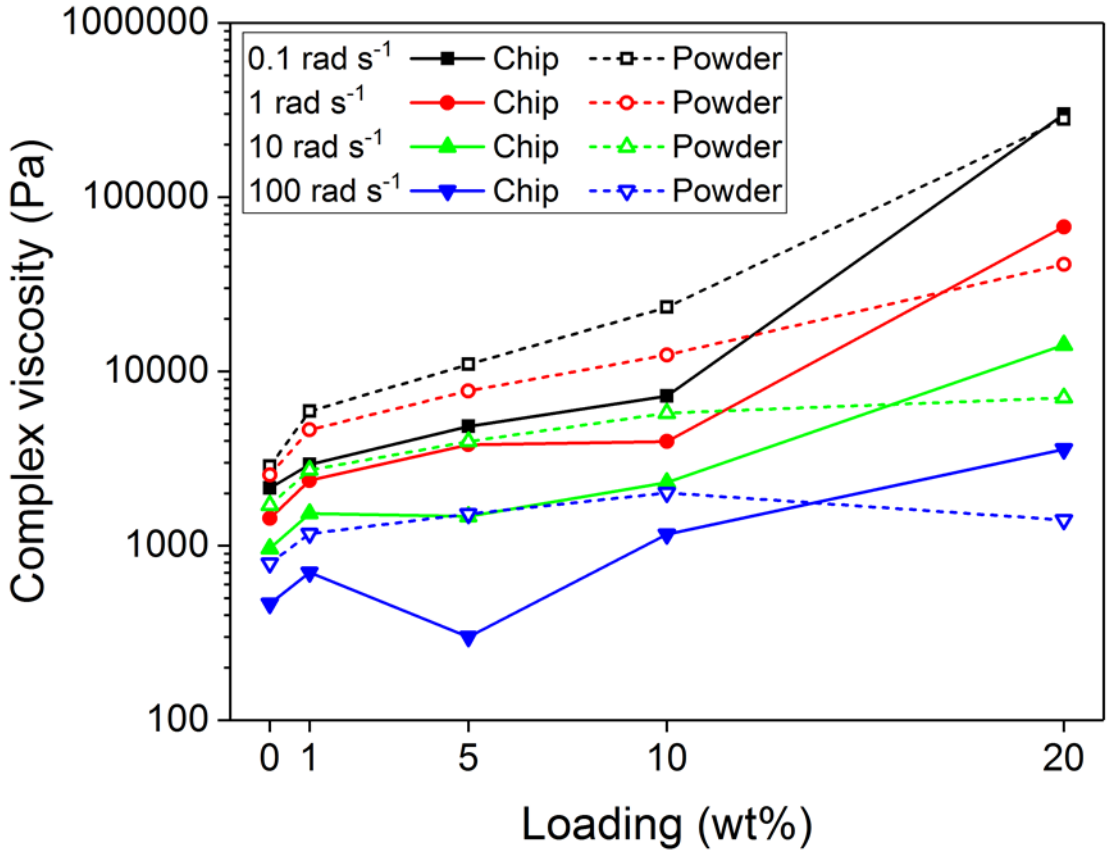

Figure 4.31. Change in complex viscosity ($|\eta^*|$) with GNP loading for the chip and powder nanocomposites at different frequencies.

The viscosities of the powder processed samples are consistently higher than the viscosities of equivalent chip processed nanocomposites until the 20 wt% loading. PA20XG25-P displays a similar viscosity to PA20XG25-C at 0.1 rad s^{-1}; however, the rate of shear thinning for PA20XG25-P is faster than that of PA20XG25-C. This is evidenced by the increasing magnitude of the gap between the powder and chip processed nanocomposite at 20 wt%, with increased oscillation frequency.

The variation of storage (elastic), *G*', and loss (viscous), *G*'', moduli are shown in Figure 4.32 and Figure 4.33 for PA*n*XG25-C and PA*n*XG25-P, respectively. The

rheological percolation threshold, that is, the GNP loading required to form a physical network of GNPs due to filler-filler interactions,[175] can be identified by the relative magnitudes of *G*' and *G*''.[174] The percolation threshold shows the loading at which a gel-like structure forms between the fillers, that is, as loading increases, the filler-filler interactions dominate over polymer-filler interations.[176] This transition from liquid-like, to solid-like behaviour may also be seen by the disappearance of the Newtonian plateau in the complex viscosity plot for the 10 and 20 wt% loadings.[177] Similar behaviour was observed by Rashmi *et al.* for PA11/GNP composites.[162] The increase in *G*' for GNP-containing nanocomposites relative to neat PA11 was attributed to confinement of polymer chains. They also observed a plateau in the *G*' at low frequency with higher loadings, suggesting pseudo-solid-like behaviour occurred (percolation was reached). This is also observed in this work for the 20 wt% nanocomposites.

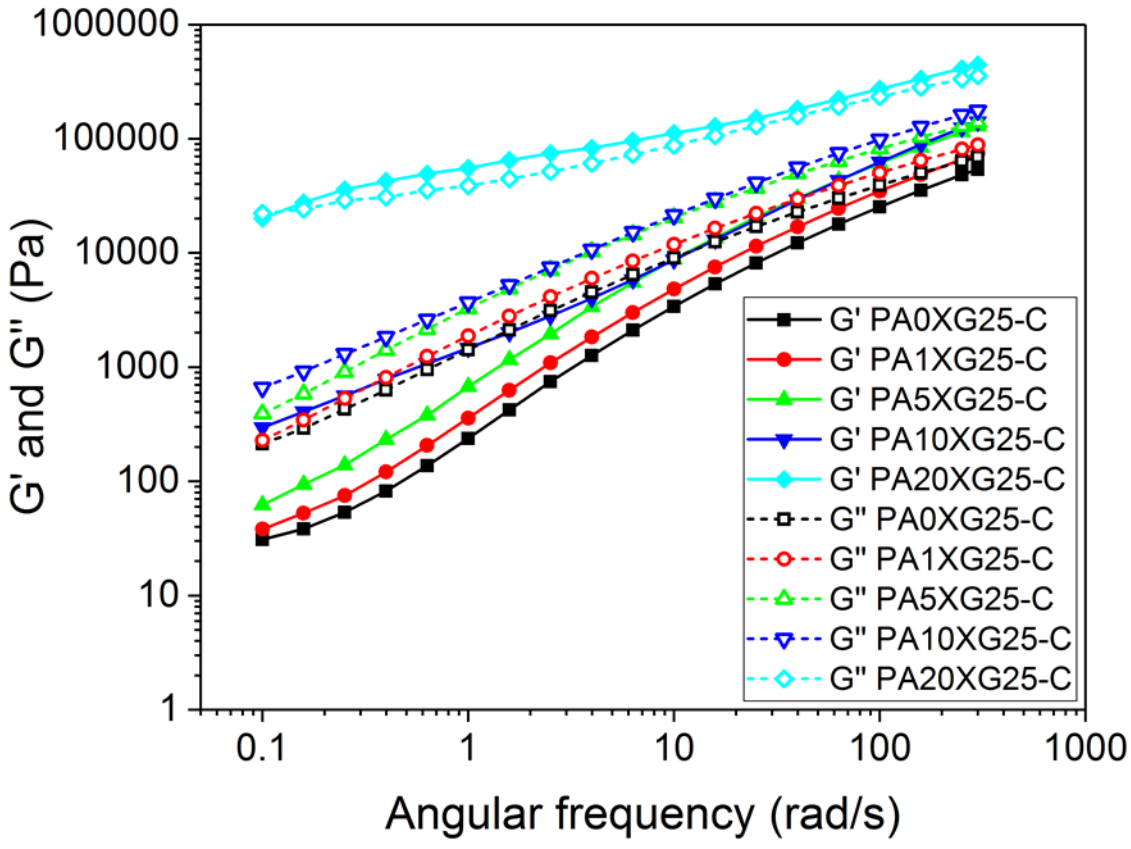

Figure 4.32. Storage and loss moduli (*G*' and *G*'') for PA*n*XG25-C at 215 °C.

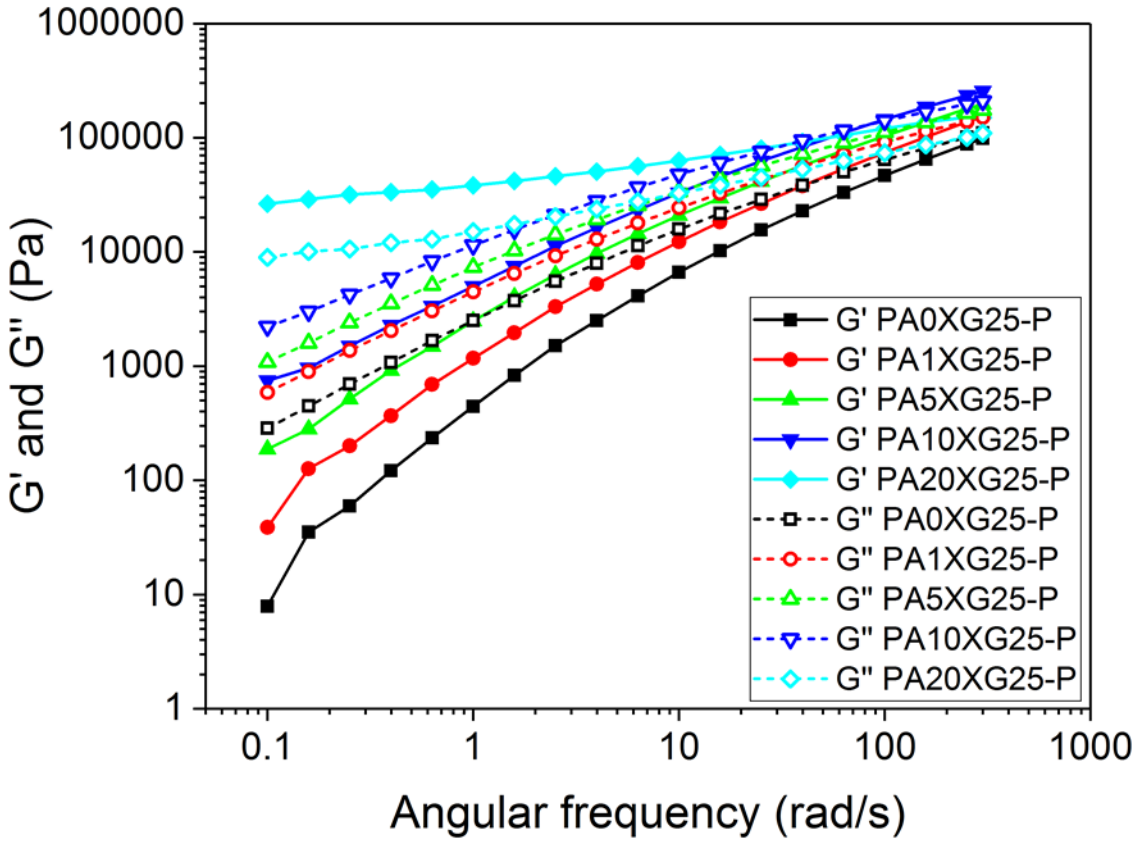

Figure 4.33. Storage and loss moduli (*G*' and *G*'') for PA*n*XG25-P at 215 °C.

Canales *et al.*[174] confirmed that no percolation was observed for 15 wt% GNPs in an amorphous polyamide because the loss (viscous) modulus had a higher relative value than the storage (elastic) modulus – that is, *G*'' > *G*'. As can be seen in Figure 4.32 and Figure 4.33, the loss modulus for 0, 1, 5 and 10 wt% is consistently greater than the storage modulus (*G*'' > *G*') across the angular frequency range. However, at 20 wt% for both chip and powder processed samples, the loss modulus is lower than the storage modulus (*G*' > *G*'') and so rheological percolation is achieved between 10 and 20 wt% GNPs. Mayoral *et al.*[178] obtained a rheological percolation threshold between 10 and 15 wt% GNPs in PA6. This was indicated by an increase in the complex viscosity – also observed in this work in Figure 4.30 for 20 wt% loading – and storage modulus at low frequencies – observed in this work in Figure 4.32 and Figure 4.33 for 20 wt% nanocomposites.

Figure 4.34a and b show the tanδ values for PA*n*XG25-C and PA*n*XG25-P, respectively. Tanδ is defined as the quotient of the loss modulus and storage modulus

(G''/G'). Generally, tanδ decreased with increasing angular frequency demonstrating that the shear deformation caused partial orientation of the polymer chains.[112] A high tanδ reveals liquid-like behaviour; whereas low tanδ show that the nanocomposites have solid-like behaviour.[177] In other words, values of tanδ below one mean that the magnitude of the storage modulus is larger than the loss modulus and so, represents a nanocomposite that has solid-like behaviour. Values approaching one, therefore, are approaching the percolation threshold, which correlates nicely with increasing loading and higher angular frequency.[177]

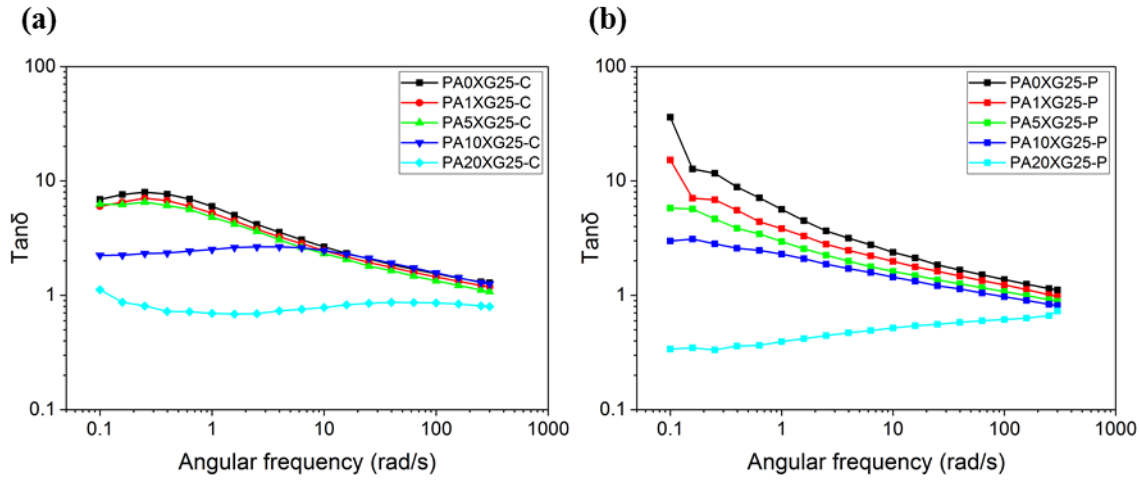

Figure 4.34. Tanδ for (a) PA*n*XG25-C and (b) PA*n*XG25-P at 215 °C.

4.6.6 Permeability Studies

Table 4.7 shows the conditions used to test the four samples prepared according to section 4.4.6. The letters in parenthesis represent the test cell that the samples were tested in. The nanocomposites used to make up the sandwich structures were produced by the chip method at a loading of 1 wt%. Gaskets were used for some samples later in the thesis in order to protect the sample surface; however, in this chapter, no gaskets were used. Estimated error on repeated permeability values has a maximum of the order of 10%.[179]

Table 4.8 shows the fugacity coefficients used for calculation of the permeability coefficients with fugacity, P_f. Values of P_f are displayed in Appendix C.

Table 4.7. Sample codes and the testing conditions used for the nanocomposite sandwich structures.

Sample	**Fluid**	***T* (°C)**	***p* (MPa)**	p_{CO2} **(MPa)**	p_{H2S} **(MPa)**	**Gasket**
PA0(A), PA1(C)	CO_2 with 1.48% H_2S	60, 35	5	4.926	0.074	No
PA0(B), PA1(D)	CO_2 with 1.48% H_2S	60, 35, 60	5, 10	4.926, 9.852	0.074, 0.148	No

Table 4.8. Relationship between total feed pressure, p, partial pressures, p_{CO2} and p_{H2S}, and fugacity values, f_{CO2} and f_{H2S}, calculated using the fugacity coefficients φ_{CO2} and φ_{H2S}.

p (MPa)	p_{CO2} (MPa)	p_{H2S} (MPa)	f_{CO2}* (MPa)	f_{H2S}* (MPa)	φ_{CO2}†	φ_{H2S}†
5	4.926	0.074	4.10	0.058	0.832	0.780
10	9.852	0.148	6.67	0.084	0.678	0.568

*Calculated by Equation 2.27

†Values calculated from NIST REFPROP software

4.6.6.1 5 MPa CO_2 with 1.48% H_2S 60 °C

The averaged CO_2 permeability, diffusion and solubility coefficients for the sandwich structures tested at 5 MPa CO_2 with 1.48% H_2S and 60 °C are shown in Figure 4.35. As can be seen, there was no appreciable difference in permeability, diffusion or solubility coefficients upon the addition of 1 wt% GNP to the central nanocomposite layer. The H_2S transport coefficients, shown in Figure 4.36 also do not appear to be altered by the presence of GNPs. This is an unexpected result, as a number of publications report permeability reductions with low loadings of GNPs or GRMs.[98,157–159]

Müller *et al.*[158] observed up to 40% reduction in the oxygen permeability of polycarbonate at 3 wt% GNP loading. Honaker *et al.*[157] observed a reduction in oxygen and fuel vapour permeation of around 25% and 40%, respectively for a loading of approximately 2.5 wt%. Al-Jabareen *et al.*[159] observed a reduction in OTR of over 75% at 1 wt% loading of GNPs in PET. Jin *et al.*[98] reported a reduction in OTR and water vapour transmission rate (WVTR) of 35% and 31%, respectively, at a loading of 1 wt% GO. They also tested PA12/GO and found a 27% reduction in both OTR and WVTR at 1 wt% loading.

The reason for the poor performance of the 1 wt% sandwich structures is unclear; however, there is a small amount of voiding in the PA1XG25-C samples (Table 4.6). This could mean that any barrier improvement due to the dispersed GNPs, is balanced by the free paths for diffusion through voids. In addition, Al-Jabareen and co-workers found that permeability reduced with increasing crystallinity of the nanocomposites, which increased with GNP loading.[159] In this work, however, there is no appreciable change in crystallinity from DSC (Table 4.4) and also no improvement in barrier performance to CO_2 or H_2S at 5 MPa and 60 °C.

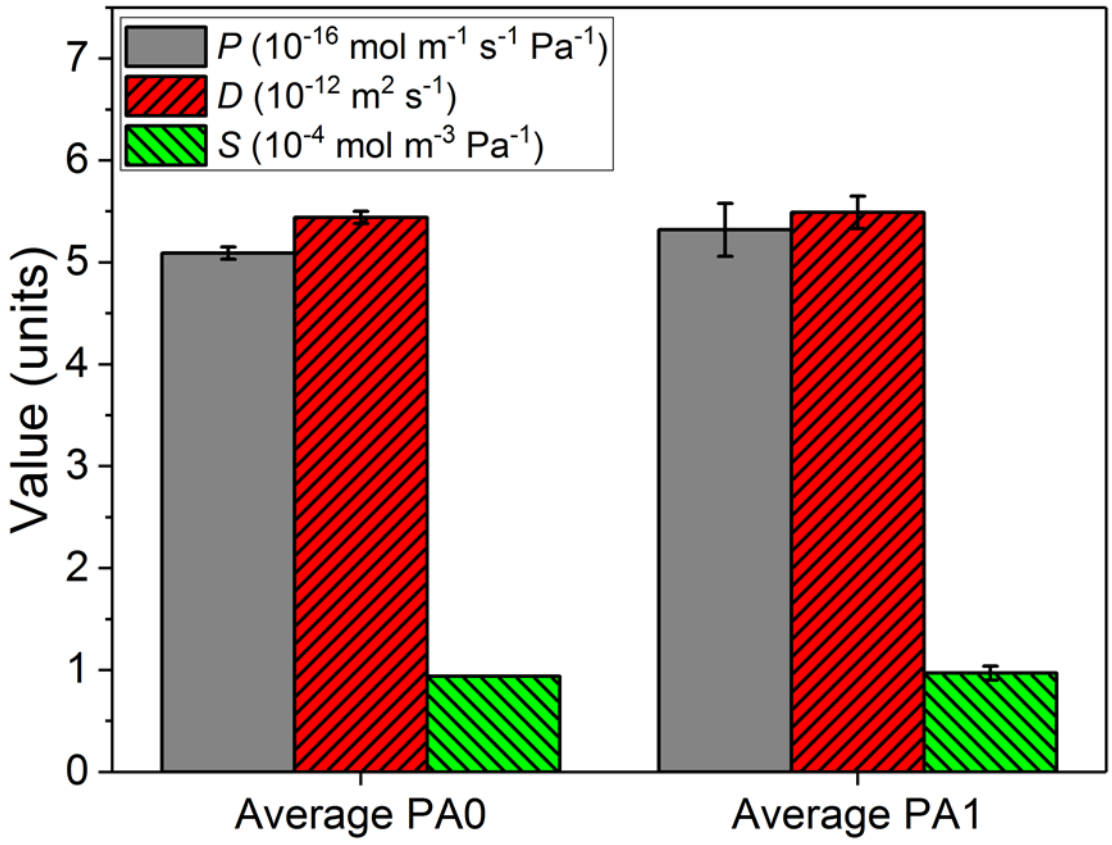

Figure 4.35. Variation of CO_2 transport coefficients at 5 MPa CO_2 with 1.48% H_2S at 60 °C for the average of PA0(A) and PA0(B) and the average of PA1(C) and PA1(D). Standard deviations are calculated from two samples. Using fugacity as the driving force increases the value of *P* to 6.1 and 6.4 and *S* to 1.1 and 1.2 for PA0 and PA1, respectively.

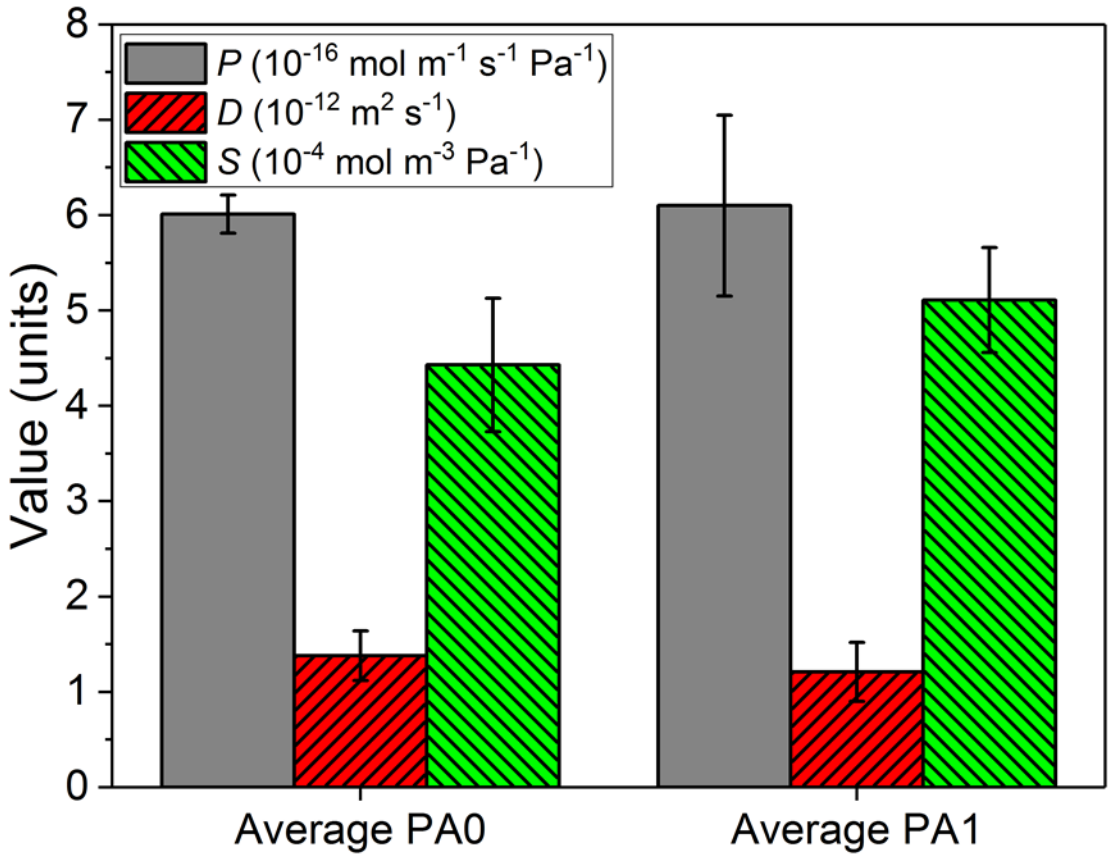

Figure 4.36. Variation of H_2S transport coefficients at 5 MPa CO_2 with 1.48% H_2S at 60 °C for the average of PA0(A) and PA0(B) and the average of PA1(C) and PA1(D). Standard deviations are calculated from two samples. Using fugacity as the driving force increases the value of *P* to 7.7 and 7.8 and *S* to 5.6 and 6.5 for PA0 and PA1, respectively.

Figure 4.37 shows the CO_2 and H_2S transport coefficients for the control PA0 samples only, so that the transport properties of the gases may be compared. According to Equation 2.9, the permeability coefficient is made up of the diffusion coefficient and solubility coefficient ($P = D.S$). *D* and *S* are competing terms and penetrants with high diffusion coefficients typically have low solubility coefficients, and *vice versa*.[53,54] As can be seen, the permeability of CO_2 and H_2S have similar magnitudes, however, the mechanism of permeation appears to be very different for the two penetrants. CO_2 appears to be a diffusion driven permeation process, perhaps due to relatively poor interactions with the polyamide compared to the PA11-H_2S interactions. H_2S permeation, however, appears to be driven by high solubility in the PA11 matrix, as shown by the low diffusion coefficient and high solubility coefficient.

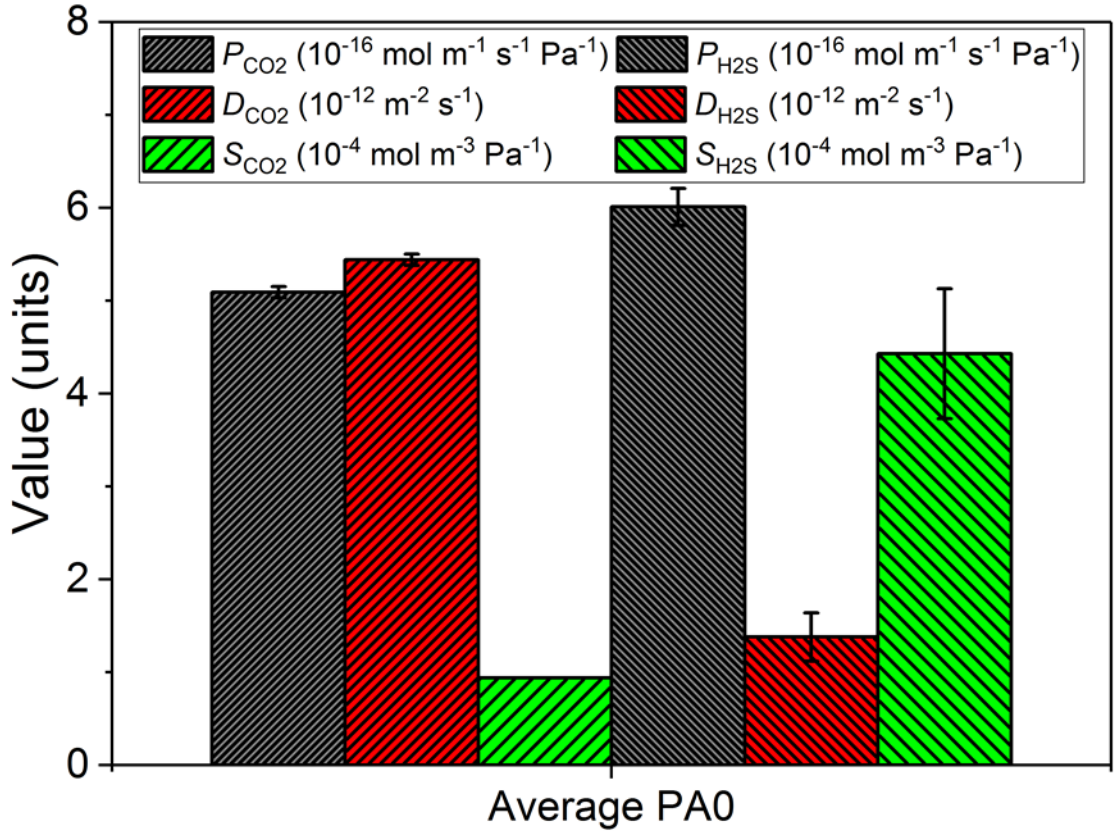

Figure 4.37. Plot comparing *P*, *D* and *S* for CO_2 and H_2S at 5 MPa CO_2 with 1.48% H_2S at 60 °C for the average control PA0. Error bars show standard deviation of the two samples. Using fugacity as the driving force increases the value of P_{CO2} and S_{CO2} to 6.1 and 1.1 and P_{H2S} and S_{H2S} to 7.7 and 5.6, respectively.

CO_2 has a smaller kinetic diameter than H_2S, at 3.3 and 3.6 Å, respectively, so diffusion should be easier for CO_2.[53] In addition, nitrogen containing materials typically have high selectivity for H_2S capture.[180] These arguments, although simple, may help explain the differences in diffusion coefficients, and subsequent differences in solubility coefficients observed in Figure 4.37 for CO_2 and H_2S.

4.6.6.2 5 MPa CO_2 with 1.48% H_2S 35 °C

As can be seen in Figure 4.38, the permeability coefficients of PA0 and PA1 at 35 °C did not differ appreciably. Evidently, H_2S permeation was shut down upon lowering the temperature to 35 °C, probably due to reduced chain mobility.[54] Discussion of the effect of temperature on the transport coefficients is presented later.

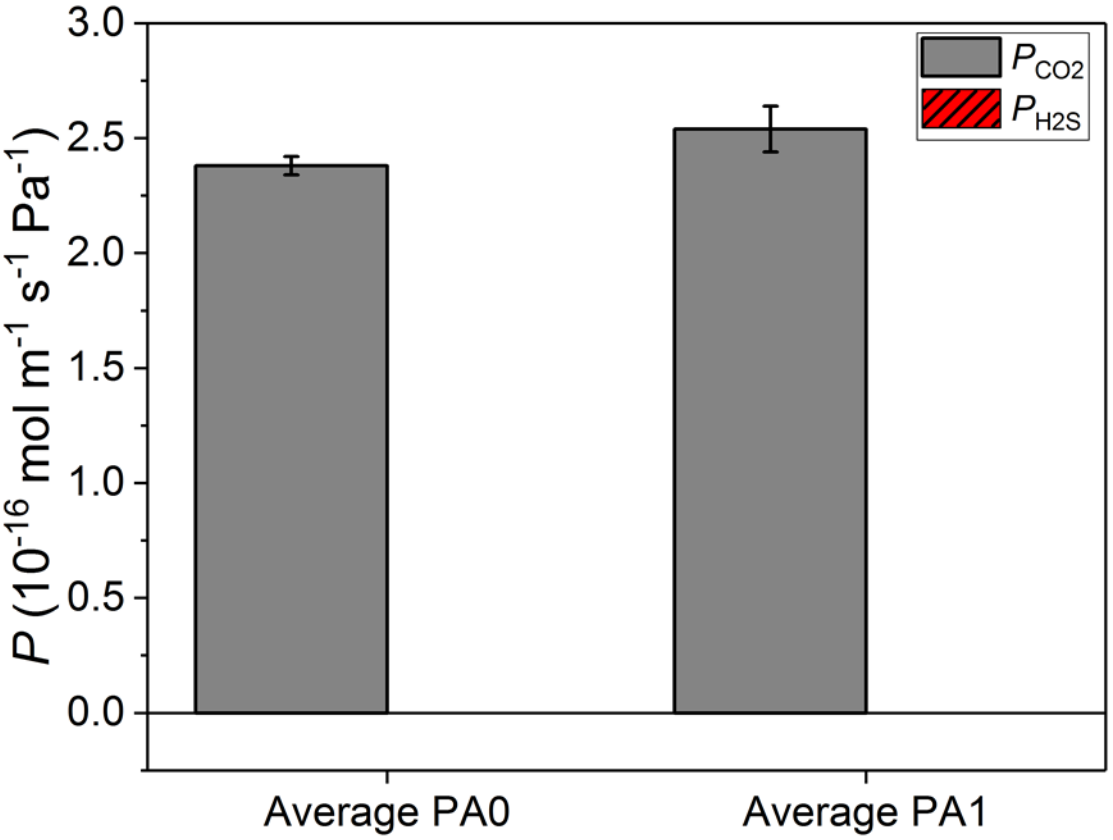

Figure 4.38. Variation of H_2S transport coefficients at 5 MPa CO_2 with 1.48% H_2S at 35 °C for the average of PA0(A) and PA0(B) and the average of PA1(C) and PA1(D). Standard deviations are calculated from two samples. Using fugacity as the driving force increases the value of *P* to 3.0 and 3.3 for PA0 and PA1, respectively.

4.6.6.3 10 MPa CO_2 with 1.48% H_2S 60 °C

The transport coefficients at 10 MPa and 60 °C for supercritical CO_2 and H_2S are shown in Figure 4.39 and Figure 4.40, respectively. The measurements are from single samples PA0(B) and PA1(D) and the error bars signify 10% estimated error.[179] As can be seen, there was no appreciable change in the transport coefficients of CO_2 at 10 MPa and 60 °C. There did appear to be a very slight increase in the permeation of H_2S through PA1(D) compared to PA0(B) (Figure 4.40), although the estimated errors for the two samples overlap slightly and so the result may not be statistically significant. This was mirrored by a slight increase in the diffusion coefficient for the 1 wt% loaded nanocomposite, which may be due to poor interfacial interactions between GNPs and PA11 leading to interfacial voiding.[181]

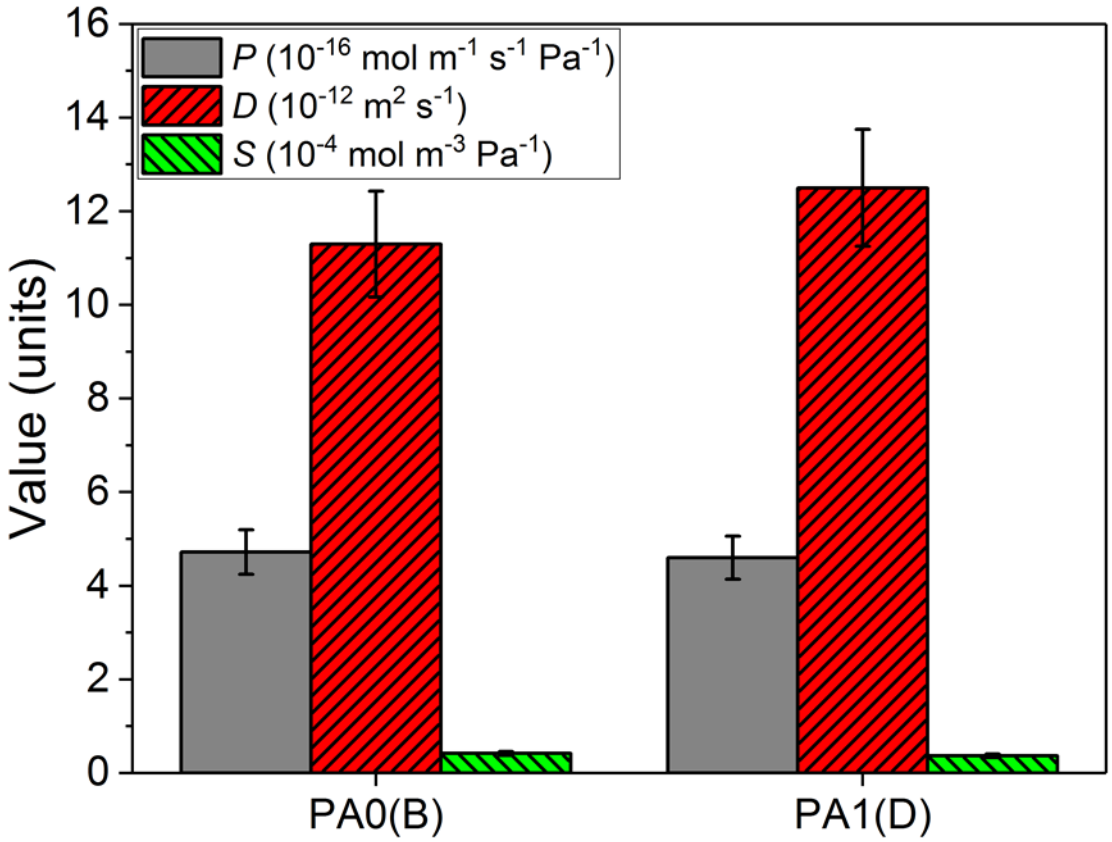

Figure 4.39. Variation of CO_2 transport coefficients at 10 MPa CO_2 with 1.48% H_2S at 60 °C for the PA0(B) and PA1(D). Error bars represent an estimated error of 10%. Using fugacity as the driving force increases the value of *P* to 7.0 and 6.8 and *S* to 0.62 and 0.54 for PA0 and PA1, respectively.

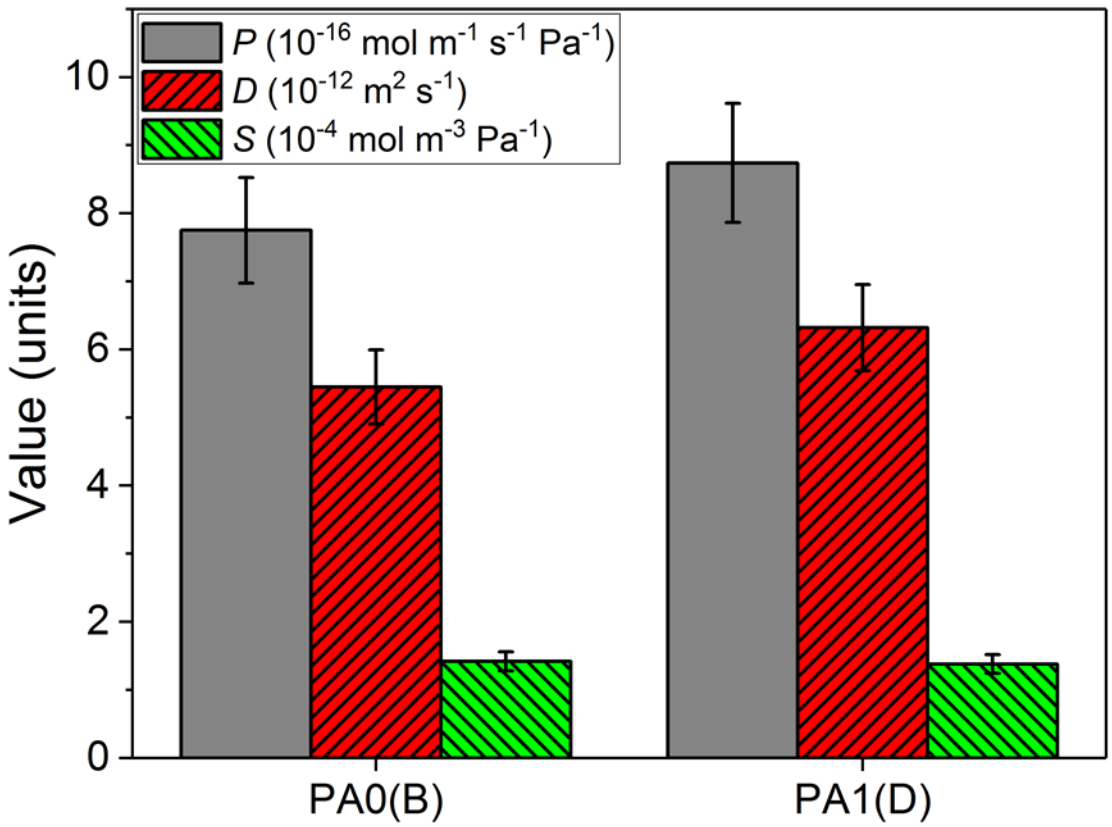

Figure 4.40. Variation of H_2S transport coefficients at 10 MPa CO_2 with 1.48% H_2S at 60 °C for the PA0(B) and PA1(D). Error bars represent an estimated error of 10%. Using fugacity as the driving force increases the value of *P* to 13.6 and 15.4 and *S* to 2.5 and 2.4 for PA0 and PA1, respectively.

Figure 4.41 shows the CO_2 and H_2S transport coefficients for PA0(B) at 10 MPa CO_2 with 1.48% H_2S with 10% estimated error.[179] At 10 MPa and 60 °C, the CO_2 is in the supercritical phase; the H_2S is assumed to be dissolved in the CO_2 phase.[92] As can be seen, CO_2 permeability was substantially lower than the H_2S permeability at 10 MPa. Diffusion was still the dominating term for CO_2 transport. However the diffusion coefficient also seems to dominate for H_2S. This is different from the 5 MPa behaviour observed for H_2S in Figure 4.37, where the diffusion coefficient was far lower than the solubility coefficient.

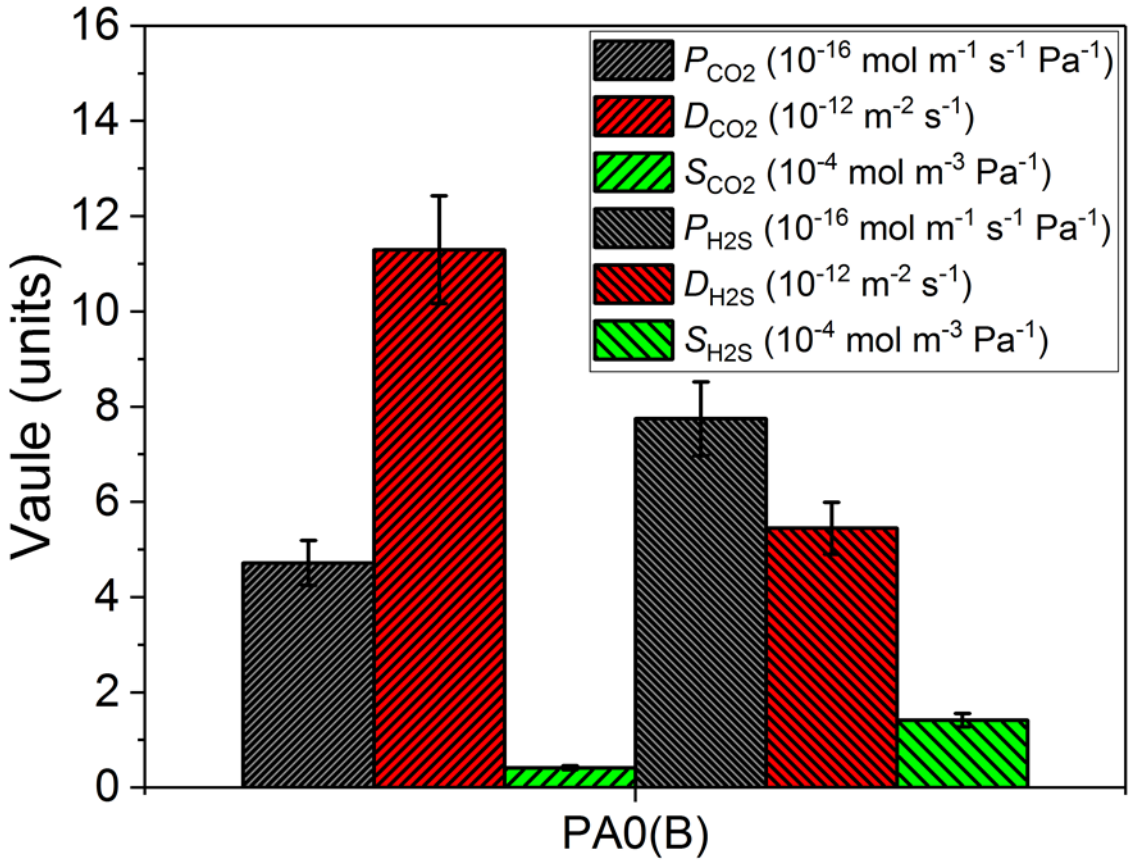

Figure 4.41. Plot comparing *P*, *D* and *S* for CO_2 and H_2S at 10 MPa CO_2 with 1.48% H_2S at 60 °C for PA0(B). Error bars represent an estimated error of 10%. Using fugacity as the driving force increases the value of P_{CO2} and S_{CO2} to 7.0 and 0.62 and P_{H2S} and S_{H2S} to 13.6 and 2.5, respectively.

4.6.6.4 Effect of Temperature

Figure 4.42 shows the permeability coefficients of CO_2 and H_2S following reduction of the temperature from 60 to 35 °C, while maintaining the 5 MPa pressure feed of gaseous CO_2 and 1.48% H_2S. As can be seen, the permeation of H_2S was undetectable following the temperature drop from 60 to 35 °C. The permeability coefficient for CO_2 was also reduced by approximately half upon temperature reduction.

PA11 has a T_g at approximately 40 °C (Table 4.4) and so is above its T_g at 60 °C but is below its T_g at 35 °C. Semi-crystalline polymers above their T_g are made up of a rubbery amorphous phase linking together crystalline phases. At temperatures below the T_g, the amorphous phase is in the glassy state, and so the polymer chain mobility is reduced. Reduced chain mobility means that the activation energy for a penetrant to make a diffusional jump is increased, that is, the chains are harder to move apart to

allow the molecule to diffuse. At temperatures above the T_g, the polymer has more free volume due to the increased chain motions, thus facilitating diffusion.[52] The activation energy for diffusion typically increases with penetrant size. Since H_2S is larger than CO_2,[53] the reduced chain mobility is likely to increase the activation energy for permeation more for H_2S than for CO_2.

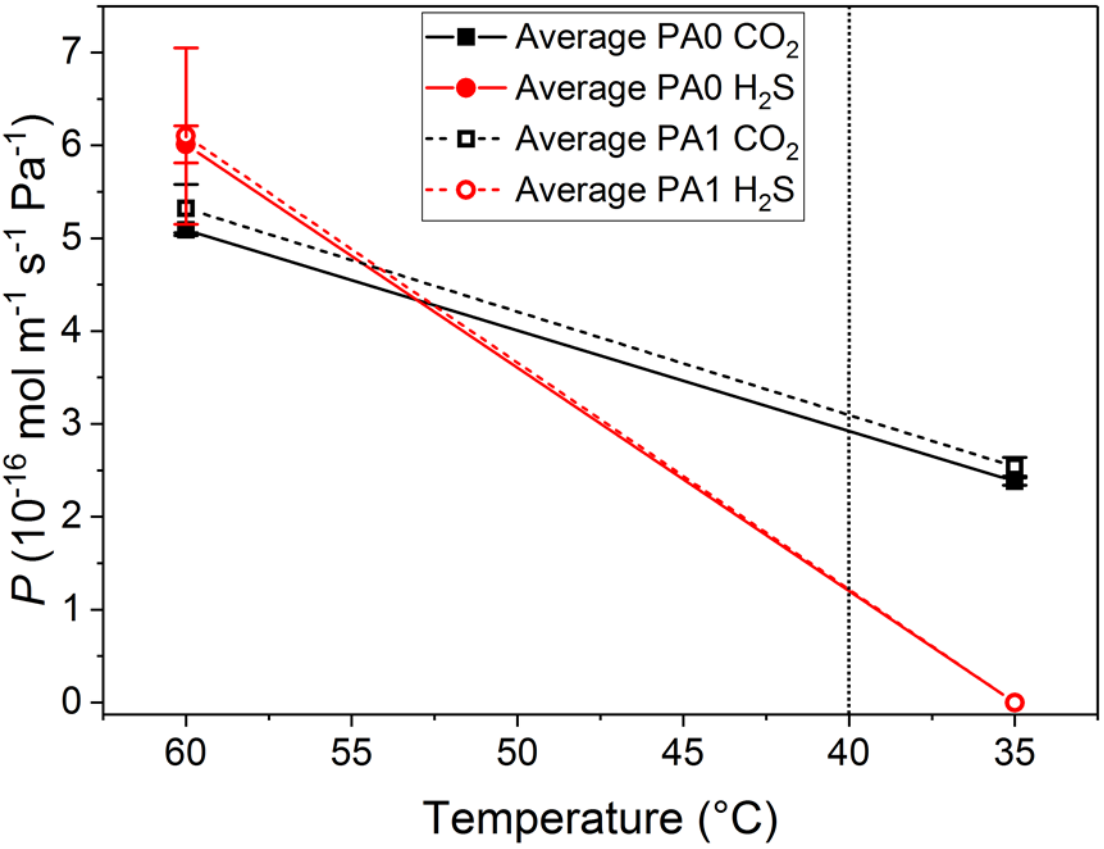

Figure 4.42. Variation of CO_2 and H_2S permeability coefficients at 5 MPa CO_2 with 1.48% H_2S at 60 then 35 °C for the average of PA0(A) and PA0(B) and the average of PA1(C) and PA1(D). Standard deviations are calculated from the two samples. Vertical dotted line marks approximate T_g of PA11.

By reducing the temperature between experiments and monitoring the steady state permeability, the activation energy for permeability may be found. As introduced in section 2.5.2, the relationship between permeability coefficient and temperature is of Arrhenius-van't Hoff form, repeated below for ease of reference:[65]

$$P(T) = P_0 \exp\left(-\frac{E_P}{RT}\right)$$ Equation 2.24

Thus, plotting the natural logarithm of $P(T)$ against $1/T$, the activation energy may be calculated from the gradient of the line of best fit (Figure 4.43). Since the steady state permeability of H_2S at 35 °C is undetectable, the activation energy of permeation for H_2S cannot be calculated.

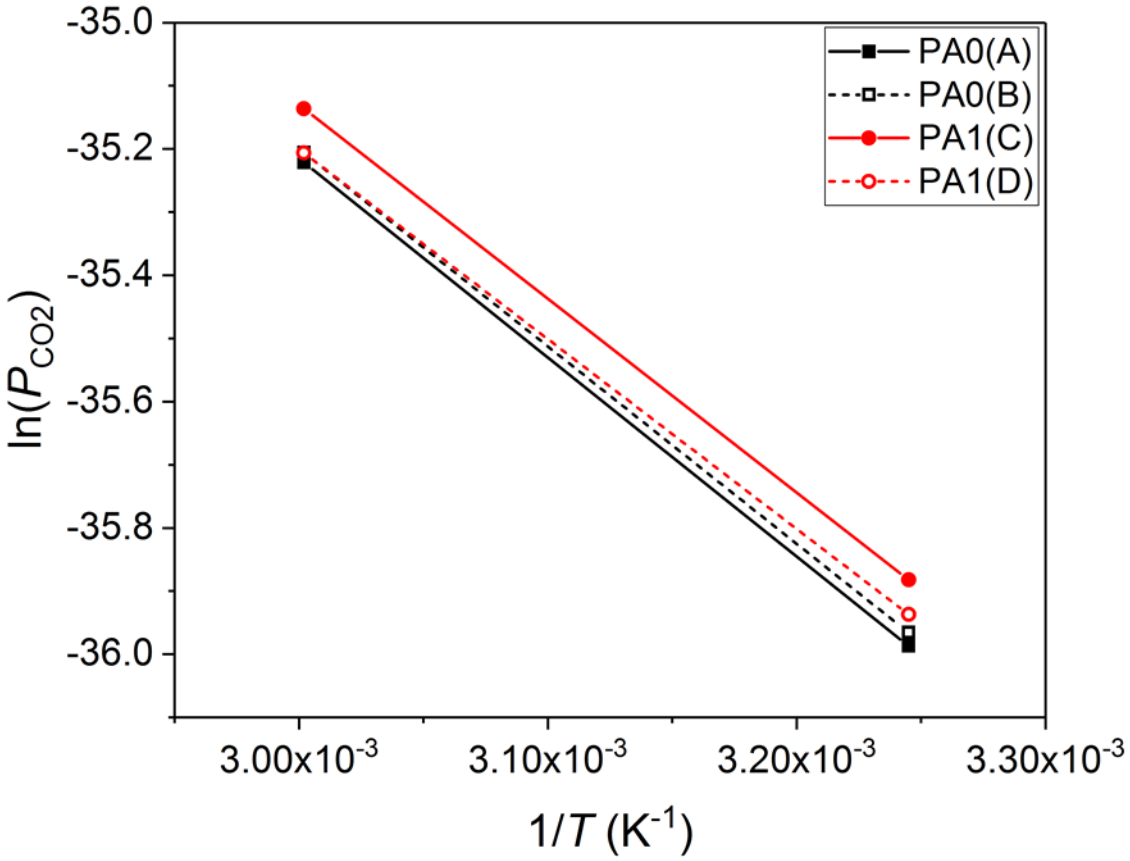

Figure 4.43. Plot of $\ln(P_{CO2})$ *versus* $1/T$ for PA0(A), PA0(B), PA1(C) and PA1(D) for 5 MPa pressure CO_2 with 1.48% H_2S at 60 then 35 °C.

From these plots, the value of the gradient is equal to the exponential term, that is:

$$\frac{\mathrm{d}\left(\ln(P)\right)}{\mathrm{d}T} = -\frac{E_\mathrm{P}}{R} \qquad \text{Equation 4.2}$$

The calculated values of E_P for PA0 and PA1 sandwich structures are shown in Table 4.9. As can be seen, the values for E_P were fairly consistent between repeated samples and between sample pairs. This was not unexpected, as the samples proved to behave similarly, regardless of the GNP loading.

The averaged values are compared with literature values for E_P as shown in Table 4.10. As can be seen, the activation energy for permeation in this work was at least 20% less than E_P found in the work of Flaconnèche *et al.*[54] and Ash *et al.*[60]. This suggested that

the permeation of CO_2 through the PA11 in this work was less energy intensive. These differences may be due to the melt processing of the central PA11 layer, or possibly simply due to the differences in the PA11 grades used.

Table 4.9. Calculated values and standard deviations of activation energy for permeation of CO_2 for PA0 and PA1 sandwich structures at 5 MPa CO_2 with 1.48% H_2S at 60 then 35 °C.

Sample	E_P **(kJ mol^{-1})**
PA0(A)	26.1
PA0(B)	25.9
PA1(C)	25.4
PA1(D)	25.0

Table 4.10. Averaged values of activation energy for permeation in this work compared to the values in the literature.[54,60]

Sample	E_P **(kJ mol^{-1})**
PA0	26.0 ± 0.1
PA1	25.2 ± 0.4
PA11 Flaconnèche *et al.*[54]	35
PA11 Ash *et al.*[60]	34

4.6.6.5 Effect of Pressure

Figure 4.44 shows a comparison between the permeability coefficients of CO_2 and H_2S at 5 and 10 MPa total feed pressure. At 60 °C the CO_2 with 1.48% H_2S mix is gaseous at 5 MPa and becomes supercritical at pressures above 7.4 MPa, as shown by the vertical dotted line. As can be seen, at 5 MPa, the permeability coefficients of CO_2 and H_2S were approximately the same, within error (single standard deviation of two samples). At 10 MPa, the CO_2 permeability coefficients did not change substantially and remained within experimental error of the 5 MPa samples. Similar results have been obtained before: Flaconnèche *et al.*[54] observed no appreciable increase or decrease in the permeability of simple gases through PE or PVDF between 4 and 10 MPa, although they did not vary the feed pressure for PA11. Andersen *et al.*[61] found no pressure dependence upon the permeability coefficient for CH_4 or CO_2 in PA11 between 7.5 and

10 MPa (Table 2.2). They did observe large changes up to 5 MPa pressure but attributed this to poor experimental practice.

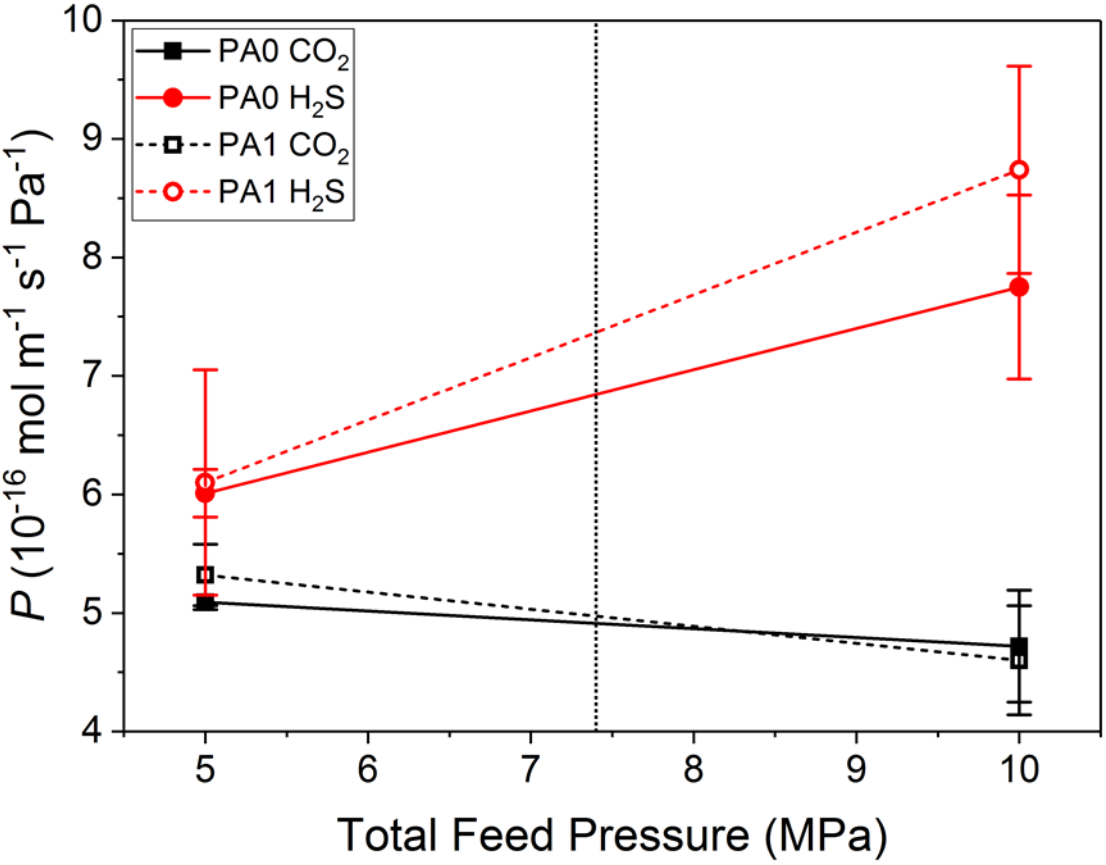

Figure 4.44. Variation of CO_2 and H_2S permeability coefficients at 5 and 10 MPa CO_2 with 1.48% H_2S PA0(B) and PA1(D). Error bars represent a single standard deviation from the PA0 samples and PA1 samples for 5 MPa values. Error bars represent 10% estimated error for 10 MPa values. Vertical dotted line marks approximate critical pressure (p_C) of CO_2 at 60 °C of 7.4 MPa. Values calculated using fugacity as the driving force are presented in earlier figure captions.

The H_2S permeability coefficient does increase substantially with increasing the pressure from 5 to 10 MPa. Data presented in Table 2.4 from the Rilsan® Handbook displays the same trend, with the H_2S permeability coefficient increasing with increasing pressure from 4 to 10 MPa.[24] The literature tests were, however, carried out with pure H_2S, rather than the mixed system presented in this work.

There appeared to be minimal difference in the permeability performance of the PA0 and PA1 samples at either pressure, although the 10 MPa H_2S value for PA1 does

appear to be higher than the PA0 value. This may not be statistically significant, and further testing of similar samples would be required to confirm this.

4.7 CONCLUSIONS

Nanocomposites comprising 0, 1, 5, 10 and 20 wt% GNPs in PA11 were manufactured *via* twin-screw extrusion on a lab-scale compounder. Characterisation and permeability testing of the nanocomposites was carried out. Two different methods were examined for incorporation of GNPs into PA11: firstly, PA11 pellets and GNP powders were sequentially added to the extruder (chip method); secondly, powdered PA11 was pre-mixed with GNP powder and simultaneously added to the extruder (powder method).

Spectroscopic studies showed that the GNPs were not functionalised by the melt processing, unlike for the *in situ* produced nanocomposites. The GNPs displayed similar Raman spectra following extrusion, suggesting that there was no alteration of the GNPs during melt mixing.

The thermal degradation of the nanocomposites appeared to be linked to their processing technique, with chip-processed samples generally displaying higher thermal stability. The thermal stability of the nanocomposites increased with increasing GNP loading due to the GNPs blocking diffusion of degradation species. *In situ* polymers showed better thermal stability than the melt blended samples by up to 20 °C.

The crystallinities in the samples were examined using DSC and XRD and it was found that the nanocomposites exhibited α' crystallinity at room temperature, resulting in a bimodal melting peak, due to low temperature melting of imperfect δ crystals, for the neat and 1 wt% loaded PA11. T_c was found to increase with GNP loading likely due to the GNPs acting as heterogeneous nucleating agents, allowing crystallisation to occur at a higher temperature. Both the chip and powder produced nanocomposites provided similar crystallinity behaviour. Similar behaviour was observed in the *in situ* polymers at low loading.

Morphological studies revealed that voiding was prevalent in all GNP loaded PA11 nanocomposites. Voiding was increased with increased GNP loading, although even at 1 wt%, some voiding was observed. It was found that altering the method of melt

blending from sequential addition of PA11 pellets then GNP powder, to simultaneous addition of pre-mixed PA11 powder and GNP powder reduced voiding significantly. *In situ* polymerised nanocomposites exhibited less voiding, probably due to improved compatibility of the functionalised GRMs. The voiding in the melt blended samples was still seen as an issue for barrier testing, and so only the lowest loading nanocomposite was tested.

Rheological studies revealed that the complex viscosity increased with increased filler levels; however, shear thinning at high frequencies reduced the complex viscosities to levels similar to neat PA11. The complex viscosities of powder processed samples were consistently higher than the equivalent loading of GNPs for chip processed samples, apart from at 20 wt%, where the powder samples displayed extremely high shear thinning. The reversal in relative magnitudes of elastic and viscous moduli at 20 wt% loading revealed that the percolation threshold had been reached at a loading between 10 and 20 wt%. The percolation threshold is the loading at which a network between fillers may be formed, or can be thought of as the transition from liquid-like to solid-like behaviour.

Permeability studies revealed that the addition of 1 wt% GNP in a nanocomposite sandwich structure did not appreciably alter the transport of CO_2 or H_2S through PA11. The activation energies for permeation of CO_2 were extracted and appeared to be substantially lower than those found in the literature, probably due to differences between PA11 grades and the melt blending step.

CHAPTER 5: GRAPHENE COATINGS

5.1 INTRODUCTION

In this chapter, instead of combining graphitic materials within the polymer matrix, and the associated problems including voiding and mechanical instability, the application of graphene coatings were investigated. The application of CVD graphene coatings to the surface of PA11 was explored as a route to producing barrier films without sacrificing the mechanical properties of the PA11.

5.2 LITERATURE REVIEW

5.2.1 CVD GRAPHENE SYNTHESIS

The production of large areas of high quality, pristine graphene can be achieved through the bottom-up process of CVD of carbon radicals upon transition metal substrates, typically nickel or copper.[182–186] A number of other studies have also been carried out on nickel-copper alloys,[187] nickel-molybdenum alloys,[188] cobalt,[189] ruthenium,[190] palladium,[191] rhenium,[192] iridium,[193] and platinum.[194] Generally, the transition metal foil, upon which the CVD is applied, is annealed under a reductive H_2 containing atmosphere at around 1000 °C. This process allows surface morphology rearrangement, reducing the number of structural defects, introducing atomic steps and increasing the grain size.[195] The process also removes natural impurities from the metal surface, such as CuO and Cu_2O for copper substrates, thus increasing the catalytic activity of the metal employed. The annealing stage is therefore critical for the production of large graphene sheets, as the nature of the CVD graphene is largely dictated by the crystal structure of the metal substrate.[196] The annealing step is then followed by the introduction of a methane (hexane, ethanol, ethylene, acetylene and other hydrocarbons have also been investigated) containing atmosphere which decomposes, allowing carbon radicals to be adsorbed by the metal.[184,197–199] At the reaction temperatures, carbon has a degree of solubility, which allows it to diffuse into the metal surface. Upon cooling, the solubility is reduced, leading to aggregation of carbon atoms upon the metal surface, for nickel substrates, the high solubility leads to high concentrations of surface carbon, thus, single to multi layered graphene is common. For copper on the other hand, the lower solubility of carbon and self-limiting nature of the copper surface means that

mostly single layer graphene is produced – up to 100 % monolayer coverage has been reported.[200]

The exact catalytic mechanism for the CVD of graphene upon metal substrates is still not fully understood and studies are ongoing. The role of oxygen in suppressing graphene nucleation site numbers leading to the production of centimetre scale, single domain graphene has been reported by Hao *et al.*[201] of the Ruoff group. The copper substrate was annealed in oxygen for up to five minutes leading to a graphene nucleation density of approximately 0.01 mm^{-2}, a reduction of five orders of magnitude compared to oxygen-free copper, with a nucleation density of 2×10^3 mm^{-2}. This decrease in nucleation, leading to the increase of individual crystal sizes, up to the centimetre scale, was attributed to oxygen passivation of active sites that would have otherwise been nucleation sites for graphene crystals.

Conventional CVD methods, however, provide polycrystalline graphene,[202] containing grain boundaries between graphene crystals growing in various orientations. Grain boundaries are known to allow for the transport of moieties through a graphene film,[203] and so the eradication of grain boundaries should result in better barrier performance. The production of large scale, single crystal graphene can be achieved through two pathways: limiting nucleation sites so large crystals can grow,[201,204] or; aligning the crystals so graphene islands spreading from different nuclei, can stitch together to form single grain graphene.[205,206] Lee *et al.*[205] produced single crystal graphene on a reusable 45 mm diameter Si wafer with a hydrogen terminated germanium coating. The method yielded single crystal graphene with an area of approximately 16 cm^2. Alternatively, a copper substrate was used,[206] the authors repeatedly annealed and polished the copper foil and reported single crystal graphene growth on a 6 × 3 cm substrate, yielding an area of approximately 18 cm^2.

5.2.2 CVD GRAPHENE TRANSFER

The transfer of CVD graphene is inherently tricky. Due to its delicate nature, CVD graphene cannot be transferred as a freestanding film and therefore must be applied either directly to the required substrate,[207–210] or transferred with a support for subsequent application.[210,211] One of the latter methods is PMMA transfer of graphene, based on a transfer method for carbon nanotubes.[212] PMMA mediated transfer is a four step method: firstly, PMMA is spin coated onto a CVD graphene layer, usually on a

copper surface; second, the copper substrate is etched away or separated;[213] third, the PMMA/CVD graphene film is applied to the required substrate; and finally, the PMMA is removed with an appropriate solvent or through heat treatment.[211] This method does have drawbacks, one of which is that the method leaves PMMA residues on the top surface of each CVD graphene layer.

An improved PMMA mediated transfer method was pioneered by Wang *et al.*[214] in 2011. Instead of coating each CVD graphene layer with PMMA prior to etching away the copper, they used a single PMMA coated CVD graphene structure and stacked the CVD graphene layers directly (Figure 5.1). Following the grey arrows through (a), (b), (c) and (d), it is possible to create a single CVD graphene layer deposited on an arbitrary substrate with PMMA residues remaining on the top surface. Any additional CVD graphene layers would each introduce more PMMA residues as the layer number increased. However, by following the grey arrows through (a), (b), (c) and then by cycling between (c) and (a) *n* times (red arrows), *n* CVD graphene layers can be deposited on a single PMMA coating. These *n* layered CVD graphene stacks, with no interlayer PMMA residues can be deposited onto arbitrary substrates as shown by step (d).

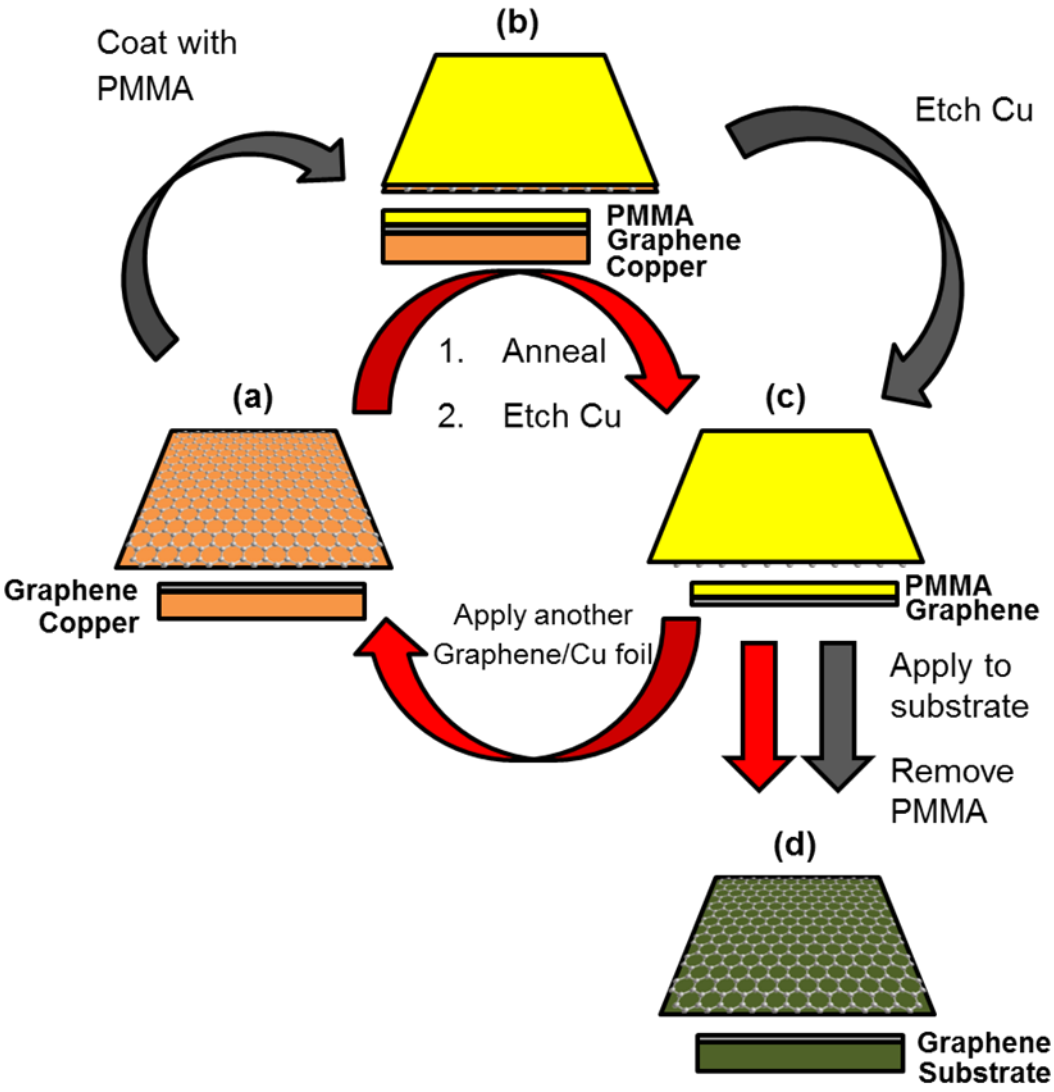

Figure 5.1. Schematic of traditional (grey arrows only) and improved (red arrows) CVD graphene transfer. Traditional transfer follows: (a), (b), (c), (d). Improved transfer follows: (a), (b), (c), *n*[(a) (c)], (d); where *n* is the number of cycles of [(a) (c)].[214]

5.2.3 CVD Graphene Barrier Performance

A single layer of defect free graphene has been proven to be a perfect barrier layer to helium,[9,10] by extension, it seems possible that CVD graphene could be produced in such a way as to yield perfect barrier performance. However, as laid out above, even if defect free CVD graphene were produced, there would almost certainly be defects imparted during transfer. Regardless of this, studies have investigated the application of CVD graphene to various polymer substrates in order to impart a better barrier properties.[203,215–221] Liu *et al.*[216] found that two or more CVD graphene layers protected against oxygen degradation of solar cells. Kim *et al.*[215] noted that the permeability of

poly(1-trimethylsilyl-1-propyne) decreased with increasing number of graphene layers, however, perfect barrier performance could not be achieved due to inherent CVD graphene defects and gaps between the graphene layers. This allowed the group to tailor the graphene system in order to selectively transport gases. Wirtz *et al.*[217] applied up to three layers of CVD graphene to a PET substrate and observed a reduction in oxygen permeability of 67% (Figure 5.2). They also compared different PMMA transfer methods, providing evidence that conventional transfer methods leave PMMA residues between CVD graphene layers, in agreement with data provided by the method pioneers.[214] Choi and co-workers went further, investigating the WVTR of PET films with up to six CVD graphene layers, using the improved PMMA mediated transfer method (Figure 5.2).[203]

A comparison of the reduction in WVTR and oxygen permeability from the work of Choi *et al.*[203] and Wirtz *et al.*[217], respectively, can be seen in Figure 5.2. The data suggest that transport of fluids across a CVD graphene barrier coating decreases quickly with increasing number of applied graphene layers. The data also suggest, however, that two or more layers of CVD graphene are required to observe a significant decrease. Interestingly, the reduction in oxygen permeability with three layers of CVD graphene is comparable to the reduction in WVTR with four layers of CVD graphene. This implies that the effect of increasing CVD graphene layers affects the transport of oxygen more than water. This could be due to the kinetic diameters of the two molecules: oxygen has a kinetic diameter of 3.46 Å,[222] whereas water has a smaller kinetic diameter of 2.68 Å.[223] This would mean that oxygen molecules may find that larger defects are shielded more effectively upon the application of another layer of CVD graphene. The smaller water molecules, on the other hand, are able to diffuse more readily through smaller defects that are likely to be more accessible for the same level of CVD graphene coating. There may also be differences in the quality of CVD graphene produced by each group, however, as both groups adopted the same transfer method, defects created through transfer should be of a similar nature.

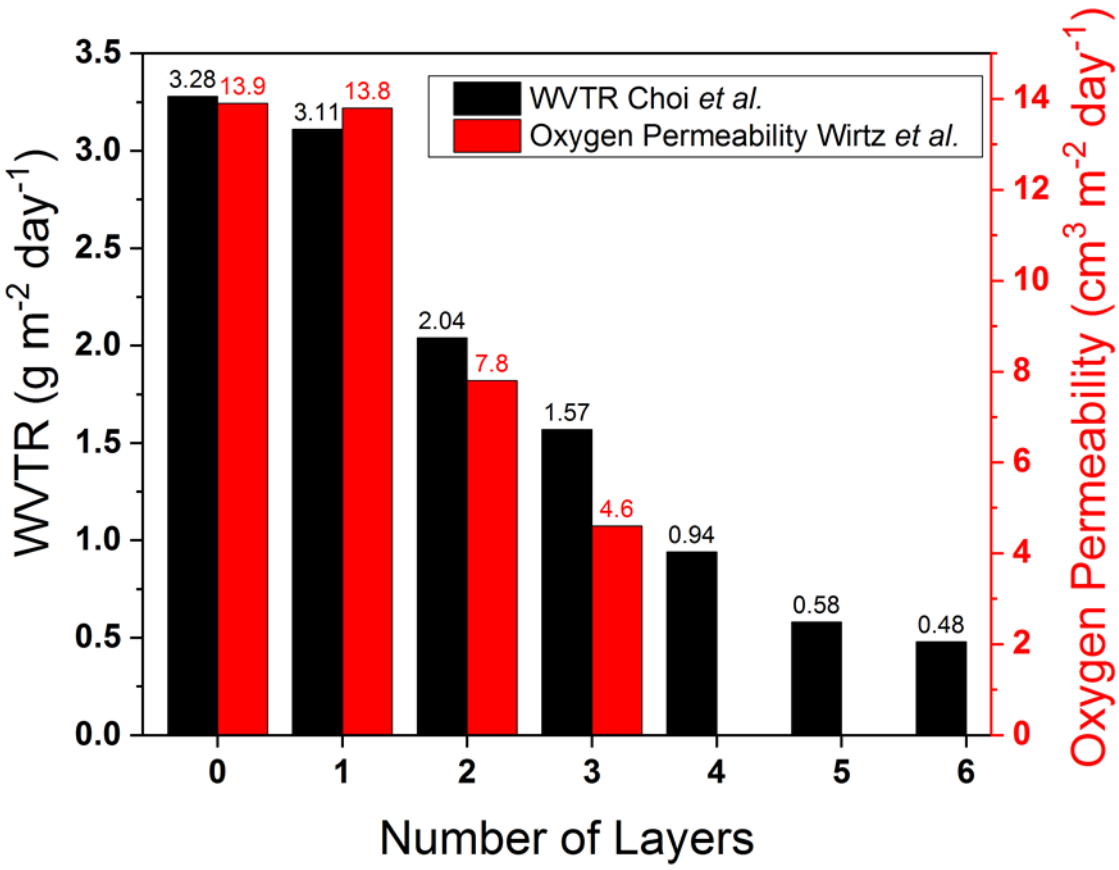

Figure 5.2. Plot showing the variation of WVTR and oxygen permeability with the number of applied CVD graphene layers. Data combined from Choi *et al.*[203] and Wirtz and co-workers.[217]

Recently, T. Seo *et al.*[218] investigated the effect of CVD graphene growth methods on the gas barrier properties of PET films. Through tailoring the CVD graphene deposition method, they were able to reduce the WVTR of PET film by 58% using a single CVD graphene layer.[218] Comparing this achievement to the 5% reduction in WVTR for a single CVD graphene layer in the work of Choi *et al.*[203], it is clear that differences in CVD graphene synthesis have a remarkable effect on the permeability. Unfortunately T. Seo *et al.*[218] did not study the change in WVTR with stacked graphene sheets. Seethamraju *et al.*[219] observed a six orders of magnitude decrease in WVTR for CVD graphene coated Surlyn® polymer. The group attributed the extraordinary barrier performance of their system to the transfer method used. The Surlyn® was directly applied to the CVD graphene by melt casting and subsequent etching rather than PMMA mediated transfer as used by Choi and co-workers and T. Seo and co-workers.[203,218] H. Seo *et al.*[220] encapsulated CVD graphene coated PET with polydimethylsiloxane (PDMS) and measured the WVTR. Compared to a graphene free encapsulated PET film, the WVTR was reduced by 84%, 89% and 95% for two, four

and six CVD graphene layers, respectively. Very recently, the CO_2 barrier performance of PDMS was improved by 30% by coating with two CVD graphene layers, only a modest decrease in permeability was observed with one CVD graphene layer.[221]

5.3 Aims and Objectives

It was the aim of this work to characterise PA11 coated with CVD graphene and investigate the permeability of the coated samples to CO_2 and H_2S under a range of conditions.

The CVD graphene coverage was established through Raman mapping of the graphene 2D peak, along with optical microscopy. The CVD graphene coverage following testing was also evaluated by the same methods.

5.4 Materials and Methods

5.4.1 Polyamide 11

PA11 was sourced from Arkema Inc., Colombes, France, provided by NCC Ltd., Ireland, under the Rilsan® trade name. Rilsan® PA11 BMNO injection moulded plaques (100 × 100 × 2 mm) were provided. Some control disks were cut from the plaques and some plaques were stencilled on one side, leaving a membrane of PA11 intact as shown in Figure 5.3.

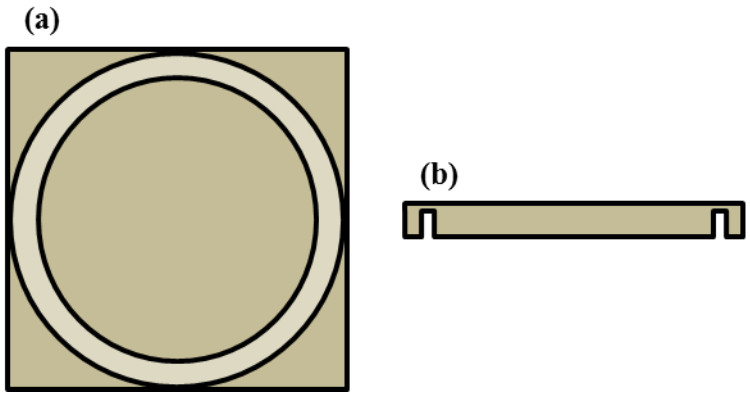

Figure 5.3. Schematic of stencilled PA11 plaque, (a) as seen from above and (b) as a cross-section.

5.4.2 *Polyethylene Terephthalate*

PET was sourced from Goodfellow Ltd., Huntingdon, UK.

5.4.3 *Polymethyl Methacrylate Solution*

PMMA solution in anisole, 'PMMA4A', was provided by MicroChem Corp., USA.

5.4.4 *CVD Graphene*

CVD graphene was grown and transferred onto PA11 by 2-DTech Ltd., Manchester. The CVD graphene growth was performed on a Cu substrate, resulting in mostly monolayer coverage. The full transfer technique used was not revealed, however, it is known to be a PMMA mediated, wet transfer method. Similar methods can be found in the literature (section 5.2.2). Additional CVD graphene was grown and transferred in-house onto PA11 disks for characterisation.

5.4.5 *CVD Graphene Coated Polyamide 11 Disks*

CVD graphene coated PA11 disks were prepared by cutting around stencilled PA11 plaques coated in CVD graphene. PA11 disks with full CVD graphene coverage could then be popped out of the plaque, as shown in Figure 5.4.

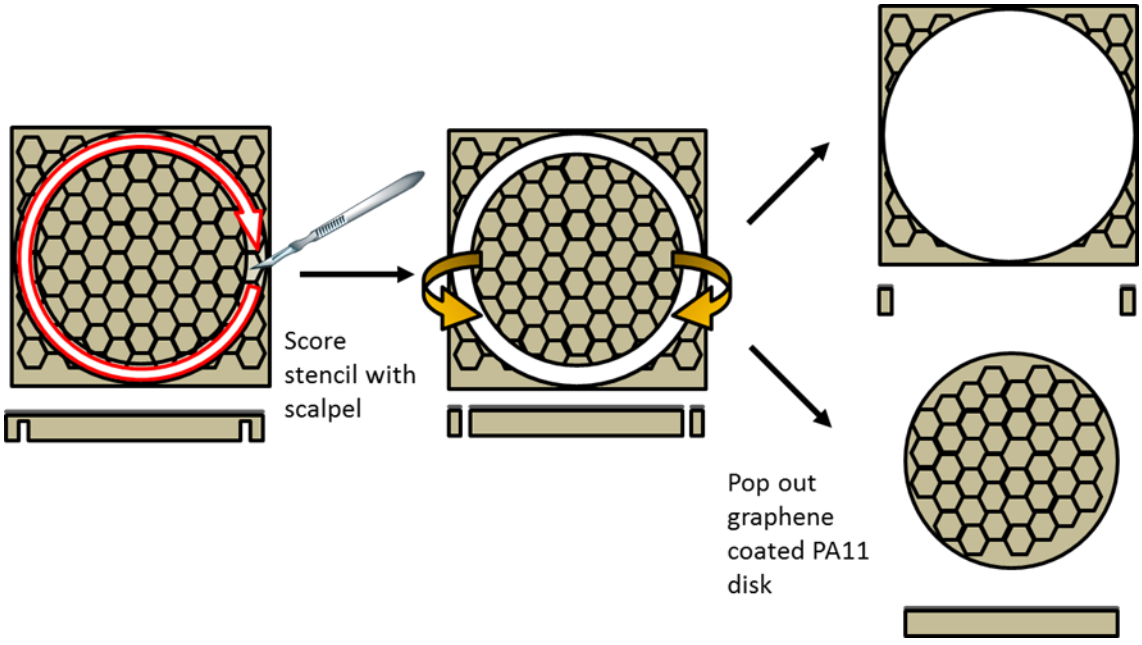

Figure 5.4. Schematic showing the removal of a CVD graphene coated PA11 disk from a CVD graphene coated plaque.

5.4.6 *In-House CVD Graphene Transfer*

In-house grown CVD graphene was applied to PA11 as shown in the schematic in Figure 5.5.

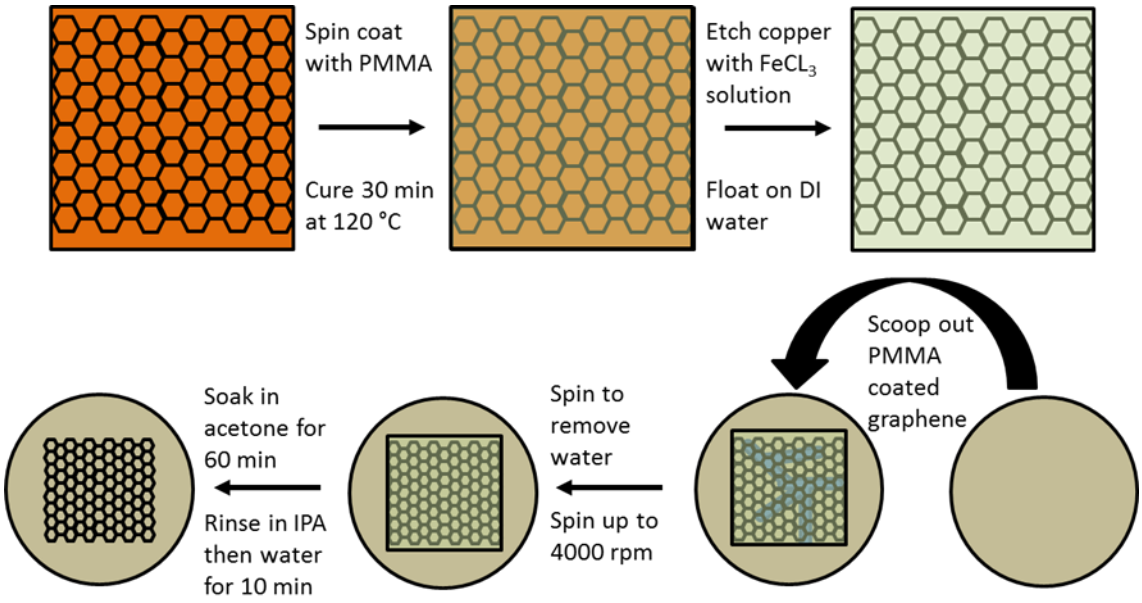

Figure 5.5. Schematic showing the process of PMMA coating CVD graphene, copper etching, scooping out PMMA coated CVD graphene, drying and PMMA removal.

First, the CVD graphene coated copper foil was taped down on a glass slide and loaded into a spin coater. PMMA solution in anisole (0.8 mL) was dropped onto the centre of the CVD graphene copper foil and spun on a dynamic programme up to 4000 rpm. The foil was then removed from the glass slide, placed onto a hot plate and heated at 120 °C for 30 min to cure the PMMA. The PMMA/CVD graphene/copper foil was then floated carefully on a 3:1 by weight DI water:$FeCl_3$ solution. The sample was allowed to etch overnight until no copper was visible to the naked eye beneath the PMMA/CVD graphene film. The film was scooped out of the clear, dark orange $FeCl_3$ solution with a clean silicon wafer, and floated on DI water to rinse. This rinsing process was repeated until the DI water remained clear and colourless upon floating the film. The film was then scooped out of the DI water with a polymer disk, ensuring that the film was as flat as possible and wrinkle-free. The PMMA/CVD graphene coated polymer was placed in the spin coater and spun up to 4000 rpm until the film was visibly water-free and flat. The dry sample was then dropped carefully into an acetone bath for 60 min, which dissolved the PMMA from the CVD graphene surface. The CVD graphene coated

polymer was then rinsed in IPA for 10 min, DI water for 10 min and then blown dry with dry nitrogen.

5.5 Characterisation Methods

5.5.1 Raman Mapping

Raman spectroscopy was carried out on a Renishaw inVia Raman Microscope equipped with 514 or 633 nm laser at a power suitable to sample stability. Spectra and optical microscope images were collected through Leica N Plan EPI objectives.

Mapping measurements were performed using the mapping function within the Wire 4.2 software. An example map was performed as follows: the sample surface is focussed using the laser spot as a guide. This initial point is set as the origin and the focussed point is used to start generating a surface, which records the *x*, *y* and *z* coordinates of each surface point. Perfectly focussed points, by laser spot, are taken at 50 µm intervals, with each point being added to the generated surface. Once all points across the mapped area (for a 200 × 200 µm map, 25 surface measurements at 50 µm intervals would be taken), an optical microscope montage (stitched optical microscope images) of the sample is gathered, across the sample area of interest. Once the montage is complete, a map is drawn out on the montage, following the generated surface, at reasonable scan intervals. For detailed maps, a step size of 1 – 2 µm was selected, however, for large maps, step sizes were increased accordingly. To map CVD graphene coverage on a PA11 surface, only the Raman shift corresponding to the 2D peak was evaluated in order to save scanning time, so that large maps could be carried out in an appropriate time frame. The laser power was reduced to 10%, approximately 1 mW at the sample surface with 50× objective, in order to maintain sample stability. The spot size at perfect focus was of the order 5 µm across. A 10 s integration time was selected to provide data with an adequate signal to noise ratio. Mapping experiments typically took 24 – 72 h to complete, dependent upon the scan size and required exposure time. Following map acquisition, the data was treated in the Wire 4.2 package. Firstly, a cosmic ray removal was performed followed by a baseline subtraction to remove PA11 fluorescence from the data. The 2D peak was then fitted and the generated mapping data

was exported to Origin where further analysis was continued. ImageJ software was used to convert the mapping data into a binary format for coverage analysis.

The spatial resolution for the Raman mapping was limited by the relatively large laser spot size, on the order of 5 μm diameter. The mapping of nanoscale defects could therefore not be carried out; however, the general coverage on the microscale could be probed.

5.5.2 Scanning Electron Microscopy

SEM was carried out on a FEI Quanta 650 FEG ESEM equipped with a Bruker X-Flash EDS detector which was used to collect characteristic X-rays during energy dispersive X-ray (EDX) elemental analysis.

5.5.3 UV-Visible Spectroscopy

UV-Vis spectroscopy was carried out using a Varian Cary UV-Vis-NIR Spectrophotometer on thin film samples.

5.5.4 Chapter Specific Permeability Testing

Permeability testing was carried out on a purpose built, high pressure barrier rig at TWI Ltd., Cambridge (more details in section 4.5.4). Samples were placed in the cell with the CVD graphene coating in the upstream feed fluid direction. A protective BMNO (manufacturer's code) PA11 gasket was placed on top and the cell was closed tightly. The gasket protected the CVD graphene from becoming deformed during cell closure. Two CVD graphene coated samples were run alongside two uncoated BMNO samples as controls. The cells were then placed into an oven at 60 °C and allowed to equilibrate. The samples were exposed to CO_2 with 1.48% H_2S at 5 MPa (gas) and reached the steady state which was maintained for six days. One sample each of CVD graphene coated BMNO and control BMNO were removed. The remaining samples were exposed to 10 MPa CO_2 with 1.48% H_2S at 60 °C (supercritical) and reached the steady state, which was maintained for thirteen days. Testing ran for a total of four weeks.

Four additional BMNO controls were run without gaskets at 5 MPa CO_2 with 1.48% H_2S and 60 °C (gas). The steady state was maintained for six days and testing ran for a total of eight days. One additional CVD graphene coated plaque was tested with a gasket at 5 MPa and 60 °C (gas). The steady state was maintained for fourteen days and testing ran for a total of three weeks.

Two CVD graphene coated BMNO samples and one control BMNO were also exposed to pure H_2S at 0.2 MPa pressure and 60 °C (gas). The steady state was maintained from nine days to four weeks and testing ran for up to six weeks.

Standard deviations were calculated according to Equation 3.7.

5.6 Results and Discussion

5.6.1 Pre-Test Characterisation

Raman mapping of the characteristic graphene 2D peak provided an indication of the CVD graphene coverage. As can be seen in Figure 5.6, good CVD graphene coverage on the in-house transferred samples was observed. The CVD graphene coating can be seen in Figure 5.6a as a bright region, the edges are highlighted by yellow arrows to guide the eye. Expanding the central region at higher magnification (Figure 5.6b) shows the scratched and pock-marked PA11 surface in more detail. Figure 5.6c shows the mapping region onto which the 2D peak map can be superimposed (Figure 5.6d). As can be seen in Figure 5.6d, the CVD graphene coating was not completely continuous. Dark regions signify areas where no 2D peak could be detected. It is worth noting that this Raman map was not generated using curve fitting as the process could not be completed on such a large file. Therefore, a signal to baseline measurement was taken at the 2D peak position. This means that the Raman 2D peak signal is likely to slightly overestimate the coverage of the CVD graphene.

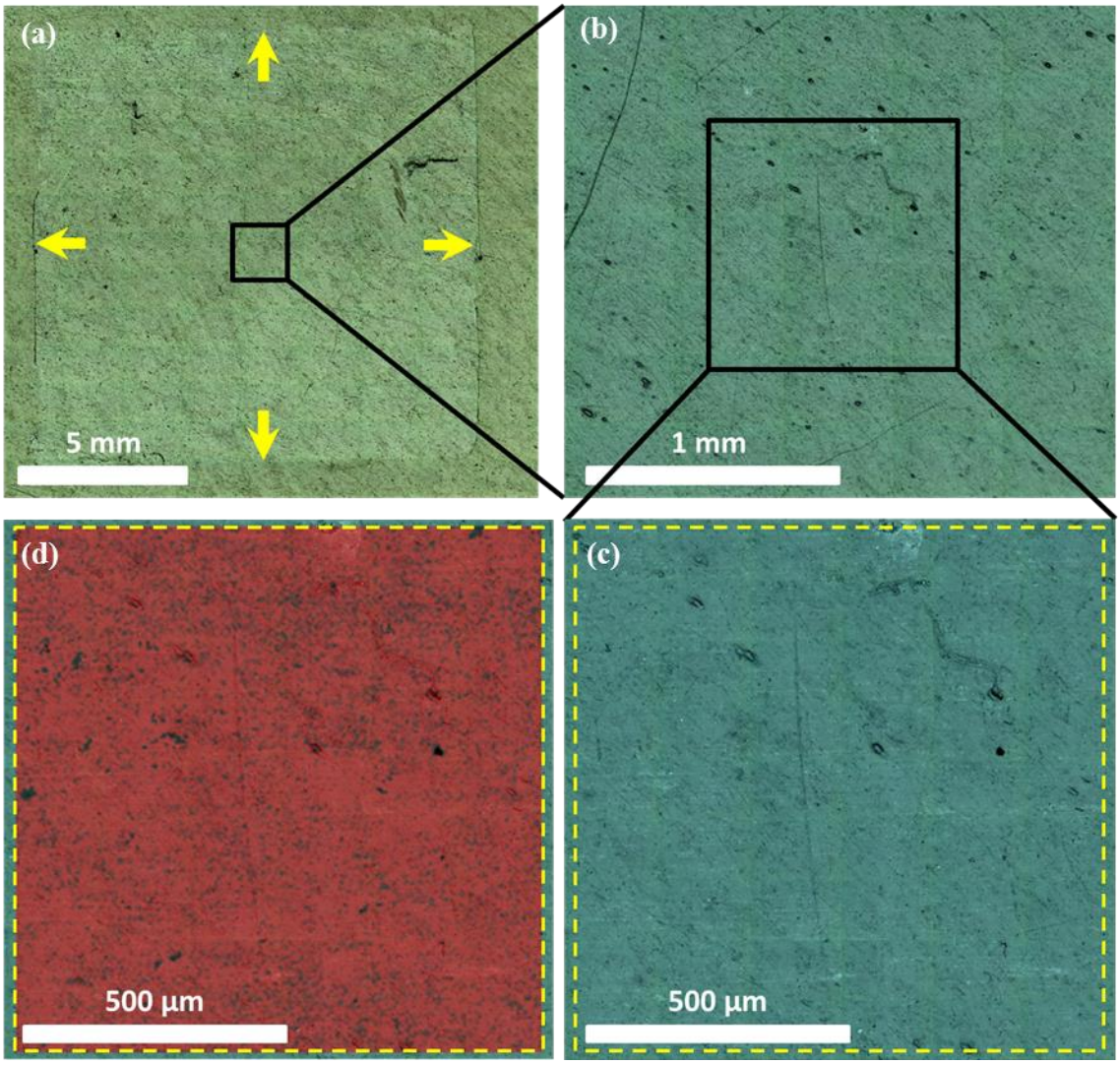

Figure 5.6. Optical microscope images of in-house transferred CVD graphene with Raman 2D peak mapping. (a) Optical microscope image of the sample surface, the yellow arrows guide the eye to the edge of the CVD graphene. (b) Central region at higher magnification. (c) Central region at highest magnification and Raman mapping region highlighted by dashed box. (d) Superimposed Raman 2D peak map at a spatial resolution of 5 µm.

Optical and Raman images of the CVD graphene coverage on a fully coated 40 mm disk, 'CVD3', are shown in Figure 5.7. Figure 5.7a shows the magnified central 1 cm^2 and the inset shows the whole 40 mm disk, mounted on a glass slide. Figure 5.7b shows the scratched and pock-marked surface in more detail. A contrast adjusted white light image of the Raman mapped region is shown in Figure 5.7c, which shows both bright and dark regions. The brightest regions were associated with a very high 2D signal and may be due to tearing or wrinkling of the CVD graphene during transfer.[224] The bright

and dark regions correspond to the regions with and without CVD graphene coverage, respectively, as shown by the Raman 2D peak map in Figure 5.7d. The 2D peak map shows that the CVD graphene coverage is quite poor for CVD3.

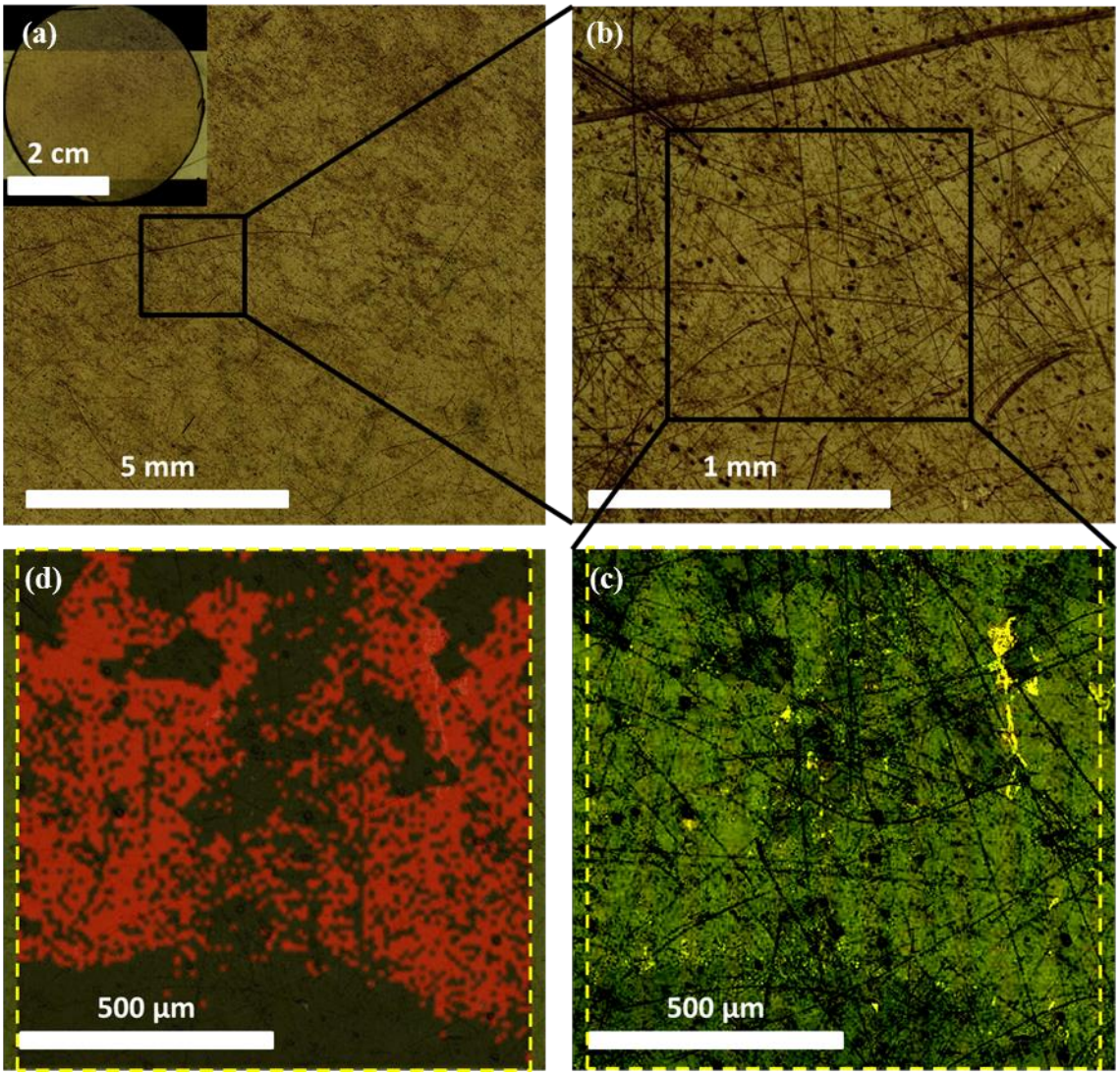

Figure 5.7. Optical microscope images of CVD3 with Raman 2D peak mapping. (a) Optical microscope image of the sample surface, inset shows whole 40 mm diameter disk. (b) Central region at higher magnification. (c) Contrast adjusted central region at highest magnification and Raman mapping region highlighted by dashed box. (d) Superimposed Raman 2D peak map at a spatial resolution of 10 µm.

Optical and Raman images of 'CVD4' are shown in Figure 5.8. Figure 5.8a is a contrast adjusted white light image showing where CVD graphene is expected to be present (bright areas). The macroscopic CVD graphene coverage appears to match with the Raman 2D peak map in Figure 5.8b and detailed 2D peak map in Figure 5.8d. As can be

seen in the high magnification white light image (Figure 5.8c), the bright areas match with the 2D peak map in Figure 5.8d.

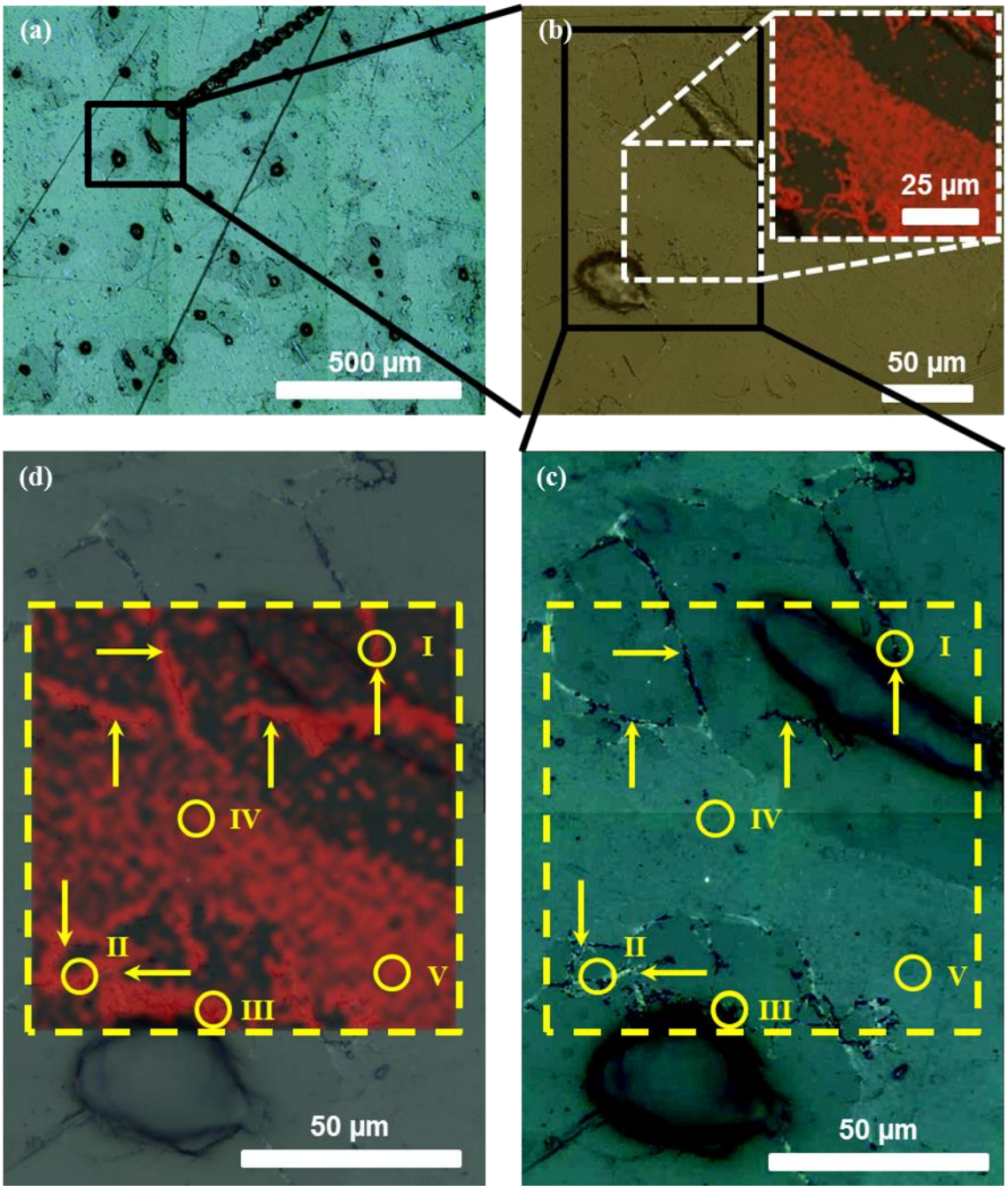

Figure 5.8. Optical microscope images of CVD4 with Raman 2D peak mapping extracted from Raine *et al.*[164]. (a) Contrast adjusted white light image of the sample surface. (b) Magnified region with Raman map inset. (c) Contrast adjusted centre and mapping region highlighted by dashed box. (d) Raman 2D map at a spatial resolution of 10 µm. Arrows identify possible torn or rolled graphene. Positions I – V correspond to Raman spectra in Figure 5.9.

It is interesting that the dark surface marks in Figure 5.8a were associated with poor CVD graphene coverage. The magnified white light image in Figure 5.8c shows that the surface marks were out of focus, which suggested that they protruded out of the surface. These rough regions may have led the CVD graphene to be torn upon transfer, an effect observed in the literature for CVD graphene transfer onto PET.[224] Figure 5.8d shows that some strong 2D peaks were observed around the high regions, which may be associated with rolled up or wrinkled CVD graphene membranes (arrows highlight possible rolled-up regions). Representative Raman spectra taken at positions I – V are shown in Figure 5.9.

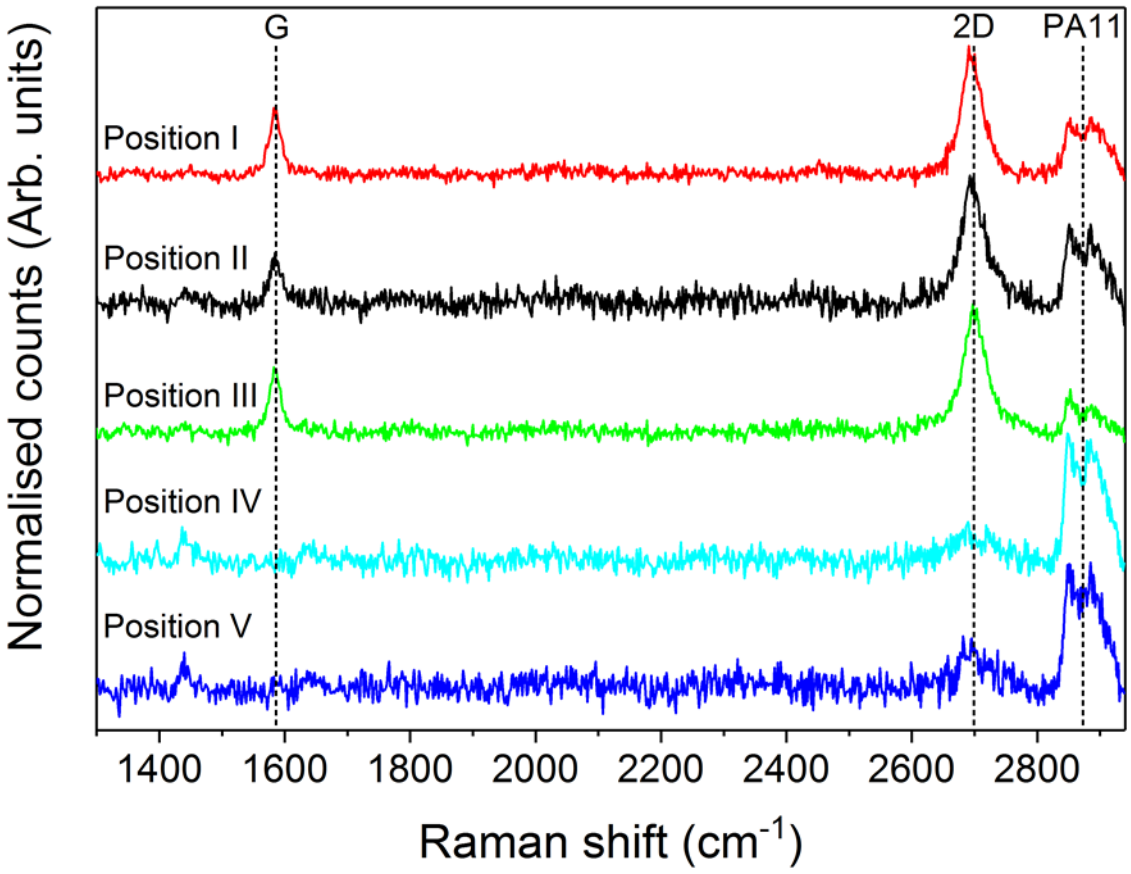

Figure 5.9. Raman spectra at 514 nm irradiation taken at positions I – V in Figure 5.8. Modified from Raine *et al.*[164].

Positions I, II and III were taken at positions where the graphene appeared to be rolled up or had a thin membranous appearance. Positions IV and V were taken on planar, continuous graphene regions. As can be seen in Figure 5.9, the 2D peak was substantially higher for the membrane-like regions (I – III) than for the planar regions

(IV and V). The I(2D)/I(G) ratios for the membranous graphene regions were one to two which is lower than expected for typical monolayer graphene.[81] The I(2D)/I(G) could not be measured for the planar region due to the weak nature of the peaks.

The Raman 2D peak maps are likely to underestimate the CVD graphene coverage. As the PA11 sample surfaces were quite rough, long range focussing on the CVD graphene layer was challenging, and therefore it is possible that weak 2D signals were lost in the noise. However, the way that the 2D peak map matches up with the contrast adjusted optical microscope image in Figure 5.8c, at least aids the identification of CVD graphene deficient areas.

Converting the 2D peak maps into binary images and counting the pixels provides a quantitative estimate for the CVD graphene coverage area (Figure 5.10).

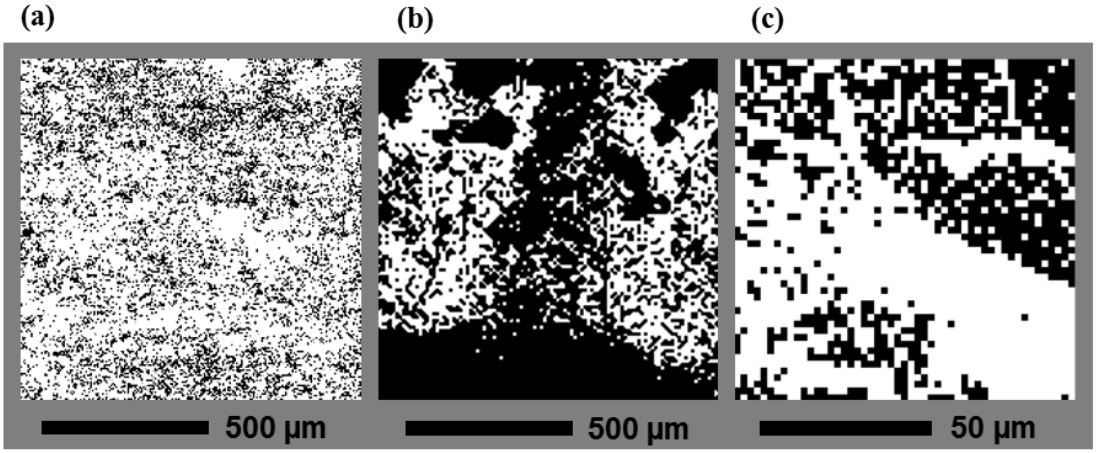

Figure 5.10. Binary conversions of the Raman maps in order to quantify the CVD graphene coverage achieved, white pixels are where a 2D peak was measured. (a) In-house CVD graphene coated PA11; (b) CVD3; (c) CVD4.

In-house transferred CVD graphene coated PA11 had coverage of 75%, whereas CVD3 had coverage of only 35%. CVD4, however, had coverage of 64%, which approached that of in-house transferred CVD graphene. The coverage of CVD graphene observed for CVD3 and CVD4 may be underestimated as focussing on the CVD graphene surface was challenging so the actual coverage may be much higher.

5.6.2 *Post-Test Characterisation*

5.6.2.1 *Polymer Yellowing*

Despite the apparent poor CVD graphene coverage, the CVD graphene coated PA11 disks were tested for their barrier performance, which will be described later in the chapter.

One particularly interesting observation of the PA11 samples following their exposure to CO_2 with 1.48% H_2S fluid is the marked yellowing of the samples. This is shown in the photographs in Figure 5.11 and occurred for all PA11 samples, regardless of the presence of CVD graphene (Figure 5.11c and d). As can be seen, the off-white semi-transparent PA11 disks and gaskets in Figure 5.11a and b developed a yellow centre following exposure to the test fluid (Figure 5.11a, c and d). Although only the central approximately 0.8 cm^2 (1 cm diameter) was exposed to the fluid, there was clearly yellowing outside of this region.

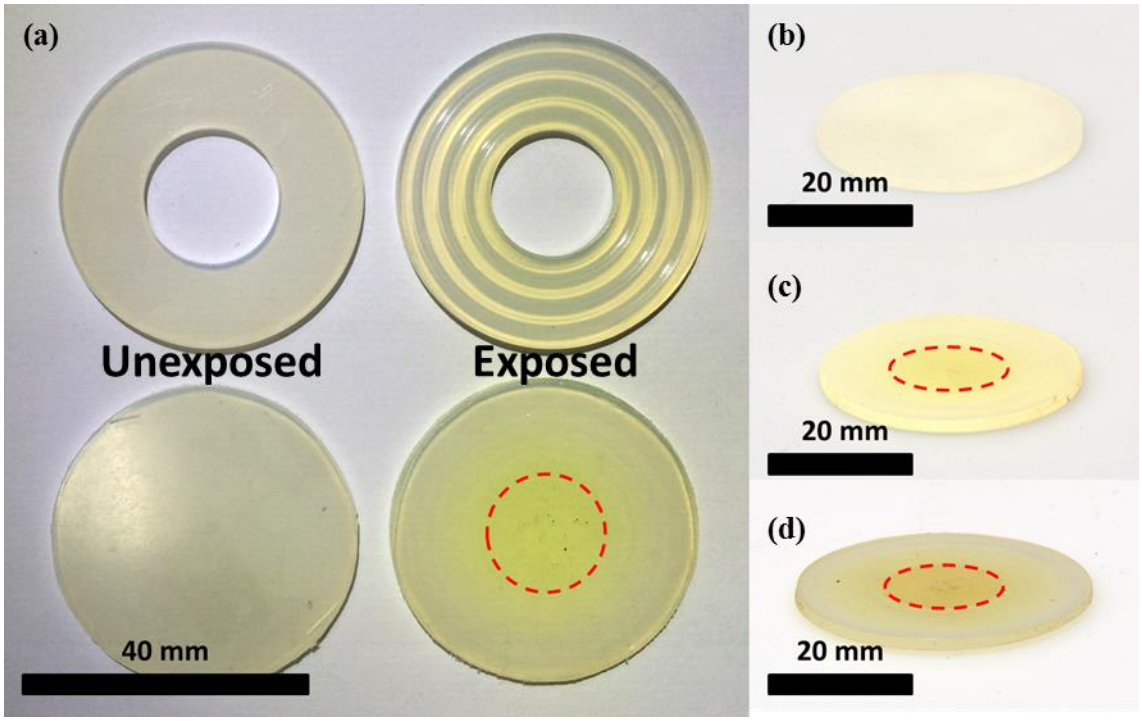

Figure 5.11. Photographs of PA11 samples before and after exposure to CO_2 with 1.48% H_2S fluid – directly exposed regions are highlighted by red dotted ellipses. (a) Unexposed and exposed CVD coated PA11 disks and protective gaskets; (b) unexposed PA11 disk; (c) exposed PA11 control disk; (d) exposed CVD coated PA11 disk (CVD1).

It was hypothesised that H_2S was being scrubbed from the feed fluid. In order to probe this, a range of experiments were carried out.

Firstly, the high pressure CO_2 with 1.48% H_2S mix was replaced for a pure 0.2 MPa H_2S feed. This was done in order to rule out possible effects related to the presence of high pressure CO_2. It also allowed the testing of thinner PA11 samples that could be analysed by UV-Vis spectroscopy. As can be seen in Figure 5.12, a thin PA11 film after exposure to 0.2 MPa H_2S for eighteen days develops an absorbance at 250 – 320 nm, with a peak absorbance at between 260 and 270 nm. The insets show a thin PA11 film with low level of yellowing that could be detected by UV-Vis spectroscopy as well as sulphur absorption spectra found in the literature.[225]

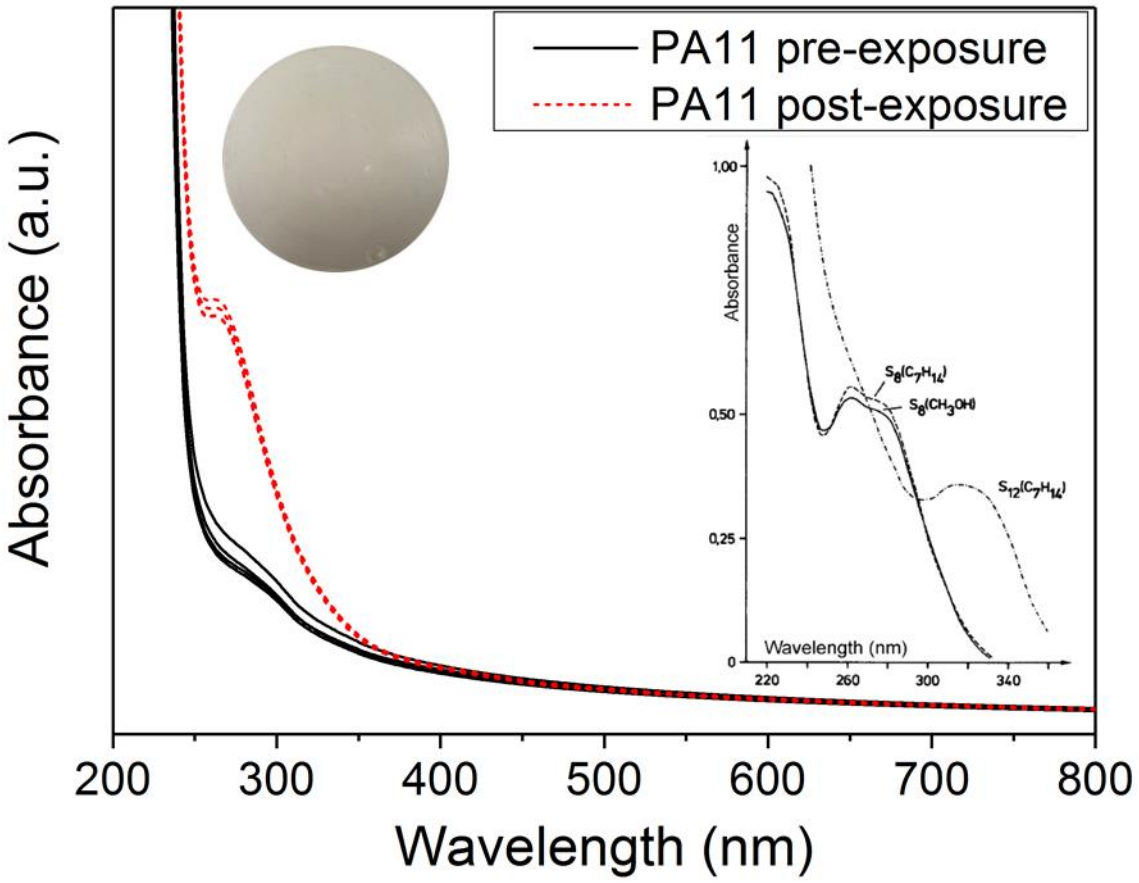

Figure 5.12. UV-Vis spectroscopy of control PA11 (pre-exposure) and PA11 exposed to 0.2 MPa H_2S gas. Insets show a yellowed thin film PA11 sample after exposure to 0.2 MPa H_2S and example of UV-Vis absorption of sulphur.[225]

The observed absorbance was compared to the absorbance of elemental sulphur dissolved in ethanol, shown in Figure 5.13. As can be seen, the absorption profile of the H_2S exposed PA11 (with control PA11 absorption removed) had a very similar shape to that of elemental sulphur in ethanol. This suggested that there was a mechanism for the conversion of H_2S into sulphur within the PA11. The presence of sulphur in the H_2S exposed PA11 was also confirmed by elemental analysis, which showed a detection limit level of sulphur in the exposed PA11.

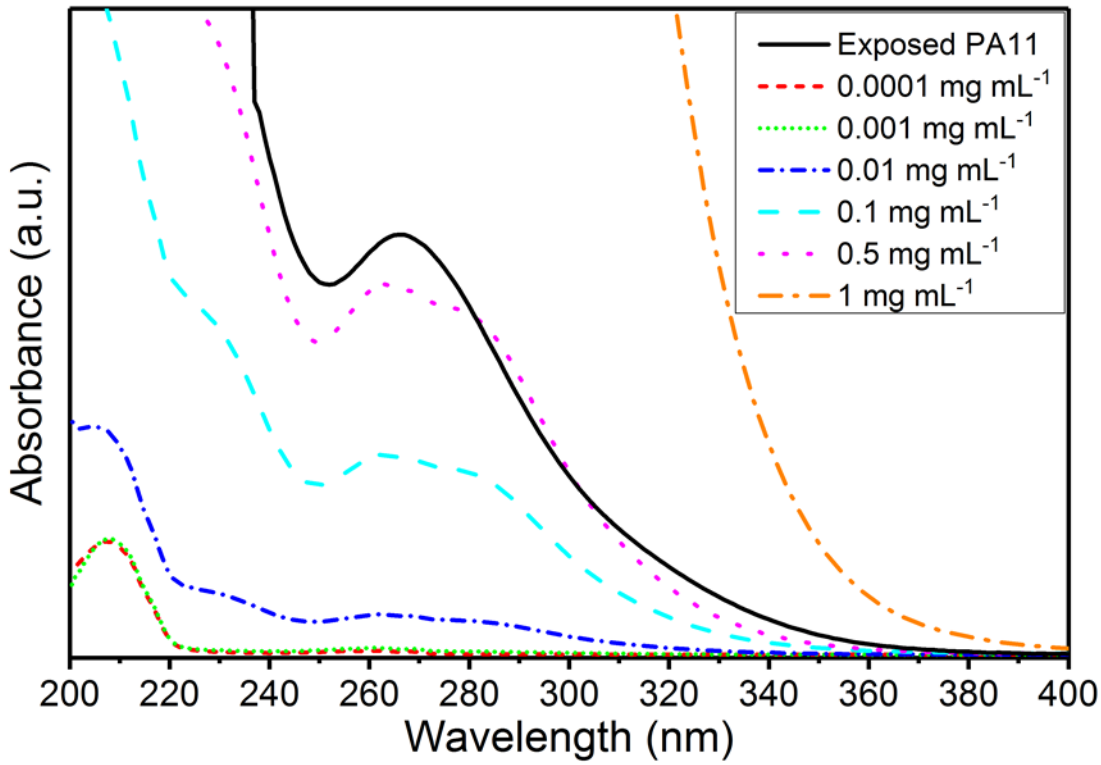

Figure 5.13. Variation of absorbance due to elemental sulphur dissolved in ethanol with concentration and comparison of PA11 exposed to H_2S.

By plotting the absorbance of sulphur in ethanol at 254 and 262 nm against concentration, an estimate of the concentration of sulphur captured in the PA11 was made (Figure 5.14). As can be seen, by reading off the absorbance at 254 and 262 nm for PA11 following exposure, a concentration × l range of 0.003 and 0.004 mol dm^{-3} cm was obtained. Division by the thickness of 200 µm reveals the effective concentration of 0.17 – 0.19 mol dm^{-3}. Working through this concentration for mass yields a concentration of 5.5 – 6.1 mg g^{-1}, that is 0.5 – 0.6 wt% sulphur in PA11.

PET and HDPE were also tested in order to see whether H_2S scrubbing was observed for polymers more widely. Thin film PET was tested and an increase in absorption could be seen following exposure, as shown in the UV-Vis spectra in Figure 5.15. 2 mm thick PET showed clear yellowing when tested as shown in the photograph in Figure 5.15, demonstrating that the sulphur evolution may be found in both polyamides and polyesters.

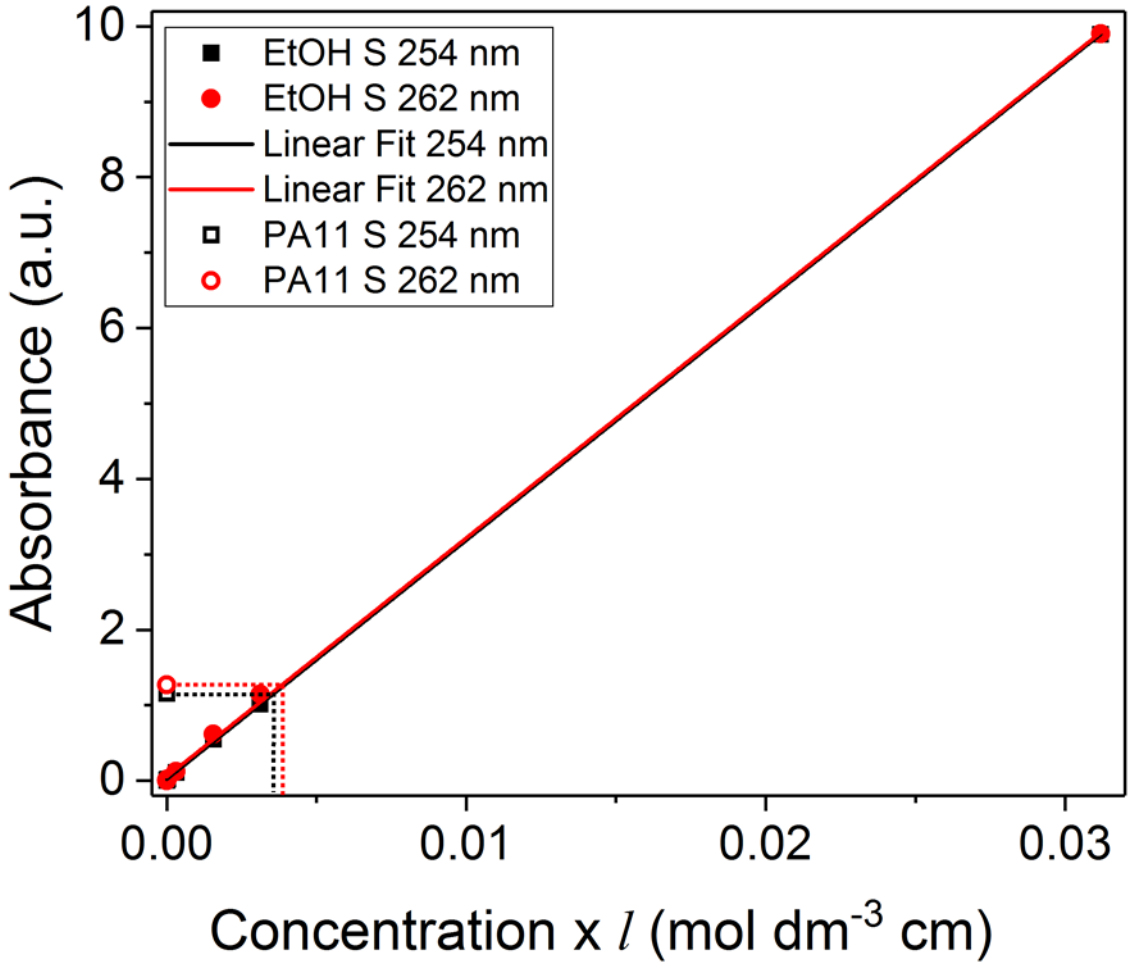

Figure 5.14. Plot of absorbance values for sulphur in ethanol at 254 nm and 262 nm with linear fitting. Equivalent concentrations for sulphur in PA11 are marked by dotted lines.

HDPE did not develop a yellow colour after exposure to H_2S by eye, however, due to its opaque nature, could not be tested with UV-Vis spectroscopy. H_2S scrubbing has not been described for PA11 or PET in the literature; however, there is a body of work

focussing on developing solid-state H_2S scrubbers.[226] It is known that good sour gas scrubbers contain nitrogen or oxygen functionality, often in the form of water soluble alkanolamines.[227,228] One patent describes the scrubbing of H_2S using silica particles covalently functionalised with polyallylamine, polyvinylamine or polyethyleneimine.[229] The scrubbing of moist or oxygen-containing H_2S streams with nitrogen-doped activated carbons yielded elemental sulphur, however, the role of oxygen is key.[226,230–234]

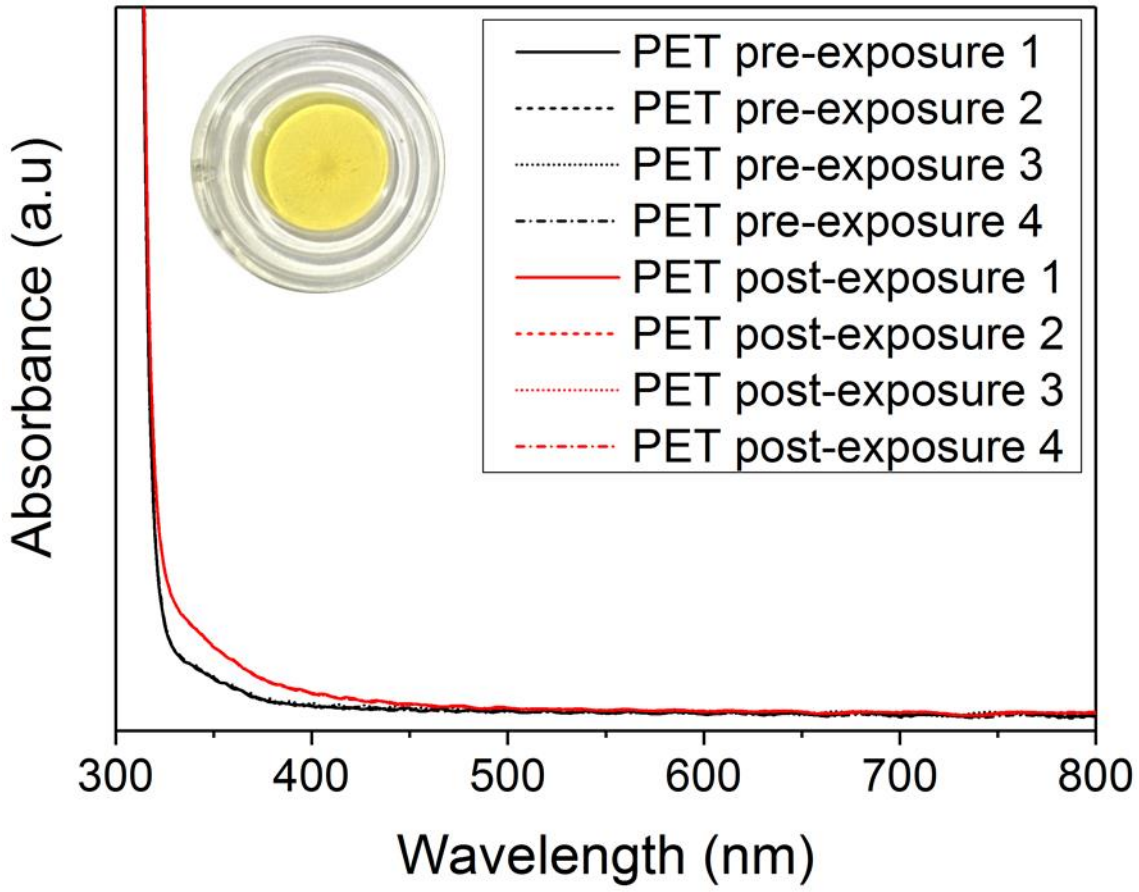

Figure 5.15. UV-Vis absorption profile of thin film PET for four different positions on the control and exposed film. Inset shows the colouration of 2 mm thick PET following testing.

It is suggested that the oxygen and nitrogen functionalities in the PET and PA11 are able to complex to the H_2S,[229,231–233] shown for PA11 in Figure 5.16. This complexed H_2S then undergoes oxidation by the reaction with oxygen dissolved in the polymer matrix. Although the concentration of dissolved oxygen may be very low, the samples did not go through a degassing step prior to exposure to H_2S, therefore, it is likely that

atmospheric oxygen would remain in the polymer. In H_2S scrubbers, it has been shown that close to stoichiometric quantities of oxygen and H_2S are required to oxidise H_2S to elemental sulphur.[235] In cases where oxygen is in excess, elemental sulphur oxidises further to SO_2, SO_3 and H_2SO_4.[234] In these experiments, H_2S is likely to be in excess compared to oxygen so the oxidation of H_2S would be unlikely to proceed beyond elemental sulphur.

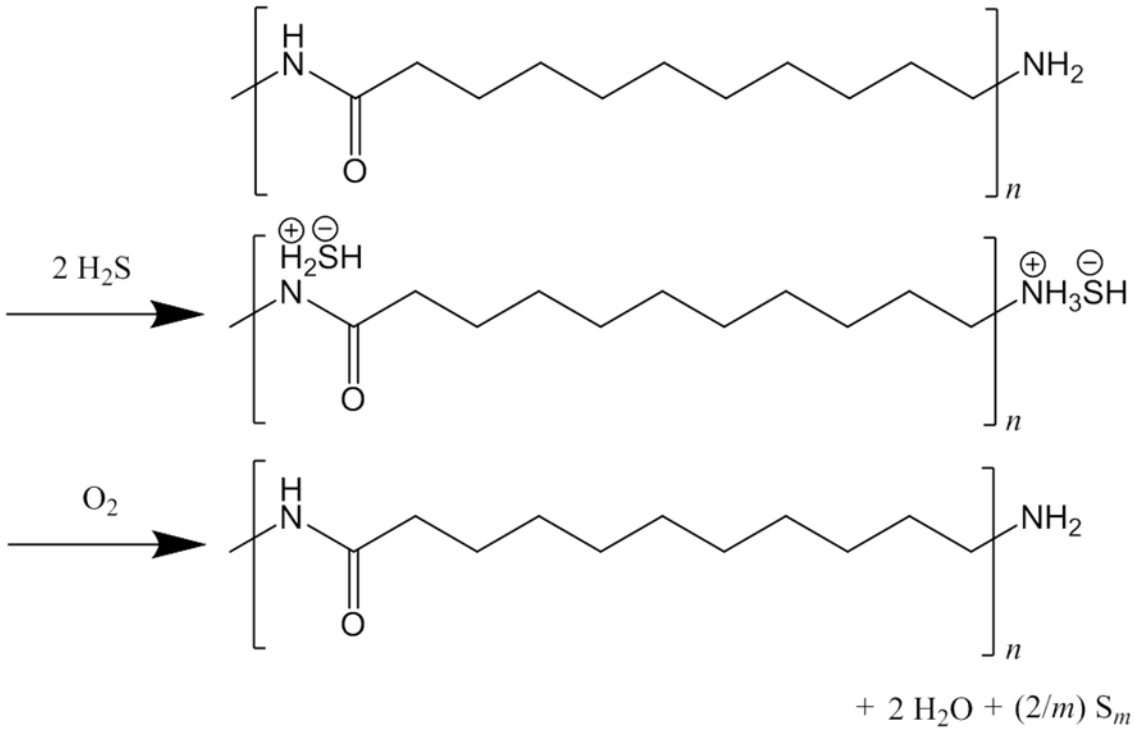

Figure 5.16. Schematic showing possible mechanism of complexation and subsequent oxidation of H_2S to sulphur.

5.6.2.2 Crystal Growth

Following the observation of substantial polymer yellowing, the appearances of CVD graphene coatings were investigated. It was found that the CVD graphene layer remained intact, even after exposure to 10 MPa and 60 °C supercritical CO_2 with 1.48% H_2S feed, as shown in Figure 5.17. The arrows that highlight regions with no 2D peak signal in Figure 5.17a match very well with the dark regions in the contrast adjusted white light image in Figure 5.17c. The detailed 100 μm^2 map in Figure 5.17b shows that the CVD graphene had a porous appearance with large and small 2D peak-free areas. It is worth noting that laser focussing remained challenging at high magnification and so these 2D peak maps are likely to underestimate the CVD graphene coverage.

Interestingly, large needle-like crystal structures were observed on the surface CVD graphene coated PA11 samples following exposure to the H_2S containing fluids. Part of one crystal is clearly visible in Figure 5.17a and c. Raman spectroscopy of the crystals yielded the spectra shown in Figure 5.18a, shown alongside an optical microscope image of two crystals in Figure 5.18b. The spectra in Figure 5.18a are indicative of elemental sulphur.[225,236–239] No such sulphur crystals were observed on the uncoated PA11 surfaces, so the presence of the sulphur crystals must be related to the presence of CVD graphene.

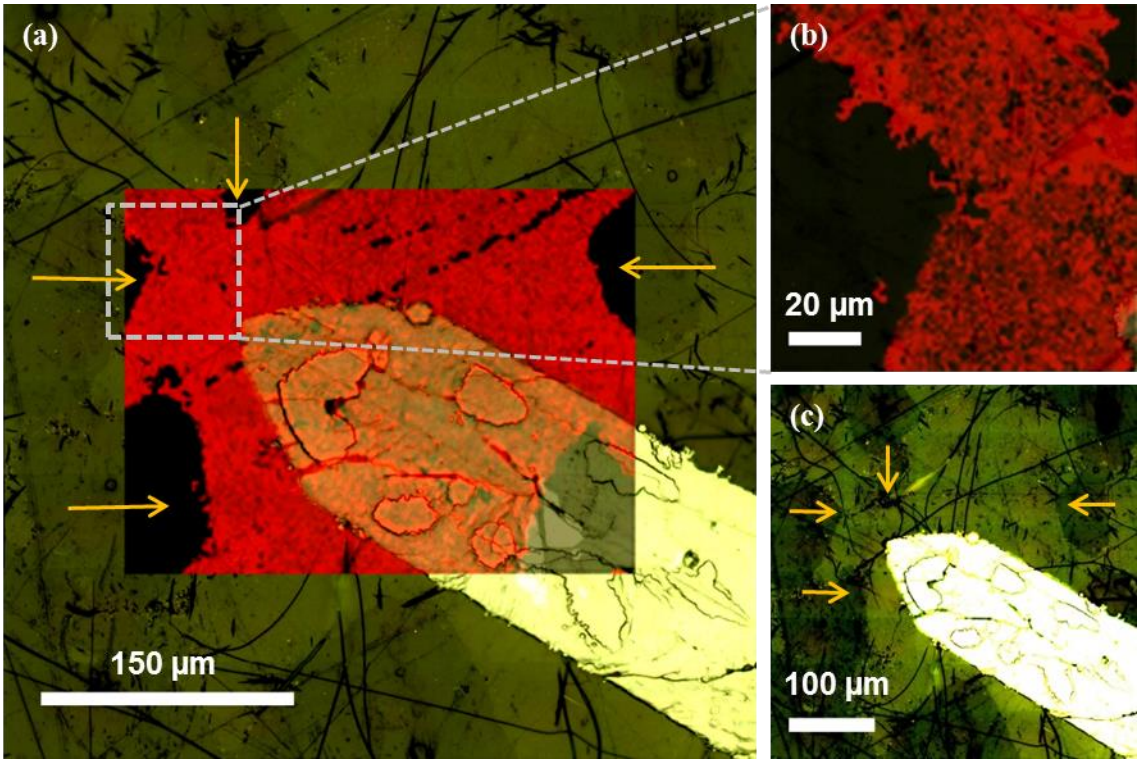

Figure 5.17. Optical microscope and Raman 2D peak mapping of CVD1 following permeability testing at 5 and 10 MPa CO_2 with 1.48% H_2S. (a) Raman mapping at 2 µm spatial resolution on white light optical image; (b) detailed Raman map of small region at 1 µm spatial resolution; (c) contrast adjusted white light image. Arrows show gaps in the CVD graphene coating.

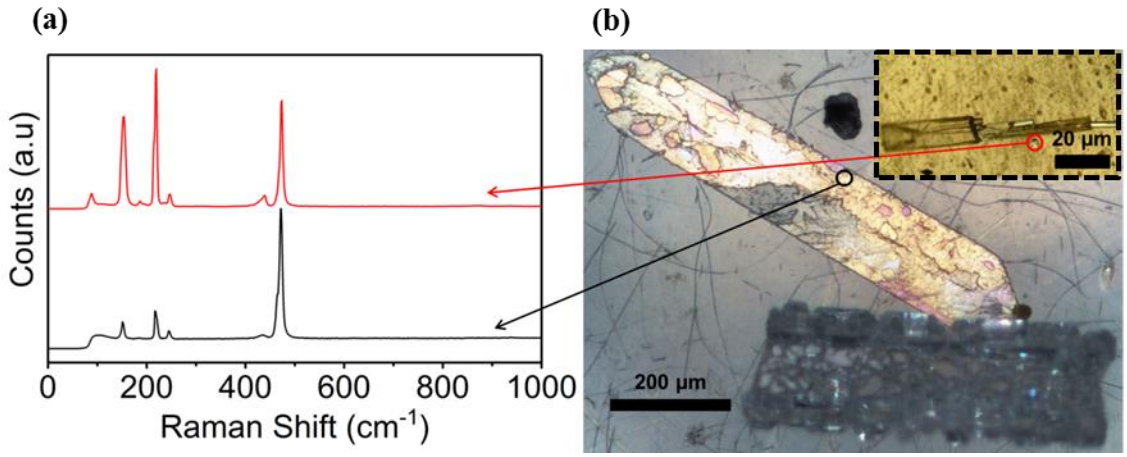

Figure 5.18. (a) Typical Raman spectra of sulphur crystals; (b) optical microscope image of two sulphur crystals on surface of CVD1, inset shows CVD2 crystals.

Figure 5.19 shows an optical image alongside a secondary electron SEM image with EDX analysis of three points.

It is interesting when comparing Figure 5.19a and b that the bright crystal in Figure 5.19a is not easily visible in Figure 5.19b. This suggests that the bright crystal was actually beneath the CVD graphene layer. The darker out of focus crystal at the bottom right of Figure 5.19a can be easily seen in Figure 5.19b, suggesting that this crystal was above the CVD graphene coating. The EDX data in Figure 5.19c, shows that there was a small amount of sulphur present in the bulk PA11 (position I), as the X-rays collected away from the sulphur crystals still indicate the presence of elemental sulphur at 2.25 keV. Position II (Figure 5.19d) shows evidence of elemental sulphur at similar levels to the bulk indicating that the bright crystal was very thin, which was perhaps due to the CVD graphene templating crystal growth laterally, rather than through the CVD graphene layer. Figure 5.19e shows a larger sulphur peak at 2.25 keV, demonstrating that there was more sulphur present at position III than at position II. This suggests that the dark sulphur crystal was much thicker than the bright sulphur crystal, which is corroborated by the crystal being out of focus when the sample surface is in focus (Figure 5.19a).

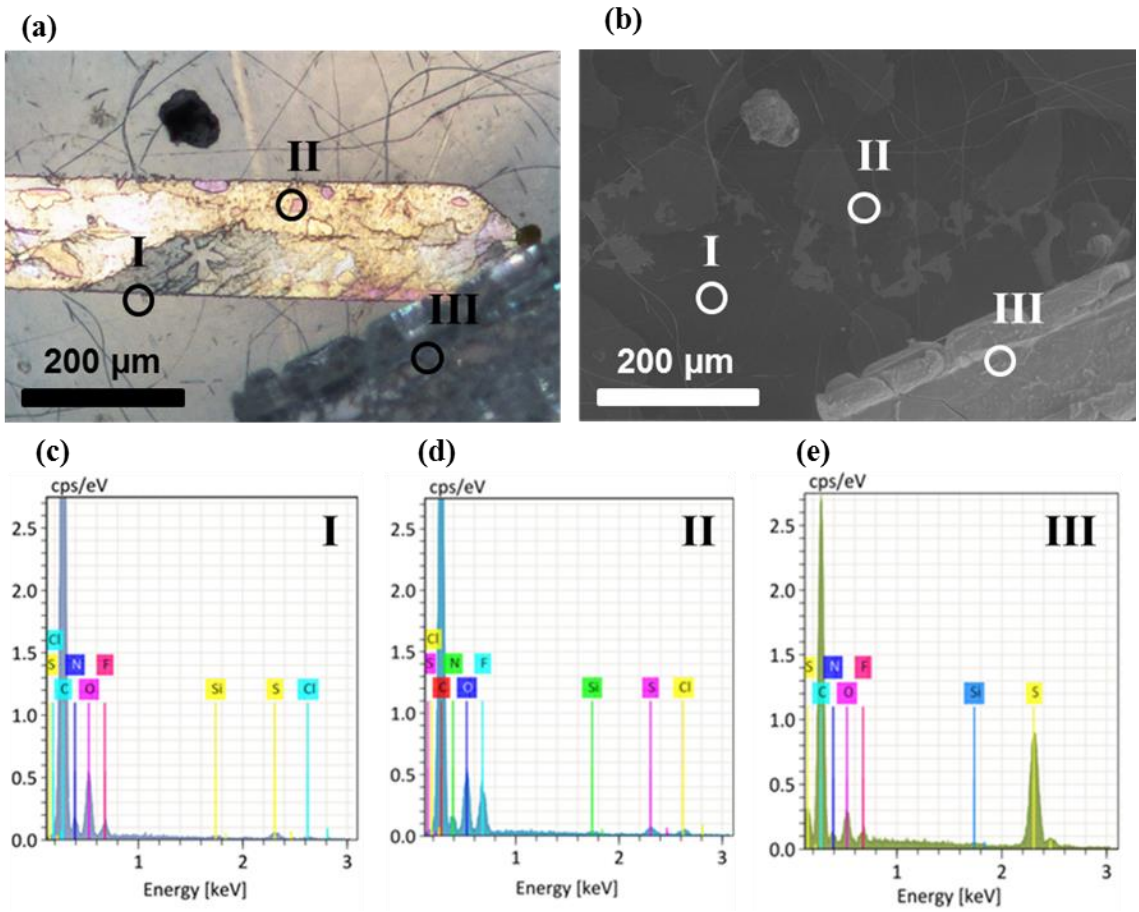

Figure 5.19. (a) Optical microscope of sulphur crystals with positions I, II and III circled. (b) Secondary electron SEM image of the same sulphur crystals with positions I, II and III circled. (c) EDX analysis of position I. (d) EDX analysis of position II. (e) EDX analysis of position III.

A selection of photographs of other sulphur crystals found on the surface of CVD1 and CVD2 are shown in Figure 5.20 and Figure 5.21, respectively.

A series of 21 images of 3D cuboid and 32 images of 3D flower-like sulphur crystals found on the CVD3 sample surface following 0.2 MPa H_2S exposure are shown in Appendix D. The vertical heights of the CVD3 sulphur crystals were approximately 105 and 160 µm for the cuboid and flower-like crystals, respectively. The lateral dimensions of the CVD3 crystals were of the order of 400 µm along their longest axis. The low pressure conditions (0.2 MPa pure H_2S) appeared to encourage 3D sulphur growth, rather than the planar needle-like sulphur crystals observed at the high pressures in Figure 5.20 and Figure 5.21. The lateral sizes (longest axis) of the needle-like crystals ranges from 250 µm (Figure 5.20a) to over 1 mm (Figure 5.21a, c and e).

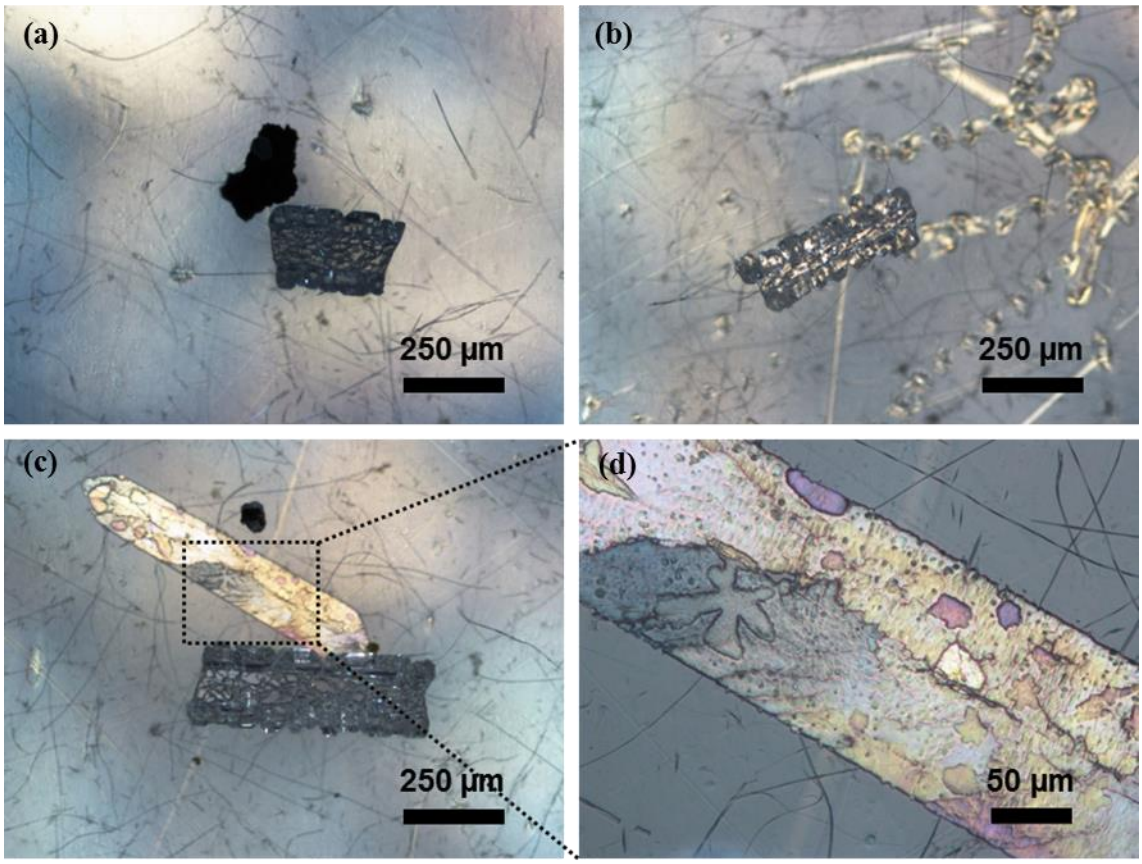

Figure 5.20. Optical microscope images of sulphur crystals found on the CVD1 sample.

The reason for the sulphur crystal formation is unclear. It was initially assumed that the H_2S was reducing the CVD graphene coating, however, as shown by the Raman mapping, the CVD graphene coating appears to be intact around the crystals. It was then thought that the CVD graphene was aiding the sulphur crystal growth through a templating effect, after a sulphur crystal nucleated on the PA11 surface. However, this mechanism seemed unlikely as no sulphur crystals or amorphous sulphurs were observed on the surface of uncoated PA11.

We now attribute the sulphur crystal growth to transition metal impurities left over from the $FeCl_3$ etchant and copper foil.[240,241] Copper has been reported to enhance the capture of sulphur from H_2S streams in polyamine based carbon absorbants.[231] Indeed, copper, iron and even tin contamination beneath CVD graphene monolayers has been reported previously.[240–242]

Figure 5.22 shows a possible route towards sulphur crystal growth after nucleation at a transition metal impurity. Further work is required to confirm the postulated mechanism including deliberate seeding of copper and $FeCl_3$ on PA11 surfaces.

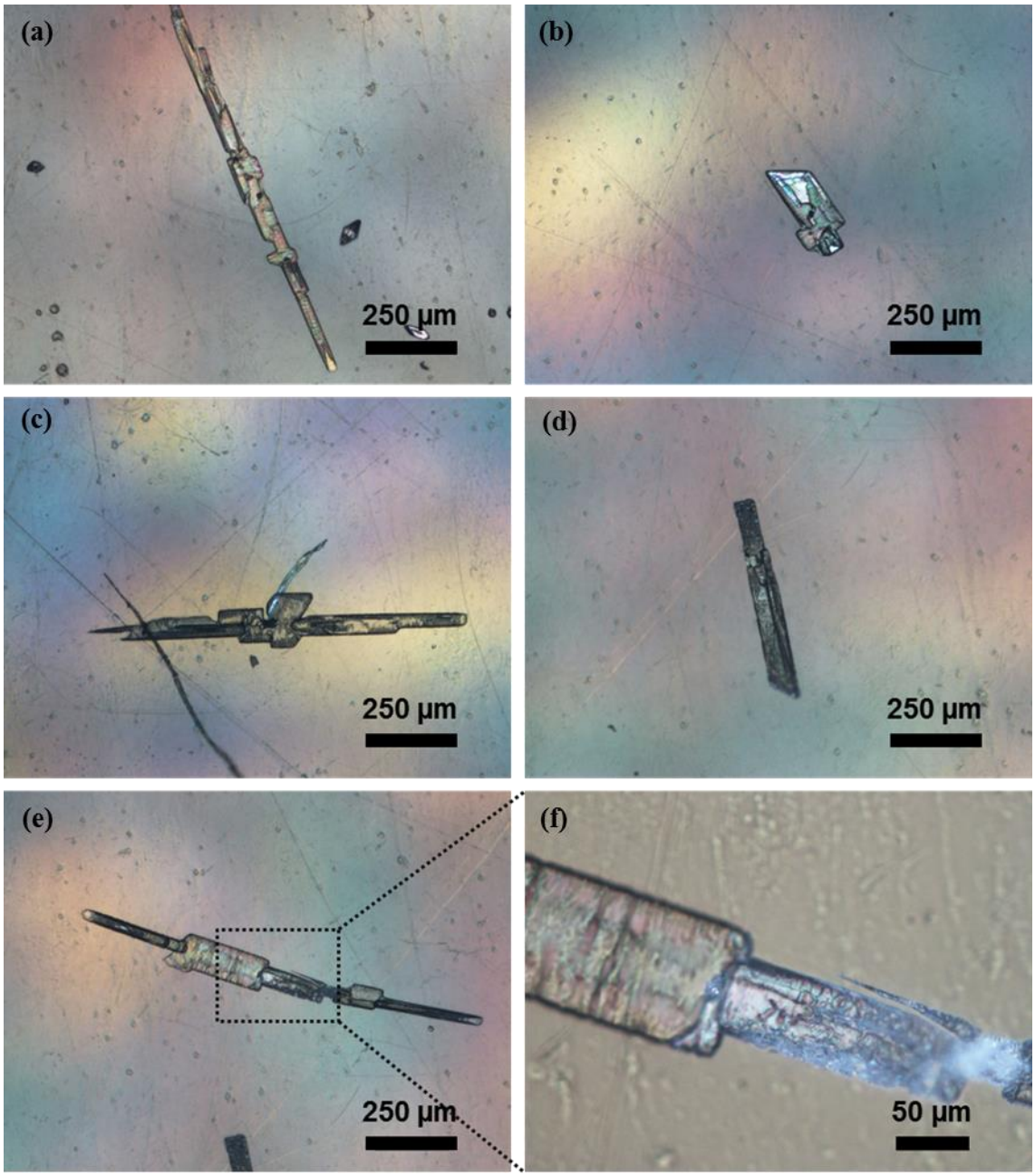

Figure 5.21. Optical microscope images of sulphur crystals found on the CVD2 sample.

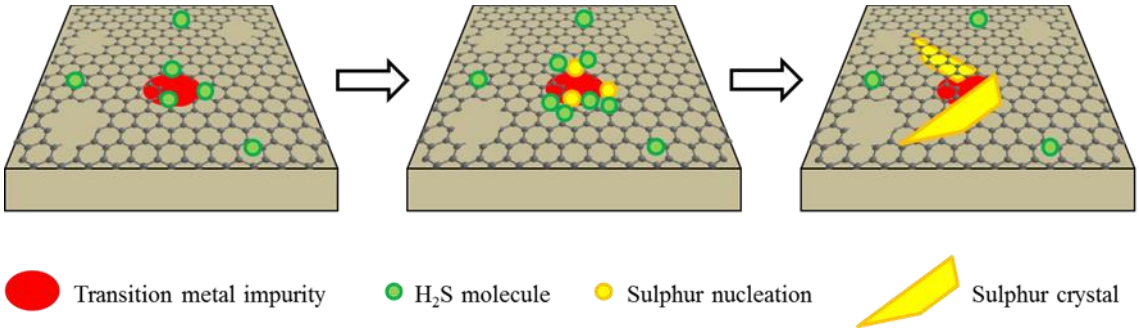

Figure 5.22. Possible mechanism for transition metal nucleation of sulphur crystals and their growth under high pressure conditions.

5.6.3 Permeability Studies

Table 5.1 shows the samples codes associated with various testing conditions. Gaskets were used to protect the CVD graphene coating and did not too greatly affect the transport coefficients, as shown in Appendix B. In this section of work PA11 is referred to specifically as BMNO.

Table 5.1. Table of samples tested under various conditions, results are presented and discussed below.

Sample	**Fluid**	***T* (°C)**	***p* (MPa)**	p_{CO2} **(MPa)**	p_{H2S} **(MPa)**	**Gasket**
BMNO	Pure H_2S	60	0.2	N/A	0.2	No
CVD3, CVD4	Pure H_2S	60	0.2	N/A	0.2	Yes
4 × BMNO	CO_2 with 1.48% H_2S	60	5	4.926	0.074	No
BMNO	CO_2 with 1.48% H_2S	60	5	4.926	0.074	Yes
CVD2, CVD5	CO_2 with 1.48% H_2S	60	5	4.926	0.074	Yes
BMNO	CO_2 with 1.48% H_2S	60	5, 10	4.926, 9.852	0.074, 0.148	Yes
CVD1	CO_2 with 1.48% H_2S	60	5, 10	4.926, 9.852	0.074, 0.148	Yes

Standard procedure for reporting the transport coefficients typically limits the data to the permeability coefficients; however, in this case the diffusion and solubility

coefficients were plotted in order to probe the differences in transport of CO_2 and H_2S. Estimated error on repeated permeability values is of the order of 10%.[179]

Table 5.2 shows the fugacity coefficients used for calculation of the permeability coefficients with fugacity, P_f, the values of which are tabulated in Appendix C.

Table 5.2. Relationship between total feed pressure, p, partial pressures, p_{CO2} and p_{H2S}, and fugacity values, f_{CO2} and f_{H2S}, calculated using the fugacity coefficients φ_{CO2} and φ_{H2S}.

p (MPa)	p_{CO2} (MPa)	p_{H2S} (MPa)	f_{CO2}* (MPa)	f_{H2S}* (MPa)	φ_{CO2}†	φ_{H2S}†
0.2	N/A	0.2	N/A	0.1968	N/A	0.9841
5	4.926	0.074	4.10	0.058	0.832	0.780
10	9.852	0.148	6.67	0.084	0.678	0.568

*Calculated by Equation 2.27

†Values calculated from NIST REFPROP software

5.6.3.1 0.2 MPa Pure H_2S 60 °C

The results for permeability testing of uncoated BMNO PA11 and CVD graphene coated BMNO PA11 (CVD3 and CVD4) to 0.2 MPa pure H_2S are summarised in Figure 5.23. As can be seen, to within error, there was no change in the PA11 transport properties with the addition of a single layer of CVD graphene. Insignificant change in permeability coefficient has been observed for other CVD graphene coated polymers, as discussed in section 5.2.3.[203,217] This is likely due to the porous graphene appearance as shown for CVD3 and CVD4 in Figure 5.7 and Figure 5.8, respectively.

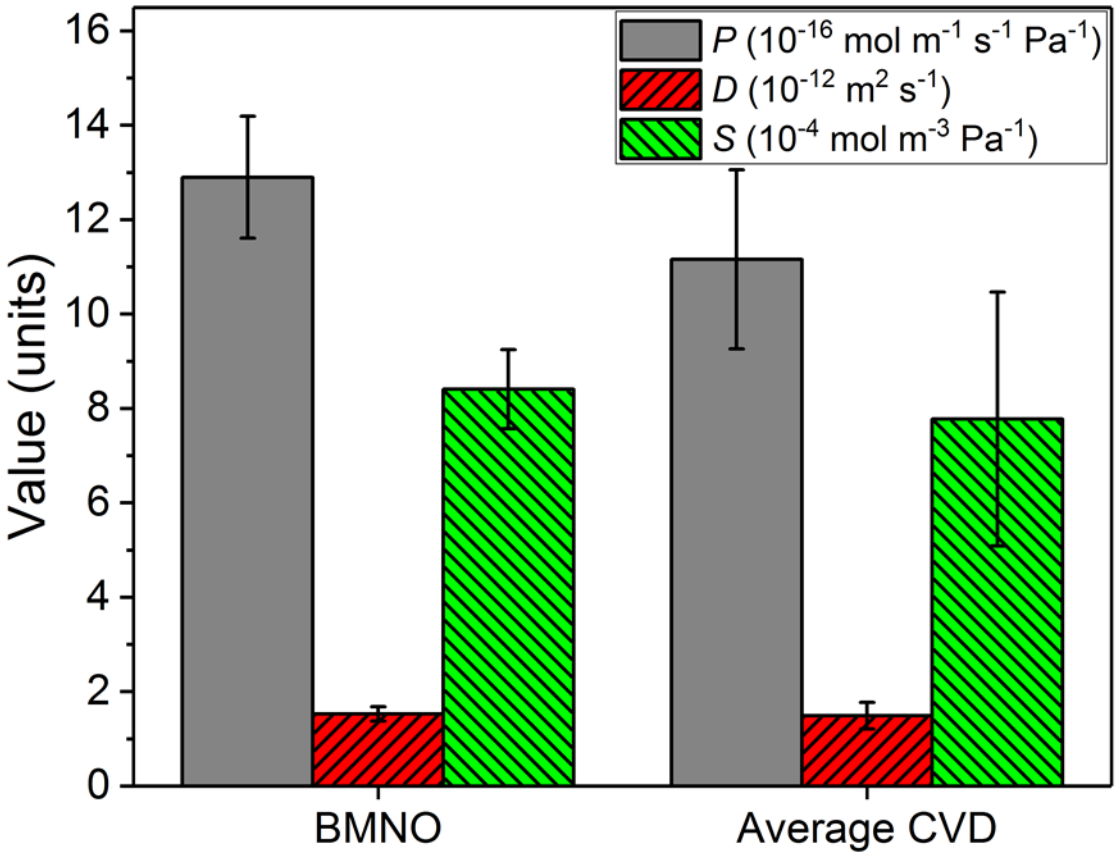

Figure 5.23. Variation in transport coefficients at 0.2 MPa pure H_2S for one BMNO control compared to the average of two CVD graphene coated BMNO samples (CVD3 and CVD4). Error bars signify an estimated error of 10% for the BMNO sample and a single standard deviation of the two CVD graphene coated samples. Using fugacity as the driving force increases the value of *P* to 13.1 and 11.3 and *S* to 8.6 and 7.6 for BMNO and CVD, respectively.

5.6.3.2 5 MPa CO_2 with 1.48% H_2S 60 °C

The CO_2 transport coefficients for averaged BMNO control samples and the average values of CVD1, CVD2 and CVD5 at 5 MPa CO_2 with 1.48% H_2S are shown in Figure 5.24. As can be seen, there was no improvement in P_{CO2}, D_{CO2} or S_{CO2} by the addition of a single CVD graphene layer. Similarly, no barrier effect was imparted by CVD graphene on the transport coefficients of H_2S compared to uncoated PA11, as shown in Figure 5.25. Again, this poor performance is not unexpected, considering the patchy CVD graphene coverage observed, for example, for CVD1in Figure 5.17.

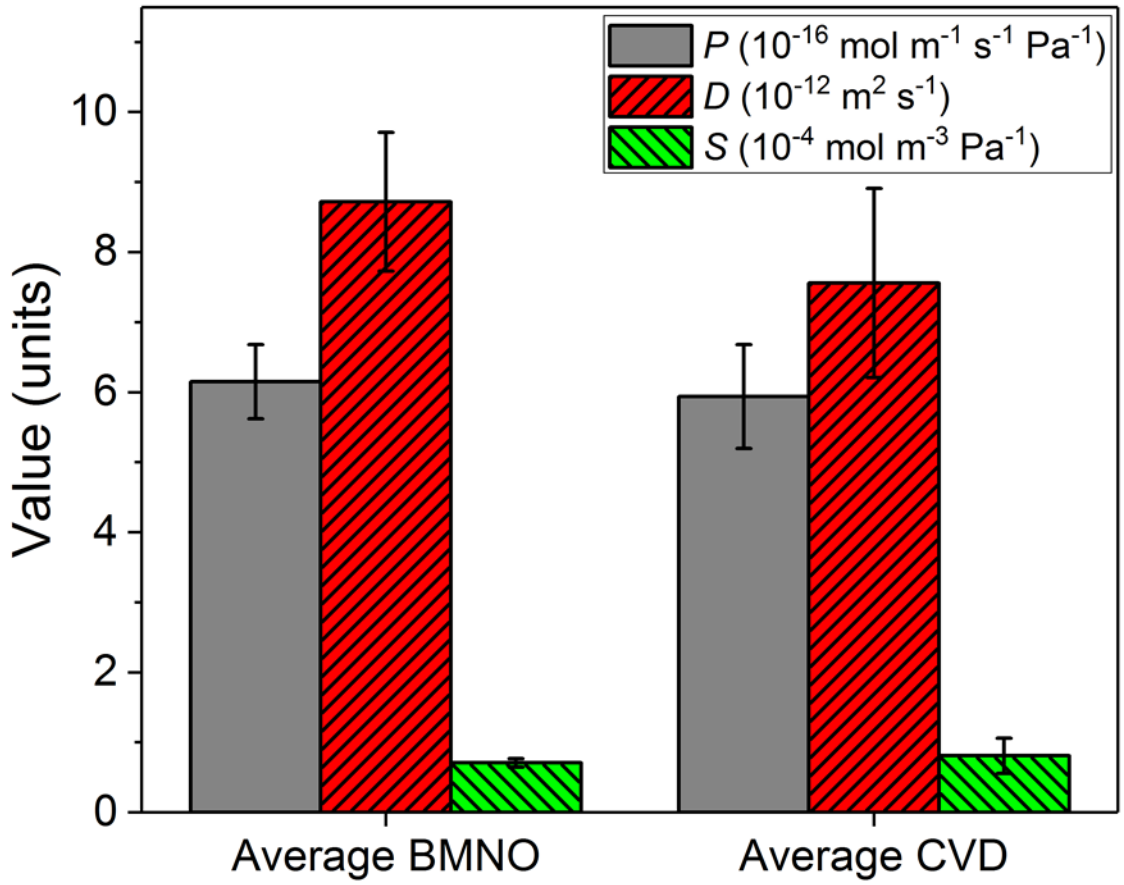

Figure 5.24. Variation of CO_2 transport coefficients at 5 MPa CO_2 with 1.48% H_2S for BMNO with the addition of a single layer of CVD graphene. Standard deviations for average BMNO are calculated from six BMNO measurements. Standard deviations for average CVD are calculated from the CVD1, CVD2 and CVD5 samples. Using fugacity as the driving force increases the value of *P* to 7.4 and 7.1 and *S* to 0.85 and 0.94 for BMNO and CVD, respectively.

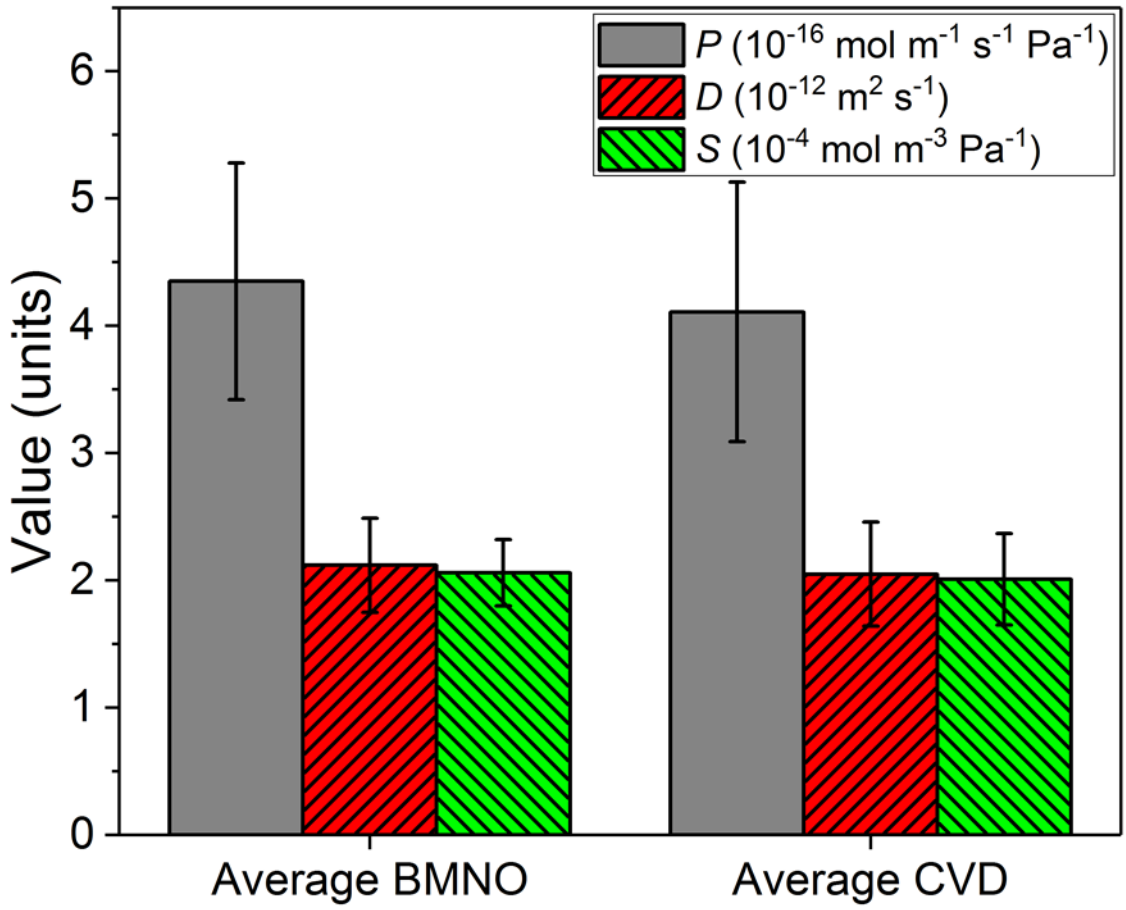

Figure 5.25. Variation of H_2S transport coefficients at 5 MPa CO_2 with 1.48% H_2S for BMNO with the addition of a single layer of CVD graphene. Standard deviations for average BMNO are calculated from six BMNO measurements. Standard deviations for average CVD are calculated from the CVD1, CVD2 and CVD5 samples. Using fugacity as the driving force increases the value of *P* to 5.6 and 5.3 and *S* to 2.6 and 2.6 for BMNO and CVD, respectively.

According to Equation 2.9, the permeability coefficient is made up of the diffusion coefficient and solubility coefficient ($P = D.S$).

It is interesting to compare the different compositions of the permeability coefficient. As can be seen in Figure 5.26, the CO_2 permeability coefficient is greater than the H_2S permeability coefficient. This appears to be due to the large CO_2 diffusion coefficient, particularly as the CO_2 solubility coefficient is very low. This suggests that CO_2 is a less interacting and a smaller penetrant than H_2S within the PA11. The diffusion and solubility coefficients for H_2S are numerically much closer, as can be seen. This suggests that the diffusion of H_2S is retarded by its greater interaction with the PA11

matrix. However, the greater interactions between H_2S and the PA11 mean that the solubility of H_2S makes up for some of the reduced rate of diffusion. Overall, for the CO_2 with 1.48% H_2S fluid mix tested, the barrier performance of PA11 to H_2S is superior to its barrier performance to CO_2.

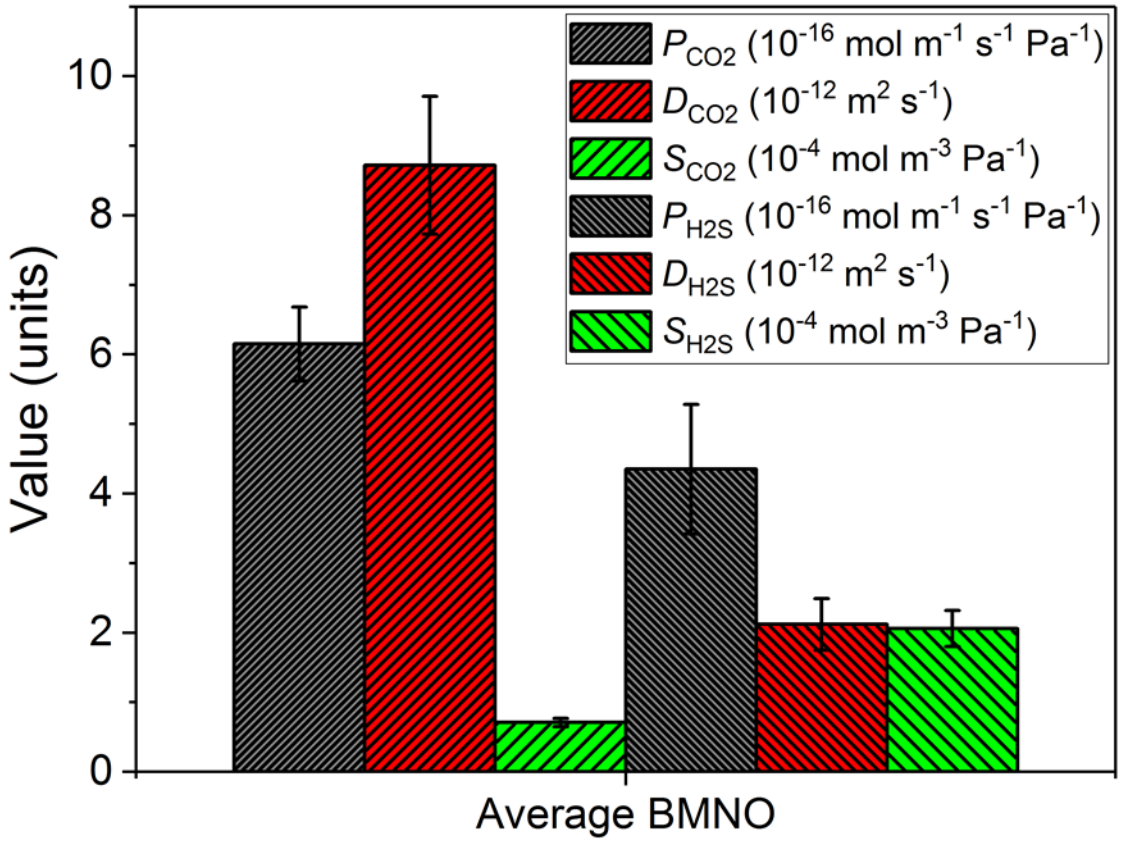

Figure 5.26. Plot comparing *P*, *D* and *S* for CO_2 and H_2S at 5 MPa CO_2 with 1.48% H_2S for the average control BMNO. Error bars show standard deviation of the six samples. Using fugacity as the driving force increases the value of P_{CO2} and S_{CO2} to 7.4 and 0.85 and P_{H2S} and S_{H2S} to 5.6 and 2.6, respectively.

5.6.3.3 10 MPa CO_2 with 1.48% H_2S 60 °C

Figure 5.27 and Figure 5.28 show the transport coefficients for single permeability measurements of BMNO PA11 and CVD graphene coated PA11 at 10 MPa CO_2 with 1.48% H_2S, immediately after exposure to the same feed at 5 MPa. Error bars represent a 10% estimated error.[179]

At 10 MPa pressure, the CO_2 is in the supercritical phase, rather than the gas phase. As can be seen in Figure 5.27, CVD graphene failed to alter the transport of 10 MPa

supercritical CO_2 through PA11, much like the performance for gaseous CO_2 at 5 MPa (Figure 5.24). The mechanism of CO_2 again appeared to be driven by a high diffusion coefficient, rather than a high solubility in the PA11 matrix.

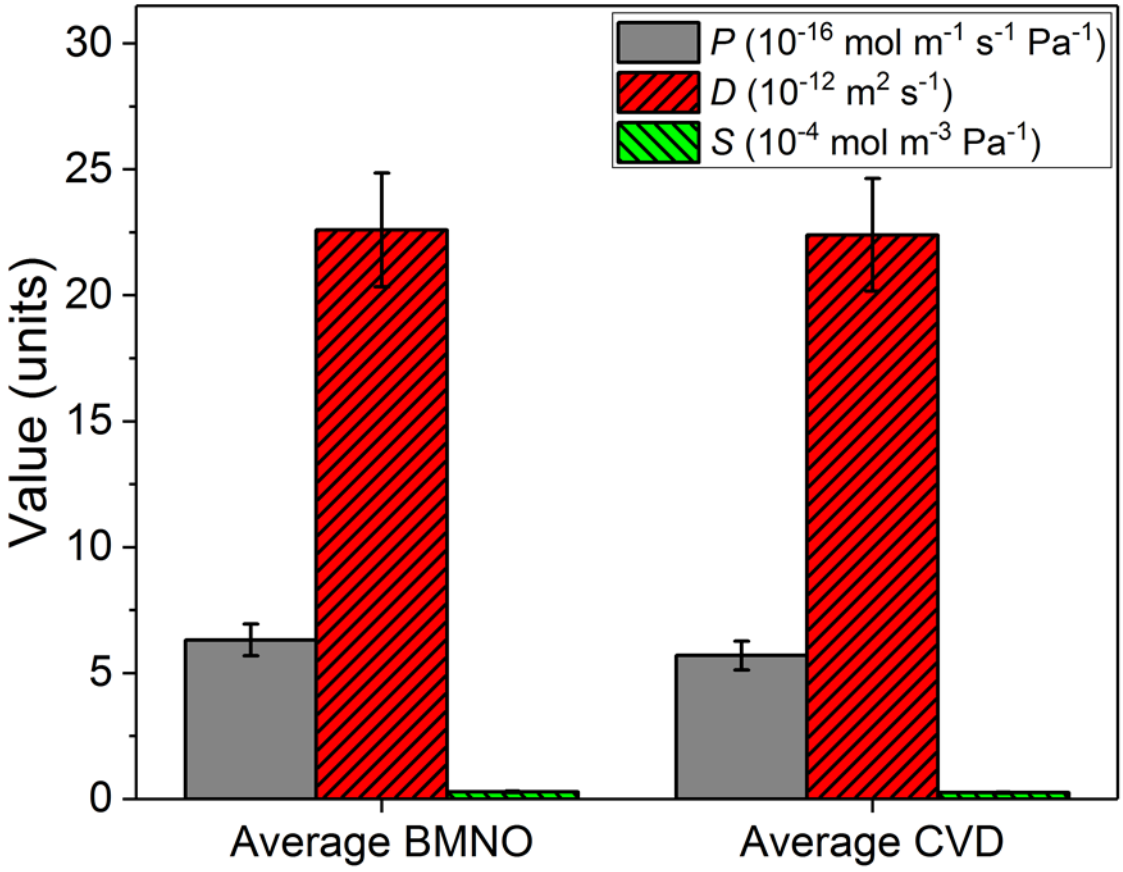

Figure 5.27. Variation of CO_2 transport coefficients at 10 MPa CO_2 with 1.48% H_2S for BMNO with the addition of a single layer of CVD graphene. Error bars signify 10% estimated error for the single measurements. Using fugacity as the driving force increases the value of *P* to 9.3 and 8.4 and *S* to 0.42 and 0.38 for BMNO and CVD, respectively.

The H_2S permeability also did not appear to be changed, as shown in Figure 5.28, although the diffusion coefficient appeared to be anomalously high for the CVD graphene coated sample. The behaviour of the BMNO control is similar to the behaviour of PA11 at 5 MPa, where solubility plays a key role in the permeation of H_2S through the PA11 matrix.

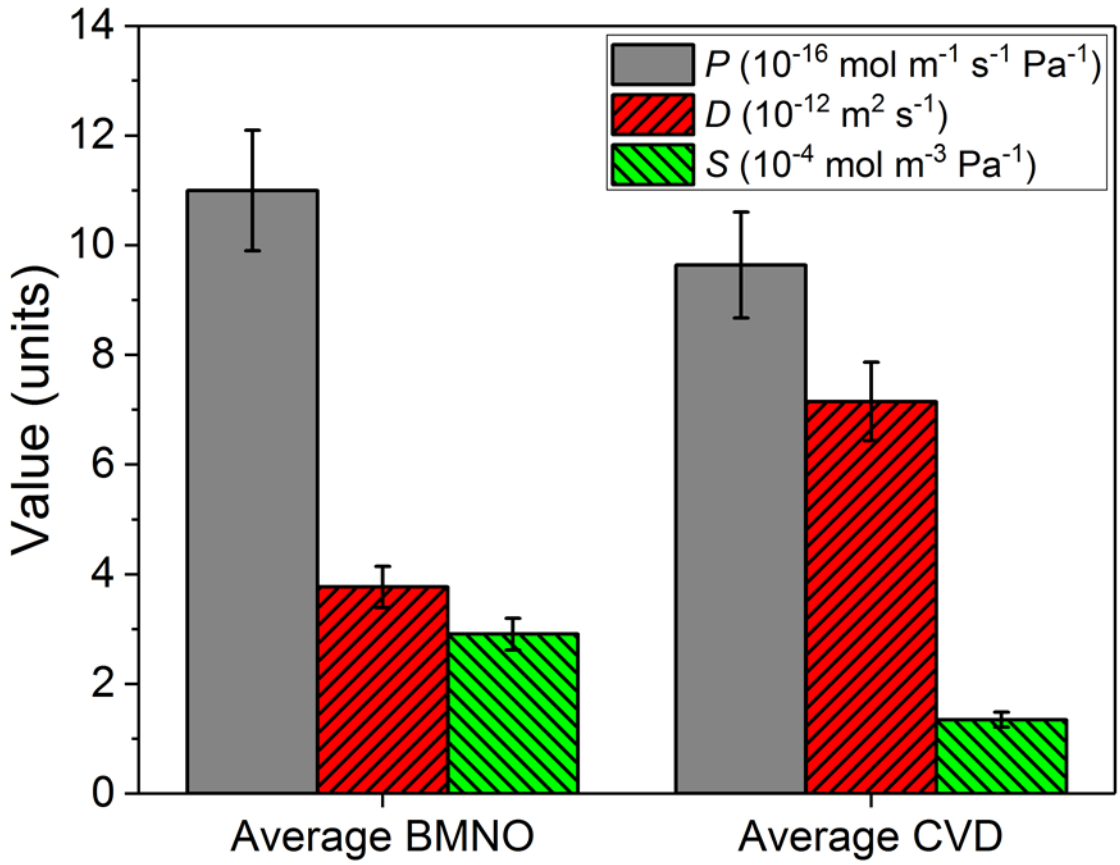

Figure 5.28. Variation of H_2S transport coefficients at 10 MPa CO_2 with 1.48% H_2S for BMNO with the addition of a single layer of CVD graphene. Error bars signify 10% estimated error for the single measurements. Using fugacity as the driving force increases the value of *P* to 19.4 and 17.0 and *S* to 5.1 and 2.4 for BMNO and CVD, respectively.

5.6.3.4 Effect of Pressure

At 10 MPa, CO_2 has a lower permeability coefficient than H_2S, whereas at 5 MPa CO_2 has a higher permeability coefficient than H_2S, as shown in Table 5.3. This may be due to compression of the PA11 matrix because of the high hydrostatic pressure exerted at 10 MPa. The diffusion of CO_2 may be reduced as compression of the PA11 matrix results in a reduced free volume.[54,93,179] In addition, as CO_2 has a low solubility in the PA11 compared to H_2S, compression of the polymer, leading to greater packing of the polymer chains is likely to favour polymer-penetrant interactions of H_2S, which relies more on its high solubility for permeation to take place.

Although the free volume may be reduced at high pressure, the concentration of CO_2 and H_2S is actually increased at the membrane and so the flux across the membrane is

higher at high pressure. The normalisation of the flux by dividing through by pressure means that the permeability coefficient should not be greatly affected by the increase in pressure. This appears to hold true for the CO_2 permeability which does not change beyond error as shown in Table 5.3, for control BMNO PA11 only. On the other hand, the permeability coefficients for H_2S increase with increasing partial pressure of H_2S (Table 5.3). It is interesting that the permeability of H_2S through PA11 is similar for partial pressures of H_2S of 0.148 and 0.2 MPa, even though the total hydrostatic pressure exerted on the sample is 50 times greater for the former experiment. What is even more surprising is that the H_2S permeability at 5 MPa total pressure is around one third of the value of that at 10 or 0.2 MPa total feed pressure. This demonstrates a balance between compaction of the polymer and increased concentration:[54,179] at 0.2 MPa total feed pressure, there is little compression of the polymer so free volume is available for permeation; however, at 5 MPa total feed pressure, compaction of the polymer makes diffusion of low levels of H_2S difficult, until at 10 MPa, the concentration of H_2S dominates. It is also worth evaluating the effect of H_2S scrubbing due to the PA11 functionalities. Perhaps for the 5 MPa experiments, the low partial pressures of H_2S are sequestered by the PA11, thus reducing the flux across the membrane, whereas at the higher partial pressures, the scrubbing of H_2S has less of an effect.

Table 5.3. Permeability of control BMNO PA11 samples at different total and partial pressures.

p_{total} (MPa)	p_{CO2} (MPa)	p_{H2S} (MPa)	P_{CO2} (10^{-16} mol m^{-1} s^{-1} Pa^{-1})	P_{H2S} (10^{-16} mol m^{-1} s^{-1} Pa^{-1})
5	4.926	0.074	6.2* ± 0.5	4.4* ± 0.9
10	9.852	0.148	6.3† ± 0.6	11† ± 1
0.2	N/A	0.2	N/A	13‡ ± 1

Using fugacity as the driving force yields the following:

*7.2 and 5.6 for CO_2 and H_2S, respectively

†9.3 and 19.4 for CO_2 and H_2S, respectively

‡13.1 for H_2S

5.7 CONCLUSIONS

PA11/graphene nanocomposites comprising a single CVD graphene layer transferred onto a PA11 plaque surface were permeability tested to pure H_2S and to CO_2 with 1.48% H_2S.

The addition of a single CVD graphene layer did not appear to alter the transport properties of PA11 to CO_2 or H_2S, due to unavoidable tearing of the CVD graphene during transfer. The CVD graphene itself remained adhered to the PA11 surface, even following depressurisation.

PA11 and PET yellowed significantly when exposed to H_2S due to a build-up of elemental sulphur within the polymer matrix. A mechanism was suggested for the sulphur sequestering by PA11 amide bonds and end groups, analogous to amine scrubbing of H_2S in alkanolamines. A similar mechanism may be at work within the PET at oxygen functionality.

When CVD graphene coated PA11 samples are exposed to H_2S, sulphur crystals are observed on top and beneath the CVD graphene surface, in addition to significant yellowing in the bulk. Surface sulphur crystal growth probably stems from transition metal catalysis of H_2S. Transition metal impurities are likely to be present beneath the CVD graphene surface due to incomplete copper etching and/or incomplete rinsing of $FeCl_3$ etchant.

CHAPTER 6: GRAPHENE PAPER LAMINATES

6.1 INTRODUCTION

Previous chapters have shown that GNP nanocomposites and single CVD graphene layers proved ineffective in reducing the permeability of CO_2 and H_2S, at both low and high pressures.

One major obstacle in the melt blended GNP nanocomposites appeared to be the voiding due to poor GNP compatibility and trapped air within the PA11 matrix, as well as a reduction in the mechanical properties. In order to overcome the voiding within the PA11 matrix, it was proposed that the PA11 matrix be removed from the equation altogether, thus fabricating a pure GNP layer.

By preparing a pure GNP paper, multiple GNP layers could act as a tortuous pathway for permeants to diffuse through. Multiple GNP layers may therefore mask defects and GNP edges, so dealing with the observed issues of incomplete coverage with CVD graphene coatings.

6.2 LITERATURE REVIEW

6.2.1 GRAPHENE NANOPLATELET PAPERS

The literature in the area of GNP papers is rather sparse, with only two papers creating filtered GNP papers for improved barrier performance.[243,244] The methodology, however, is based on CNT buckypaper production.[245,246]

Wu and Drzal filtered a porous GNP paper from a polyethyleneimine (PEIn)/GNP/water solution, following ultrasonication. The GNP paper was then annealed to remove any remaining PEIn and the paper was impregnated with thermoset or soluble thermoplastic matrices. The GNP was soaked in the thermoset (epoxy) system for 1 h before the epoxy was cured in a hot press at 10 MPa and 150 °C, yielding GNP-E. Alternatively, the GNP paper was soaked in polyetherimide (PEId) solution for 1 h before drying at room temperature. The PEId/GNP paper was then compression moulded at 10 MPa and 340 °C to form a void-free composite. The oxygen permeability of the PEId/GNP paper was 1.1% of the control PEId. By inserting the GNP-E paper into a carbon fibre pre-

preg composite, the oxygen permeability was reduced to 11% compared to the pure carbon fibre pre-preg.

Pierleoni *et al.*[244] also produced a range of GNP papers from electrochemically exfoliated GO and a range of commercial GNPs, by filtering IPA-diluted DMF/GNP dispersions. The filtered GNP papers were then transferred to a range of substrates by hydraulic pressing or roll-to-roll application. The OTR was reduced by approximately 75% for GNP coated PET and up to 90% for GNP coated PP. Pierleoni *et al.* deduced the permeability of the substrate (P_S) and coating (P_C) by using the series resistance formula for multi-layer films:[244]

$$\frac{1}{\mathrm{OTR_M}} = \frac{1}{\mathrm{OTR_S}} + \frac{1}{\mathrm{OTR_C}} = \frac{l_S}{P_S} + \frac{l_C}{P_C} \qquad \text{Equation 6.1}$$

where $\mathrm{OTR_M}$, $\mathrm{OTR_S}$ and $\mathrm{OTR_C}$ are the measured OTR, OTR of the substrate and OTR of the coating, respectively. The thickness of the substrate and coating is l_S and l_C, respectively. This accounts for the relative barrier resistance of the various substrates, for example, a 75% reduction in OTR in PET is more significant than a 90% reduction in OTR in PP as virgin PP has quite a high OTR, compared to virgin PET. The calculated permeability of PET and PP are 1.41×10^{-17} and 4.84×10^{-16} mol m^{-1} s^{-1} Pa^{-1}, respectively and the GNP coatings on these substrates have a calculated permeability of 1.2×10^{-20} and 6.2×10^{-20} mol m^{-1} s^{-1} Pa^{-1}, respectively. The excellent reduction in oxygen permeation was found to be independent of transfer technique and GNP source, provided the source contained no surfactant. The performance of the GNP coatings was attributed to their physical barrier in the through coating direction, and their tight packing in the horizontal direction, reducing the lateral diffusion between layers.

Studies on the production of GNP papers for other applications ranging from radio frequency shielding to mechanical properties, have been made.[243,247–249] In addition, layer-by-layer production of layered GNP composites has also been attempted, resulting in excellent barrier performance.[250]

6.2.2 Transport in Multi-Layered Systems

As shown by Equation 6.1, it is possible to calculate individual components of OTR across a membrane.[244] By extension, it is possible to calculate the individual permeabilities of each layer in a multi-layered sample. The measured permeability of a

multi-layered composite, $P_{composite}$, with a total thickness of $l_{composite}$, may be expressed in terms of permeability of each layer, P_i, with thicknesses l_i, according to:[164,251–253]

$$\frac{1}{P_{composite}} = \frac{1}{l_{composite}} \sum \left(\frac{l_i}{P_i} \right) \quad \text{Equation 6.2}$$

6.3 Aims and Objectives

It was the aim of this section of work to evaluate the barrier properties of GNP layers in a multi-layered PA11 laminate structure.

Firstly, porous GNP papers were filtered from ultrasonicated NMP/GNP dispersions. The papers were then compression moulded between PA11 films to create layered laminate structures that could be permeability tested.

Preliminary testing in 0.2 MPa pure H_2S was performed and the effect of GNP lateral size was investigated, by altering the GNP platelet size from 25 µm to 15 µm.

Following preliminary testing, thorough investigation of performance at high pressures of CO_2 with 1.48% H_2S was performed. Pressures of up to 40 MPa were tested and the transport properties were extracted for each pressure step from 5, 10, 20 and 40 MPa.

SEM characterisation was carried out to investigate the GNP layer morphology following testing in order to probe the barrier mechanism of the GNPs. The permeability performance of the GNP papers was extracted and compared to the apparent permeability of pure PA11.

Preliminary testing of htGO25 laminate at 5 MPa CO_2 with 1.48% H_2S was also carried out.

6.4 Materials and Methods

6.4.1 Polyamide 11

PA11 was sourced as outlined previously (section 3.4.2).

6.4.2 Graphene Nanoplatelets

GNPs were sourced as outlined in section 3.4.3. According to the datasheet, the GNPs had an average lateral size of 25 µm (GNPs-25) and 15 µm (GNPs-15) with surface areas of 120 – 150 m^2 g^{-1} and average thickness of 6 – 8 nm.[37]

6.4.3 N-Methyl-2-pyrrolidone

NMP was supplied by Sigma-Aldrich Company Ltd., UK and used as received.

6.4.4 Preparation of Graphene Nanoplatelet Papers

Figure 6.1 shows a schematic of the GNP paper production. GNPs-25 or GNPs-15 (80 mg, accurately weighed) were suspended in NMP (160 mL) by ultrasonication in a temperature controlled (10 °C) Hilsonic Ultrasonicator (300 W) for 3 h. The resulting unstable suspension (2 mg mL^{-1}) was immediately vacuum filtered through a sintered glass funnel covered with a nylon filter paper (GVS Life Sciences) with 0.45 µm pores. The funnel was covered with a glass petri dish during filtration to reduce the possibility of contaminants entering the solution.

Air was drawn through the resultant highly porous GNP cake for 24 h. The GNP paper was then removed from the filtration apparatus, ensuring that the nylon filter paper remained adhered to the GNP paper. The nylon filter acted as a support for the delicate GNP paper. Any remaining NMP was removed by placing the GNP coated nylon filter in a vacuum oven at 50 – 80 °C for at least 24 h. A steel washer was placed around the GNP paper, on the nylon filter, in order to keep the nylon filter and GNP paper flat during solvent removal. The GNP paper was stored on the nylon filter in a vacuum desiccator until required. Two different diameters of GNP paper were produced – with 40 and 35 mm diameters.

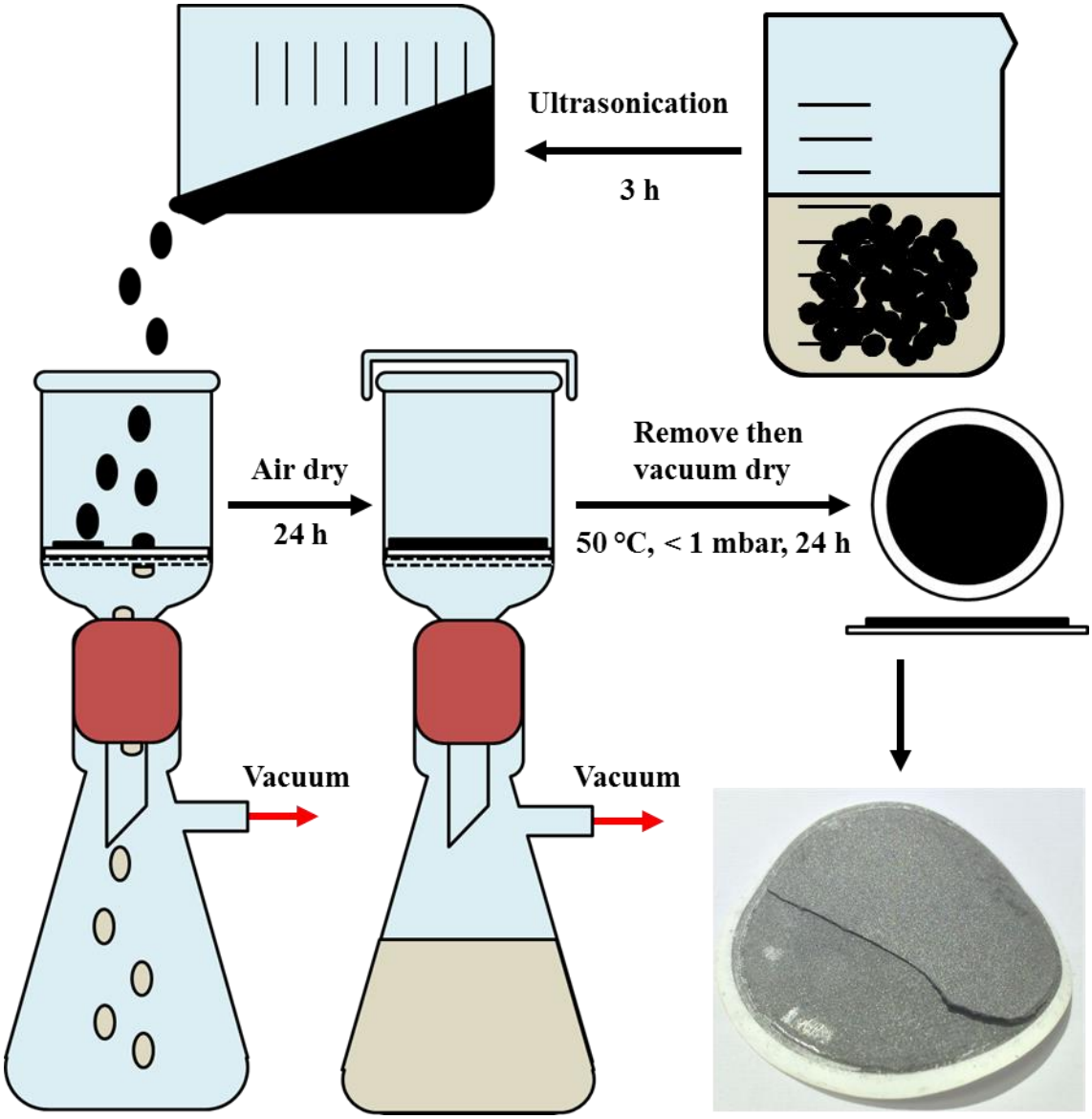

Figure 6.1. Schematic of the preparation of a GNP paper. Inset shows a fractured GNP paper.

6.4.5 Preparation of Graphene Oxide Paper

GO25 solution was prepared by the modified Hummer's method, described in detail in section 3.4.4. In order to produce GO25 papers, GO25 solution (80 mg, 10.3 mL, 7.8 mg mL^{-1}) was sonicated for 3 h in a 300 W Hilsonic Ultrasonicator at 10 °C. The GO25 solution was then vacuum filtered through a pre-weighed Anodisk™ ceramic filter with 0.2 µm pore size. The filter funnel was covered with a glass petri dish to protect the GO25 during filtration. Filtration took at least 24 h, suggesting that the GO25 created an excellent barrier. Upon removal from the filter funnel, some GO25 was lost as residues

remained coated to the interior of the funnel. The resultant GO25 papers had a mass of around 60 mg.

As the GO25 papers were intended to be incorporated into a laminate system, the GO25 had to be stable at the processing temperatures (240 °C). For this reason, the GO25 papers were thermally reduced. The GO25 was left adhered to the Anodisk™ membrane during thermal reduction in a nitrogen purged furnace. In order to limit damage due to the diffusion of evolved degradation products, a heating rate of 0.1 °C min^{-1} was used up to 300 °C and held for 1 h before slow cooling to RT. The resultant heat treated GO25 (htGO25) papers were approximately 50% the mass of the loaded GO25 paper.

6.4.6 Preparation of Graphene Nanoplatelet Laminates

The compression moulding regime is detailed in section 4.4.4. Briefly, the platens were heated to 240 °C and the loaded mould was compression moulded at touching pressure (0 MPa) for 4 min, 1.2 MPa for 4 min, 2.5 MPa for 2 min and finally 8.6 MPa pressure for 30 s. The final pressure was maintained during cooling which was at a rate of approximately 10 °C min^{-1}.

BESVO PA11 pellets and GNP papers (on nylon filters) were dried under vacuum at 50 °C for at least 16 h. Two 40 mm diameter 1 mm thick PA11 films were compression moulded and dried for at least 16 h at 50 °C. One 1 mm PA11 disk was placed in a 2 mm thick mould. Upon the PA11, the GNP paper was placed, following careful peeling of the backing nylon filter paper (Figure 6.2a). The second PA11 disk was carefully deposited on the GNP paper and pressed gently down by hand (Figure 6.2b). The mould arrangement was completed, placed in the compression moulder and pressed (Figure 6.2c). The same process was used to create htGO25 PA11 laminates. 2 mm control samples were pressed directly from pellets (referred to as laminate controls).

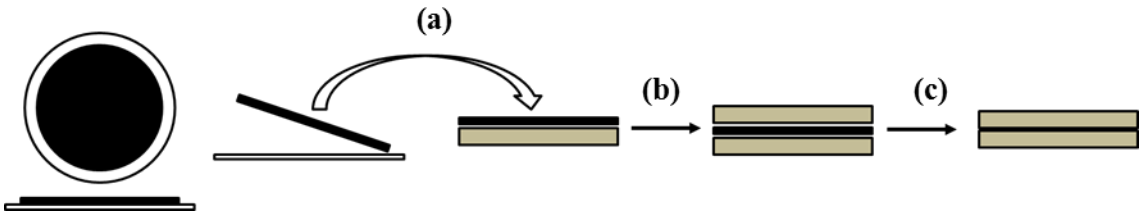

Figure 6.2. Laminate production: (a) peel GNP paper from nylon filter and place on PA11 disk; (b) place second PA11 disk on GNP paper; (c) compression mould.

Figure 6.3 shows photographs and schematics of the laminate control samples (Figure 6.3a) and GNP-containing laminates (Figure 6.3b and c). One type of GNP laminate contained a 40 mm diameter GNP paper that coated the entire laminate, adhered at only a few locations at the very edge (Figure 6.3b). A second type of GNP laminate contained a 35 mm diameter, resulting in partial GNP coverage within the laminate and a complete PA11 seal around the GNP paper (Figure 6.3c).

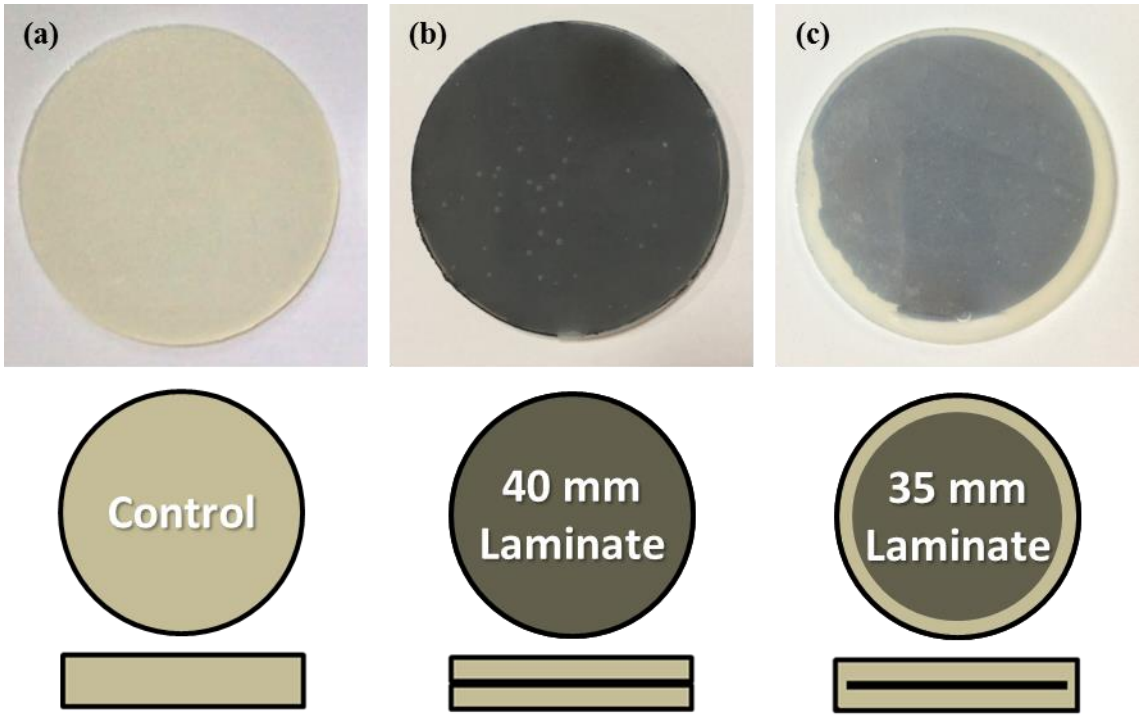

Figure 6.3. Photographs and schematic diagrams of: (a) laminate control; (b) 40 mm GNP laminate; (c) 35 mm GNP laminate.

6.5 CHARACTERISATION METHODS

6.5.1 PREVIOUSLY OUTLINED METHODS

Raman spectroscopy has been previously outlined in section 3.5.3. SEM with the Quanta 250 and Zeiss EVO60 were outlined in sections 3.5.7 and 4.5.2, respectively. Standard deviations were calculated according to Equation 3.7.

6.5.2 X-RAY FLUORESCENCE

X-ray fluorescence (XRF) was carried out on a FEI Quanta 650 FEG ESEM equipped with a Bruker X-Trace μXRF system which used a rhodium X-ray source. A Bruker X-Flash EDS detector was used to collect characteristic X-rays during XRF elemental analysis.

6.5.3 CHAPTER SPECIFIC PERMEABILITY TESTING

Permeability testing was carried out on a purpose built, high pressure barrier rig at TWI Ltd., Cambridge (more details in section 4.5.4). The samples were placed into the cell, in some cases, a protective PA11 gasket (BMNO) was placed on top and the cell was closed tightly. The cells were then placed into an oven at 60 °C and allowed to equilibrate. The samples were then exposed to 0.2 MPa pure H_2S or 5, 10, 20 then 40 MPa CO_2 with 1.48% H_2S.

At 0.2 MPa and 60 °C, the samples ran to the steady state which was maintained for at least seven days and up to three weeks.

At 5 MPa and 60 °C (gas), the samples ran at the steady state for a total of twelve days. At 10 MPa and 60 °C (supercritical), the samples ran at the steady state for a total of six days. At 20 MPa and 60 °C (supercritical), the samples ran at the steady state for a total of six days. At 40 MPa and 60 °C (supercritical), the samples ran at the steady state for a total of fifteen days. At 40 MPa and 21 °C (liquid), the samples ran at the steady state for a total of eight days. The test ran for approximately two months.

6.6 RESULTS AND DISCUSSION

6.6.1 LOW PRESSURE PERMEABILITY STUDIES

Four GNP laminates were prepared with 40 mm diameter GNP papers and permeability tested at 0.2 MPa pure H_2S as shown in Table 6.1. This was a preliminary test to investigate the efficacy of GNP papers as barrier materials. A particularly interesting effect was observed when the GNP laminates were tested with and without gaskets. Samples tested with gaskets remained flat during testing, denoted 'F', whereas those without a protective gasket deformed into the upstream direction, denoted 'E'. Laminate 25E and Laminate 25F were produced from GNPs-25 and Laminate 15E and Laminate 15F were produced from GNPs-15, as shown in Table 6.1. As shown previously in Table 5.2, the fugacity of H_2S (f_{H2S}) at 0.2 MPa and 60 °C was 0.1968 (fugacity coefficient = 0.9841).

Table 6.1. Sample codes and test conditions for samples in this section of work. All carried out at 60 °C.

Sample	GNP flake diameter (µm)	GNP paper diameter (mm)	Fluid	*p* (MPa)	Gasket
Laminate control E*	N/A	N/A	Pure H_2S	0.2	No
Laminate control F†	N/A	N/A	Pure H_2S	0.2	Yes
Laminate 25E*	25	40	Pure H_2S	0.2	No
Laminate 15E*	15	40	Pure H_2S	0.2	No
Laminate 25F†	25	40	Pure H_2S	0.2	Yes
Laminate 15F†	15	40	Pure H_2S	0.2	Yes

*Laminate became deformed (E)

†Laminate remained flat (F)

Photographs of examples of the deformation effect are shown in Figure 6.4 for the laminate controls (Figure 6.4a – e) and GNP laminates (Figure 6.4f – j). As can be seen, the planar appearance of the Laminate control and GNP Laminate before exposure (Figure 6.4a and f) was retained when tested with a gasket (Figure 6.4b, c, g and h). Samples tested without a gasket clearly deformed and showed indicative compression rings around the circumference of the test region (Figure 6.4d, e, i and j), due to the cell closure mechanism, shown schematically in Figure 6.5. The unusual deformation observed for Laminate control E, Laminate 25E and Laminate 15E samples occurred in

the upstream direction. Yellowing was also observed due to H_2S scrubbing yielding elemental sulphur, as discussed previously (section 5.6.2.1).

It is known that H_2S can swell rubbery and glassy polymers during permeation testing, due to favourable interactions between the H_2S and polymer functionality.[254,255] This leads to the postulation that H_2S swells the PA11 matrix leading to a volume expansion of the membrane. The gaskets appeared to protect the sample surfaces from the high compression of the metal cell surface. This meant that the PA11 of the sample was able to expand radially by slipping under the PA11 gasket. Samples tested without a gasket were mechanically restrained around the circumference by metal compression, as indicated in the cell schematic in Figure 6.5. This meant that expansion of the PA11 matrix could not occur radially or in the downstream direction due to the sinter. Thus, the increased volume led the polymer to deform into the upstream direction.

It is interesting that the deformation of the Laminate control E is qualitatively less than the deformation of the Laminate 25E, as shown in Figure 6.4. This may be due to the stiffness of the samples; it may be assumed that one 2 mm thick PA11 sample is stiffer than two 1 mm thick PA11 disks with a lubricating GNP centre. Indeed, the GNP layer was deduced to be disrupted in the deformed samples due to the permeability data presented in Figure 6.6.

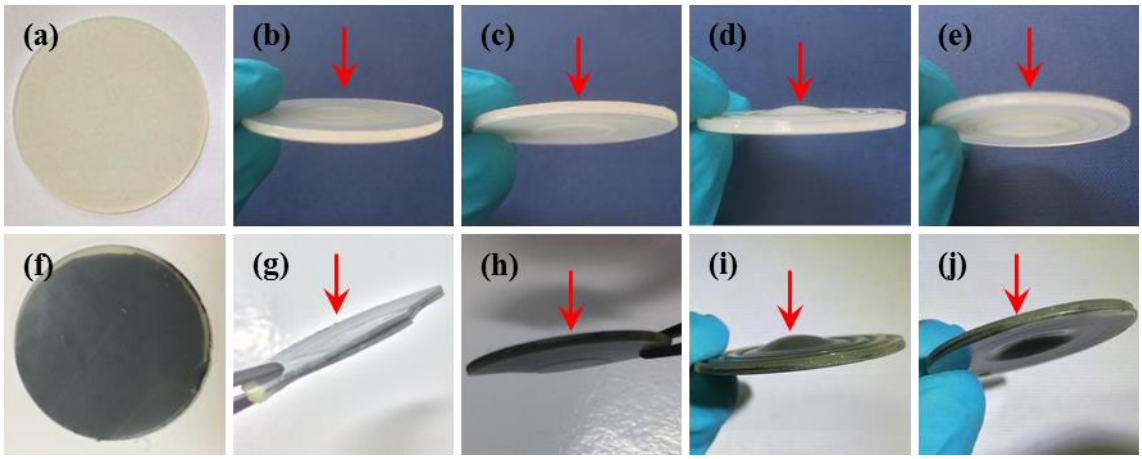

Figure 6.4. Photographs of (a) unexposed Laminate control; (b) and (c) exposed Laminate control F; (d) and (e) exposed Laminate control E; (f) unexposed GNP Laminate; (g) and (h) exposed Laminate 25F; (i) and (j) exposed Laminate 25E. Red arrows indicate the direction of H_2S flow from upstream to downstream.

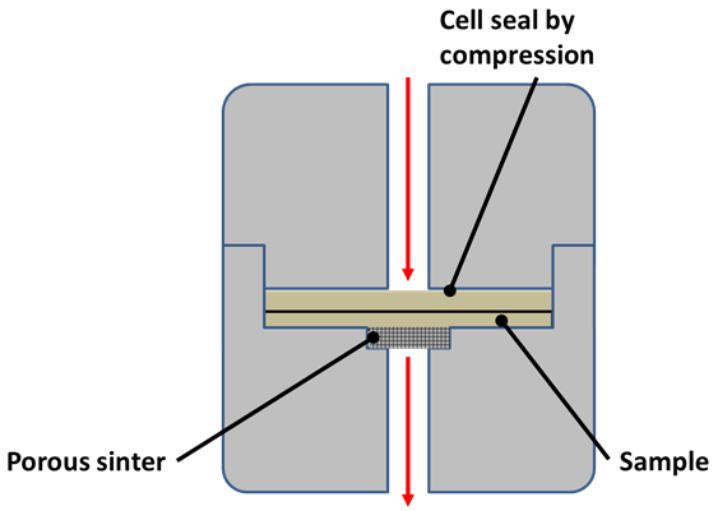

Figure 6.5. Cell schematic showing sample loading arrangement with porous sinter beneath sample and compression seal around sample circumference. Red arrows show the direction of feed and permeant gas flow.

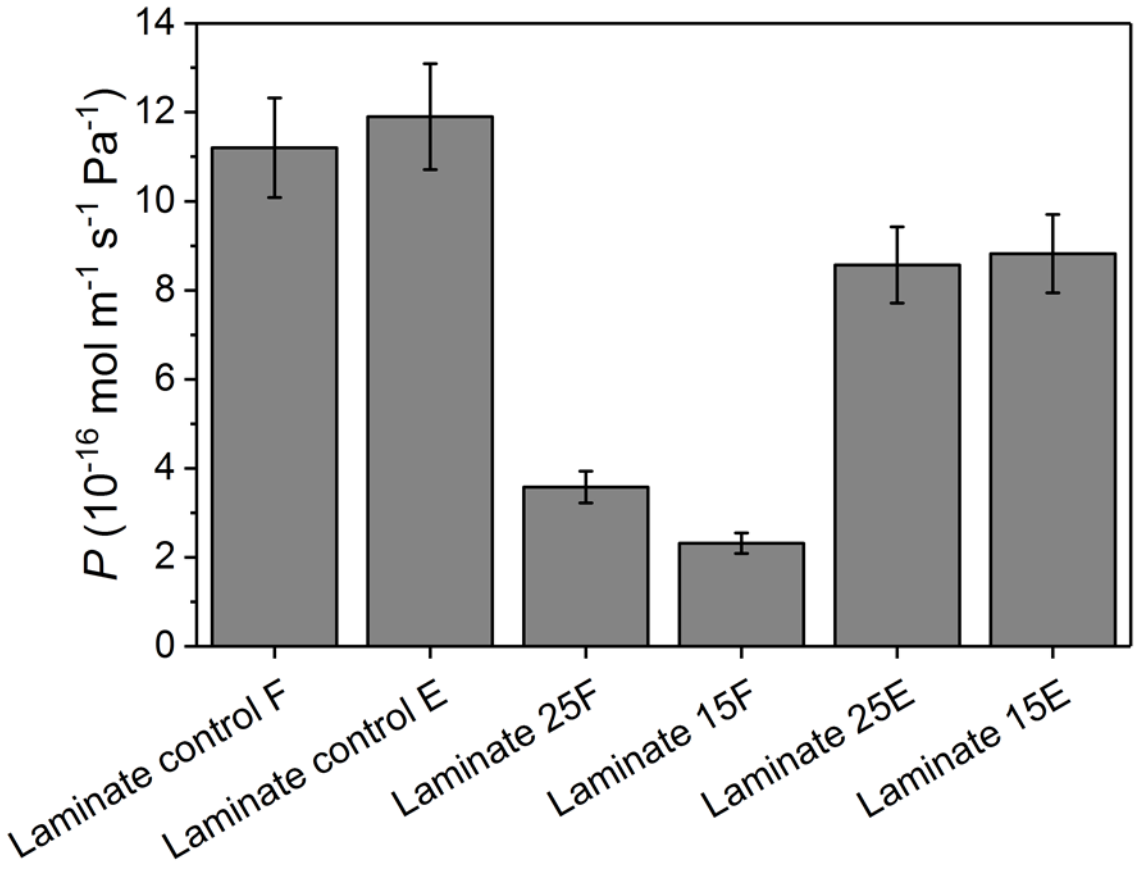

Figure 6.6. H_2S permeability coefficients of the laminate controls and GNP laminates tested at 0.2 MPa pure H_2S and 60 °C. Error bars signify a 10% estimated error.[179] Using fugacity as the driving force increases the value of *P* to 11.4, 12.1, 3.6, 2.4, 8.7 and 9.0 for the laminate samples from left to right.

The permeability coefficients of the laminated samples tested at 0.2 MPa pure H_2S and 60 °C are shown in Figure 6.6, with estimated error of 10%.[179] As can be seen, the deformed samples all had a higher permeability coefficient than the flat samples. The difference in permeability for the laminate controls did not appear to be statistically significant. Laminate 25F and Laminate 15F, showed exceptional barrier performance, reducing the permeability by almost 70 and 80%, respectively, compared to Laminate control F. Laminate 25E and Laminate 15E display a slight reduction in H_2S permeation of 20 – 30% compared to Laminate control E. The difference in permeation for GNP papers made with 25 µm and 15 µm GNPs was minimal and may not be statistically significant, particularly for the deformed samples. In any case, the improvement in barrier properties for Laminate 15F compared to Laminate 25F, due to different GNP diameters, was far less significant than the differences due to the test method employed.

SEM (Zeiss EVO60) images of Laminate 25F central GNPs-25 paper are shown in Figure 6.7. The central GNP layer delaminated into a number of layers. As shown in Figure 6.7a, there were two PA11/GNP interfaces above and below the central pure GNP paper and the central GNP paper was split in two. This shows that the adhesion between PA11 and GNPs was better than the cohesion between GNP platelets. Figure 6.7b shows the lower PA11/GNP interface, displaying quite random GNP arrangement. As can be seen in Figure 6.7c, one thin and wrinkled GNP flake could be observed folded over at the fracture surface, highlighted by an arrow, showing that there were single and few layer GNPs in the GNP paper. Figure 6.7d shows an image of a few-layered GNP protruding from the PA11 matrix, as can be seen, there was a space between the GNP flake and PA11, suggesting that there was some interfacial voiding observed.[181] It would appear, though, that the adhesion between the PA11 and GNPs was adequate to form a partially intercalated region during compression moulding.

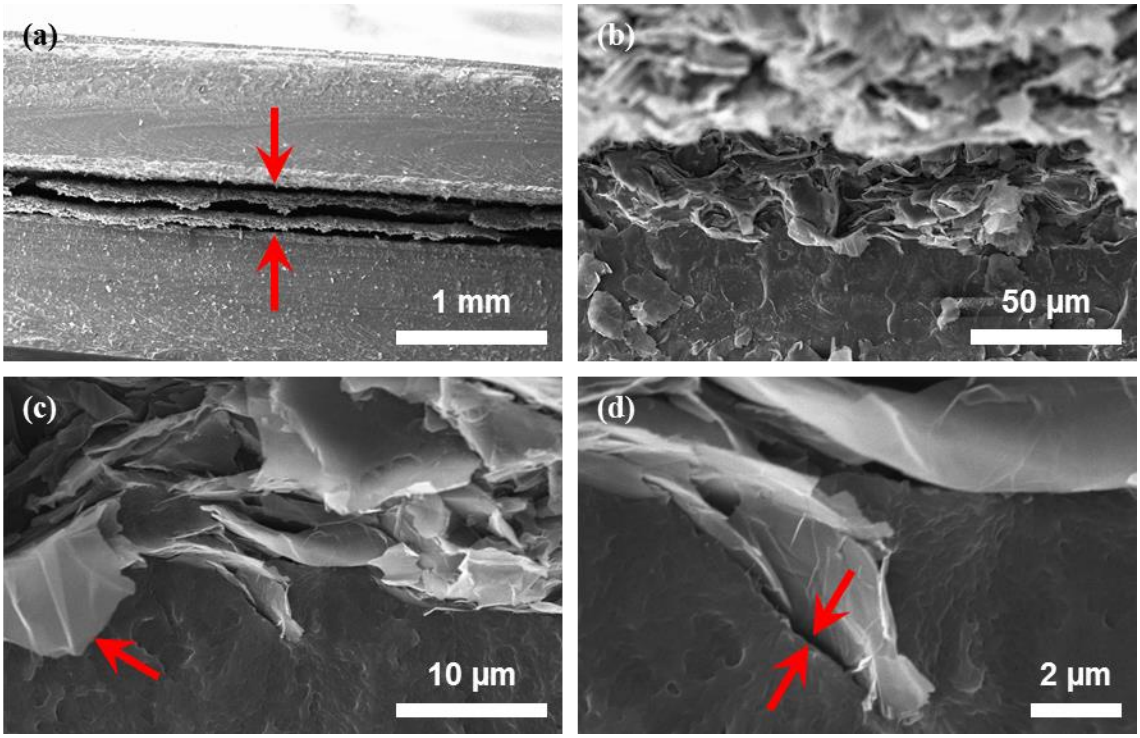

Figure 6.7. SEM images at different magnifications of Laminate 25F following testing at 0.2 MPa pure H_2S. Arrows highlight: (a) delaminated central GNP paper; (c) thin folded and wrinkled GNP flake; (d) possible interfacial void.

In order to understand the permeation behaviour of the samples, the diffusion and solubility coefficients were investigated and are presented in Figure 6.8.

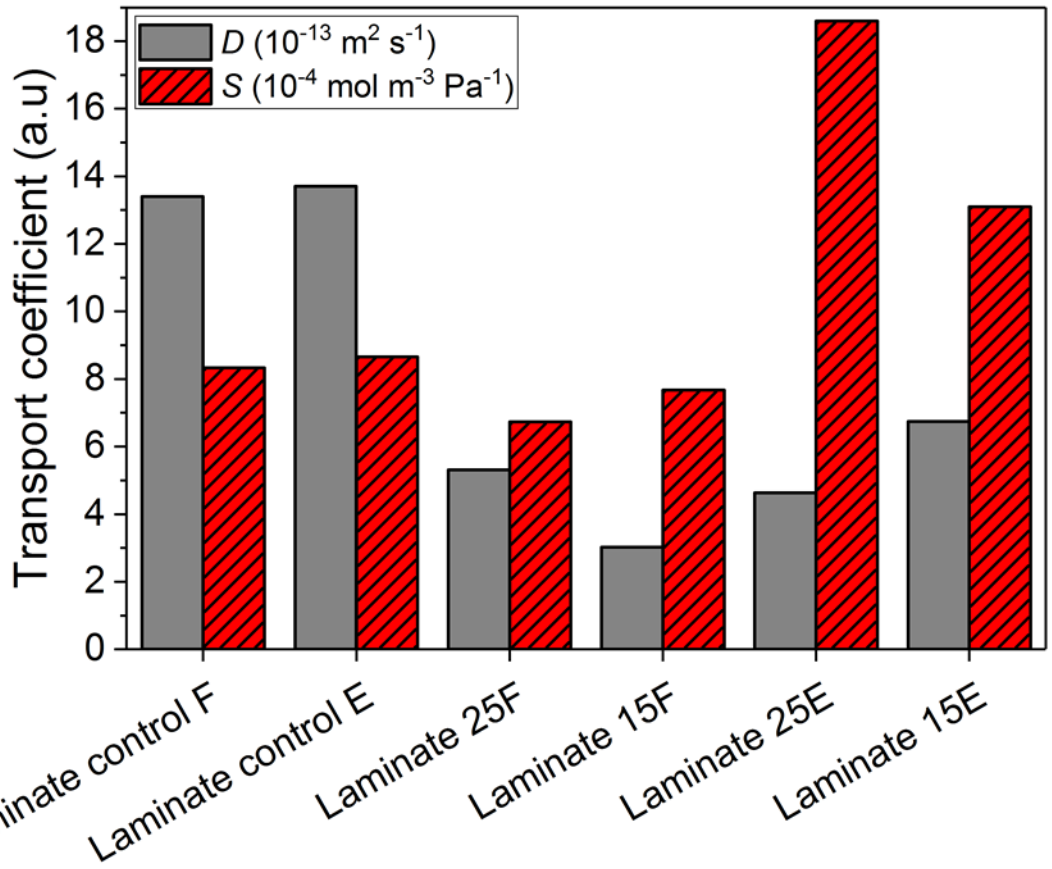

Figure 6.8. Diffusion and solubility coefficients calculated for the laminate samples tested at 0.2 MPa pure H_2S at 60 °C. Using fugacity as the driving force increases the value of *S* to 8.5, 8.8, 6.9, 7.8, 18.8 and 13.3 for the laminate samples from left to right.

As can be seen in Figure 6.8, the diffusion and solubility coefficients for the laminate control samples had very similar values. The addition of GNP papers led to a striking reduction in the diffusion coefficient due to an increasingly tortuous diffusion route for the H_2S.

The solubility coefficients for Laminate 25F and Laminate 15F were similar to the solubility coefficients for the pure polymer. The solubility coefficients for Laminate 25E and Laminate 15E increased remarkably compared to the control laminates and flat samples. The reason for such behaviour is not fully understood, however, it could be a mathematical quirk of the calculation of solubility, as follows.

It is probable that the low diffusion coefficient was the result of the highly tortuous pathway through the GNP paper at the start of the experiment. However, as the experiment continued, swelling of the matrix may have reached the threshold for

substantial deformation to occur. Upon deformation, it is likely that the GNP paper would be disturbed, possibly allowing greater diffusion, yielding an increase in the steady state permeation coefficient. That is, the initial diffusion coefficient may not be the final diffusion coefficient due to the deformation of the sample. This means that the diffusion coefficient measured in the case of the deformed samples is likely to be the diffusion coefficient associated with a sample prior to deformation. However, the steady state permeability is that associated with a deformed sample with a damaged GNP centre. As the solubility coefficient is calculated from the ratio of the permeability coefficient over the diffusion coefficient, it is possible that the solubility coefficient is artificially increased. It is worth noting at this point that the true steady state was not reached for the flat GNP laminates, suggesting that the diffusion coefficients yielded are likely to be an underestimate of the true *D* value. Additionally, the final permeability values may also be underestimated for the flat samples as the gradient used to calculate *P* was still increasing, albeit at a very slow rate. See Appendix B for experimental data plots.

6.6.2 HIGH PRESSURE PERMEABILITY STUDIES

6.6.2.1 Effect of Pressure

Table 6.2 shows the samples tested at high pressures in this section of work. The samples were initially run to the steady state at 60 °C for each pressure up to 40 MPa. Afterwards the temperature was reduced to 21 °C by ambient air cooling in order to extract preliminary activation energy data. At 40 MPa, the CO_2 undergoes a phase change upon cooling from supercritical fluid to liquid at T_C = 31.04 °C. As shown in Table 6.2, all GNP papers used in this section of work were fabricated with GNPs-25.

Table 6.3 shows the partial pressures of CO_2 and H_2S at the various applied pressures. These partial pressures were used to calculate the transport coefficients of each discrete component of the permeate.

Table 6.2. Sample codes and test conditions for samples tested at up to 40 MPa CO_2 with 1.48% H_2S in this section of work.

Sample	GNP flake diameter (μm)	GNP paper diameter (mm)	Fluid	*p* (MPa)	*T* (°C)	Gasket
2 × Laminate control	N/A	N/A	CO_2 with 1.48% H_2S	5	60	Yes
Laminate control D	N/A	N/A	CO_2 with 1.48% H_2S	5, 10, 20, 40	60, 21	Yes
Laminate A	25	40	CO_2 with 1.48% H_2S	5, 10, 20, 40	60, 21	Yes
Laminate B	25	35	CO_2 with 1.48% H_2S	5, 10, 20, 40	60, 21	Yes
Laminate C	25	35	CO_2 with 1.48% H_2S	5, 10, 20, 40	60, 21	Yes

Table 6.3. Partial pressure of CO_2 and H_2S in the feed fluid with total feed pressure, *p*.

p (MPa)	p_{CO2} (MPa)	p_{H2S} (MPa)
5	4.926	0.074
10	9.852	0.148
20	19.704	0.296
40	39.408	0.592

Photographs are presented of Laminate A (Figure 6.9a), Laminate B (Figure 6.9b), Laminate C (Figure 6.9c) and Laminate control D (Figure 6.9d) following testing at 5, 10, 20 and 40 MPa CO_2 with 1.48% H_2S. The central regions that were directly exposed to the fluid are highlighted by red dashed ellipses. As can be seen, there was substantial yellowing observed for the control sample. This was again attributed to elemental sulphur, as discussed in section 5.6.2.1. As can be seen, there are no compression rings around the circumference due to the use of gaskets for testing. Gaskets were used to reduce the likelihood of the same bulging deformation occurring during the low pressure testing in pure H_2S (Figure 6.4d, e, i and j). The large bubbles around the circumference of Laminate A were not within the test area so would not affect the barrier performance of the laminate. Quite severe bubbling may be seen within the

polymer in Laminate C which was due to insufficient drying of the PA11 prior to compression moulding.

A form of bulging occurred in Laminates B and C, as can be seen in Figure 6.9b and c, although Laminate A shows no deformation. This difference in behaviour appears to be due to the different sample construction and the way these samples reacted upon decompression. Firstly, the GNP centre became saturated with the high pressure CO_2 and 1.48% H_2S. Upon decompression, the high pressure fluid could escape from Laminate A from the unsealed edges between the two PA11 surfaces. For Laminates B and C, however, no such mechanism for pressure release from the GNP layer was possible due to the PA11 seal around the circumference. As the cell was opened, the mechanical restraints afforded by the tight seal of the cell top were relaxed and the samples were exposed to the external atmospheric pressure. Due to the large pressure gradient between the laminate centre and the relatively low pressure ambient conditions, the GNP centre was effectively inflated. This is analogous to blistering during rapid gas decompression, an important matter for polymers in high pressure applications such as oil and gas risers.[4,26,256]

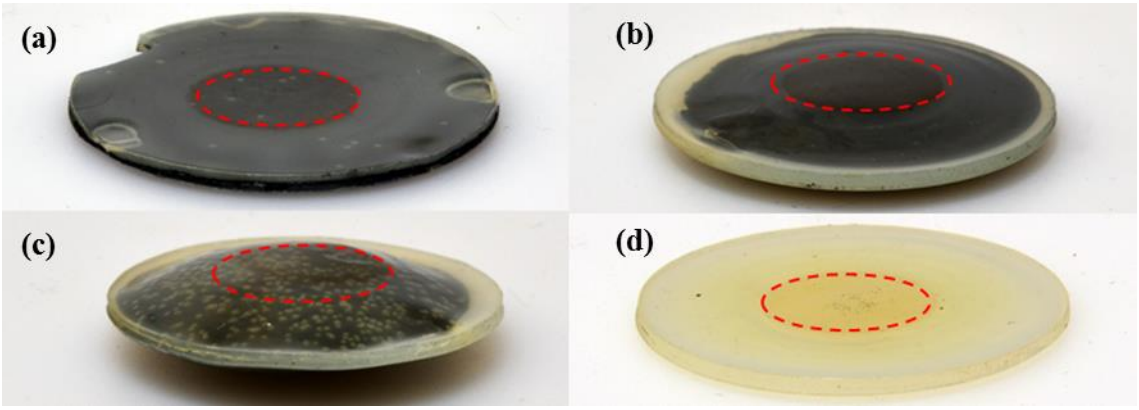

Figure 6.9. Photographs of samples following testing (a) Laminate A; (b) Laminate B; (c) Laminate C; (d) Laminate control D. The central test region is highlighted by dashed red ellipses.

As shown in Table 6.2, three control samples were ran at 5 MPa and 60 °C which were used as the control laminate average for the 5 MPa test stage. The results of which are shown in Figure 6.10. The fugacity coefficient used to calculate P_f is 0.832 and 0.78 for CO_2 and H_2S, respectively, as shown previously in Table 5.2.

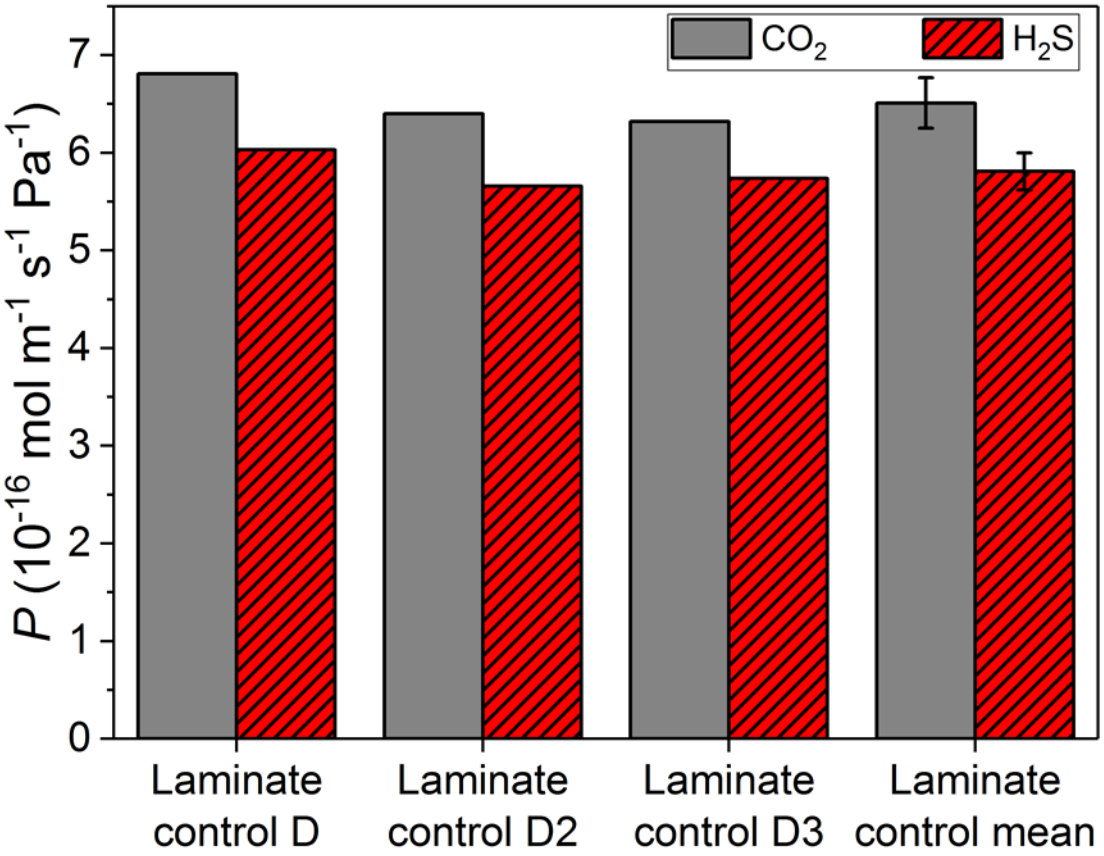

Figure 6.10. Plot showing the permeability coefficients of three control laminate samples with the average laminate control value. Error bars signify one standard deviation of the three samples. Using fugacity as the driving force increases the value of P_{CO2} to 8.2, 7.7, 7.6 and 7.8 and P_{H2S} to 7.7, 7.3, 7.4 and 7.5 for Laminate control D, D2, D3 and mean, respectively.

For pressures of 10, 20 and 40 MPa, only Laminate control D was tested, alongside single runs of Laminates A, B and C. The transport coefficients of Laminates B and C were combined ('Laminates B + C') yielding average transport coefficients for the laminates made using 35 mm diameter GNP paper. Figure 6.11 shows how the permeability coefficients of Laminates A, B, C and control D vary with total feed pressure. Generally, the permeability was reduced with increasing pressure, consistent with a reduction in free volume with increased polymer compaction.[54,93,179] There are two notable exceptions. Firstly, the selectivity of the control switches from favouring CO_2 permeation in the gas phase, to favouring H_2S permeation in the supercritical phase. This behaviour is not reflected in the GNP containing Laminates B and C, as CO_2 permeability remains higher than H_2S permeability up to 40 MPa. Secondly, the increase in H_2S permeability between 5 and 10 MPa for Laminates B and C arises as

H_2S was only detectable at pressures of 10 MPa and above. The apparent PA11 selectivity for H_2S permeation over CO_2 permeation in the control sample is not observed for the GNP laminates. This suggests that there is some size-selective sieving occurring in the GNP layers, allowing transport of CO_2 in favour of H_2S.

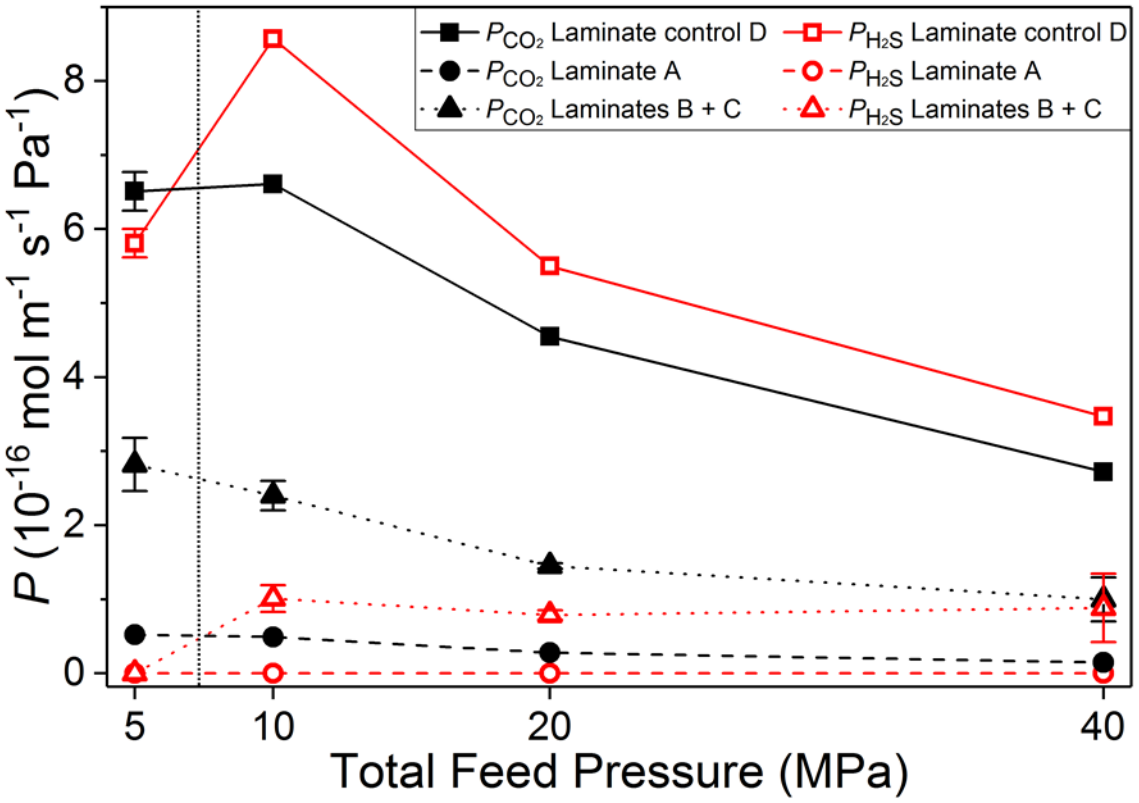

Figure 6.11. Plot of the permeability coefficients of Laminate A, combined Laminates B and C and Laminate control D. Values for Laminates B and C are averaged with the error bars signifying a single standard deviation of the two samples. Values for Laminate control D at 5 MPa are the average of all three laminate control samples shown in Figure 6.10, with standard deviation indicated by error bars. Modified from Raine *et al.*[164]. Fugacity values are provided later in section 6.6.2.3.

Compared to Laminate control D, CO_2 permeability was reduced by over half for Laminates B and C and reduced by over an order of magnitude for Laminate A for all pressures. As alluded to above, H_2S permeation was undetectable for all GNP laminates at 5 MPa. At pressures of 10 MPa and above, H_2S permeation was detected for Laminates B and C with H_2S permeability of around 20% of the Laminate control D. Remarkably, no H_2S was detected at any pressure for Laminate A. The increased barrier properties were probably due to the well-ordered GNP layers found within the laminates, leading to increased diffusion path length and blocking of defects. It would

appear that the high pressure conditions contribute substantially to the increased barrier performance. For instance, in section 6.6.1, the maximum reduction in permeability coefficient was approximately 80% at 0.2 MPa H_2S; at higher pressures the maximum reduction was over 90% for CO_2 with apparent complete shutdown in H_2S permeation. This suggests that hydrostatic compression due to the fluid pressure compresses the GNP layer into a structure approaching that of graphite, thus creating an almost impenetrable layered structure. This effect is most prominent in Laminate A as there are no radial constraints imposed on the GNP flakes and so highly efficient rearrangement and packing may block more diffusion paths. A similar explanation was suggested by Pierleoni *et al.*, whereby the platelets acted as a physical barrier to vertical transport and their efficient packing also suppressed horizontal permeation.[244] The GNP layer in Laminates B and C are constrained by the PA11 seal and so the GNPs may not rearrange to block permeation as efficiently.

SEM (Quanta 250) images of post-test Laminate control D and Laminate A following cryogenic fracture are shown in Figure 6.12 – Figure 6.15. Laminates B and C were not examined by SEM due to the inflation shown in Figure 6.9b and c.

Figure 6.12 shows the macroscopic difference between Laminate control D (Figure 6.12a) and Laminate A (Figure 6.12b), the GNP layer is highlighted with red arrows in the centre of Laminate A.

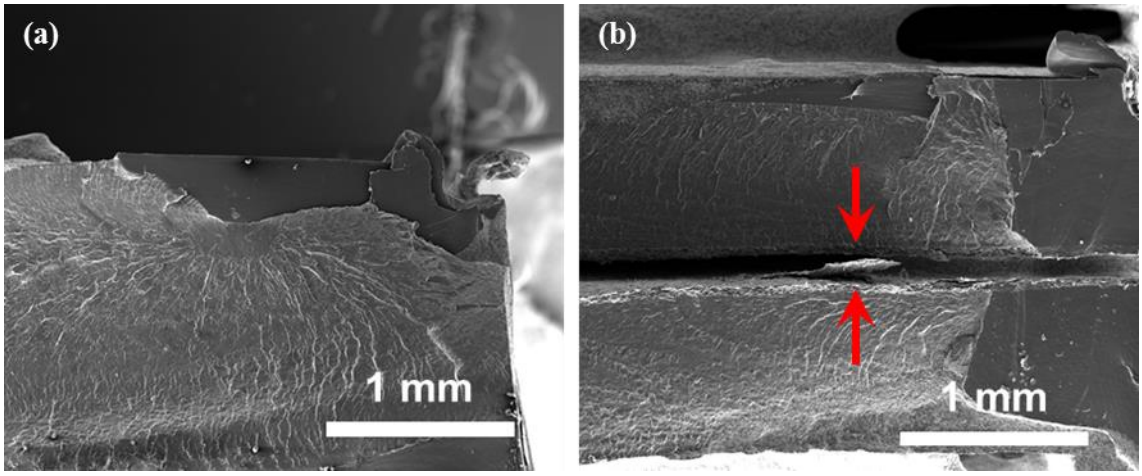

Figure 6.12. SEM image of cryogenically fractured (a) Laminate control D and (b) Laminate A. Red arrows highlight central GNP layer. Modified from Raine *et al.*[164].

More detailed morphology of the control is displayed in Figure 6.13a and the layered GNP centre of Laminate A is shown in Figure 6.13b, highlighted by red arrows. The bright regions in Figure 6.13a and b are due to partial charging at the edges of the fractured surface. As can be seen, the GNPs are arranged in a layered structure with preferential alignment perpendicular to the flow direction, which is indicated by the right hand arrow. This contrasts with the relatively random arrangement observed in the SEM of the low pressure GNP laminate (Figure 6.7b). The GNP layer structure was partially delaminated in the centre due to the SEM preparation method, thus, this structure is likely to be expanded compared to the arrangement during testing, particularly at the higher hydrostatic pressures.

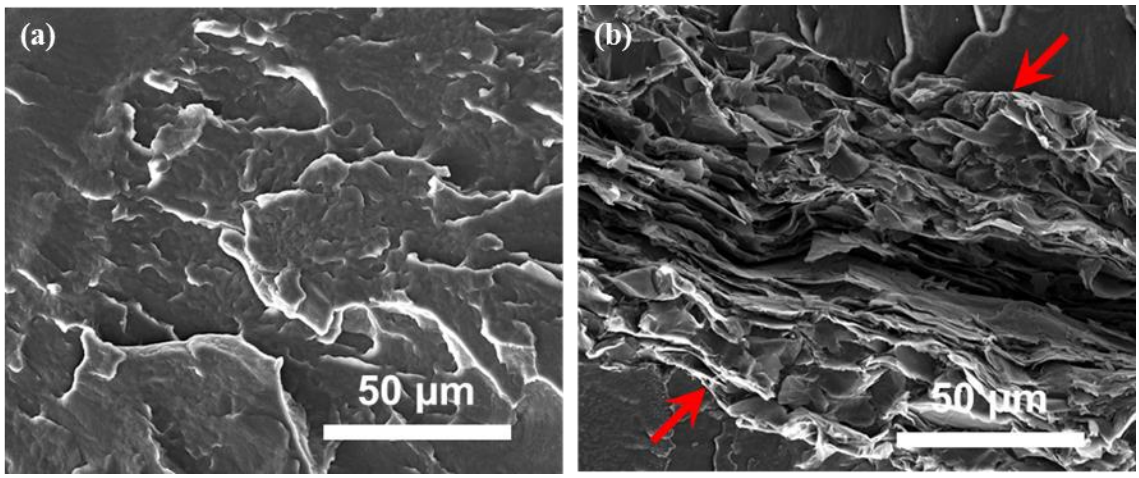

Figure 6.13. SEM image of cryogenically fractured (a) Laminate control D and (b) Laminate A. Red arrows highlight central GNP layer. Modified from Raine *et al.*[164].

Figure 6.14a shows the polymer morphology at high magnification with edge charging clearly visible. Figure 6.14b shows a GNP flake protruding from the GNP centre following delamination of the GNP paper centre. The flake has a diameter of approximately 25 µm which is the quoted average diameter of the supplied GNPs.[37]

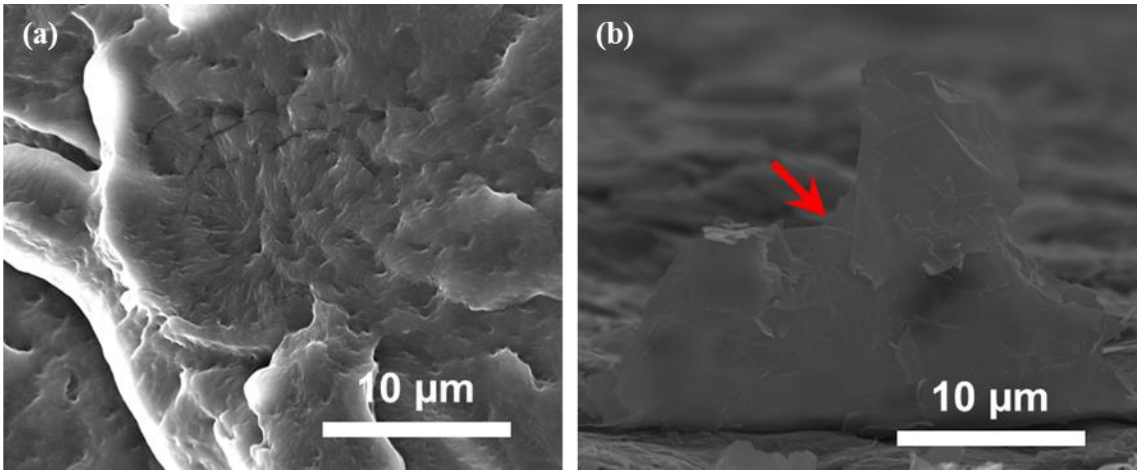

Figure 6.14 SEM image of cryogenically fractured (a) Laminate control D and (b) Laminate A. Red arrow highlights a single GNP flake protruding from the GNP paper centre. Modified from Raine *et al.*[164].

Figure 6.15a shows the polymer morphology at very high magnification. Figure 6.15b shows the PA11/GNP interface, demonstrating that some polymer flowed between GNP flakes during compression moulding. The red arrows highlight a possible interfacial void between the PA11 and GNPs which suggests that the interfacial adhesion was poor. A similar region was identified in the low pressure GNP laminate SEM (Figure 6.7d). The GNPs have a wrinkled morphology but still appear to be arranged perpendicular to the penetrant diffusion direction, indicated by the top arrow.

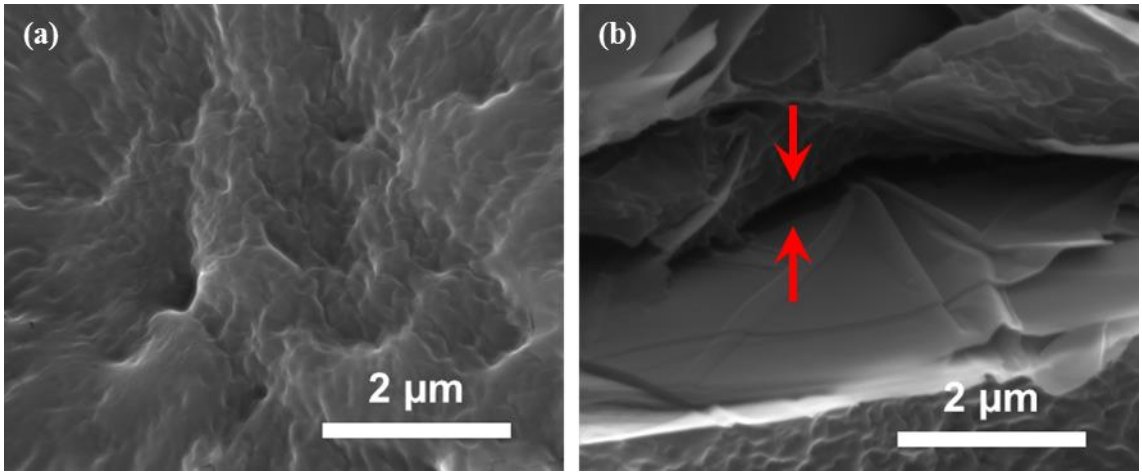

Figure 6.15. SEM image of cryogenically fractured (a) Laminate control D and (b) Laminate A. Red arrows highlight a potential interfacial void between PA11 and GNPs. Modified from Raine *et al.*[164].

Assuming that the GNPs are compressed to a structure approaching the density of graphite, ρ_{GNP} = 2.2 g cm^{-3},[37,257,258] then the thickness of the GNP papers, l_{GNP}, can be calculated using Equation 6.3.

$$l_{GNP} = \frac{m_{GNP}}{\rho_{GNP} . A_{GNP}} \qquad \text{Equation 6.3}$$

where m_{GNP} and A_{GNP} are the mass of GNPs in the laminate and surface area of the GNP layer, respectively.

The true mass of the GNP papers was calculated by subtraction of residual mass left on the nylon filter following peeling, from the mass of filtered GNPs. For Laminates A, B and C, the mass of GNPs filtered was 80.2, 80.3 and 80.2 mg, respectively. The mass of residue on the filter paper of Laminate A was not recorded; however, the residue masses for Laminates B and C were 6.1 and 4.3 mg, respectively. This gives GNP paper loadings in Laminates B and C of 74.2 and 75.9 mg, respectively. The actual mass loaded in Laminate A was estimated by subtracting the average residue mass from nine different samples, shown in Table 6.4. The mass of GNPs in Laminate A was therefore estimated as 73.5 mg (74 ± 1 mg).

Utilising Equation 6.3, the following thicknesses were calculated for the GNP layers in Laminates A, B and C: 27, 35 and 36 µm, respectively.

Table 6.4. Mass of residue left on nylon filter papers after the peeling of GNP papers for nine separate preparations. The average mass was subtracted from the filtered GNP mass for Laminate A.

Sample	**Residue mass (mg)**
1	6.1
2	4.3
3	6.6
4	8.6
5	5.8
6	6.9
7	6.5
8	8.2
9	6.9
Average	**6.7 ± 1.2**

Assuming that the permeability of neat PA11, P_{PA11}, is consistent between the control laminate and GNP-containing laminates, then the permeability of the pure GNP papers, P_{GNP}, may be calculated according to a modified and rearranged Equation 6.2:

$$\frac{1}{P_{GNP}} = \frac{1}{l_{GNP}}\left(\frac{l_{composite}}{P_{composite}} - \frac{l_{composite} - l_{GNP}}{P_{PA11}}\right) \qquad \text{Equation 6.4}$$

Total laminate thicknesses, $l_{composite}$, were measured prior to testing and had values of 1.8126, 1.8324 and 1.8566 mm for Laminates A, B and C, respectively.

The calculated values for P_{GNP} are shown in Figure 6.16, compared to P_{PA11}. Note that permeability values are on a $\log_{10}$ scale. The values for Laminates B and C are separated in the plot below and the $P_{GNP}(H_2S)$ values for Laminate A were zero so could not be plotted. $P_{GNP}(H_2S)$ values for Laminates B and C were over two orders of magnitude lower than $P_{PA11}(H_2S)$. The $P_{GNP}(CO_2)$ values for Laminates B and C were almost two orders of magnitude less than $P_{PA11}(CO_2)$. The $P_{GNP}(CO_2)$ for Laminate A was three orders of magnitude less than $P_{PA11}(CO_2)$. Although permeability is a material property and so should be consistent for particular materials, it appeared that the behaviour of the GNP layer was dependent upon laminate preparation.

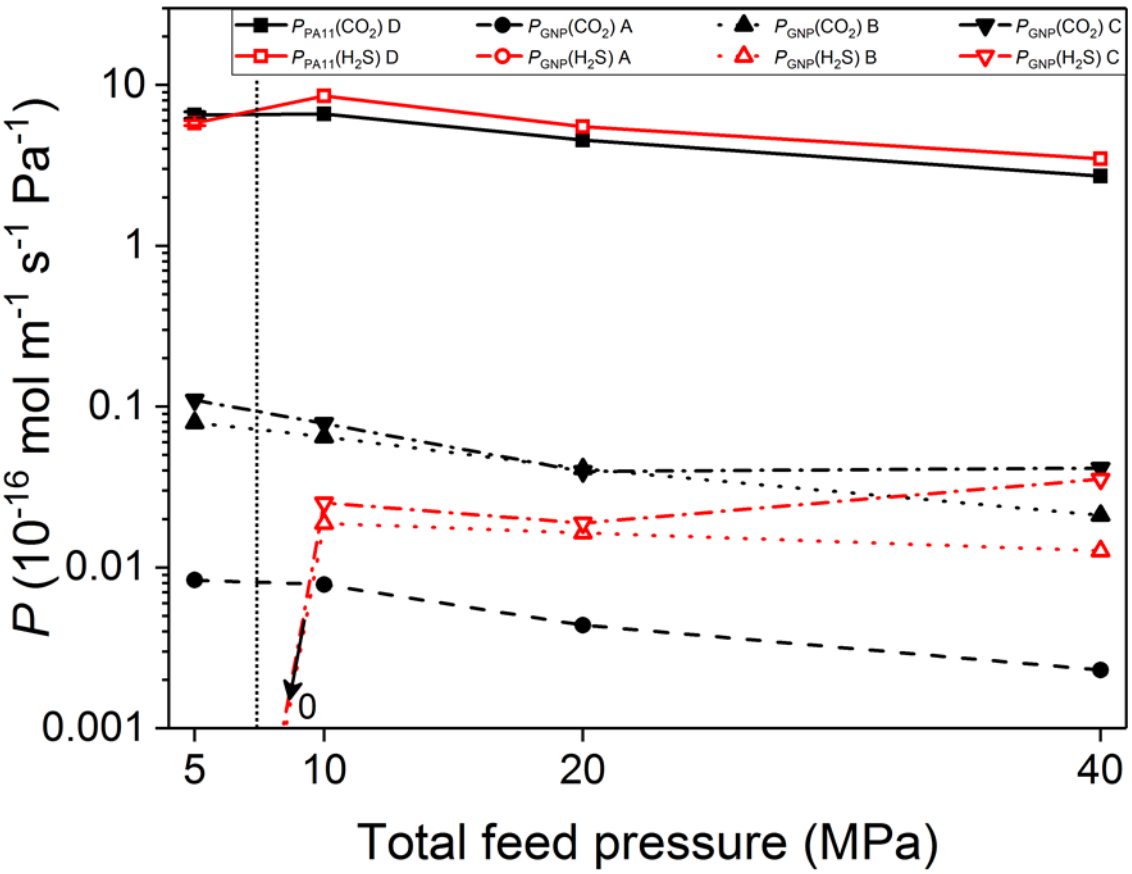

Figure 6.16. Plot showing variation in CO_2 and H_2S permeability of the GNP layers in Laminates A, B and C compared to the permeability of pure PA11, Laminate control D. Laminate control D values at 5 MPa are averaged for three laminate control samples.

The variation of flux with applied pressure is shown in Figure 6.17. Flux, *J*, is described by Equation 2.1, repeated below for clarity, and is essentially a measure of permeation without accounting for sample thickness or pressure of the system.

$$J = \frac{Q}{A.t} \qquad \text{Equation 2.1}$$

where *Q* is the amount of permeant detected for sample area, *A*, at time, *t*. Note that the *y*-axis contains a break as the CO_2 flux of Laminate control D and Laminates B and C are approximately an order of magnitude higher than the CO_2 flux for Laminate A. The control flux for H_2S is over an order of magnitude less than the control CO_2 flux due to the mismatch in partial pressures of each component. Comparing the permeability coefficients (Figure 6.11) to the flux in Figure 6.17, it can be seen that regardless of the low flux, the permeability of H_2S was very high and comparable to CO_2.

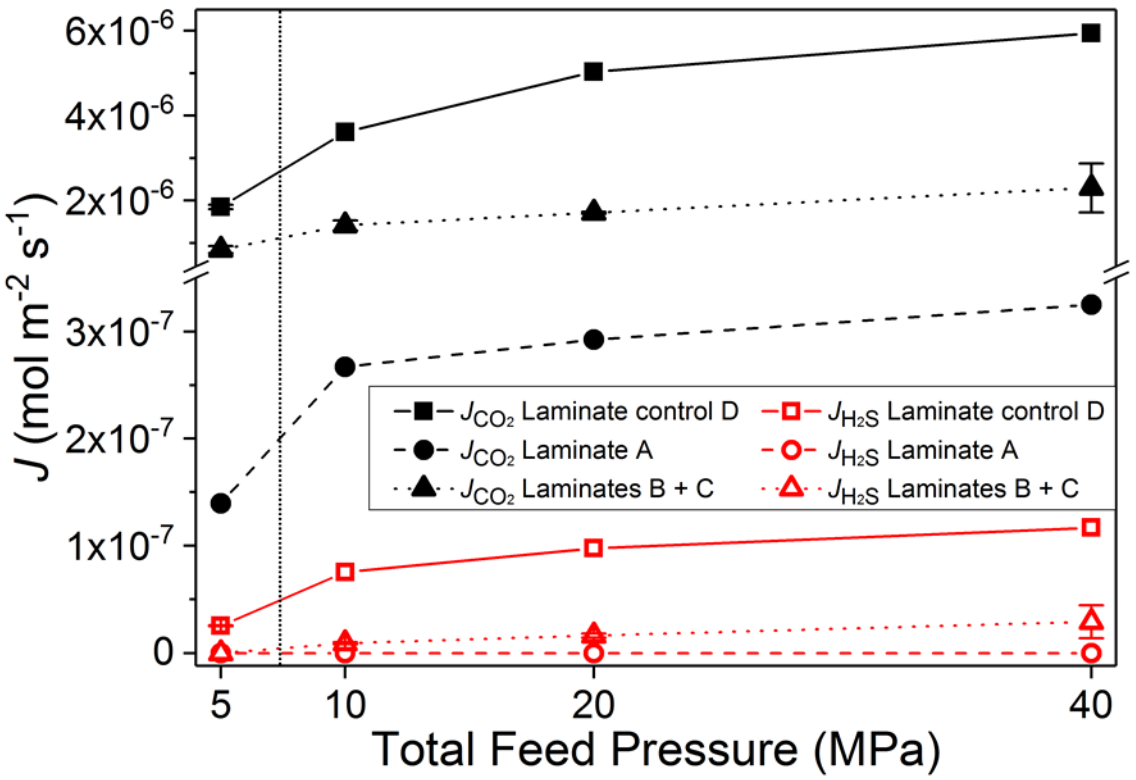

Figure 6.17. Plot of the flux of Laminate A, combined Laminates B and C and Laminate control D. Values for Laminates B and C are averaged with the error bars signifying a single standard deviation for the two samples. Values for Laminate control D at 5 MPa are the average of all three laminate control samples, with standard deviation indicated by error bars. Modified from Raine *et al.*[164].

As can be seen, the flux rises quite sharply between 5 and 10 MPa for each sample before beginning to level off at higher pressures. Since the flux does not greatly increase with pressure, the apparent permeability reduces due to division by the total pressure. The levelling off of the flux at higher pressures suggests that the polymer becomes compressed so transport of CO_2 and H_2S becomes more difficult, regardless of the increased concentration of potential penetrants. The true barrier properties of the specific laminates may be observed by comparing the flux permeating through the membranes.

The diffusion coefficients are shown in Figure 6.18 for the laminates tested. For the same sample, the diffusion coefficients for CO_2 were higher than those of H_2S. CO_2 therefore appeared to behave as a smaller, less-interacting penetrant than H_2S. This may be due to dipole-dipole interactions between H_2S and amide bonds in the PA11

backbone. The same interactions are likely to lead to the binding and subsequent oxidation of H_2S to yield elemental sulphur as shown in Figure 5.16.

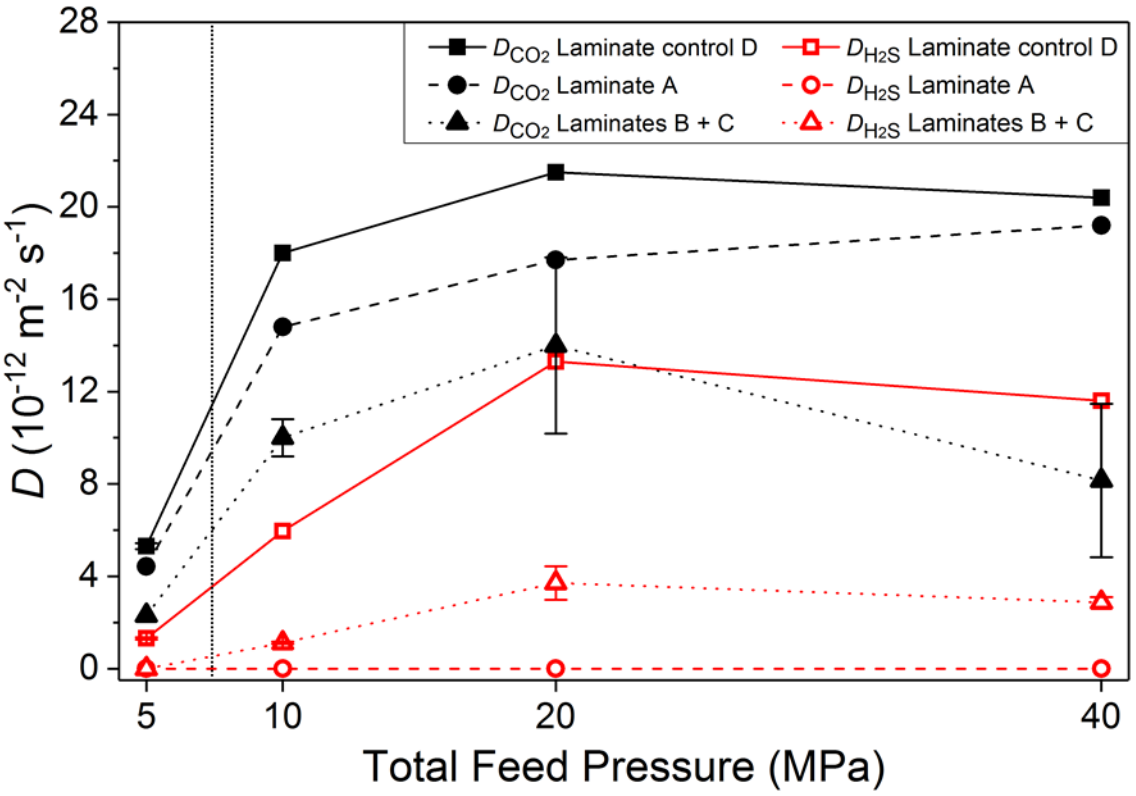

Figure 6.18. Plot of the diffusion coefficients of Laminate A, combined Laminates B and C and Laminate control D. Values for Laminates B and C are averaged with the error bars signifying a single standard deviation for the two samples. At 5 MPa, *D* was calculated for Laminate C only, due to missing Laminate B data. Values for Laminate control D at 5 MPa are the average of two laminate control samples with standard deviation indicated by error bars. Modified from Raine *et al.*[164].

The slower diffusion of H_2S is reflected in the very high solubility coefficients shown in Figure 6.19. Slow diffusion of H_2S, and subsequent high solubility compared to CO_2 has been observed in polyamide-imide systems.[255] At high pressures, a decrease in *S* with increasing pressures has been observed.[93]

Interestingly, the CO_2 diffusion coefficients for Laminate A were not reduced as much as those of Laminates B and C. This may be due to the increased thickness of GNP layer in Laminates B and C, creating a more tortuous path for diffusion than in Laminate A. Regardless of the relatively large CO_2 diffusion coefficient for Laminate A, the steady state permeability was by far the lowest. This manifests itself by Laminate

A having a very low solubility coefficient, as can be seen in Figure 6.19. The solubility of CO_2 in Laminates B and C and Laminate control D were comparable, suggesting that the solubility behaviour of Laminate A was unusual.

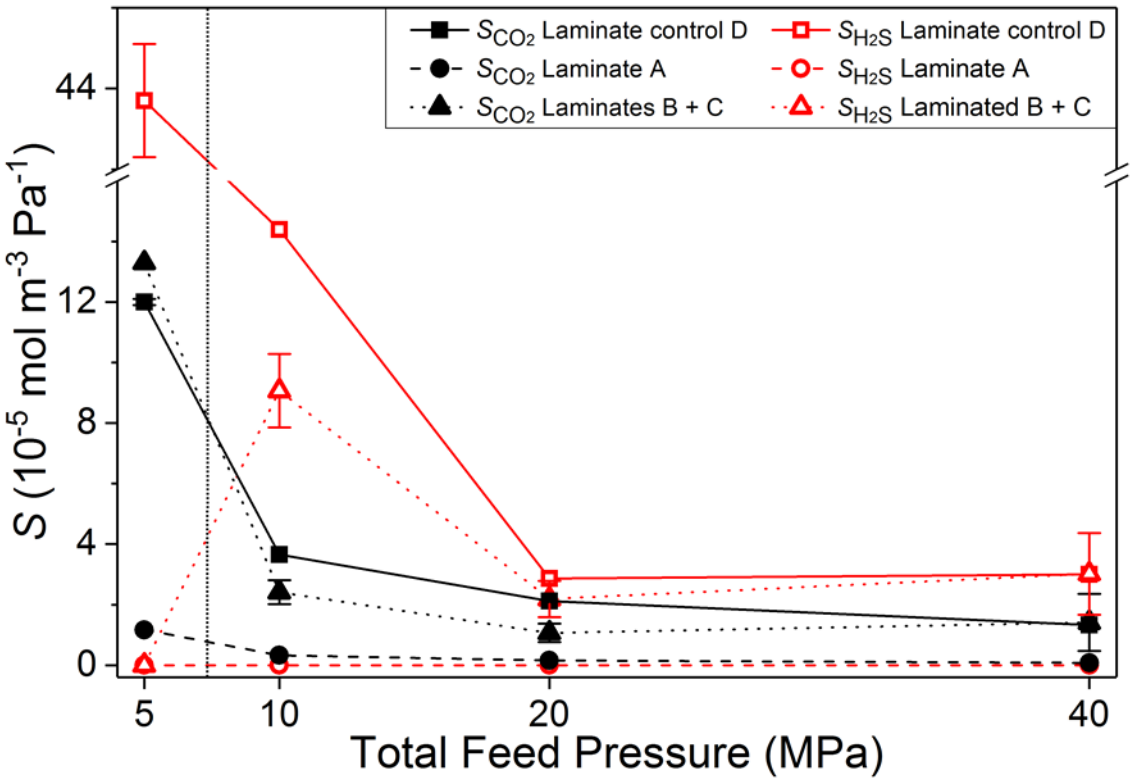

Figure 6.19. Plot of the solubility coefficients of Laminate A, combined Laminates B and C and Laminate control D. Values for Laminates B and C are averaged with the error bars signifying a single standard deviation for the two samples. At 5 MPa, *S* was calculated for Laminate C only, due to missing Laminate B data. Values for Laminate control D at 5 MPa are the average of two laminate control samples with standard deviation indicated by error bars. The values of *S* derived from fugacity are tabulated in Appendix C.

The apparent complete shutdown in H_2S leads to two possible conclusions: either the GNP layer acts as a molecular sieve, blocking H_2S permeation while letting CO_2 through; or the H_2S permeation is reduced to a level undetectable to the GC. If small quantities of H_2S were diffusing through the GNP layer then it would be expected, from earlier experiments, that the PA11 would capture some H_2S as elemental sulphur. To test this, the top and bottom PA11 layer in Laminate A were peeled apart and separately mounted for SEM and XRF characterisation, with the GNP layer facing up (Figure 6.20).

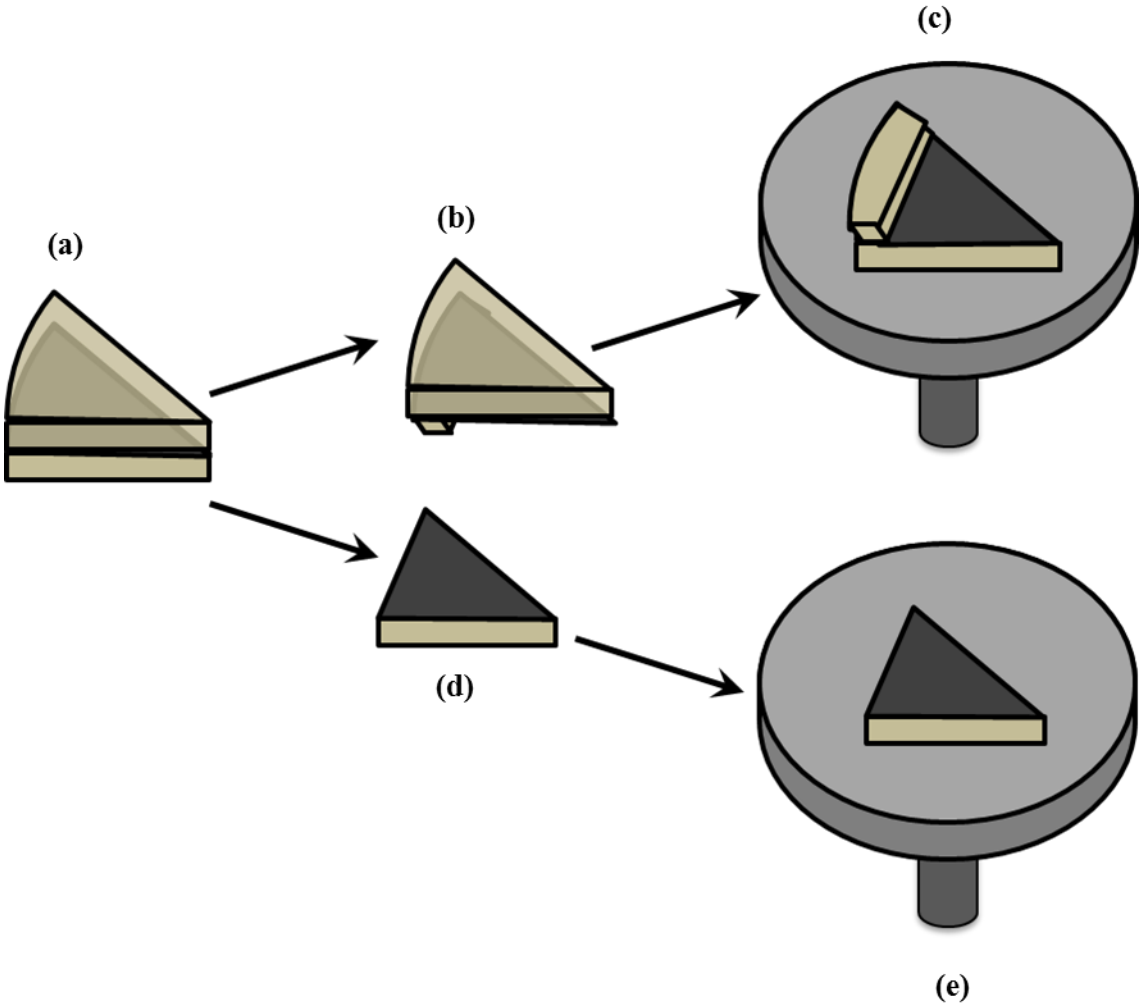

Figure 6.20. XRF sample preparation: (a) sectioned Laminate A sample is fractured into sample. Top surface (b), mounted as shown in (c). Bottom surface (d), mounted as shown in (e).

Elemental analysis was performed in a SEM chamber by collecting characteristic X-rays. XRF mapping of the sulphur K_α peak is shown for the top layer and bottom layer of Laminate A in Figure 6.21 and Figure 6.22, respectively. Since the incident X-rays travelled through the whole sample, there was no depth sensitivity, so the sulphur could be contained at any point in the side of the laminate that was tested.

As shown in Figure 6.21 there was sulphur present in Laminate A above the GNP paper layer. This was to be expected as scrubbing of H_2S has been observed in an earlier section (5.6.2). The presence of sulphur beneath the GNP layer (Figure 6.22) suggests that the small amounts of H_2S that did diffuse through the GNP layer were possibly scrubbed by the PA11. Since no H_2S was detected at any pressures, it would appear that

the PA11 still had capacity to adsorb H_2S, thus keeping the flow of H_2S below the GC detection limit.

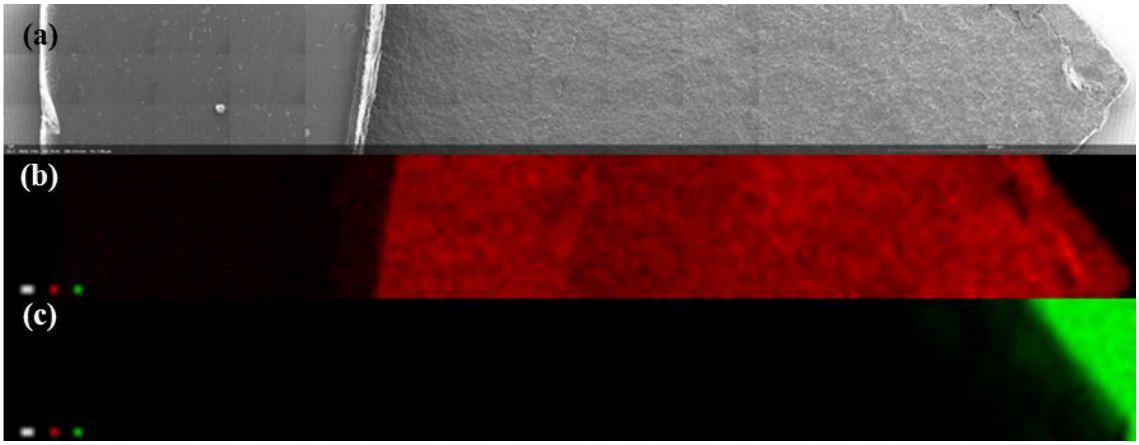

Figure 6.21. Internal surface of the top PA11 layer in Laminate A. (a) SEM image of the surface; (b) sulphur XRF map in red; (c) aluminium (stub) XRF map in green.

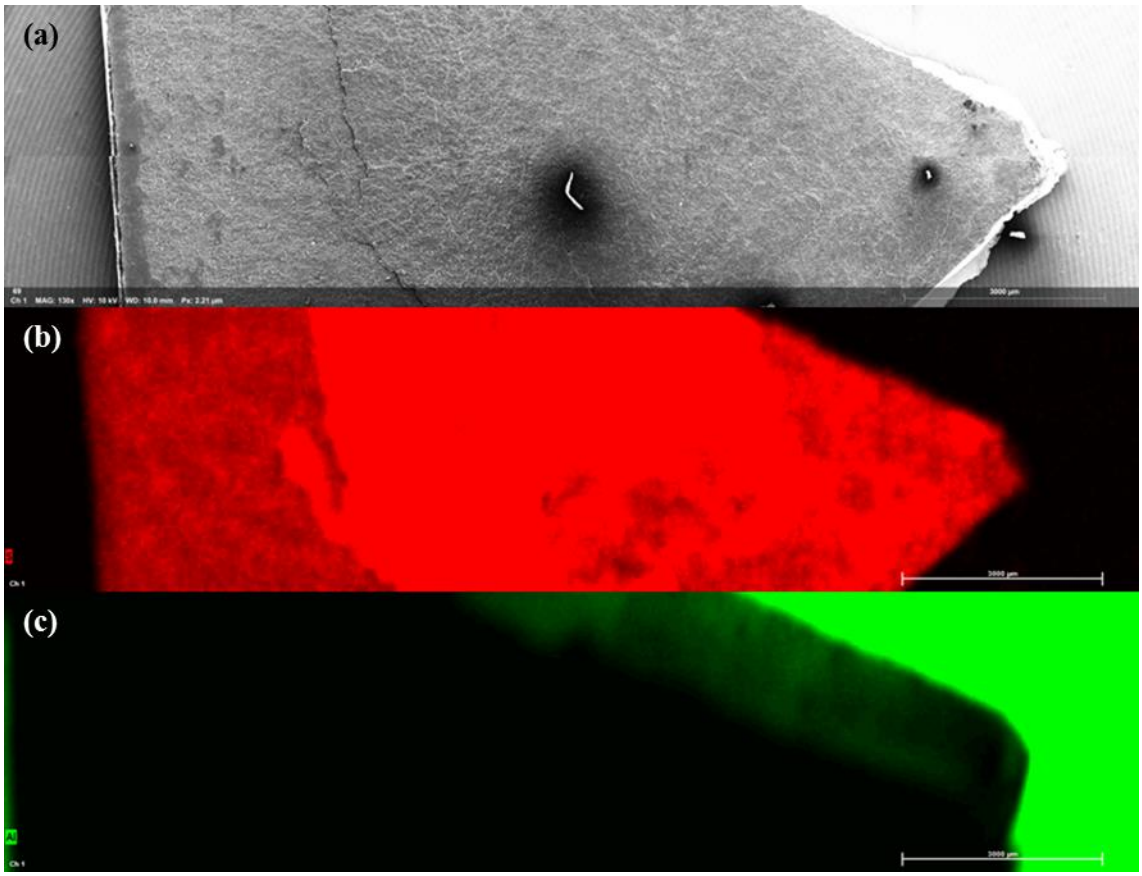

Figure 6.22. Internal surface of the bottom PA11 layer in Laminate A. (a) SEM image of the surface; (b) sulphur XRF map in red; (c) aluminium (stub) XRF map in green.

6.6.2.2 Effect of Temperature

As outlined in section 2.5.2, the activation energy of permeation, E_P, may be extracted from a plot of ln$P$ against 1/T, as shown in Equation 2.24, repeated below for clarity:

$$P(T) = P_0 \exp\left(-\frac{E_P}{RT}\right) \qquad \text{Equation 2.24}$$

The plot of ln(P) against 1/T yields a straight line with the equation shown below, where the gradient is the negative activation energy over the ideal gas constant, R.

$$\ln\left(\frac{P(T)}{P_0}\right) = \left(-\frac{E_P}{R}\right).\frac{1}{T} \qquad \text{Equation 6.5}$$

Typically, the steady state permeabilities are used for calculation of E_P, which was only possible for CO_2 as the permeability of H_2S was reduced to below the detection limit at between 40 and 50 °C. It would be useful to be able to extract activation energies without necessarily reaching the steady state at each temperature. This would reduce experimental times but would also allow activation energies to be extracted for H_2S, as H_2S could only be detected during the dynamic cooling stage.

In this work, the temperature was reduced to 21 from 60 °C by ambient air cooling. The temperature reduction was not controlled and the steady state was not reached at individual temperatures. The instantaneous flux across the membrane was simply multiplied by the sample thickness and divided by partial pressure to yield a value for the permeability with reducing temperature. As the temperature was reduced, the quantity of H_2S quickly became undetectable, and for Laminate A, no H_2S was detected at all. CO_2 reached the steady state at 21 °C for all samples. At 40 MPa, the fluid mix was supercritical above T_C = 31 °C and liquid below T_C. It is worth noting that the temperature was reduced from above the PA11 T_g (~ 40 °C) to below the T_g. However, supercritical CO_2 has been known to reduce the T_g of some polymers.[259]

A plot of ln(P_{CO2}) at 60 and 21 °C against 1/T is shown in Figure 6.23 (solid symbols and lines). Also plotted are ln(P_{CO2}) calculated from individual flux values for the dynamic cooling between the two steady state regions, that is, permeability calculated from non-steady state data (hollow symbols and dashed lines). As can be seen, there was reasonable agreement between the visual appearance of the plots regardless of the method. Indeed, the values of E_P calculated are shown in Table 6.5, and show reasonably good agreement with all values around 40 kJ mol^{-1}. The values are around 5

kJ mol^{-1} higher than literature values.[54,60] The greater activation energy found in this work, compared to the literature, may be due to compression of the PA11 matrix because of the 40 MPa applied pressure. Matrix compression would mean that the energy required to push chain segments apart would be higher than at lower applied pressures. The literature values were calculated at 10 and 0.02 MPa pressure differences which are unlikely to have compressed the PA11 to such a great extent.[54,60] The GNP paper does not appear to have altered the CO_2 E_P. As the E_P remained constant regardless of the GNP layer, the permeation of CO_2 appeared to be defect driven.[260] That is, permeation through pinholes or defects in flakes, or around flakes through porous regions dominated. It may therefore be assumed that the CO_2 did not interact strongly with the GNP layer.

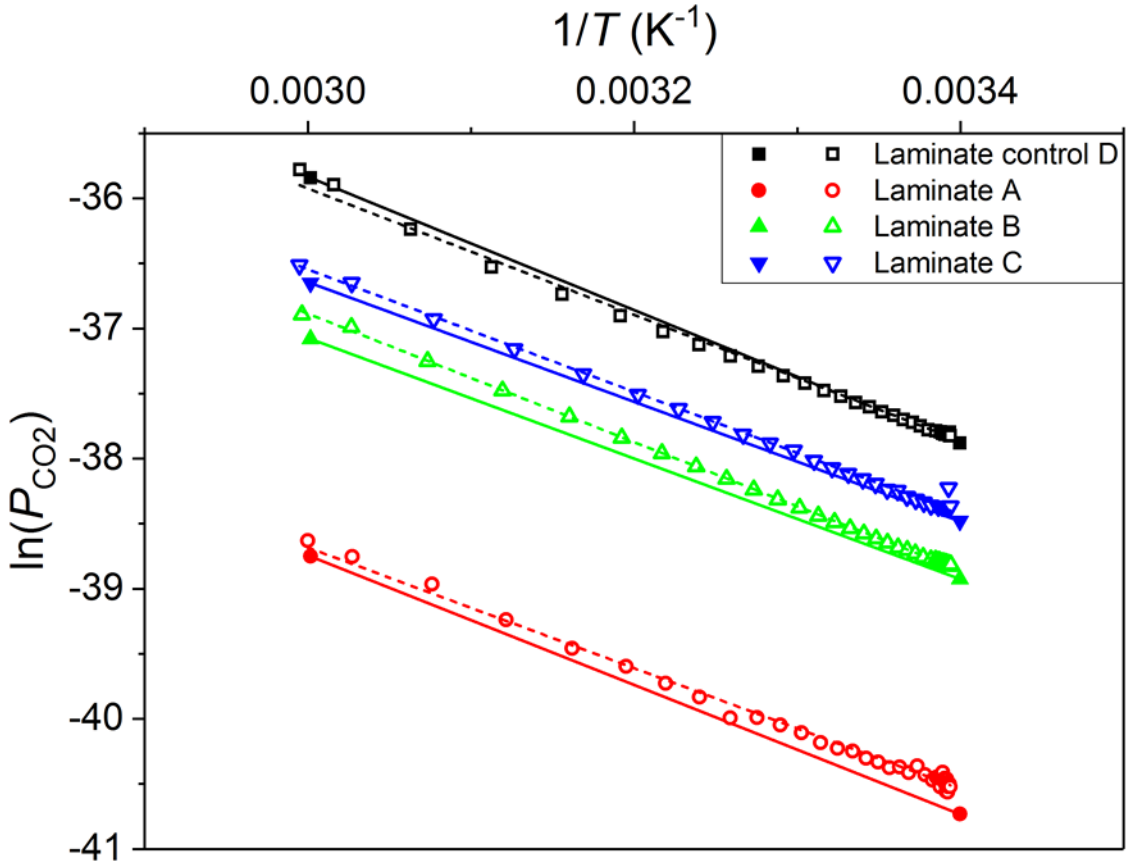

Figure 6.23. Plot of ln(P_{CO2}) against 1/T with P_{CO2} values calculated from steady state at 40 MPa, 60 °C and at 40 MPa, 21 °C (solid symbols and lines) compared to values when P_{CO2} is calculated for individual flux quantities for temperatures from 60 to 21 °C (hollow symbols and dashed lines).

Table 6.5. Calculated CO_2 E_P values for the two different methods of extracting activation energy data.

Sample	E_P **(kJ mol^{-1})***	E_P **(kJ mol^{-1})†**
Laminate control D	42.6	40.4
Laminate A	41.4	38.5
Laminate B	38.5	41.0
Laminate C	38.2	39.1
PA11 Flaconnèche *et al.*[54]	35	N/A
PA11 Ash *et al.*[60]	34	N/A

*Values from steady state calculation

†Values from dynamic cooling calculation

Figure 6.24 shows the CO_2 and H_2S data calculated from individual flux values as the temperature was reduced. Note the break in *y*-axis. The H_2S plots clearly have a steeper gradient than the CO_2 plots meaning that the calculated E_P values for H_2S were greater than those of CO_2. The calculated values are shown in Table 6.6. The activation energy of permeation for H_2S appeared to be affected by the addition of a GNP layer. This suggested that it was harder for the H_2S to diffuse through the GNP layer than the CO_2. However, the data used for the calculation is limited, due to the shutdown of H_2S permeation after only a few data points were collected (Figure 6.24). No data in the literature was available as a comparison for the activation energy of permeation for H_2S. As previously discussed in section 4.6.6.4, the activation energy for diffusion is expected to increase with increased penetrant size. H_2S has a larger kinetic diameter than CO_2 at 3.6 Å compared to 3.3 Å, so activation energy for H_2S is likely to be higher than for CO_2.[53]

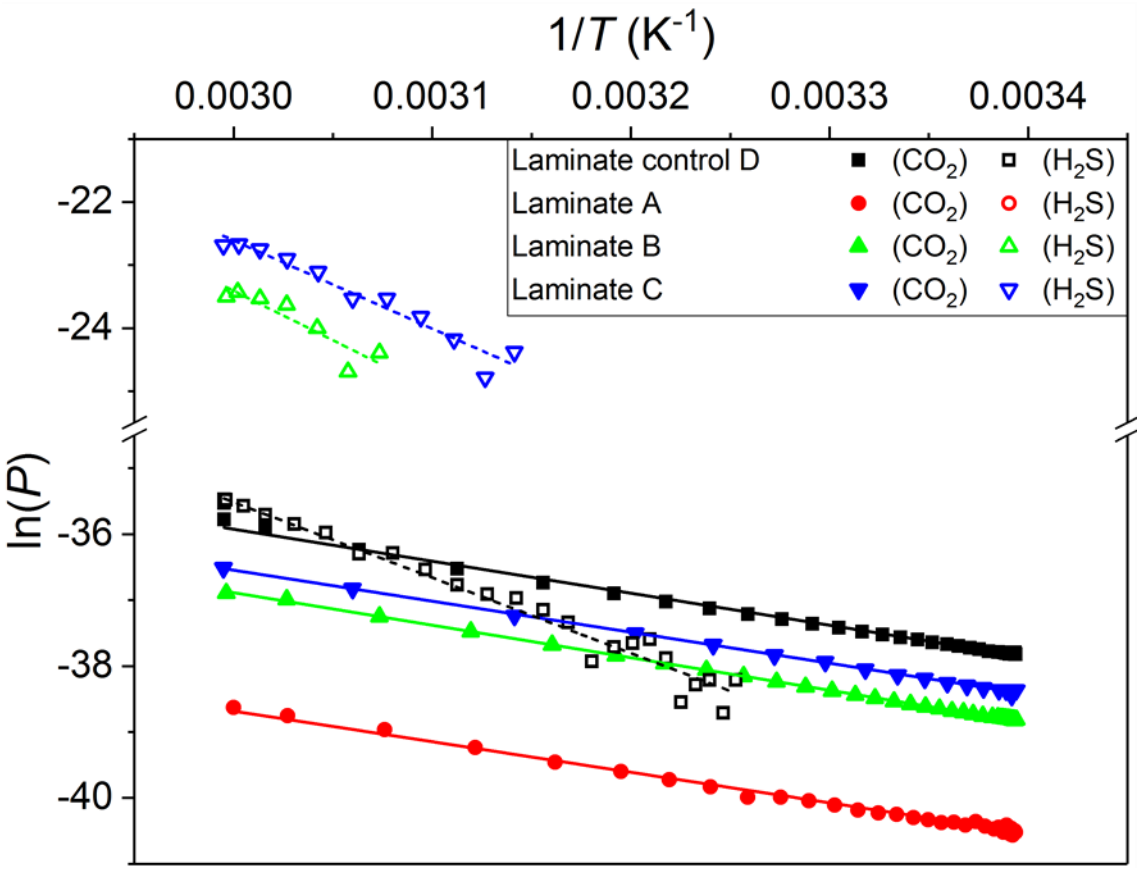

Figure 6.24. Plot of ln(P) against 1/T where P is calculated for individual flux quantities for temperatures from 60 to 21 °C for CO_2 and H_2S. Solid symbols correspond to CO_2 values and hollow symbols correspond to H_2S values.

Table 6.6. Calculated H_2S E_P values for the laminate samples.

Sample	**E_P (kJ mol^{-1})**
Laminate control D	95.2*
Laminate A	N/A†
Laminate B	130*
Laminate C	116*

*Values from dynamic cooling calculation
†No data

6.6.2.3 Effect of Fugacity

As outlined in section 2.8.3 and section 4.5.6, the nonideality of CO_2 and H_2S leads to deviations from ideal behaviour.

Figure 6.25 shows the change in apparent CO_2 permeability when the permeability coefficient is calculated with either the partial pressure or partial fugacity. Figure 6.26

shows the variation in apparent H_2S permeability when calculated with partial pressure or partial fugacity. The fugacity coefficients used for the 10 MPa were interpolated from the data supplied by the NIST REFPROP software, as shown in section 4.5.6. The permeability values are plotted against the total feed pressure rather than partial pressure or equivalent component fugacity, however the component fugacity values are shown in Table 6.7. All values of fugacity derived transport coefficients are displayed in Appendix C.

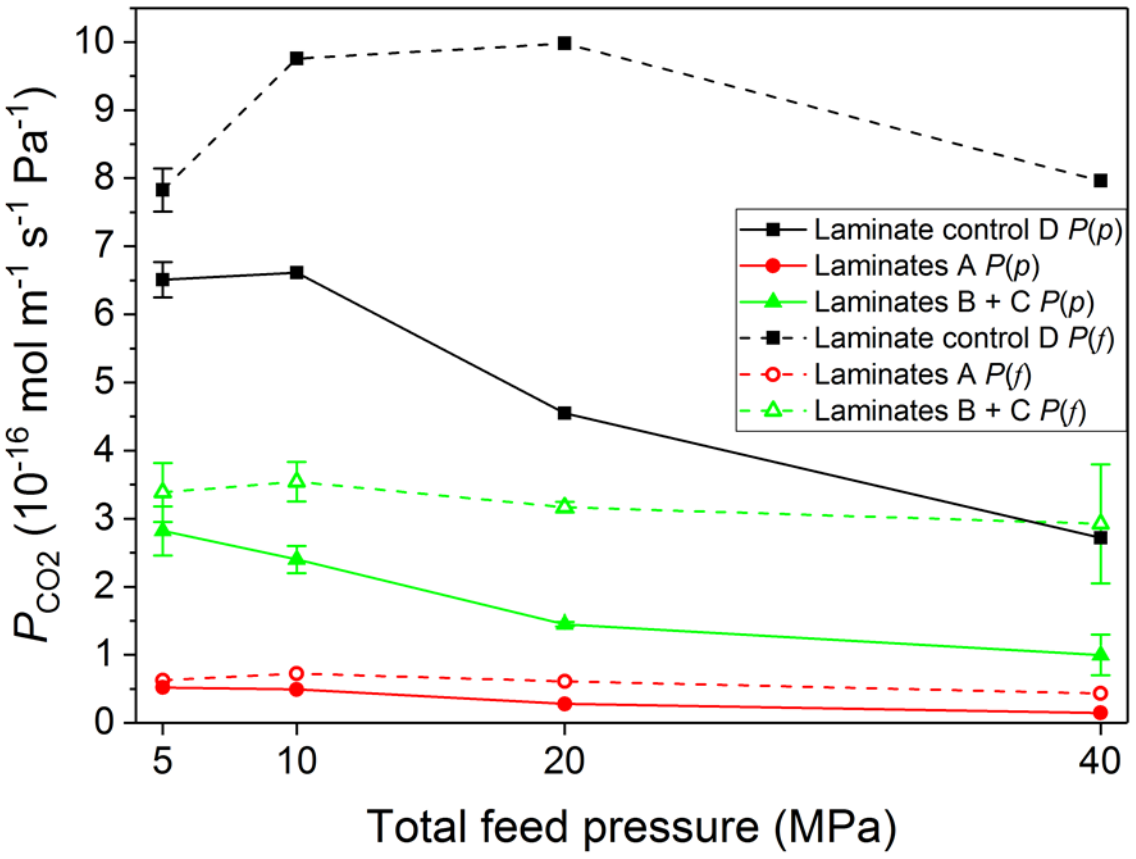

Figure 6.25. Variation of CO_2 permeability coefficient when calculated with partial pressure, $P(p)$, or component fugacity, $P(f)$, with total feed pressure. 10 MPa fugacity coefficients were not yielded from NIST REFPROP software, so were interpolated. Standard deviation of samples shown by error bars.

As can be seen in Figure 6.25 and Figure 6.26, the effect of using fugacity instead of pressure is to increase the permeability coefficient, particularly at higher pressure/fugacity. It is worth noting, however, that the change in barrier performance at a particular pressure remains consistent, as the permeability values are simply scaled by a constant. Therefore, for comparison purposes for a particular permeating molecule at a particular pressure, there is no change in the relative barrier performance when using

partial fugacity instead of partial pressure. There is a change in the general shape of the permeability coefficient variation with pressure, when using fugacity. This suggests that the shutdown in permeation is exaggerated when using hydrostatic pressure, instead of fugacity, at higher feed pressures.

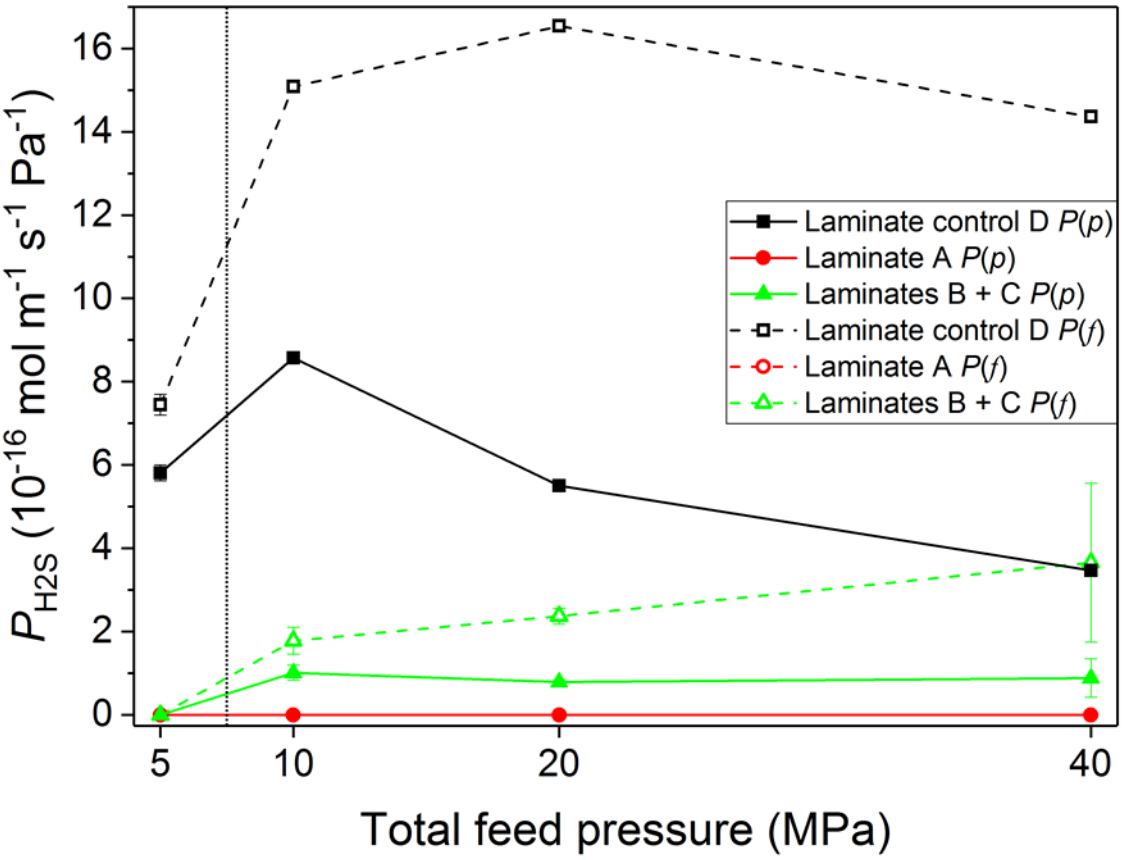

Figure 6.26. Variation of H_2S permeability coefficient when calculated with partial pressure, $P(p)$, or partial fugacity, $P(f)$, with total feed pressure. 10 MPa fugacity coefficients were not yielded from NIST REFPROP software, so were interpolated. Standard deviation of samples shown by error bars.

Table 6.7. Relationship between total feed pressure, p, partial pressures, p_{CO2} and p_{H2S}, and partial fugacity values, f_{CO2} and f_{H2S}, calculated using the fugacity coefficients φ_{CO2} and φ_{H2S}.

p (MPa)	p_{CO2} (MPa)	p_{H2S} (MPa)	f_{CO2}* (MPa)	f_{H2S}* (MPa)	φ_{CO2}†	φ_{H2S}†
5	4.926	0.074	4.10	0.058	0.832	0.780
10	9.852	0.148	6.67	0.084	0.678	0.568
20	19.704	0.296	8.98	0.098	0.460	0.332
40	39.408	0.592	13.5	0.14	0.342	0.242

*Calculated by Equation 2.29
†Values calculated from NIST REFPROP software

Figure 6.27 compares how the permeability coefficients of CO_2 and H_2S are changed when calculated with component fugacity. Figure 6.27 is the fugacity analogue of Figure 6.11. As the fugacity coefficients for CO_2 and H_2S differ, the relative changes in permeability coefficients cannot be disregarded. Using fugacity instead of pressure appears to increase the H_2S permeability coefficients relative to the CO_2 permeability coefficients. Indeed, the H_2S permeability coefficients are around 40% greater than the CO_2 permeability coefficients in the control samples at 10 MPa and above. The difference between H_2S and CO_2 permeability coefficients when using partial pressure, rather than fugacity is only around 20% (Figure 6.11).

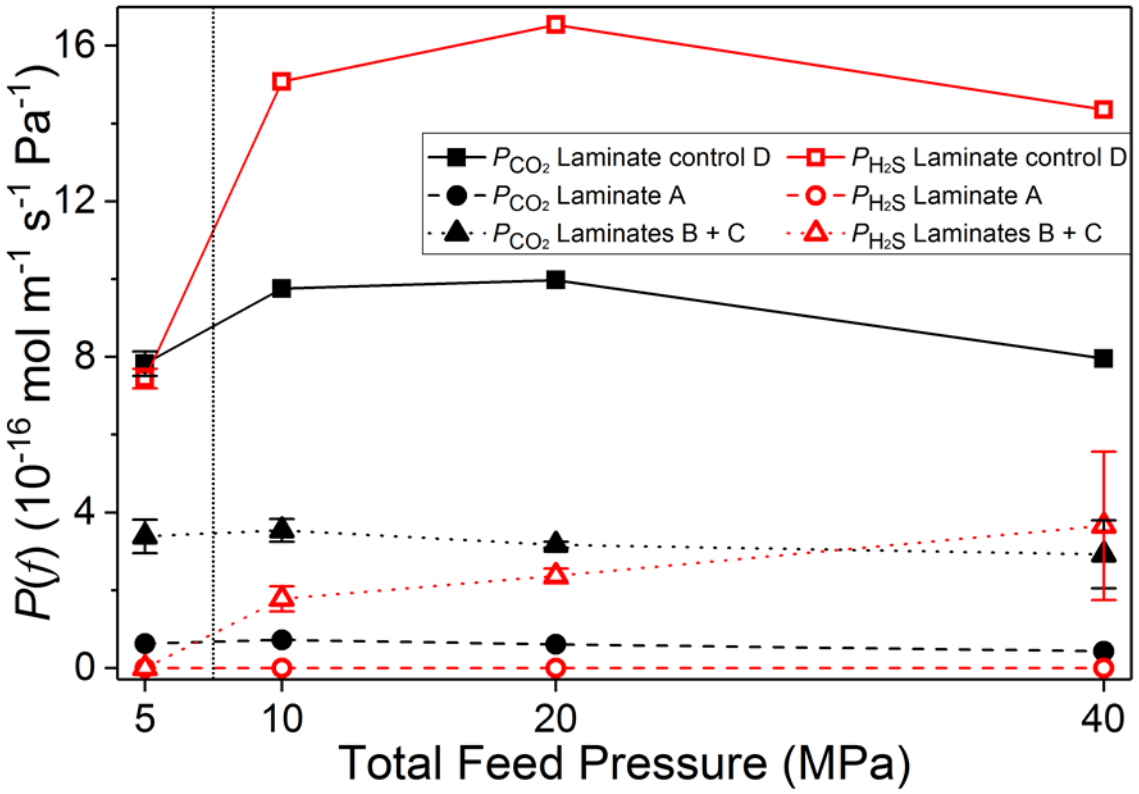

Figure 6.27. Plots of apparent permeability coefficients for CO_2 and H_2S against total feed pressure, calculated with component fugacity rather than partial pressure. Standard deviation of samples shown by error bars.

6.6.2.4 Graphene Oxide Laminate Sample – Preliminary Results

As outlined in the preparation of GO25 paper in section 6.4.5, the GO25 appeared to form an excellent barrier layer by maintaining a high vacuum during filtration. GO has already been proved to form an excellent barrier layer, as demonstrated in the literature.[261,262] Therefore, a preliminary investigation of a single htGO25 (40 mm diameter GO25 heat treated at 300 °C) laminate was carried out at 5 MPa CO_2 with 1.48% H_2S at 60 °C, the results of which are compared to the GNP laminates and control laminates (Figure 6.28). It is clear from the results presented that the htGO25 layer does not reduce the permeability coefficients of CO_2 and H_2S to levels comparable to the GNP papers, when comparing apparent permeabilities.

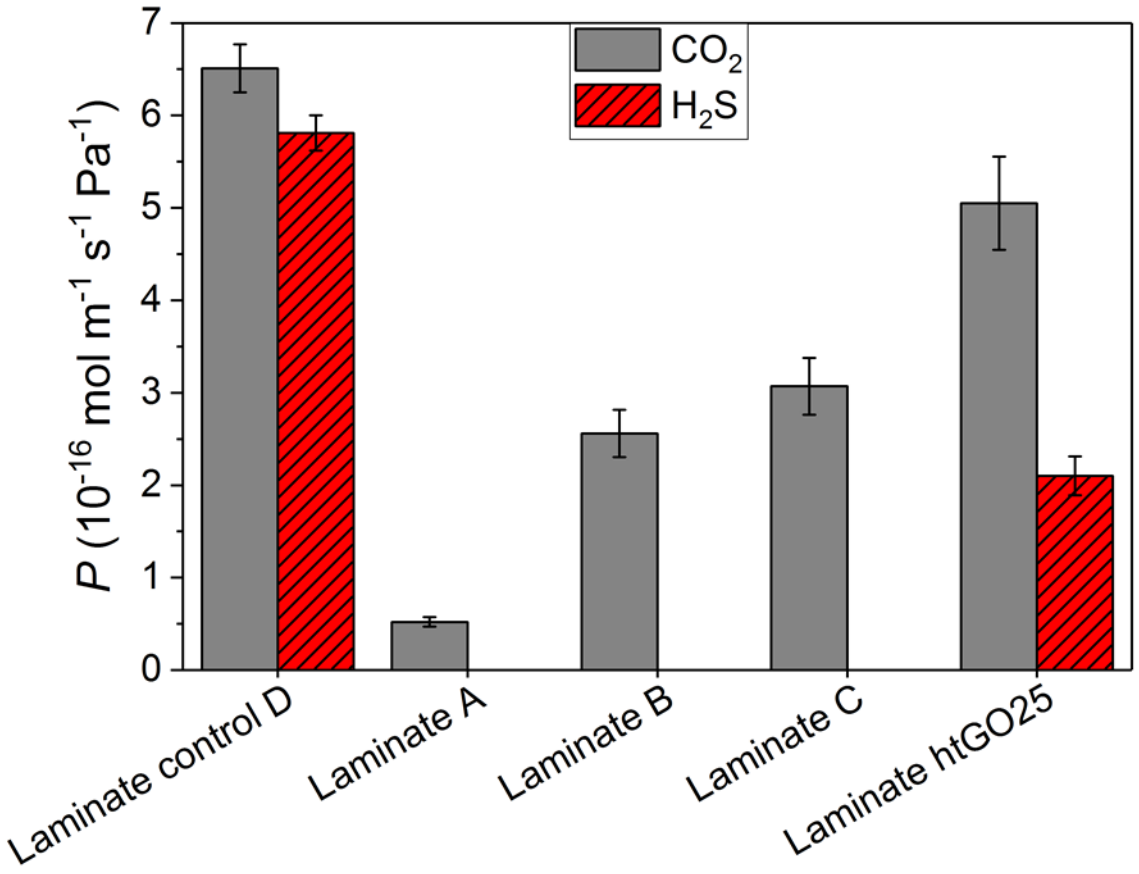

Figure 6.28. Comparison of the apparent CO_2 and H_2S permeability coefficients for the Laminate samples. Error bars for Laminate control D are the standard deviation of the three samples tested. All other error bars are 10% estimated error. Using fugacity as the driving force increases the value of P_{CO2} to 7.8, 0.63, 3.1, 3.7 and 6.1 and P_{H2S} to 7.5, 0, 0, 0 and 2.7 for Laminate control D, Laminate A, B, C and htGO25, respectively.

There is a reduction in CO_2 permeability of around 30% and H_2S permeation was reduced by approximately 65%. This behaviour suggests that the htGO25 has molecular sieving properties, with preferential transport of CO_2 over H_2S.

Although every effort was made to heat treat the GO25 paper slowly, in order to allow slow diffusion of degradation species from the matrix, it would appear that the hole defects left behind allowed permeation. Upon heat treatment, the *d*-spacings for GO25 are reduced as the functionality that keeps the basal planes of the GO apart is reduced. XRD confirmed the reduction of *d*-spacings as shown in Figure 6.29 and Table 6.8.

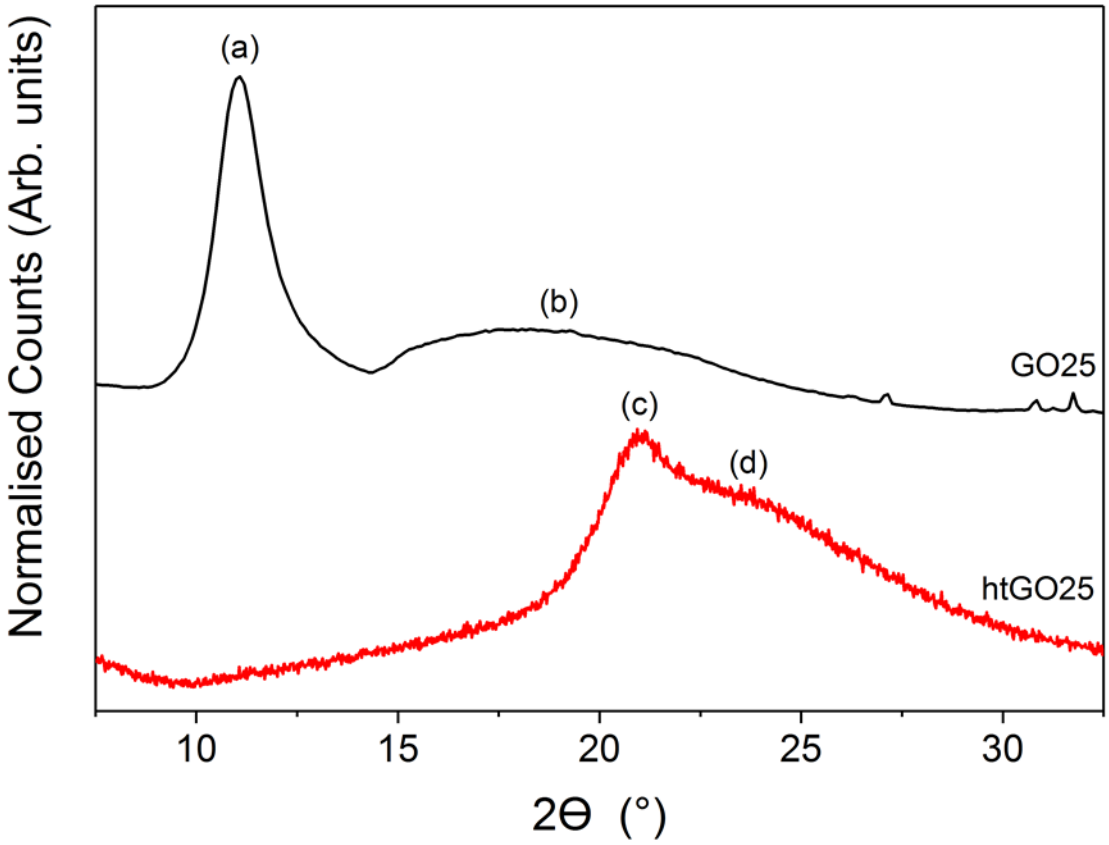

Figure 6.29. XRD diffractograms of GO25 and htGO25 (heat treated at 300 °C). Note that htGO25 (300 °C) is not to be confused with trGO25 (220 °C) in Figure 3.10.

Lorentzian curve fitting of the GO25 and htGO25 peaks was carried out and the *d*-spacings were calculated according to Bragg's Law, Equation 3.8, repeated below. The results are shown in Table 6.8.

$$d = \frac{\lambda}{2 \sin \theta}$$ Equation 3.8

Table 6.8. Peak properties for labelled peaks in Figure 6.29 following Lorentzian curve fitting.

Peak	**2Θ (°)**	***d* (nm)**
a	11.1	0.80
b	18.5	0.48
c	21.0	0.42
d	23.8	0.37

Additionally, the mechanism for the high permeation reduction observed in the GNP laminates seemed to be reliant on the rearrangement of flakes to block permeation. Qualitatively, the GO25 paper remained quite flexible after heat treatment, suggesting excellent adhesion was maintained between the GO platelets. This adhesion meant that the htGO25 flakes would not be able to rearrange effectively to block permeation.

Calculation of the permeability of the htGO25 layer may be calculated in an analogous fashion to the GNP calculation earlier. Assuming that the majority of the htGO25 has a *d*-spacing of 0.37 nm, according to the XRD in Figure 6.29, then the density of the htGO25 may be calculated. 0.37 nm is the smallest *d*-spacing identified by XRD fitting and so will yield the densest possible configuration of the htGO25. This would yield the thinnest value for the htGO25 thickness and, thus, the lowest value for the htGO25 permeability.

It was assumed that the htGO25 would be less dense than graphite (GNP layer) with ρ_{GNP} = 2.2 g cm^{-3}.[37,257,258] Multiplication of ρ_{GNP} by the *d*-spacing of the GNPs (0.34 nm) yields a mass per unit area for graphene-like planes; division by the htGO25 *d*-spacing (0.37 nm) provides an estimated density of htGO25 of ρ_{htGO25} = 2.02 g cm^{-3}. Substituting GNP values for htGO25 values in Equation 6.3 with m_{htGO25} = 29.8 mg, ρ_{htGO25} = 2.02 g cm^{-3} and A_{htGO25} = 12.57 cm^2 yields a thickness for htGO25 paper of l_{htGO25} = 11.7 µm. The total thickness of the htGO25 laminate was 1.8662 mm. Substituting htGO25 values into Equation 6.4 yields the htGO25 paper result shown in Table 6.9, compared to the values for the GNP layers and pure PA11 at 5 MPa.

As can be seen, the effective CO_2 permeability of htGO25 paper, $P_{htGO25}(CO_2)$, is 50 times less than the value of $P_{PA11}(CO_2)$. The value of $P_{htGO25}(H_2S)$, is almost 300 times less than the value of $P_{PA11}(H_2S)$. However, the GNPs consistently out-perform the htGO25 – particularly for H_2S – although the effective CO_2 permeability of the htGO25 is comparable to those of Laminates B and C.

Table 6.9. Permeability of Laminate control D (neat PA11, P_{PA11}) compared to the calculated values for pure GNP A, GNP B, GNP C and htGO25 papers. Data for 5 MPa CO_2 with 1.48% H_2S, 60 °C.

Sample	P_{CO2} **(10^{-16} mol m^{-1} s^{-1} Pa^{-1})**	P_{H2S} **(10^{-16} mol m^{-1} s^{-1} Pa^{-1})**
Laminate control D	6.51	5.81
GNP layer A*	0.00835	0
GNP layer B*	0.0797	0
GNP layer C*	0.110	0
htGO25 layer*	0.139	0.0206

*Calculated using Equation 6.4

Photographs of Laminate htGO25 following testing with a protective gasket are shown in Figure 6.30. Red dotted circles indicate the region directly exposed to the feed gas (top) and pressed onto the sinter support (bottom). Extensive bubbling was observed within both PA11 layers. The warped top surface of Laminate htGO25 (Figure 6.30a) appeared to be due to hydrostatic compression of the PA11 into the bubble voids during testing at 5 MPa. The bubbles beneath the htGO25 can be clearly seen in Figure 6.30b. The bubbles occurred during sample preparation, not during high pressure testing, possibly due to trapped degradation products that were squeezed from the paper during moulding. These bubbles are likely to have affected the performance of the htGO25 paper centre somewhat, as they are directly within the test region and were large enough to cause sample deformation.

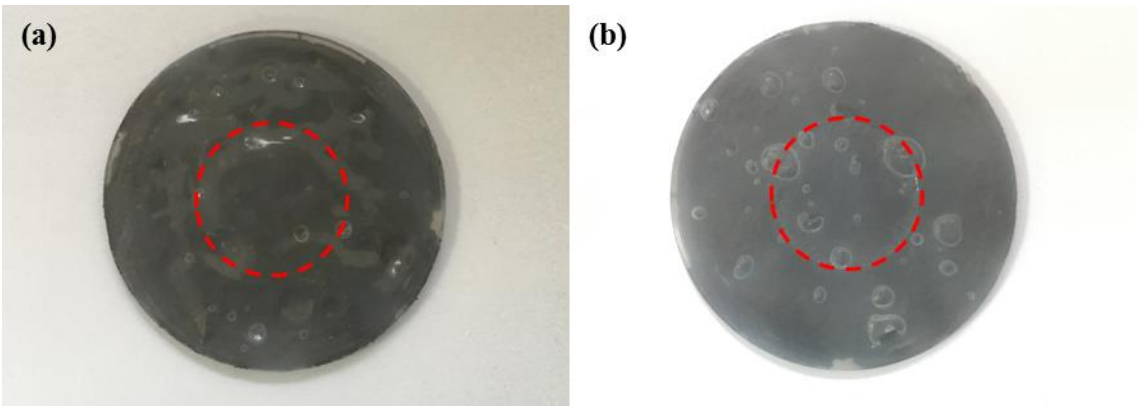

Figure 6.30. Photographs of Laminate htGO25: (a) top surface – exposed to upstream 5 MPa pressure CO_2 with 1.48% H_2S; (b) bottom surface – pressed onto sinter support. Red dotted circles indicate the test region, directly exposed to the feed gas (top) and sinter (bottom).

6.7 CONCLUSIONS

A new class of laminate structures, comprising pure GNP paper sandwiched between two PA11 disks have been fabricated, and their barrier properties to pure H_2S and CO_2 with 1.48% H_2S mixtures evaluated.

The inclusion of a GNP paper in a compression moulded PA11 laminate structure can reduce the permeability of 0.2 MPa H_2S by up to 80%. In pure H_2S at 0.2 MPa pressure, samples that deformed due to unfavourable swelling had poorer barrier performance compared to their flat analogues, but still reduced permeability by about 30% compared to a GNP-free control. The improved barrier performance appeared to be due to a reduced diffusion coefficient as the tortuosity of the path of diffusion was increased by the GNP layer.

Under high pressure conditions with feeds of CO_2 with 1.48% H_2S, sample construction had great bearing on the performance of the laminate samples. Compared to a control laminate, a laminate with complete GNP paper coverage reduced permeation of CO_2 by over 90% and reduced H_2S permeation to an undetectable level. Laminates with a PA11 seal around the circumference reduced CO_2 permeation by a factor of two and reduced H_2S permeation to about 20% of the control permeability. Extraction of the effective permeabilities of the GNP layers showed that their permeabilities were greatly affected by the sample configuration. The GNP layer in Laminate A had a CO_2 permeability three orders of magnitude lower than the pure PA11 control. The GNP layers in Laminates B and C had a CO_2 permeability that was two orders of magnitude lower than the pure PA11. The H_2S permeability was at least two orders of magnitude lower than that of the PA11, for the GNP papers in Laminates B and C, and Laminate A displayed no H_2S permeability whatsoever. The permeability of pure PA11 to CO_2 dominates at 5 MPa, however, at 10 MPa and above, H_2S permeation dominates.

Surprisingly, the diffusion coefficient for CO_2 in Laminate A was not greatly reduced compared to Laminate control D, although the steady state permeation was greatly reduced. Laminates B and C did have a lower CO_2 diffusion coefficient than Laminate A which was also surprising, given the apparent poorer barrier performance. H_2S diffusion was much slower than the CO_2 diffusion, probably due to strong interactions between the H_2S and PA11. The solubility coefficients reflected the diffusion behaviour, with H_2S solubilities generally having greater values.

The activation energy for CO_2 permeation did not appear to be affected by the inclusion of a GNP paper and the results were approximately 5 kJ mol^{-1} larger than the activation energies in the literature. This disparity could be explained due to the high pressure testing employed in this work, meaning that polymer compression may increase the activation energy for permeation. The activation energy for permeation was greater for H_2S compared to CO_2, possibly due to the greater size of H_2S. The GNP layer also appeared to increase the activation energy for permeation of H_2S compared to a GNP-free control.

Preliminary measurements show that the inclusion of htGO25 did reduce the permeation of CO_2 and H_2S by around 30 and 65%, respectively, at 5 MPa feed pressure. The htGO25 did not perform as well as the GNPs, possibly due to defects imparted during the thermal reduction of the GO25 paper. Additionally, the htGO25 flakes appeared to remain adhered to one another following reduction, meaning that rearrangement to block permeation would be unlikely. Extensive bubbling in the laminate may have reduced the efficacy of the htGO25 layer.

CHAPTER 7: CONCLUSIONS AND RECOMMENDATIONS

7.1 INTRODUCTION

The following chapter compares the permeation data from each section of work, draws conclusions and makes recommendations for further work. Permeability data were collected for laminated GNP papers, melt blended sandwich structures and CVD graphene coated PA11 plaques. Appendix B contains the raw data plots received, from which permeability data was calculated. A schematic of the samples discussed in the following section is shown in Figure 7.1.

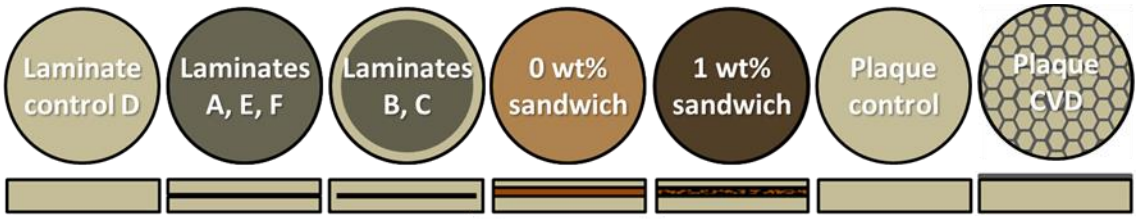

Figure 7.1. Schematic of samples tested in this work and compared in the following section. Modified from Raine *et al.*[164].

7.2 COMPARISON OF BARRIER PROPERTIES OF GNP LAMINATES, GNP NANOCOMPOSITES AND CVD GRAPHENE

Figure 7.2 shows the results for each section of work where permeability testing was carried out at 0.2 MPa pure H_2S. Comparisons between PA11 grades is tricky, however, given that the control performance of the laminate samples (BESVO) is similar to the Plaque control and CVD graphene coated plaque (BMNO), a comparison may be made. The GNP laminates have a much greater barrier property than the CVD graphene coated plaques. As previously discussed in section 5.6.3, the CVD graphene coating did not appear to affect the permeability due to tears imparted during transfer onto the PA11 surface. The tears meant that much of the surface had no CVD graphene coverage, thus, the H_2S could permeate freely through the porous coating. The barrier performance of the laminate samples was due to an increased time-lag resulting from the high tortuosity of the GNP layer. The reduced diffusion coefficient resulted in a much reduced permeability coefficient. It is worth noting that the permeability of the deformed laminate samples was much poorer, and therefore the testing method had a strong

bearing on performance. Regardless, even the deformed samples had far better barrier performance compared to a single CVD graphene layer.

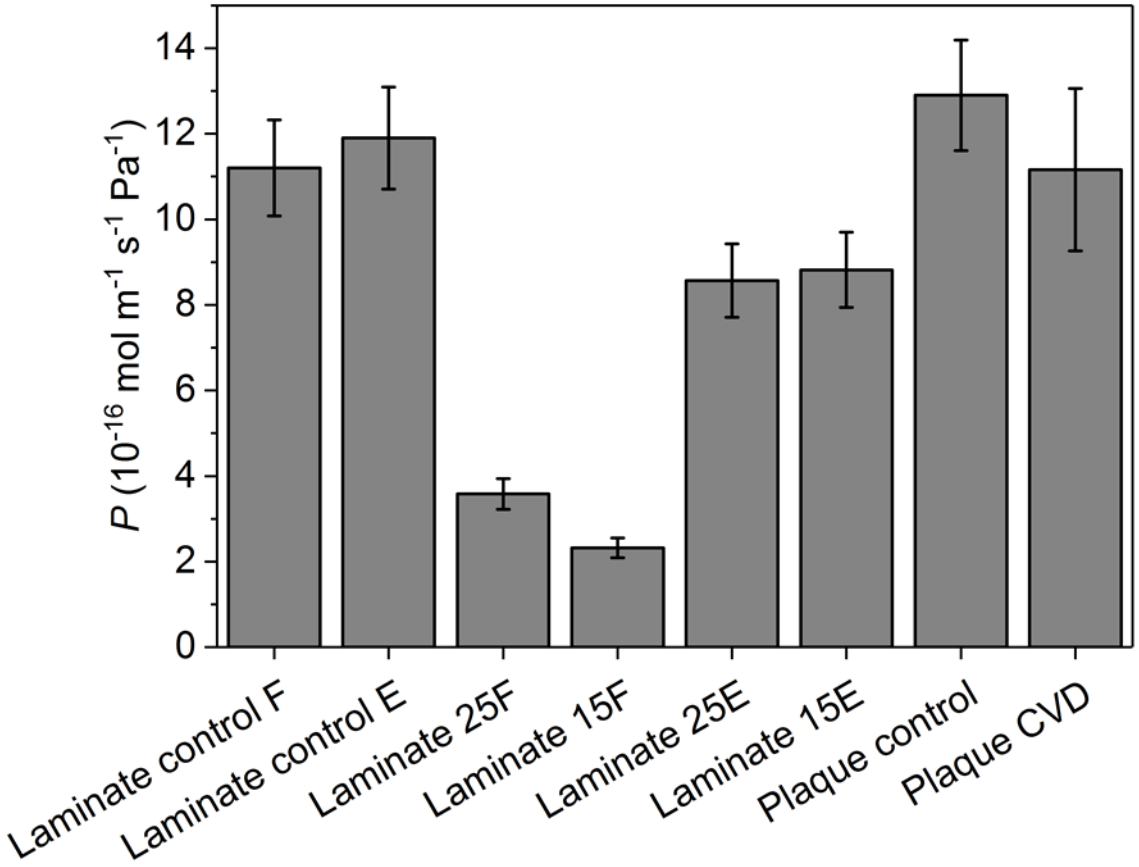

Figure 7.2. Summary plot of permeability data for 0.2 MPa pure H_2S showing the laminate performance compared to CVD graphene coated PA11 plaques. Note that the laminates were BESVO PA11 whereas the plaques were BMNO PA11, so slight permeability differences were expected. Error bars for Plaque CVD represent standard deviation from two samples. All other error bars represent 10% estimated error. Extracted and modified from Raine *et al.*[164]. Fugacity derived values supplied in earlier sections and Appendix C.

As shown for low pressure pure H_2S, the GNP paper laminates far outperform the CVD graphene coated PA11 plaques.

To observe the efficacy of the GNP laminates compared to other graphene-containing nanocomposites, data extracted from 5 MPa CO_2 with 1.48% H_2S is compared, as shown in Figure 7.3. A 10% estimated error is marked by error bars for Laminates A, B, C and htGO25.[179] All other errors represent a single standard deviation of the samples.

The Laminate control, 0 wt% sandwich and Plaque control samples are all graphene-free samples, yet have different permeabilities. The Laminate control was pure compression moulded BESVO PA11, whereas the 0 wt% sandwich had a central region made up of melt processed BESVO, which seems to have affected the resultant permeability of the PA11. It is interesting that the melt processing of BESVO appears to alter the selectivity for permeation of CO_2 and H_2S compared to neat BESVO PA11. This seemed to be due to a reduction in permeability of CO_2, rather than an increase in the permeation of H_2S, as can be seen from the relative magnitudes of the permeabilities of the Laminate control and 0 wt% melt processed sandwich structure.

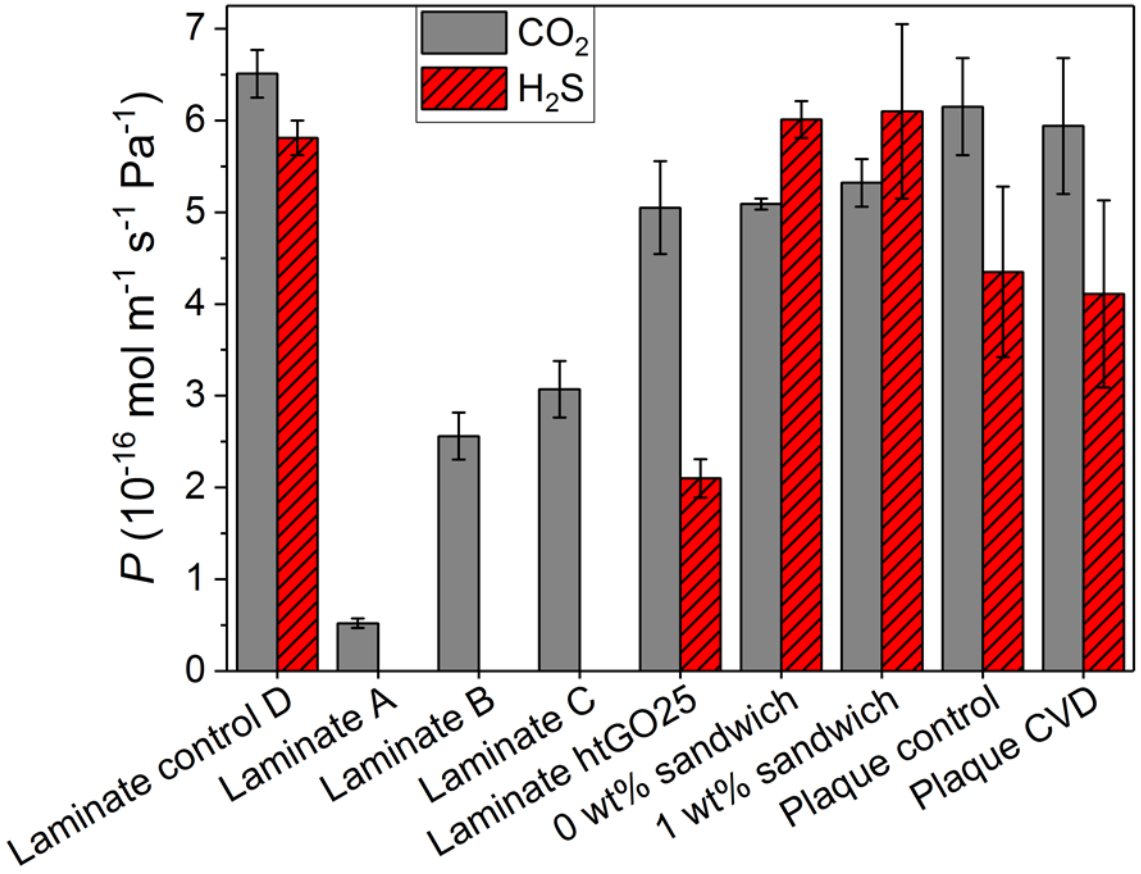

Figure 7.3. Summary plot of permeability data for 5 MPa CO_2 with 1.48% H_2S showing the performance of laminates compared to melt processed nanocomposite sandwich structures and CVD graphene coated PA11 plaques. Modified from Raine *et al.*[164]. Laminates A, B, C and htGO25 have error bars representing estimated 10% error.[179] All other error bars signify a single standard deviation of the samples. Fugacity derived values supplied in earlier sections and Appendix C.

Comparing the neat BESVO Laminate control to the BMNO Plaque control, it is evident that the relative CO_2 permeabilities are the same, within error. The H_2S permeability of BMNO PA11 appears to be far lower than the BESVO values.

The differences in permeabilities between the control samples seem to be intrinsic to the specific processing conditions and PA11 grade. This means that comparison between different samples is challenging, however, general trends may be discussed carefully.

There is a striking reduction in CO_2 permeability upon the addition of GNP paper in a laminate structure, compared to the Laminate control. The complete shutdown of H_2S can also be seen for each GNP-containing laminate structure. No appreciable difference in permeability is observed for any other graphene-containing samples apart from for the htGO25 laminate. As discussed in section 6.6.2, the GNPs appear to be capable of rearrangement in order to block permeation through Laminate A and Laminates B and C.

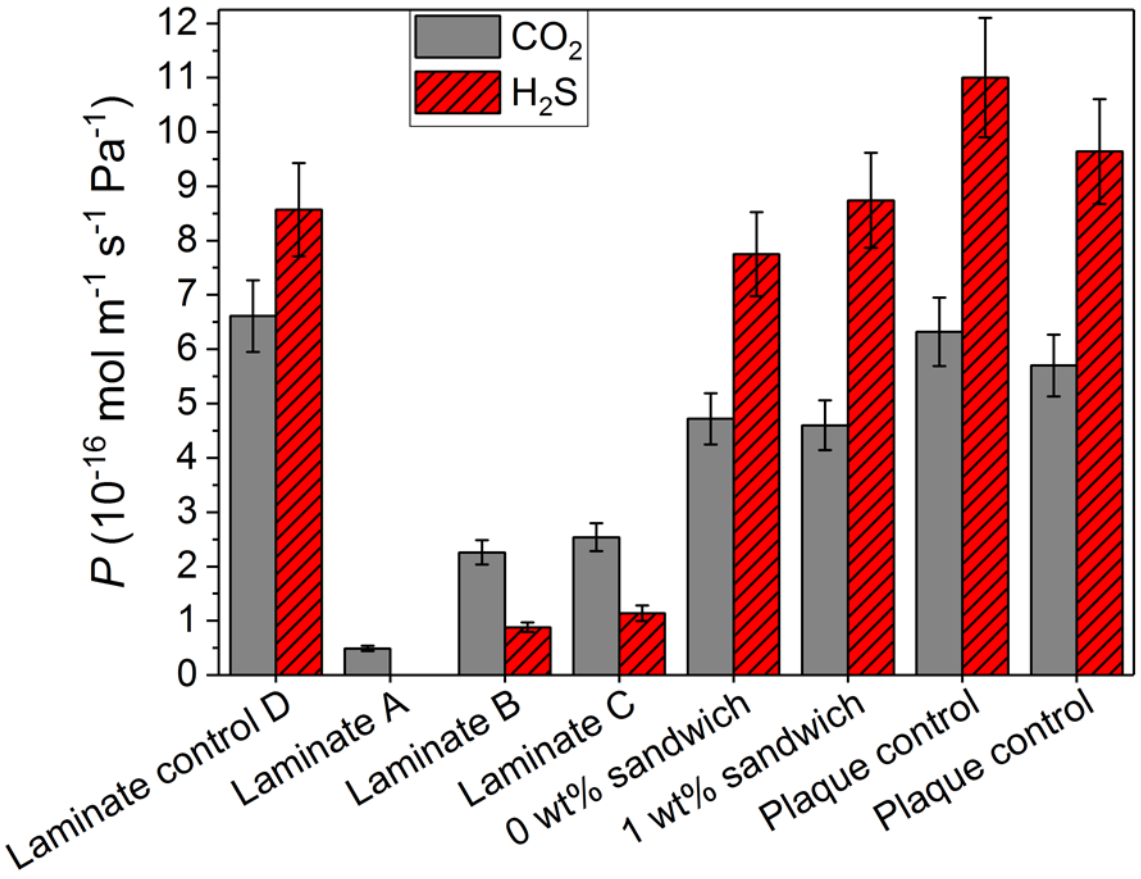

Figure 7.4. Summary plot of permeability data for 10 MPa CO_2 with 1.48% H_2S showing the performance of laminates compared to melt processed nanocomposite sandwich structures and CVD graphene coated PA11 plaques. All samples have error bars representing estimated 10% error.[179] Fugacity derived values supplied in earlier sections.

Figure 7.4 shows that upon increasing the pressure from 5 to 10 MPa, generally, the permeation of CO_2 remained consistent or decreased slightly while the permeation of H_2S increased. Permeability is linked to the flux by multiplying by the thickness (which is assumed to be consistent for individual samples) and dividing by partial pressure (which doubles) or fugacity, as shown in Equation 2.11, repeated below for ease of reference.

$$P = \frac{J.l}{p_1} \qquad \text{Equation 2.11}$$

The increase in H_2S permeability is due to over doubling the H_2S flux across the samples. The CO_2 flux only doubled, so the permeability remained consistent. This switch from CO_2 to H_2S selectivity with increasing pressure occurs after the phase

change from gaseous to supercritical CO_2. Compression of the PA11 matrix may have led to increased favourable interactions between PA11 and H_2S, thus increasing its permeation through the PA11. On the other hand, compression of the matrix would likely reduce the CO_2 diffusion rate; however, this appears to be balanced by the increased CO_2 concentration.

The extraordinary performance of the GNP laminates is still clear at 10 MPa with CO_2 permeability remaining very similar to the 5 MPa values. H_2S permeation became detectable for Laminates B and C, although remained lower than the CO_2 permeation value. Laminate A continued to have a CO_2 permeability far lower than any of the PA11 samples tested and no H_2S permeation was detectable.

7.3 CONCLUSIONS

Presently, there is a drive towards extending the operational lifetimes of PA11-containing flexible risers. Reducing the permeability of PA11 to corrosive gases such as CO_2 and H_2S can potentially reduce the likelihood of corrosion of the strengthening steel layers. Thus, the operational lifetime of an oil and gas riser may be extended. It was hypothesised that graphene or GRMs would increase the barrier properties of PA11 to CO_2 and H_2S.

We demonstrated, for the first time, the barrier performance of GRMs to gaseous, liquid and supercritical CO_2 and H_2S mixtures. In particular, the investigation of GRMs and their nanocomposites has not previously been undertaken at such high pressures, or to supercritical fluids of any kind.

A number of methods of incorporating graphene or GRMs into PA11 were examined.

In situ polymerisation of GNPs and GO in the presence of PA11 monomer was performed. The resultant functionalised GNPs and GOs were characterised, however, permeation testing was not carried out. The grafting of GNPs and GO25 to PA11 appeared to improve the compatibility of the fillers to the rest of the PA11 matrix, resulting in less voiding than that observed for the melt blending work. Thermal stability was also better for the *in situ* samples, compared to those prepared by melt blending. The materials appeared to be promising for future barrier work.

The industrially favoured method of twin-screw extrusion was used to produce a range of PA11/GNP nanocomposites. Extensive voiding was observed in the nanocomposites due to inherent poor compatibility and air incorporation during extrusion, so reducing the nanocomposites' attractiveness for use as barrier materials. Efforts to reduce the voiding behaviour by pre-mixing cryogenically milled PA11 powder with GNP powder substantially reduced the observed voiding, however, it failed to eradicate the behaviour entirely. The voiding increased with increased GNP loading, therefore, the lowest loaded GNP nanocomposite (1 wt%) was selected for permeation testing. In order to provide structural support, the brittle 1 wt% nanocomposite was sandwiched between two neat PA11 disks, as was a 0 wt% control. The GNPs failed to alter the permeability of CO_2 or H_2S through the nanocomposite. The activation energies of permeation were extracted for CO_2 and had values around 25 kJ mol^{-1}, approximately 10 kJ mol^{-1} lower than literature values.

In an effort to reduce the possibility of affecting the structural properties of the PA11 matrix, pure PA11 was coated with CVD graphene. A range of interesting effects were found. Firstly, it was found that the CVD graphene was torn upon application to the PA11 surface, meaning that the CVD graphene had a porous appearance. This meant that there was no improvement in barrier performance, to within the error of the experiments. Interestingly, and for the first time, it was reported that the PA11 became yellow upon exposure to a H_2S-containing feed. This could be attributed to amine scrubbing of H_2S by amide bonds or amine end groups, yielding elemental sulphur within the polymer. PET was also found to yellow appreciably, presumably by a similar mechanism at oxygen functionality. It was observed that the CVD graphene nucleated elemental sulphur crystals at both low pressure H_2S and high pressure CO_2 with 1.48% H_2S feeds. The crystal appearance seemed to depend on the pressure regime, with low pressure crystals growing into 3D flower-like or cuboid structures (Appendix D), while at high pressure, thin, needle-like crystals grew in the plane of the CVD graphene coating.

The final method investigated was to create a pure GNP layer within a compression moulded PA11 laminate. The as-fabricated GNP paper was porous; however, following compression moulding, the GNP layer demonstrated exceptional barrier performance. Low pressure testing revealed that the GNP layer reduced the permeation of pure H_2S by up to 80%, dependent upon the loading of the sample into the cell. Over a range of

higher pressures of CO_2 with 1.48% H_2S, the laminate samples were found to reduce H_2S permeation to undetectable levels, and CO_2 permeation was reduced by up to an order of magnitude. The activation energy for permeation was calculated for the laminate structures upon cooling from 60 to 21 °C through the phase change from supercritical to liquid. The activation energies for permeation of CO_2 were 38.2 – 42.6 kJ mol^{-1} for the GNP-containing and control laminates, approximately 5 kJ mol^{-1} larger than literature values. Activation energy for H_2S permeation was 95.2 kJ mol^{-1} for the control laminate, however, it was found to be increased to 116 – 130 kJ mol^{-1} for the GNP laminate structures. Finally, a heat treated GO laminate also displayed good barrier properties, but was found to be inferior to the pure GNP laminates.

7.4 Recommendations for Future Work

The current study was undertaken in order to investigate the efficacy of GRMs for high pressure barrier applications. Although a number of research avenues led to no improvement in permeation resistance, the project has yielded at least one method for improving barrier properties. A number of issues do still require solution and a plethora of further work is envisaged.

The *in situ* polymerised nanocomposites offer an interesting opportunity to incorporate functionalised GRMs into PA11 by masterbatch processing. The grafted GRMs could be added to neat PA11 by twin-screw extrusion to produce nanocomposites of platelet materials with excellent compatibility. It would be expected that compatibility between PA11 and PA11 functionalised GRMs would be much better than that between PA11 and GNPs investigated in this thesis.

One of the major problems with the melt blending section of work was voiding due to poor compatibility and the incorporation of air during extrusion. It would be interesting to investigate the effect of using a larger twin-screw extruder that would produce the nanocomposites by a single pass, rather than the cycling of the melt required in this work. In particular, the use of a pilot-sized extruder would likely allow the GNP powders to be added directly to the polymer melt. This would give a clearer indication of whether the voiding is, indeed, intrinsic to PA11/GNP nanocomposites, or due to the specific extrusion technique used. Should voiding persist, the use of functionalised

GRMs, such as *in situ* polymerised nanocomposites, or a compatibiliser could be investigated to eradicate the voiding behaviour.

There is also scope to extend the work regarding the coating of PA11 with graphene. In this work, only a single CVD graphene layer was examined, however, multiple layers may provide superior performance. Although interesting from an academic point of view, utilising CVD graphene industrially is still some way off. For example, one major issue with CVD graphene coatings, along with their tricky transfer, is the cost of production. Indeed, economics is likely to be the limiting factor, particularly for industrial applications.

In addition to practical problems, it would be interesting to examine the sulphur crystal growth mechanism in more detail. This would involve additional experiments carried out over a range of timescales with transition metal seeds upon PA11 surfaces. For example, another 2D material, such as MoS_2, could be tested to see if sulphur crystal growth could be controlled. Additionally, if sulphur crystals could be nucleated, could they reach a stage at which they would coalesce to create an impenetrable sulphur barrier layer?

The most promising avenue for future work comes from the GNP laminates. Some particularly interesting work may be carried out in order to find the limiting thickness for barrier property improvement. For example, halving or doubling the thickness of the GNP layer should double or half the permeation flux across the membrane, respectively. Building on this academic understanding, it would be necessary to develop a scalable approach to creating the GNP layered system by industrially relevant techniques. For example, coatings are used extensively in the polymer industry to impart particular characteristics upon films, a technique that could be applicable to GNP dispersions. It would also be interesting to alter the polymer system used, for example to PVDF, for use under even more extreme conditions. Alternatively, rather than focussing on thermoplastic pipes, it may be possible to tackle permeation of elastomeric gaskets to CO_2 and H_2S with this method. Such samples could be produced with minimal upscaling issues.

In terms of specific permeation testing, it would be very interesting to investigate the permeation of water through the GNP laminates, as water is a key ingredient in the corrosive mix found in flexible risers. Additionally, it would be fascinating to monitor

the change in permeability with temperature for more samples. Allowing the steady state to be reached at multiple temperatures would also allow correlation between the dynamic cooling method attempted in this thesis and the staged cooling method usually used. This could lead to a method of activation energy extraction that could speed up the current norms for permeation testing.

REFERENCES

1 Y. Shen, J. Zhao, Z. Tan and T. Sheldrake, in *Proceedings of ASME 2012 31st International Conference on Ocean, Offshore and Arctic Engineering*, OMAE, Rio de Janerio, Brazil, 2012.

2 S. Groves, in *Proceedings of 20th International Conference on Offshore Mechanics and Arctic Engineering*, OMAE, Rio de Janeiro, Brazil, 2001.

3 F. A. Dawans, J. A. Jarrin, T. O. Lefevre and M. A. Pelisson, in *Proceedings of 18th Annual Offshore Technology Conference*, Offshore Technology Conference, Houston, USA, 1986.

4 A. Rubin and C. Wang, in *Proceedings of 2012 Offshore Technology Conference*, Offshore Technology Conference, Houston, Texas, USA, 2012.

5 A. J. M. Glover, College of William and Mary in Virginia, 2011.

6 G. P. Drumond, I. P. Pasqualino, B. C. Pinheiro and S. F. Estefen, *Ocean Eng.*, 2018, **148**, 412–425.

7 K. S. Novoselov, A. K. Geim, S. V Morozov, D. Jiang, Y. Zhang, S. V Dubonos, I. V Grigorieva and A. A. Firsov, *Science*, 2004, **306**, 666–669.

8 K. S. Novoselov, D. Jiang, F. Schedin, T. J. Booth, V. V Khotkevich, S. V Morozov and A. K. Geim, *Proc. Natl. Acad. Sci. U.S.A.*, 2005, **102**, 10451–10453.

9 J. S. Bunch, S. S. Verbridge, J. S. Alden, A. M. van der Zande, J. M. Parpia, H. G. Craighead and P. L. McEuen, *Nano Lett.*, 2008, **8**, 2458–2462.

10 O. Leenaerts, B. Partoens and F. M. Peeters, *Appl. Phys. Lett.*, 2008, **93**, 193107.

11 C. Casiraghi, S. Pisana, K. S. Novoselov, A. K. Geim and A. C. Ferrari, *Appl. Phys. Lett.*, 2007, **91**, 233108.

12 A. H. Castro Neto, F. Guinea, N. M. R. Peres, K. S. Novoselov and A. K. Geim, *Rev. Mod. Phys.*, 2009, **81**, 109–162.

13 A. K. Geim, *Science*, 2009, **324**, 1530–1534.

14 C. Soldano, A. Mahmood and E. Dujardin, *Carbon*, 2010, **48**, 2127–2150.

15 Y. Zhu, S. Murali, W. Cai, X. Li, J. W. Suk, J. R. Potts and R. S. Ruoff, *Adv. Mater.*, 2010, **22**, 3906–3924.

16 K. S. Novoselov, V. I. Fal'ko, L. Colombo, P. R. Gellert, M. G. Schwab and K. Kim, *Nature*, 2012, **490**, 192–200.

17 D. A. C. Brownson, D. K. Kampouris and C. E. Banks, *Chem. Soc. Rev.*, 2012, **41**, 6944–6976.

18 A. Ambrosi, C. K. Chua, A. Bonanni and M. Pumera, *Chem. Rev.*, 2014, **114**, 7150–7188.

19 E. P. Randviir, D. A. C. Brownson and C. E. Banks, *Mater. Today*, 2014, **17**, 426–432.

20 Thompson Reuters, Web of Science, http://apps.webofknowledge.com, (accessed 26 March 2018).

21 M. Genas, *Angew. Chemie*, 1962, **74**, 535–540.

22 J. Mason, in *235th ACS National Meeting*, American Chemical Society, New Orleans, USA, 2008.

23 B. Jacques, M. Werth, I. Merdas, F. Thominette and J. Verdu, *Polymer*, 2002, **43**, 6439–6447.

24 Reid Brothers UK, Rilsan® Polyamide 11 in Oil & Gas, http://www.reidbrothers.co.uk, (accessed 6 January 2015).

25 S. Berge and T. Glomsaker, *Robust material selection in the offshore industry - flexible risers*, 2004.

26 C. Taravel-Condat and T. Epsztein, in *Proceedings of the ASME 2012 31st International Conference on Ocean, Offshore and Arctic Engineering*, 2012, pp. 251–259.

27 S. McIntyre, *Polymer Liners for Pipelines: The Cost and Benefits of Polymer Liners in Subsea Pipeline Applications*, 2010.

28 A. D. McNaught and W. A., *IUPAC. Compendium of Chemical Terminology (the 'Gold Book')*, Blackwell Scientific Publications, Oxford, 2nd edn., 1997.

29 X. Qin, Q. Meng, Y. Feng and Y. Gao, *Surf. Sci.*, 2013, **607**, 153–158.

30 S. Park and R. S. Ruoff, *Nat. Nano*, 2009, **4**, 309.

31 Y. Zhu, H. Ji, H.-M. Cheng and R. S. Ruoff, *Natl. Sci. Rev.*, 2017, **5**, 90–101.

32 Y. Zhang, L. Zhang and C. Zhou, *Acc. Chem. Res.*, 2013, **46**, 2329–2339.

33 A. Ciesielski and P. Samori, *Chem. Soc. Rev.*, 2014, **43**, 381–398.

34 A. Ambrosi, C. K. Chua, N. M. Latiff, A. H. Loo, C. H. A. Wong, A. Y. S. Eng, A. Bonanni and M. Pumera, *Chem. Soc. Rev.*, 2016, **45**, 2458–2493.

35 US 2004/0127621 A1, *US Pat.*, 2004.

36 L. T. Drzal and H. Fukushima, in *NSTI Nanotech*, Boston, 2006, vol. 1, pp. 170–173.

37 XG Sciences Inc, xGnP® Graphene Nanoplatelets Technical Data Sheet: Grade M Characteristics, http://xgsciences.com/wp-content/uploads/2012/10/10-15-13_xGnP-M_Data-Sheet.pdf, (accessed 9 December 2014).

38 B. C. Brodie, *Philos. Trans. R. Soc. Lond.*, 1859, **149**, 249–259.

39 L. Staudenmaier, *Ber. Dtsch. Chem. Ges.*, 1898, **31**, 1481–1487.

40 W. S. Hummers and R. E. Offeman, *J. Am. Chem. Soc.*, 1958, **80**, 1339–1339.

41 J. P. Rourke, P. A. Pandey, J. J. Moore, M. Bates, I. A. Kinloch, R. J. Young and N. R. Wilson, *Angew. Chemie*, 2011, **123**, 3231–3235.

42 A. Lerf, H. He, J. Klinowski and M. Forster, *J. Phys. Chem. B*, 1998, **102**, 4477–4482.

43 H. He, J. Klinowski, M. Forster and A. Lerf, *Chem. Phys. Lett.*, 1998, **287**, 53–56.

44 D. R. Dreyer, S. Park, C. W. Bielawski and R. S. Ruoff, *Chem. Soc. Rev.*, 2010, **39**, 228–240.

45 D. R. Dreyer, A. D. Todd and C. W. Bielawski, *Chem. Soc. Rev.*, 2014, **43**, 5288–5301.

46 T. Graham, *Q. J. Sci.*, 1829, **100**, 88–89.

47 T. Graham, *J. Memb. Sci.*, 1831, **100**, 17–21.

48 J. K. Mitchell, *J. Memb. Sci.*, 1830, **100**, 11–16.

49 A. Fick, *Philos. Mag.*, 1855, **10**, 30–39.

50 T. Graham, *Philos. Trans. R. Soc. Lond.*, 1866, **156**, 399–439.

51 B. Flaconnèche, J. Martin and M. H. Klopffer, *Oil Gas Sci. Technol.*, 2001, **56**, 245–259.

52 M. H. Klopffer and B. Flaconnèche, *Oil Gas Sci. Technol.*, 2001, **56**, 223–244.

53 S. Matteucci, Y. Yampolskii, B. D. Freeman and I. Pinnau, in *Materials Science of Membranes for Gas and Vapor Separation*, eds. Y. Yampolskii, I. Pinnau and B. D. Freeman, John Wiley & Sons, Ltd, Chichester, England, 2006, pp. 1–47.

54 B. Flaconnèche, J. Martin and M. H. Klopffer, *Oil Gas Sci. Technol.*, 2001, **56**, 261–278.

55 M.-B. Hägg, in *Encyclopedia of Membranes*, eds. E. Drioli and L. Giorno, Springer Berlin Heidelberg, Berlin, Germany, 2016, pp. 849–852.

56 C. Hall, *Polymer materials: an Introduction for Technologists and Scientists*, Wiley, 1989.

57 R. M. Barrer, J. A. Barrie and J. Slater, *J. Polym. Sci.*, 1958, **27**, 177–197.

58 H. A. Daynes, *Proc. Roy. Soc.*, 1920, **97**, 286–307.

59 J. Crank, *The Mathematics of Diffusion*, Oxford University Press, Oxford, Second Edi., 1975.

60 R. Ash, R. M. Barrer and D. G. Palmer, *Polymer*, 1970, **11**, 421–435.

61 T. R. Andersen, J. I. Skar and C. Hansteen, in *Proceedings of Corrosion 1999*, 1999, pp. 1–16.

62 J. K. Sears and J. R. Darby, *The Technology of Plasticizers*, John Wiley & Sons, Ltd, New York, New York, 1982.

63 R. M. Barrer, *Nature*, 1937, **140**, 106–107.

64 R. M. Barrer and E. K. Rideal, *Trans. Faraday Soc.*, 1939, **35**, 628–643.

65 D. W. Van Krevelen and K. Te Nijenhuis, in *Properties of Polymers*, 2009, pp. 655–702.

66 H. H. Yu, *Mater. Chem. Phys.*, 1998, **56**, 289–293.

67 T. Liu, D. Chen, I. Y. Phang and C. Wei, *Chinese J. Polym. Sci.*, 2014, **32**, 115–122.

68 Q. Zhang, Z. Mo, H. Zhang, S. Liu and S. Z. D. Cheng, *Polymer*, 2001, **42**, 5543–5547.

69 L. Chocinski-Arnault, V. Gaudefroy, J. L. Gacougnolle and A. Riviere, *J. Macromol. Sci. - Phys.*, 2002, **B41**, 777–785.

70 G. Stoclet, R. Seguela and J. M. Lefebvre, *Polymer*, 2011, **52**, 1417–1425.

71 L. Martino, L. Basilissi, H. Farina, M. A. Ortenzi, E. Zini, G. Di Silvestro and M. Scandola, *Eur. Polym. J.*, 2014, **59**, 69–77.

72 A. Mollova, R. Androsch, D. Mileva, C. Schick and A. Benhamida, *Macromolecules*, 2013, **46**, 828–835.

73 J. O. Fernandez, G. M. Swallowe and S. F. Lee, *J. Appl. Polym. Sci.*, 2001, **80**, 2031–2038.

74 L. Jolly, A. Tidu, J. J. Heizmann and B. Bolle, *Polymer*, 2002, **43**, 6839–6851.

75 P. Ricou, E. Pinel and N. Juhasz, *Advances*, 2005, **48**, 170–175.

76 H. H. Yu, *Mater. Sci. Eng., A*, 1998, **254**, 53–62.

77 J. Pepin, V. Miri and J.-M. Lefebvre, *Macromolecules*, 2016, **49**, 564–573.

78 S. S. Nair, C. Ramesh and K. Tashiro, *Macromolecules*, 2006, **39**, 2841–2848.

79 S. S. Nair, C. Ramesh and K. Tashiro, *Macromol. Symp.*, 2006, **242**, 216–226.

80 K. G. Kim, B. A. Newman and J. I. Scheinbeim, *J. Polym. Sci., Polym. Phys. Ed.*, 1985, **23**, 2477–2482.

81 A. C. Ferrari, J. C. Meyer, V. Scardaci, C. Casiraghi, M. Lazzeri, F. Mauri, S. Piscanec, D. Jiang, K. S. Novoselov, S. Roth and A. K. Geim, *Phys. Rev. Lett.*, 2006, **97**, 187401.

82 A. Eckmann, University of Manchester, 2013.

83 A. C. Ferrari, *Solid State Commun.*, 2007, **143**, 47–57.

84 M. B. Khan, M. Parvaz and Z. H. Khan, in *Recent Trends in Nanomaterials: Synthesis and Properties*, ed. Z. H. Khan, Springer Singapore, Singapore, 2017, pp. 1–28.

85 S. Eigler and A. M. Dimiev, in *Graphene Oxide: Fundamentals and Applications*, eds. S. Eigler and A. M. Dimiev, John Wiley & Sons, Ltd, Chichester, UK, 2016, pp. 85–120.

86 A. C. Ferrari and J. Robertson, *Phys. Rev. B*, 2000, **61**, 14095–14107.

87 L. M. Malard, M. A. Pimenta, G. Dresselhaus and M. S. Dresselhaus, *Phys. Rep.*, 2009, **473**, 51–87.

88 A. Witkowski and M. Majkut, in *Advances in Carbon Dioxide Compression and Pipeline Transportation Processes*, eds. A. Witkowski, A. Rusin, M. Majkut, S. Rulik and K. Stolecka, Springer International Publishing, Cham, 2015, pp. 5–12.

89 R. M. Smith, *Pure Appl. Chem.*, 1993, **65**, 2397–2403.

90 S. M. Hitchen and J. R. Dean, in *Applications of Supercritical Fluids in Industrial Analysis*, ed. J. R. Dean, Springer Netherlands, Dordrecht, 1993, pp. 1–11.

91 N. Budisa and D. Schulze-Makuch, *Life*, 2014, **4**, 331–340.

92 D. P. Sobocinski and F. Kurata, *AIChE J.*, 1959, **5**, 545–551.

93 F. Sarrasin, P. Memari, M. H. Klopffer, V. Lachet, C. Taravel-Condat, B.

Rousseau and E. Espuche, *J. Memb. Sci.*, 2015, **490**, 380–388.

94 A. O'Neill, D. Bakirtzis and D. Dixon, *Eur. Polym. J.*, 2014, **59**, 353–362.

95 A. O'Neill, E. Archer, A. McIlhagger, P. Lemoine and D. Dixon, *Polym. Compos.*, 2017, **38**, 528–537.

96 D. Yuan, B. B. Wang, L. Y. Wang, Y. P. Wang and Z. W. Zhou, *Compos. Part B-Eng.*, 2013, **55**, 215–220.

97 C. J. Jacobs, J. S. Tate, B. Olson, N. Theodoropoulou and J. H. Koo, *J. Nanosci. Nanotechnol.*, 2012, **12**, 1799–1805.

98 J. Jin, R. Rafiq, Y. Q. Gill and M. Song, *Eur. Polym. J.*, 2013, **49**, 2617–2626.

99 C.-Y. Chen, C.-X. Zhao, W.-N. Guo, J.-L. Ma, S. Lin and B.-B. Wang, *Suliao*, 2012, **41**, 67–70.

100 C.-Y. Chen, W.-N. Guo, J.-L. Ma, S. Lin and B.-B. Wang, *Gaofenzi Cailiao Kexue Yu Gongcheng*, 2012, **28**, 100–104+108.

101 C.-Y. Chen, J.-L. Ma, W.-N. Guo, S. Lin and B.-B. Wang, *Huagong Xinxing Cailiao*, 2012, **40**, 128–130.

102 L. Sisti, G. Totaro, M. Vannini, L. Giorgini, S. Ligi and A. Celli, *J. Nanosci. Nanotechnol.*, **18**, 1169–1175.

103 D. Chen, H. Feng and J. Li, *Chem. Rev.*, 2012, **112**, 6027–6053.

104 N. I. Kovtyukhova, P. J. Ollivier, B. R. Martin, T. E. Mallouk, S. A. Chizhik, E. V Buzaneva and A. D. Gorchinskiy, *Chem. Mater.*, 1999, **11**, 771–778.

105 D. C. Marcano, D. V Kosynkin, J. M. Berlin, A. Sinitskii, Z. Sun, A. Slesarev, L. B. Alemany, W. Lu and J. M. Tour, *ACS Nano*, 2010, **4**, 4806–4814.

106 N. R. Wilson, P. A. Pandey, R. Beanland, R. J. Young, I. A. Kinloch, L. Gong, Z. Liu, K. Suenaga, J. P. Rourke, S. J. York and J. Sloan, *ACS Nano*, 2009, **3**, 2547–2556.

107 M. Hirata, T. Gotou, S. Horiuchi, M. Fujiwara and M. Ohba, *Carbon*, 2004, **42**, 2929–2937.

108 T. G. Scholte, N. L. J. Meijerink, H. M. Schoffeleers and A. M. G. Brands, *J. Appl. Polym. Sci.*, 1984, **29**, 3763–3782.

109 M. G. Neira-Velázquez, M. T. Rodríguez-Hernández, E. Hernández-Hernández and A. R. Y. Ruiz-Martínez, in *Handbook of Polymer Synthesis, Characterization, and Processing*, John Wiley & Sons, Inc., 2013, pp. 355–366.

110 C. C. Terán, E. M. Macchi and R. V Figini, *J. Appl. Polym. Sci.*, 1987, **34**, 2433–2444.

111 D. Z. Chen, S. C. Lao, J. H. Koo, M. Londa and Z. Alabdullatif, in *Proc. 2010 Solid Freeform Fabrication Symposium, Austin, TX, August*, 2010, pp. 2–4.

112 S. Huang, M. Wang, T. Liu, W.-D. Zhang, W. C. Tjiu, C. He and X. Lu, *Polym. Eng. Sci.*, 2009, **49**, 1063–1068.

113 S. C. Lao, M. F. Kan, C. K. Lam, D. Z. Chen, J. H. Koo, T. Moon, M. Londa, T. Takatsuka, E. Kuramoto, G. Wissler, L. Pilato and Z. P. Luo, in *Solid Freeform Fabr. Symp. Proc.*, University of Texas at Austin, 2010, pp. 451–467.

114 A. Kiziltas, D. J. Gardner, Y. Han and H.-S. Yang, *Thermochim. Acta*, 2011, **519**, 38–43.

115 Q. Zhang, Z. Mo, S. Liu and H. Zhang, *Macromolecules*, 2000, **33**, 5999–6005.

116 S. Liu, Y. Yu, C. Yi, H. Zhang and Z. Mo, *J. Appl. Polym. Sci.*, 1998, **70**, 2371–2380.

117 XG Sciences Inc, About xGnP®, http://xgsciences.com/wp-content/uploads/2013/01/About-xGnP-August-2012.pdf, (accessed 9 December 2014).

118 H. S. Kim, H. S. Bae, J. Yu and S. Y. Kim, *Sci. Rep.*, 2016, **6**, 26825.

119 H. C. Kim, H. T. Hahn and Y. S. Yang, *J. Compos. Mater.*, 2012, **47**, 501–509.

120 M. Acik, G. Lee, C. Mattevi, M. Chhowalla, K. Cho and Y. J. Chabal, *Nat. Mater.*, 2010, **9**, 840–845.

121 K. S. S. K. Muhamad, F. Mohamed, S. Radiman, A. Hamzah, S. Sarmani, K. K.

Siong, M. S. Yasir, I. A. Rahman and N. R. A. M. Rosli, in *AIP Conference Proceedings*, American Institute of Physics, 2016, vol. 1784, p. 40013.

122 S. H. Huh, *Phys. Appl. Graphene—Experiments*.

123 E. Tegou, G. Pseiropoulos, M. K. Filippidou and S. Chatzandroulis, *Microelectron. Eng.*, 2016, **159**, 146–150.

124 H.-K. Jeong, Y. P. Lee, M. H. Jin, E. S. Kim, J. J. Bae and Y. H. Lee, *Chem. Phys. Lett.*, 2009, **470**, 255–258.

125 A. Felten, B. S. Flavel, L. Britnell, A. Eckmann, P. Louette, J.-J. Pireaux, M. Hirtz, R. Krupke and C. Casiraghi, *Small*, 2013, **9**, 631–639.

126 P. Bandyopadhyay, W. B. Park, R. K. Layek, M. E. Uddin, N. H. Kim, H.-G. Kim and J. H. Lee, *J. Memb. Sci.*, 2016, **500**, 106–114.

127 S. Peretz Damari, L. Cullari, R. Nadiv, Y. Nir, D. Laredo, J. Grunlan and O. Regev, *Compos. Part B Eng.*, 2017, **134**, 218–224.

128 B. Fultz and J. M. Howe, in *Transmission Electron Microscopy and Diffractometry of Materials*, eds. B. Fultz and J. M. Howe, Springer Berlin Heidelberg, Berlin, Heidelberg, 2008, pp. 1–59.

129 H. Yu, B. Zhang, C. Bulin, R. Li and R. Xing, *Sci. Rep.*, 2016, **6**, 36143.

130 J. Rafiee, X. Mi, H. Gullapalli, A. V Thomas, F. Yavari, Y. Shi, P. M. Ajayan and N. A. Koratkar, *Nat. Mater.*, 2012, **11**, 217–222.

131 Q. Huang, M. Xu, R. Sun and X. Wang, *Ind. Crops Prod.*, 2016, **85**, 198–203.

132 R. L. G. Lecaros, G. E. J. Mendoza, W.-S. Hung, Q.-F. An, A. R. Caparanga, H.-A. Tsai, C.-C. Hu, K.-R. Lee and J.-Y. Lai, *Carbon*, 2017, **123**, 660–667.

133 D. Cai and M. Song, *J. Mater. Chem.*, 2007, **17**, 3678–3680.

134 L. Q. Xu, W. J. Yang, K.-G. Neoh, E.-T. Kang and G. D. Fu, *Macromolecules*, 2010, **43**, 8336–8339.

135 L. Sun and B. Fugetsu, *Mater. Lett.*, 2013, **109**, 207–210.

136 O. C. Compton, D. A. Dikin, K. W. Putz, L. C. Brinson and S. T. Nguyen, *Adv. Mater.*, 2010, **22**, 892–896.

137 T. N. Blanton and D. Majumdar, *Powder Diffr.*, 2012, **27**, 104–107.

138 A. Meyer, N. Jones, Y. Lin and D. Kranbuehl, *Macromolecules*, 2002, **35**, 2784–2798.

139 S. J. A. Hocker, N. V Hudson-Smith, P. T. Smith, C. H. Komatsu, L. R. Dickinson, H. C. Schniepp and D. E. Kranbuehl, *Polymer*, 2017, **126**, 248–258.

140 E. Domingos, T. M. C. Pereira, E. V. R. de Castro, W. Romão, G. L. de Sena and R. C. L. Guimarães, *Polímeros*, 2013, **23**, 37–41.

141 C. Wang, F. Hu, K. Yang, T. Hu, W. Wang, R. Deng, Q. Jiang and H. Zhang, *Rsc Adv.*, 2016, **6**, 45014–45022.

142 I.-H. Kim and Y. G. Jeong, *J. Polym. Sci. Part B Polym. Phys.*, 2010, **48**, 850–858.

143 H. Liu, P. Bandyopadhyay, N. H. Kim, B. Moon and J. H. Lee, *Polym. Test.*, 2016, **50**, 49–56.

144 T. Kuila, S. Bose, A. K. Mishra, P. Khanra, N. H. Kim and J. H. Lee, *Polym. Test.*, 2012, **31**, 31–38.

145 I. M. Kamal, G. A. Adam and H. K. Al Getta, *Thermochim. Acta*, 1983, **62**, 355–359.

146 C. L. Bao, L. Song, W. Y. Xing, B. H. Yuan, C. A. Wilkie, J. L. Huang, Y. Q. Guo and Y. Hu, *J. Mater. Chem.*, 2012, **22**, 6088–6096.

147 N. Du, C. Zhao, Q. Chen, G. Wu and R. Lu, *Mater. Chem. Phys.*, 2010, **120**, 167–171.

148 G. Mago, D. M. Kalyon and F. T. Fisher, *J. Polym. Sci. Part B Polym. Phys.*, 2011, **49**, 1311–1321.

149 J. Bai, S. Yuan, F. Shen, B. Zhang, C. K. Chua, K. Zhou and J. Wei, *Virtual Phys. Prototyp.*, 2017, **12**, 235–240.

150 P. Latko, D. Kolbuk, R. Kozera and A. Boczkowska, *J. Mater. Eng. Perform.*, 2016, **25**, 68–75.

151 Z. Yang, S. Huang and T. Liu, *J. Appl. Polym. Sci.*, 2011, **122**, 551–560.

152 M. Naffakh, P. S. Shuttleworth and G. Ellis, *Rsc Adv.*, 2015, **5**, 17879–17887.

153 Y. Wang, S. Liu, Q. Zhang and Q. Meng, *J. Mater. Sci.*, 2015, **50**, 6291–6301.

154 C. Schick, *Anal. Bioanal. Chem.*, 2009, **395**, 1589.

155 S. Gogolewski, *Colloid Polym. Sci.*, 1979, **257**, 811–819.

156 T. Wang and D. Liu, *Polym. Plast. Technol. Eng.*, 2007, **46**, 893–899.

157 K. Honaker, F. Vautard and L. T. Drzal, *Mater. Sci. Eng., B*, 2017, **216**, 23–30.

158 M. T. Müller, K. Hilarius, M. Liebscher, D. Lellinger, I. Alig and P. Pötschke, *Materials*, 2017, **10**, 545.

159 A. Al-Jabareen, H. Al-Bustami, H. Harel and G. Marom, *J. Appl. Polym. Sci.*, 2013, **128**, 1534–1539.

160 K. Kalaitzidou, H. Fukushima and L. T. Drzal, *Carbon*, 2007, **45**, 1446–1452.

161 S. Gaikwad, J. S. Tate, N. Theodoropoulou and J. H. Koo, *J. Compos. Mater.*, 2013, **47**, 2973–2986.

162 B. J. Rashmi, K. Prashantha, M.-F. Lacrampe and P. Krawczak, *Adv. Polym. Technol.*, 2016, 21757.

163 B. Pan, G. Xu, B. Zhang, X. Ma, H. Li and Y. Zhang, *Polym. Plast. Technol. Eng.*, 2012, **51**, 1163–1166.

164 T. P. Raine, O. M. Istrate, B. E. King, B. Craster, I. A. Kinloch and P. M. Budd, *Adv. Mater. Interfaces*, 2018, **0**, 1800304.

165 L. M. Costello and W. J. Koros, *Ind. Eng. Chem. Res.*, 1993, **32**, 2277–2280.

166 T. Ramanathan, A. A. Abdala, S. Stankovich, D. A. Dikin, M. Herrera-Alonso, R. D. Piner, D. H. Adamson, H. C. Schniepp, X. Chen, R. S. Ruoff, S. T. Nguyen, I. A. Aksay, R. K. Prud'Homme and L. C. Brinson, *Nat. Nanotechnol.*,

2008, 3, 327–31.

167 I. Tantis, G. C. Psarras and D. Tasis, *eXPRESS Polym. Lett.*, 2012, **6**, 283–292.

168 J. R. Potts, The University of Texas at Austin, 2012.

169 R. M. Barrer, *J. Membr. Sci.*, 1984, **18**, 25–35.

170 K. Magniez, R. Iftikhar and B. L. Fox, *Polym. Compos.*, 2015, **36**, 668–674.

171 H. C. Bidsorkhi, A. G. D'Aloia, G. De Bellis, A. Proietti, A. Rinaldi, M. Fortunato, P. Ballirano, M. P. Bracciale, M. L. Santarelli and M. S. Sarto, *Mater. Today Commun.*, 2017, **11**, 163–173.

172 R. Nadiv, G. Shachar, S. Peretz-Damari, M. Varenik, I. Levy, M. Buzaglo, E. Ruse and O. Regev, *Carbon*, 2018, **126**, 410–418.

173 R. Nadiv, G. Vasilyev, M. Shtein, A. Peled, E. Zussman and O. Regev, *Compos. Sci. Technol.*, 2016, **133**, 192–199.

174 J. Canales, M. Fernández, J. J. Peña, M. Eugenia Muñoz and A. Santamaría, *Polym. Eng. Sci.*, 2015, **55**, 1142–1151.

175 C.-M. Wu, S.-S. Cheong and T.-H. Chang, *J. Polym. Res.*, 2016, **23**, 242.

176 J. Abraham, T. Sharika, S. C. George and S. Thomas, *Rheology*, 2017, **1**, 1–15.

177 C. Penu, G.-H. Hu, A. Fernandez, P. Marchal and L. Choplin, *Polym. Eng. Sci.*, 2012, **52**, 2173–2181.

178 B. Mayoral, E. Harkin-Jones, P. N. Khanam, M. A. AlMaadeed, M. Ouederni, A. R. Hamilton and D. Sun, *RSC Adv.*, 2015, **5**, 52395–52409.

179 J. K. Adewole, L. Jensen, U. A. Al-Mubaiyedh, N. von Solms and I. A. Hussein, *J. Polym. Res.*, 2012, **19**, 9814.

180 H. R. Godini and D. Mowla, *Chem. Eng. Res. Des.*, 2008, **86**, 401–409.

181 K. J. Berean, J. Z. Ou, M. Nour, M. R. Field, M. M. Y. A. Alsaif, Y. Wang, R. Ramanathan, V. Bansal, S. Kentish, C. M. Doherty, A. J. Hill, C. McSweeney, R. B. Kaner and K. Kalantar-zadeh, *J. Phys. Chem. C*, 2015, **119**, 13700–13712.

182 Q. Yu, J. Lian, S. Siriponglert, H. Li, Y. P. Chen and S.-S. Pei, *Appl. Phys. Lett.*, 2008, **93**, 113103.

183 L. G. De Arco, Z. Yi, A. Kumar and Z. Chongwu, *IEEE Trans. Nanotechnol.*, 2009, **8**, 135–138.

184 G. Faggio, A. Capasso, G. Messina, S. Santangelo, T. Dikonimos, S. Gagliardi, R. Giorgi, V. Morandi, L. Ortolani and N. Lisi, *J. Phys. Chem. C*, 2013, **117**, 21569–21576.

185 C. Wang, W. Chen, C. Han, G. Wang, B. Tang, C. Tang, Y. Wang, W. Zou, W. Chen, X.-A. Zhang, S. Qin, S. Chang and L. Wang, *Sci. Rep.*, 2014, **4**, 4537.

186 Z. Yan, J. Lin, Z. Peng, Z. Sun, Y. Zhu, L. Li, C. Xiang, E. L. Samuel, C. Kittrell and J. M. Tour, *ACS Nano*, 2012, **6**, 9110–9117.

187 Y. Takesaki, K. Kawahara, H. Hibino, S. Okada, M. Tsuji and H. Ago, *Chem. Mater.*, 2016, **28**, 4583–4592.

188 B. Dai, L. Fu, Z. Zou, M. Wang, H. Xu, S. Wang and Z. Liu, *Nat. Commun.*, 2011, **2**, 522.

189 H. Ago, Y. Ito, N. Mizuta, K. Yoshida, B. Hu, C. M. Orofeo, M. Tsuji, K. Ikeda and S. Mizuno, *ACS Nano*, 2010, **4**, 7407–7414.

190 P. W. Sutter, J.-I. Flege and E. A. Sutter, *Nat. Mater.*, 2008, **7**, 406–411.

191 S.-Y. Kwon, C. V Ciobanu, V. Petrova, V. B. Shenoy, J. Bareño, V. Gambin, I. Petrov and S. Kodambaka, *Nano Lett.*, 2009, **9**, 3985–3990.

192 E. Miniussi, M. Pozzo, A. Baraldi, E. Vesselli, R. R. Zhan, G. Comelli, T. O. Menteş, M. A. Niño, A. Locatelli, S. Lizzit and D. Alfè, *Phys. Rev. Lett.*, 2011, **106**, 216101.

193 J. Coraux, A. T. N'Diaye, C. Busse and T. Michely, *Nano Lett.*, 2008, **8**, 565–570.

194 P. W. Sutter, J. T. Sadowski and E. A. Sutter, *Phys. Rev. B*, 2009, **80**, 245411.

195 C. Mattevi, H. Kim and M. Chhowalla, *J. Mater. Chem.*, 2011, **21**, 3324–3334.

196 H. C. Lee, W.-W. Liu, S.-P. Chai, A. R. Mohamed, A. Aziz, C.-S. Khe, N. M. S. Hidayah and U. Hashim, *RSC Adv.*, 2017, **7**, 15644–15693.

197 A. Srivastava, C. Galande, L. Ci, L. Song, C. Rai, D. Jariwala, K. F. Kelly and P. M. Ajayan, *Chem. Mater.*, 2010, **22**, 3457–3461.

198 L. Zhao, K. T. Rim, H. Zhou, R. He, T. F. Heinz, A. Pinczuk, G. W. Flynn and A. N. Pasupathy, *Solid State Commun.*, 2011, **151**, 509–513.

199 R. Munoz and C. Gomez-Aleixandre, *Chem. Vap. Depos.*, 2013, **19**, 297–322.

200 X. Li, W. Cai, J. An, S. Kim, J. Nah, D. Yang, R. Piner, A. Velamakanni, I. Jung, E. Tutuc, S. K. Banerjee, L. Colombo and R. S. Ruoff, *Science*, 2009, **324**, 1312–1314.

201 Y. F. Hao, M. S. Bharathi, L. Wang, Y. Y. Liu, H. Chen, S. Nie, X. H. Wang, H. Chou, C. Tan, B. Fallahazad, H. Ramanarayan, C. W. Magnuson, E. Tutuc, B. I. Yakobson, K. F. McCarty, Y. W. Zhang, P. Kim, J. Hone, L. Colombo and R. S. Ruoff, *Science*, 2013, **342**, 720–723.

202 A. W. Tsen, L. Brown, R. W. Havener and J. Park, *Acc. Chem. Res.*, 2013, **46**, 2286–2296.

203 K. Choi, S. Nam, Y. Lee, M. Lee, J. Jang, S. J. Kim, Y. J. Jeong, H. Kim, S. Bae, J.-B. Yoo, S. M. Cho, J.-B. Choi, H. K. Chung, J.-H. Ahn, C. E. Park and B. H. Hong, *ACS Nano*, 2015, **9**, 5818–5824.

204 J. Li, X.-Y. Wang, X.-R. Liu, Z. Jin, D. Wang and L.-J. Wan, *J. Mater. Chem. C*, 2015, **3**, 3530–3535.

205 J.-H. Lee, E. K. Lee, W.-J. Joo, Y. Jang, B.-S. Kim, J. Y. Lim, S.-H. Choi, S. J. Ahn, J. R. Ahn, M.-H. Park, C.-W. Yang, B. L. Choi, S.-W. Hwang and D. Whang, *Science*, 2014, **344**, 286–289.

206 V. L. Nguyen, B. G. Shin, D. L. Duong, S. T. Kim, D. Perello, Y. J. Lim, Q. H. Yuan, F. Ding, H. Y. Jeong, H. S. Shin, S. M. Lee, S. H. Chae, Q. A. Vu, S. H. Lee and Y. H. Lee, *Adv. Mater.*, 2015, **27**, 1376–1382.

207 E. H. Lock, M. Baraket, M. Laskoski, S. P. Mulvaney, W. K. Lee, P. E. Sheehan,

D. R. Hines, J. T. Robinson, J. Tosado, M. S. Fuhrer, S. C. Hernández and S. G. Walton, *Nano Lett.*, 2012, **12**, 102–107.

208 V. P. Verma, S. Das, I. Lahiri and W. Choi, *Appl. Phys. Lett.*, 2010, **96**, 203108.

209 G. J. M. Fechine, I. Martin-Fernandez, G. Yiapanis, R. Bentini, E. S. Kulkarni, R. V. Bof de Oliveira, X. Hu, I. Yarovsky, A. H. Castro Neto and B. Özyilmaz, *Carbon*, 2015, **83**, 224–231.

210 I. A. Kostogrud, E. V Boyko and D. V Smovzh, *Mater. Today Proc.*, 2017, **4**, 11476–11479.

211 Y. Chen, X.-L. Gong and J.-G. Gai, *Adv. Sci.*, 2016, **3**, 1500343.

212 L. Jiao, B. Fan, X. Xian, Z. Wu, J. Zhang and Z. Liu, *J. Am. Chem. Soc.*, 2008, **130**, 12612–12613.

213 P. Gupta, P. D. Dongare, S. Grover, S. Dubey, H. Mamgain, A. Bhattacharya and M. M. Deshmukh, *Sci. Rep.*, 2014, **4**, 3882.

214 Y. Wang, S. W. Tong, X. F. Xu, B. Özyilmaz and K. P. Loh, *Adv. Mater.*, 2011, **23**, 1514–1518.

215 H. W. Kim, H. W. Yoon, S.-M. Yoon, B. M. Yoo, B. K. Ahn, Y. H. Cho, H. J. Shin, H. Yang, U. Paik, S. Kwon, J.-Y. Choi and H. B. Park, *Science*, 2013, **342**, 91–95.

216 Z. Liu, J. Li and F. Yan, *Adv. Mater.*, 2013, **25**, 4296–4301.

217 C. Wirtz, N. C. Berner and G. S. Duesberg, *Adv. Mater. Interfaces*, 2015, **2**, 1500082.

218 T. H. Seo, S. Lee, H. Cho, S. Chandramohan, E.-K. Suh, H. S. Lee, S. K. Bae, S. M. Kim, M. Park, J. K. Lee and M. J. Kim, *Sci. Rep.*, 2016, **6**, 24143.

219 S. Seethamraju, S. Kumar, K. B. B, G. Madras, S. Raghavan and P. C. Ramamurthy, *ACS Nano*, 2016, **10**, 6501–6509.

220 H.-K. Seo, M.-H. Park, Y.-H. Kim, S.-J. Kwon, S.-H. Jeong and T.-W. Lee, *ACS Appl. Mater. Interfaces*, 2016, **8**, 14725–14731.

221 M. O. Paraense, T. H. R. da Cunha, A. S. Ferlauto and K. C. de Souza Figueiredo, *J. Appl. Polym. Sci.*, 2017, **134**, 45521.

222 J. Duan, M. Higuchi, R. Krishna, T. Kiyonaga, Y. Tsutsumi, Y. Sato, Y. Kubota, M. Takata and S. Kitagawa, *Chem. Sci.*, 2014, **5**, 660–666.

223 T. Borjigin, F. Sun, J. Zhang, K. Cai, H. Ren and G. Zhu, *Chem. Commun.*, 2012, **48**, 7613–7615.

224 C. J. An, S. J. Kim, H. O. Choi, D. W. Kim, S. W. Jang, M. L. Jin, J.-M. Park, J. K. Choi and H.-T. Jung, *J. Mater. Chem. A*, 2014, **2**, 20474–20480.

225 B. Eckert and R. Steudel, in *Elemental Sulfur und Sulfur-Rich Compounds II*, ed. R. Steudel, Springer Berlin Heidelberg, Berlin, Heidelberg, 2003, pp. 31–98.

226 J. Bimer, P. D. Sałbut, S. Berłożecki, J.-P. Boudou, E. Broniek and T. Siemieniewska, *Fuel*, 1998, **77**, 519–525.

227 B. P. Mandal and S. S. Bandyopadhyay, *Chem. Eng. Sci.*, 2005, **60**, 6438–6451.

228 Y. Alqaheem, A. Alomair, M. Vinoba and A. Pérez, *Int. J. Polym. Sci.*, 2017, **2017**, 4250927.

229 Google Patents, US20090277, 2009.

230 F. Adib, A. Bagreev and T. J. Bandosz, *Langmuir*, 2000, **16**, 1980–1986.

231 T. J. Bandosz, M. Seredych, J. Allen, J. Wood and E. Rosenberg, *Chem. Mater.*, 2007, **19**, 2500–2511.

232 M. Seredych and T. J. Bandosz, *J. Phys. Chem. C*, 2008, **112**, 4704–4711.

233 M. Seredych and T. J. Bandosz, *Mater. Chem. Phys.*, 2009, **113**, 946–952.

234 S. Tian, H. Mo, R. Zhang, P. Ning and T. Zhou, *Adsorption*, 2009, **15**, 477–488.

235 X. Wu, A. K. Kercher, V. Schwartz, S. H. Overbury and T. R. Armstrong, *Carbon*, 2005, **43**, 1087–1090.

236 D. W. Scott and J. P. McCullough, *J. Mol. Spectrosc.*, 1961, **6**, 372–378.

237 A. T. Ward, *J. Phys. Chem.*, 1968, **72**, 4133–4139.

238 V. V Poborchii, *Solid State Commun.*, 1998, **107**, 513–518.

239 S. N. White, *Chem. Geol.*, 2009, **259**, 240–252.

240 G. Lupina, J. Kitzmann, I. Costina, M. Lukosius, C. Wenger, A. Wolff, S. Vaziri, M. Östling, I. Pasternak, A. Krajewska, W. Strupinski, S. Kataria, A. Gahoi, M. C. Lemme, G. Ruhl, G. Zoth, O. Luxenhofer and W. Mehr, *ACS Nano*, 2015, **9**, 4776–4785.

241 A. Ambrosi and M. Pumera, *Nanoscale*, 2014, **6**, 472–476.

242 S. Průša, P. Procházka, P. Bábor, T. Šikola, R. ter Veen, M. Fartmann, T. Grehl, P. Brüner, D. Roth, P. Bauer and H. H. Brongersma, *Langmuir*, 2015, **31**, 9628–9635.

243 H. Wu and L. T. Drzal, *Carbon*, 2012, **50**, 1135–1145.

244 D. Pierleoni, Z. Y. Xia, M. Christian, S. Ligi, M. Minelli, V. Morandi, F. Doghieri and V. Palermo, *Carbon*, 2016, **96**, 503–512.

245 J. Liu, A. G. Rinzler, H. Dai, J. H. Hafner, R. K. Bradley, P. J. Boul, A. Lu, T. Iverson, K. Shelimov, C. B. Huffman, F. Rodriguez-Macias, Y.-S. Shon, T. R. Lee, D. T. Colbert and R. E. Smalley, *Science*, 1998, **280**, 1253–1256.

246 S. M. Cooper, H. F. Chuang, M. Cinke, B. A. Cruden and M. Meyyappan, *Nano Lett.*, 2003, **3**, 189–192.

247 A. Tamburrano, L. Paliotta, A. Rinaldi, G. De Bellis and M. S. Sarto, in *2014 IEEE International Symposium on Electromagnetic Compatibility (EMC)*, 2014, pp. 186–191.

248 L. Cai, A. Al-Ostaz, X. Li, L. T. Drzal, B. P. Rook, A. H.-D. Cheng and H. Alkhateb, *J. Nanomechanics Micromechanics*, 2016, **6**, 1.

249 H. Wu and L. T. Drzal, *Mater. Chem. Phys.*, 2016, **182**, 110–118.

250 A. A. Gokhale, J. Lu, N. J. Parker, A. P. Izbicki, O. Sanyal and I. Lee, *J. Colloid Interface Sci.*, 2013, **409**, 219–226.

251 A. Grüniger and P. Rudolf von Rohr, *Thin Solid Films*, 2004, **459**, 308–312.

252 J. A. Barrie, J. D. Levine, A. S. Michaels and P. Wong, *Trans. Faraday Soc.*, 1963, **59**, 869–878.

253 R. A. Brown, P. M. Budd, C. Price and R. Satgurunathan, *Eur. Polym. J.*, 1993, **29**, 337–342.

254 T. C. Merkel and L. G. Toy, *Macromolecules*, 2006, **39**, 7591–7600.

255 J. Vaughn and W. J. Koros, *Macromolecules*, 2012, **45**, 7036–7049.

256 J. D. Alkire and J. F. Mason., in *Proceedings of CORROSION 2000*, NACE International, Orlando, Florida, 2000.

257 C. R. Hammond and D. R. Lide, in *CRC Handbook of Chemistry and Physics, Internet Version*, 2005, p. 4.1-4.166.

258 V. V Chaban and J. S. Nazarenko, *Mater. Chem. Phys.*, 2011, **129**, 1240–1246.

259 S. G. Kazarian, *Polym. Sci.*, 2000, **42**, 78–101.

260 J. Fahlteich, M. Fahland, W. Schönberger and N. Schiller, *Thin Solid Films*, 2009, **517**, 3075–3080.

261 R. R. Nair, H. A. Wu, P. N. Jayaram, I. V Grigorieva and A. K. Geim, *Science*, 2012, **335**, 442–444.

262 Y. Su, V. G. Kravets, S. L. Wong, J. Waters, A. K. Geim and R. R. Nair, *Nat. Commun.*, 2014, **5**, 4843.

263 Wolfram Alpha, http://www.wolframalpha.com, (accessed 15 May 2018).

264 N. von Solms, A. Rubin, S. I. Andersen and E. H. Stenby, *Int. J. Thermophys.*, 2005, **26**, 115–125.

265 S. A. E. Boyer, M.-H. Klopffer, J. Martin and J.-P. E. Grolier, *J. Appl. Polym. Sci.*, 2007, **103**, 1706–1722.

APPENDIX A

A.1 DERIVATION OF TIME-LAG EQUATION

Q, the amount of permeate at time *t* is shown in Equation 2.18.[59] *D* is the diffusion coefficient, *l* is the membrane thickness and C_1 C_2 and C_0 is the concentration of molecules in the upstream, downstream and membrane, respectively. *n* and *m* are discrete slices of the membrane so that the summation yields the quantity diffusion for the full membrane.

$$Q = \int_0^t -D\left(\frac{\partial C}{\partial x}\right)_{x=l} \mathrm{d}t$$

$$= D(C_1 - C_2)\frac{t}{l} + \frac{2l}{\pi^2}\sum_{n=1}^{\infty}\frac{C_1.\cos n\pi - C_2}{n^2}\left\{1 - \exp\left(-\frac{Dn^2\pi^2 t}{l^2}\right)\right\} \qquad \text{Equation 2.18}$$

$$+ \frac{4l.C_0}{\pi^2}\sum_{m=0}^{\infty}\frac{1}{(2m+1)^2}\left\{1 - \exp\left(-\frac{D(2m+1)^2\pi^2 t}{l^2}\right)\right\}$$

Assume $C_2 = 0$ due to N_2 sweep gas removing downstream concentration.

Assume steady state, thus, $t \to \infty$ so exponential $\to 0$.

Therefore:

$$Q = D(C_1 - 0)\frac{t}{l} + \frac{2l}{\pi^2}\sum_{n=1}^{\infty}\frac{C_1.\cos n\pi - 0}{n^2}\{1 - 0\}$$

$$+ \frac{4l.C_0}{\pi^2}\sum_{m=0}^{\infty}\frac{1}{(2m+1)^2}\{1 - 0\} \qquad \text{Equation A1}$$

Take C_1 out of summation:

$$Q = \frac{D.C_1.t}{l} + \frac{2l.C_1}{\pi^2}\sum_{n=1}^{\infty}\frac{\cos n\pi}{n^2} + \frac{4l.C_0}{\pi^2}\sum_{m=0}^{\infty}\frac{1}{(2m+1)^2} \qquad \text{Equation A2}$$

According to Wolfram Alpha:[263]

$$\sum_{n=1}^{\infty} \frac{\cos n\pi}{n^2} = -\frac{\pi^2}{12}$$ Equation A3

$$\sum_{m=0}^{\infty} \frac{1}{(2m+1)^2} = \frac{\pi^2}{8}$$ Equation A4

Therefore:

$$Q = \frac{D.C_1.t}{l} + \frac{2l.C_1}{\pi^2}.\left(-\frac{\pi^2}{12}\right) + \frac{4l.C_0}{\pi^2}.\left(\frac{\pi^2}{8}\right)$$ Equation A5

$$= \frac{D.C_1.t}{l} - \frac{2l.C_1.\pi^2}{12\pi^2} + \frac{4l.C_0.\pi^2}{8\pi^2}$$

$$= \frac{D.C_1.t}{l} - \frac{l.C_1}{6} + \frac{l.C_0}{2}$$

Take out factor of $(D.C_1)/l$:

$$Q = \frac{D.C_1}{l}\left(t - \frac{l^2}{6D} + \frac{l^2.C_0}{2D.C_1}\right)$$ Equation A6

For time-lag, Θ, set $Q = 0$ and substitute t for Θ:

$$0 = \frac{D.C_1}{l}\left(\Theta - \frac{l^2}{6D} + \frac{l^2.C_0}{2D.C_1}\right)$$ Equation A7

$$0 = \Theta - \frac{l^2}{6D} + \frac{l^2.C_0}{2D.C_1}$$

$$\Theta = \frac{l^2}{6D} - \frac{l^2.C_0}{2D.C_1}$$

Take out factor of l^2/D:

$$\Theta = \frac{l^2}{D}\left(\frac{1}{6} - \frac{C_0}{2C_1}\right) \quad \text{Equation A8}$$

$$D = \frac{l^2}{\Theta}\left(\frac{1}{6} - \frac{C_0}{2C_1}\right) \quad \text{Equation A9}$$

A.2 Effect of Membrane Penetrant Concentration

In order to investigate the effect of C_0 on the diffusion coefficient, a reasonable value of C_0 was required. This was estimated by extrapolation of a straight line through the concentration of CO_2 in PA11 at 50 °C (thus, an overestimation as solubility tends to be reduced with higher temperature) found in the work of von Solms *et al.*[264] (Figure A1). Of course, such a straight line extrapolation is likely to overestimate the concentration of CO_2 in PA11 at higher pressures, as solubility typically plateaus at higher pressures, as shown by Sarrasin *et al.*[93] for PE and Boyer *et al.*[265] for PVDF.

The concentration of CO_2 in PA11, assuming that the straight line extrapolation overestimates the concentration will be less than C_0 = 0.03, 0.06, 0.12 and 0.24 g_{gas} g_{PA11}^{-1} at 5, 10, 20 and 40 MPa, respectively. In standard units, C_0 ($\times 10^{-10}$) = 6.6, 13, 27 and 53 mol m^{-3}, at 5, 10, 20 and 40 MPa, respectively.

The concentration of CO_2 in the feed stream may be estimated by dividing the density (NIST REFPROP software) of the feed fluid by the molar mass of CO_2 (assuming 100% CO_2). The concentrations yielded are as follows for 5, 10, 20 and 40 MPa measured pressures, C_1 = 2246, 7485, 15980, and 19297 mol m^{-3}.

Using Equation 2.23, rearranged and displayed below (Equation A9), the effect of C_0 on D may be calculated:

$$D = \frac{l^2}{\Theta}\left(\frac{1}{6} - \frac{C_0}{2C_1}\right)$$

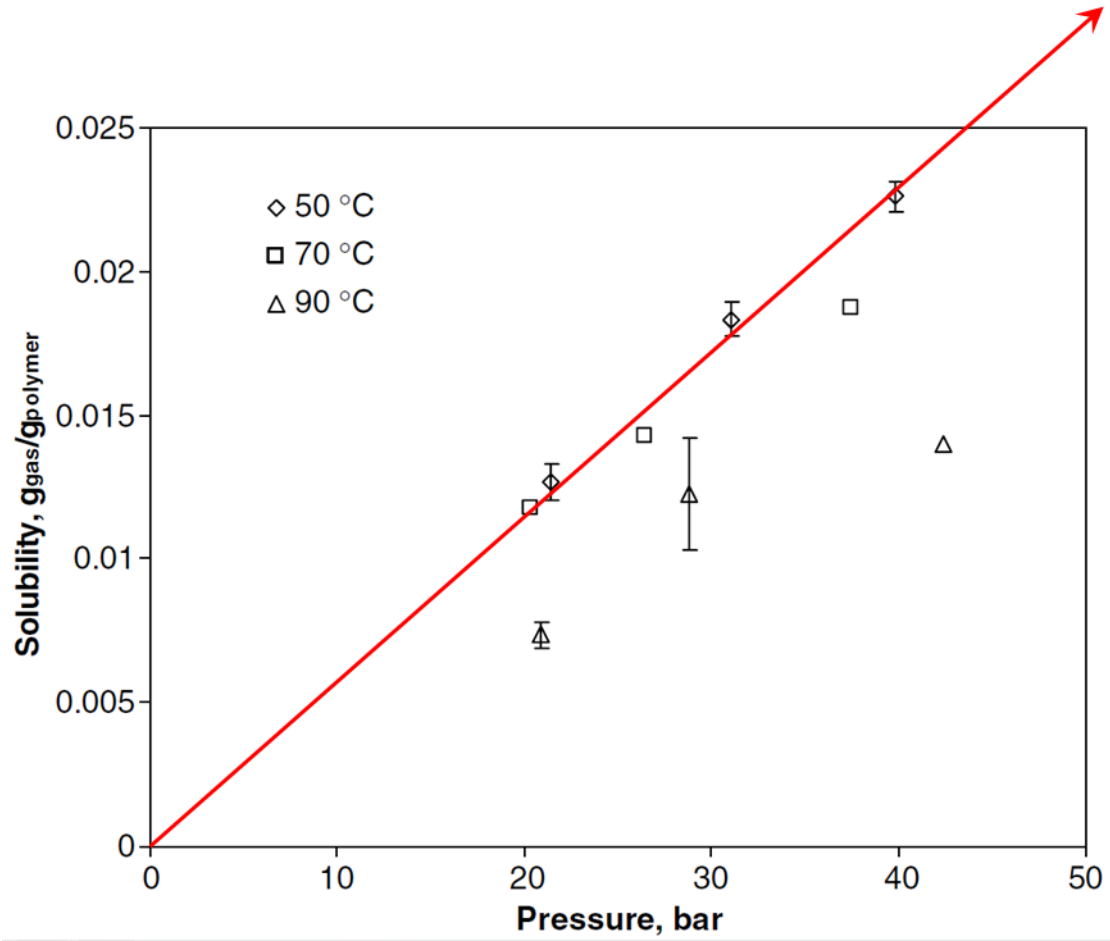

Figure A1. Plot of solubility of CO_2 in PA11 from the work of von Solms *et al.*[264], extracted using https://automeris.io/WebPlotDigitizer/. Red line indicates extrapolation used to estimate C_0. Formula of line: $y = 0.0006x - 0.00002$.

5 MPa:

$$D = \frac{l^2}{\theta}\left(\frac{1}{6} - \frac{6.6 \times 10^{-10}}{2 \times 2246}\right)$$

$$= \frac{l^2}{\theta}\left(\frac{1}{6} - 1.5 \times 10^{-13}\right)$$

$$\approx \frac{l^2}{6\theta}$$

10 MPa:

$$D = \frac{l^2}{\Theta}\left(\frac{1}{6} - \frac{1.3 \times 10^{-9}}{2 \times 7485}\right)$$

$$= \frac{l^2}{\Theta}\left(\frac{1}{6} - 8.7 \times 10^{-14}\right)$$

$$\approx \frac{l^2}{6\Theta}$$

20 MPa:

$$D = \frac{l^2}{\Theta}\left(\frac{1}{6} - \frac{2.7 \times 10^{-9}}{2 \times 15980}\right)$$

$$= \frac{l^2}{\Theta}\left(\frac{1}{6} - 8.4 \times 10^{-14}\right)$$

$$\approx \frac{l^2}{6\Theta}$$

40 MPa:

$$D = \frac{l^2}{\Theta}\left(\frac{1}{6} - \frac{5.3 \times 10^{-9}}{2 \times 19297}\right)$$

$$= \frac{l^2}{\Theta}\left(\frac{1}{6} - 1.4 \times 10^{-13}\right)$$

$$\approx \frac{l^2}{6\Theta}$$

Therefore, in each case investigated in this work where $C_0 > 0$, the value of D is still approximately equal to $l^2/6\Theta$, due to the low solubility of CO_2 in the polymer and high feed concentration, C_1.

APPENDIX B

B.1 EFFECT OF GASKETS

As shown in Figure B2, the use of gaskets did not affect the permeability coefficient of CO_2 or H_2S to within a single standard deviation. The diffusion coefficients for CO_2 do seem to be slightly affected by the use of gaskets, although the diffusion coefficients for H_2S are not affected. The solubility coefficients for CO_2 and H_2S are both affected by the use of gaskets. Typically, comparisons were only drawn between self-consistent samples, that is, samples with gaskets were compared to other samples with gaskets, and samples without gaskets were compared to other samples without gaskets.

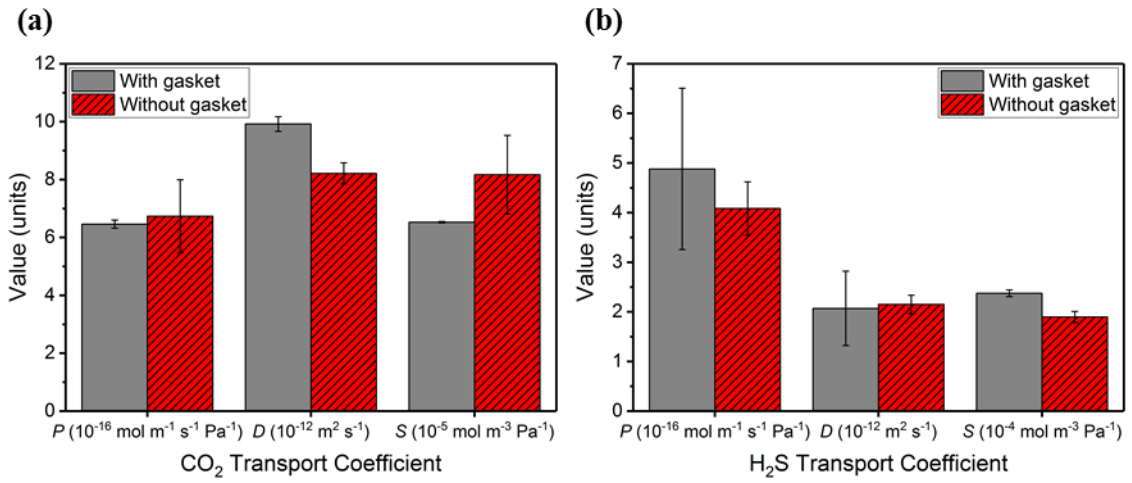

Figure B2. Representation of the effect of gaskets upon the transport coefficients measured of pure BMNO PA11 for CO_2 and H_2S in a mix of 5 MPa CO_2 with 1.48% H_2S. Extracted from Raine *et al.*[164].

B.2 0.2 MPA PURE H_2S EXPERIMENTAL DATA

The raw data was provided from TWI Ltd. in Excel spreadsheets. Summary plots were included as shown below, for the samples compared in Chapter 7.

Experimental data for the low pressure pure H_2S permeability coefficients, presented in Chapter 7 of the main text, are shown in Figure B3 – Figure B10.

Laminate control F:

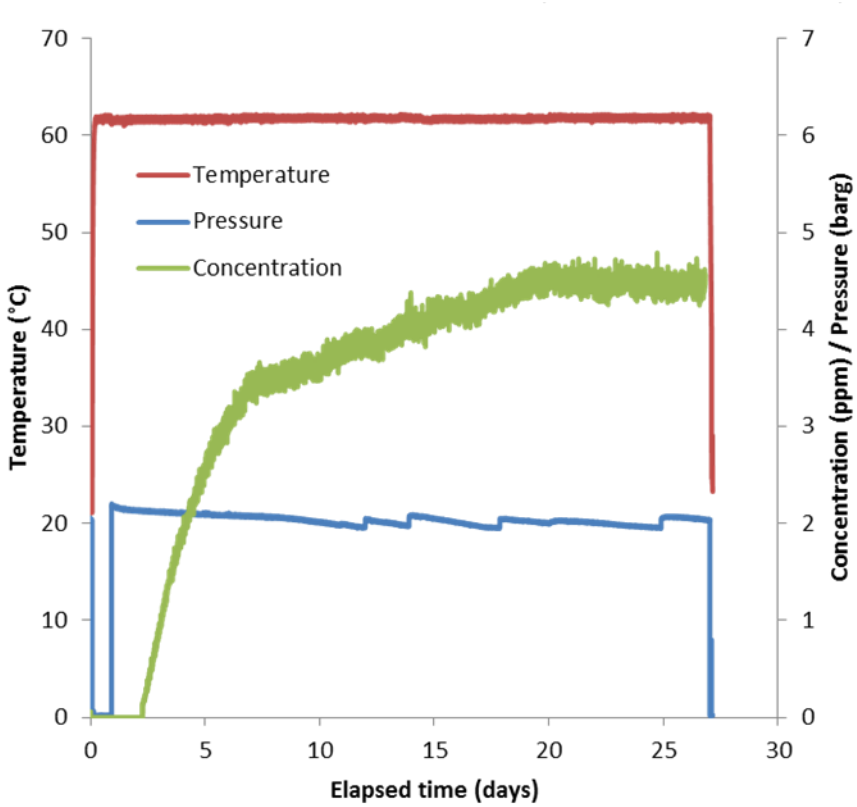

Figure B3. Laminate control F. Plot of experimental temperature, pressure and sweep gas H_2S concentration against experimental time.

Laminate control E:

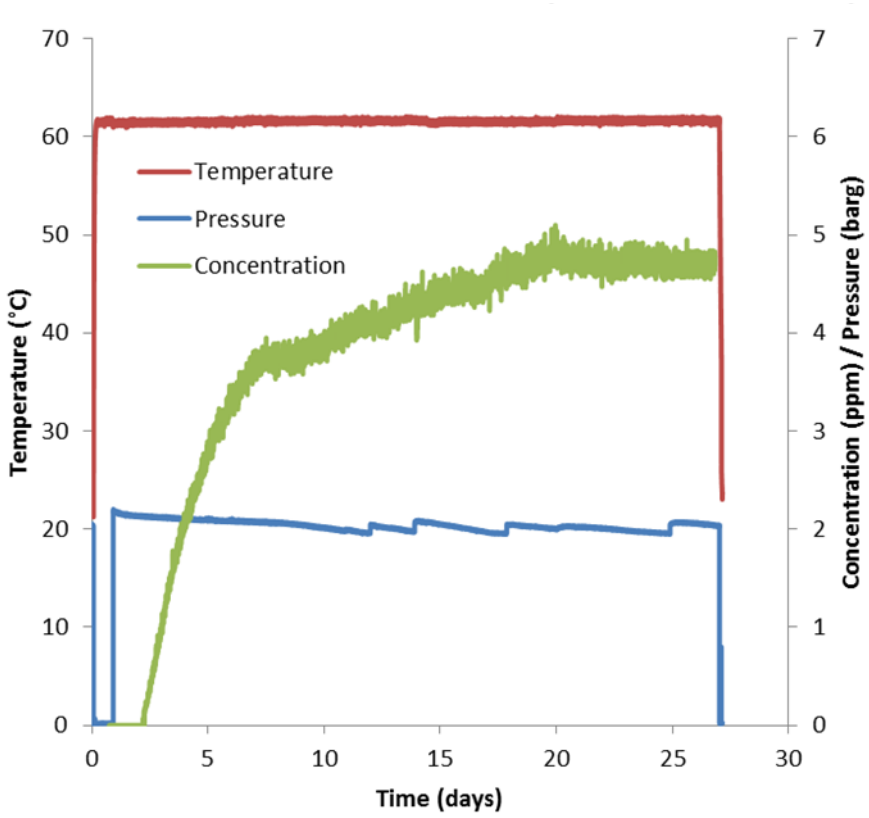

Figure B4. Laminate control E. Plot of experimental temperature, pressure and sweep gas H_2S concentration against experimental time.

Laminate 25F:

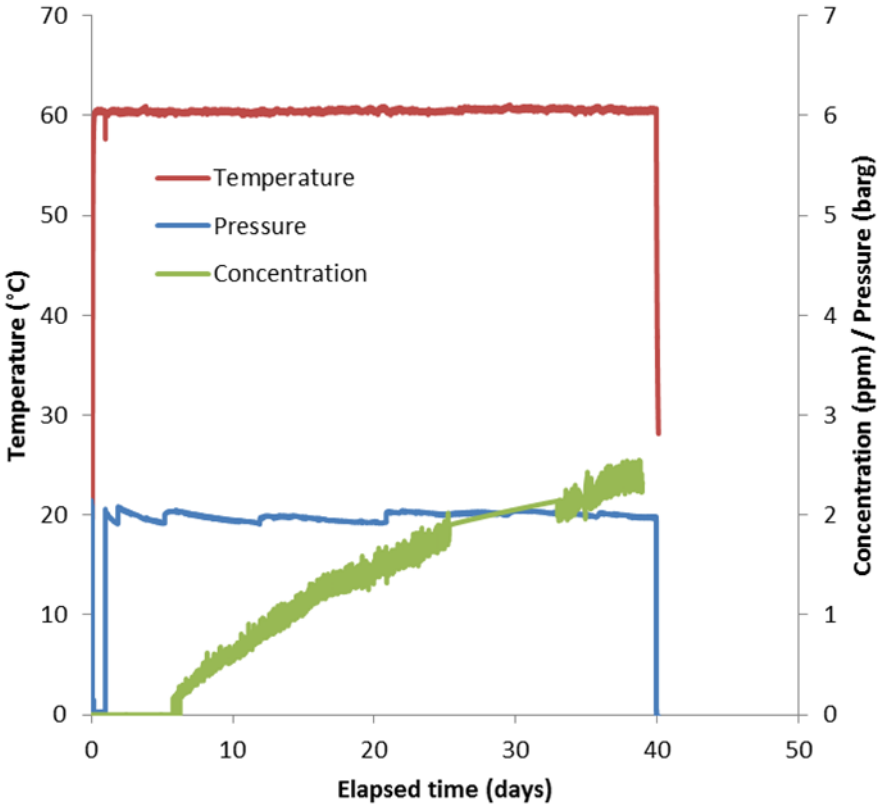

Figure B5. Laminate 25F. Plot of experimental temperature, pressure and sweep gas H_2S concentration against experimental time.

Laminate 15F:

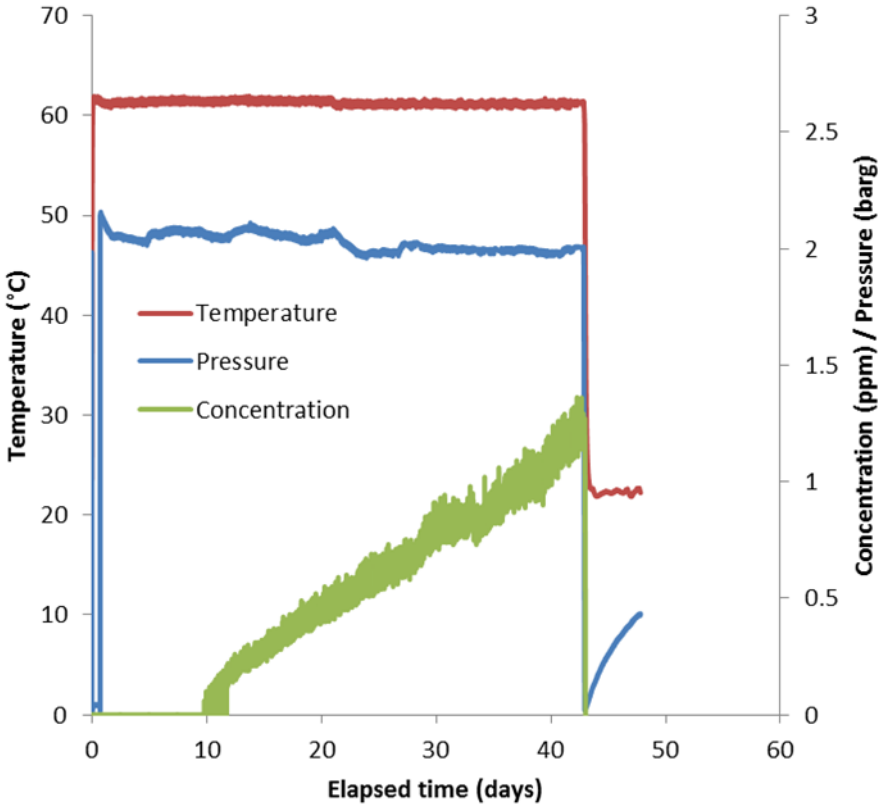

Figure B6. Laminate 15F. Plot of experimental temperature, pressure and sweep gas H_2S concentration against experimental time.

Laminate 25E:

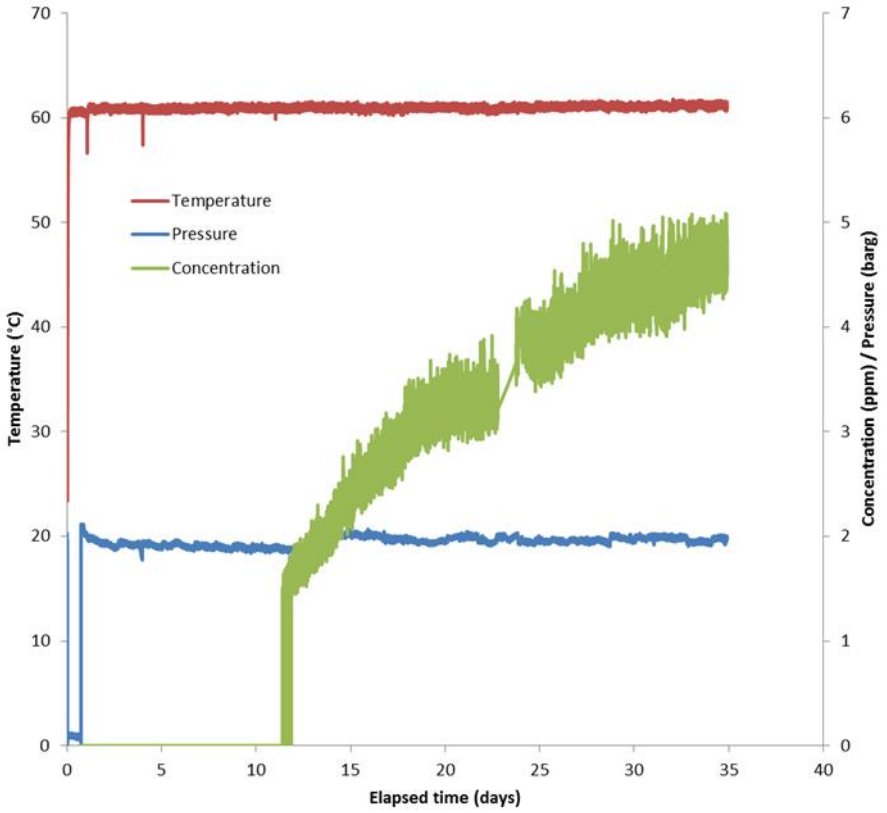

Figure B7. Laminate 25E. Plot of experimental temperature, pressure and sweep gas H_2S concentration against experimental time.

Laminate 15E:

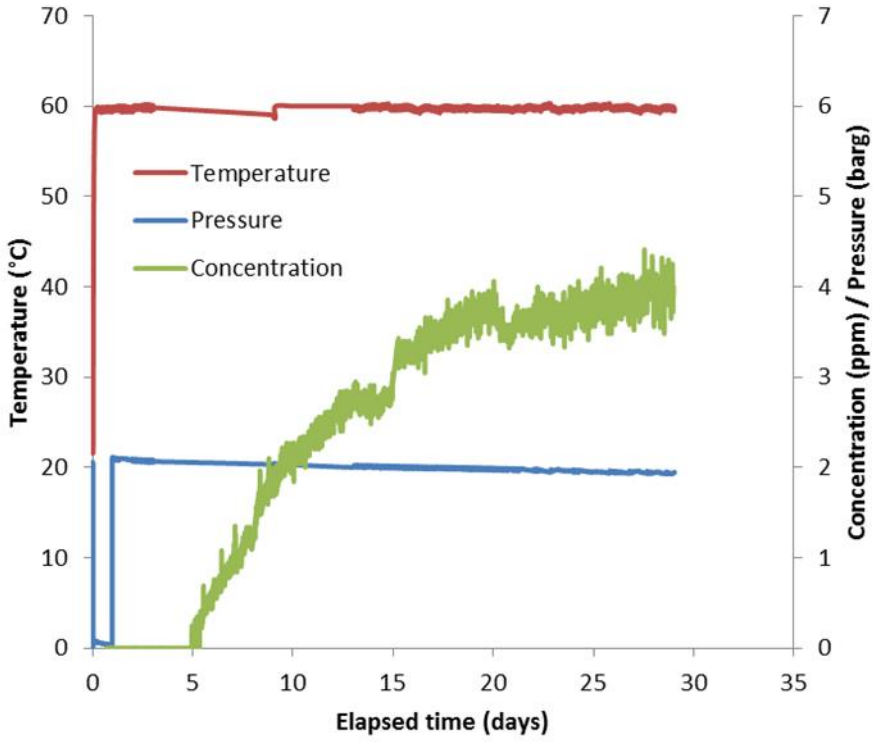

Figure B8. Laminate 15E. Plot of experimental temperature, pressure and sweep gas H_2S concentration against experimental time.

Plaque control:

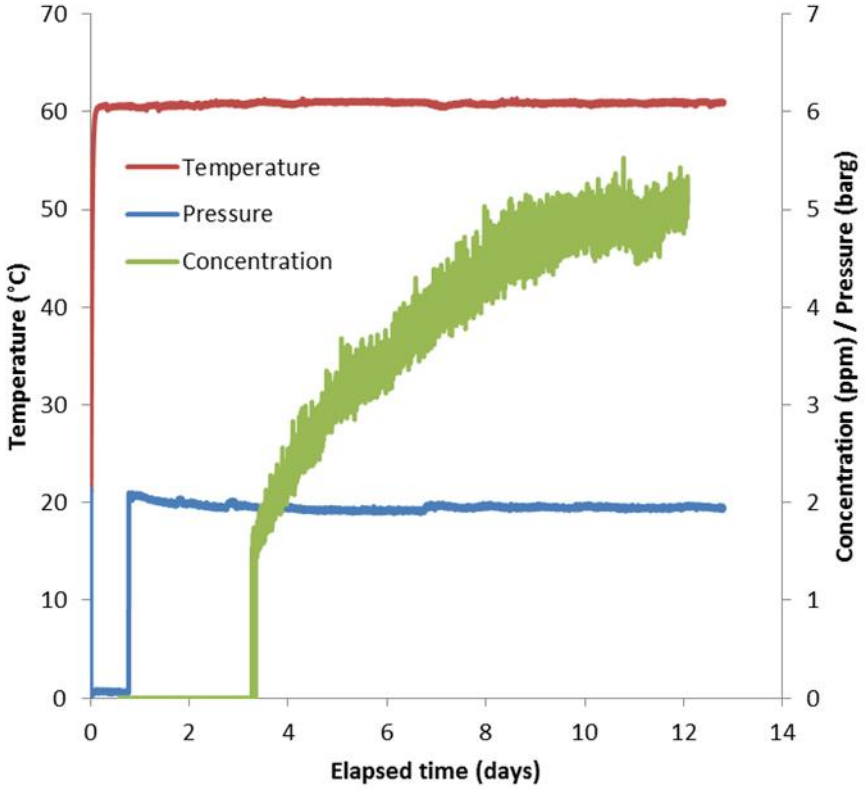

Figure B9. Plaque control. Plot of experimental temperature, pressure and sweep gas H_2S concentration against experimental time.

Plaque CVD:

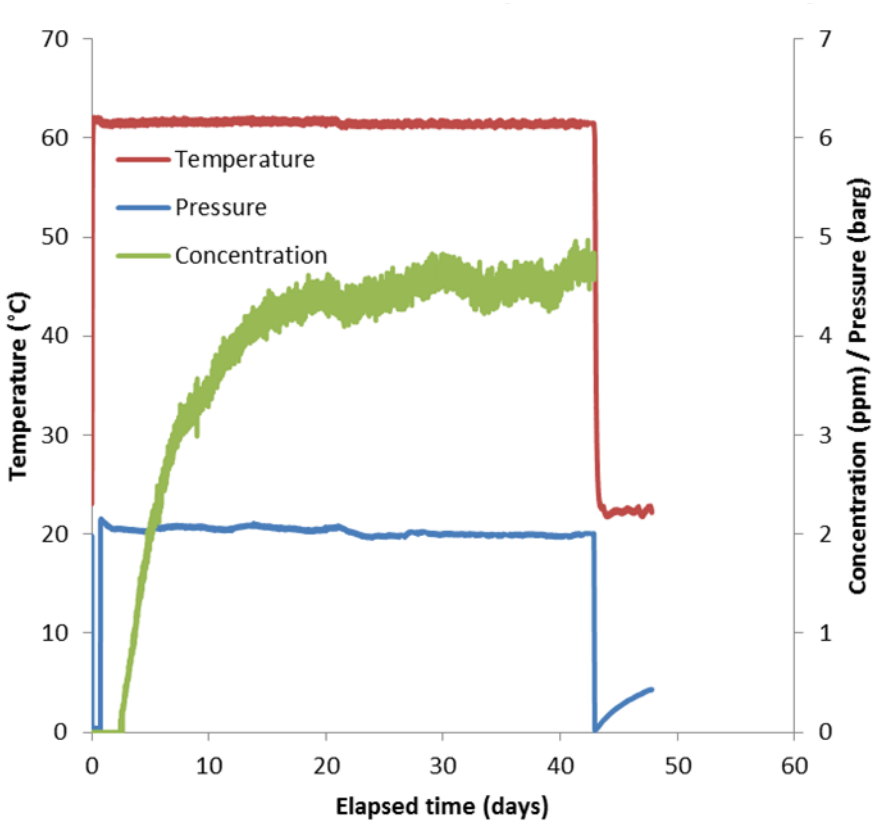

Figure B10. Plaque CVD. Plot of experimental temperature, pressure and sweep gas H_2S concentration against experimental time.

B.3 High Pressure CO_2 with 1.48% H_2S Experimental Data

Experimental data for the high pressure CO_2 with 1.48% H_2S permeability coefficients, presented in Chapter 7 of the main text, are shown in Figure B11 – Figure B19.

Laminate control D:

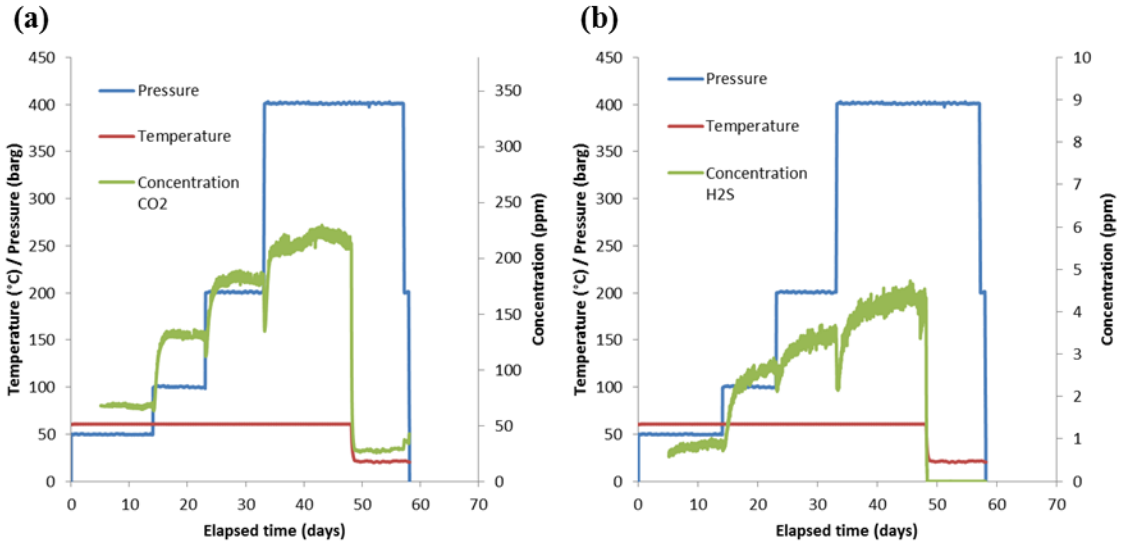

Figure B11. Laminate control D. Plots of experimental temperature, pressure and sweep gas permeant concentration against experimental time for (a) CO_2 and (b) H_2S.

Laminate A:

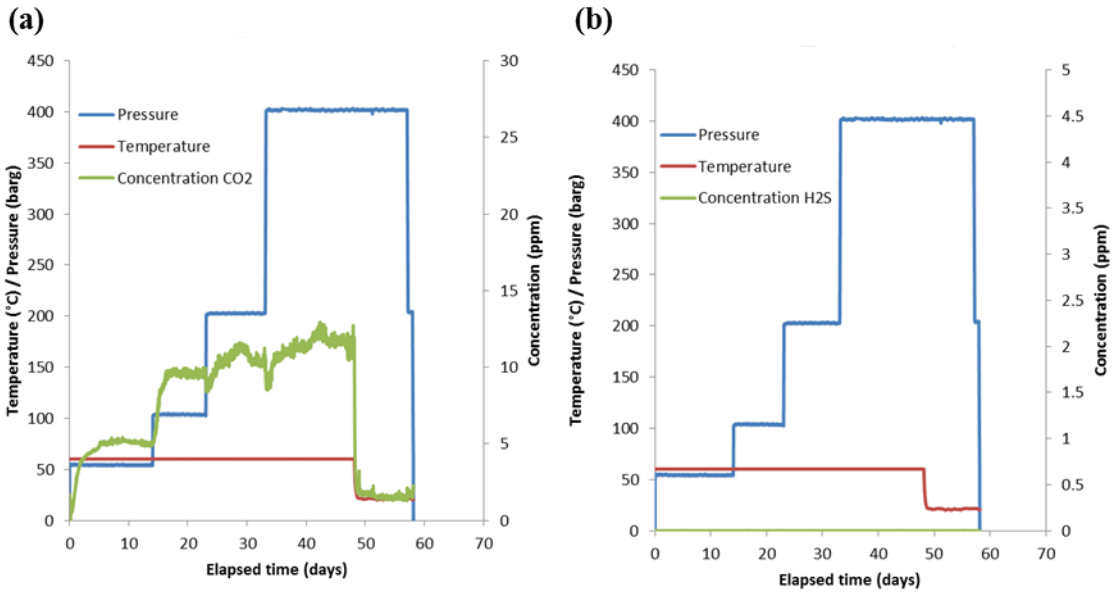

Figure B12. Laminate A. Plots of experimental temperature, pressure and sweep gas permeant concentration against experimental time for (a) CO_2 and (b) H_2S.

Laminate B:

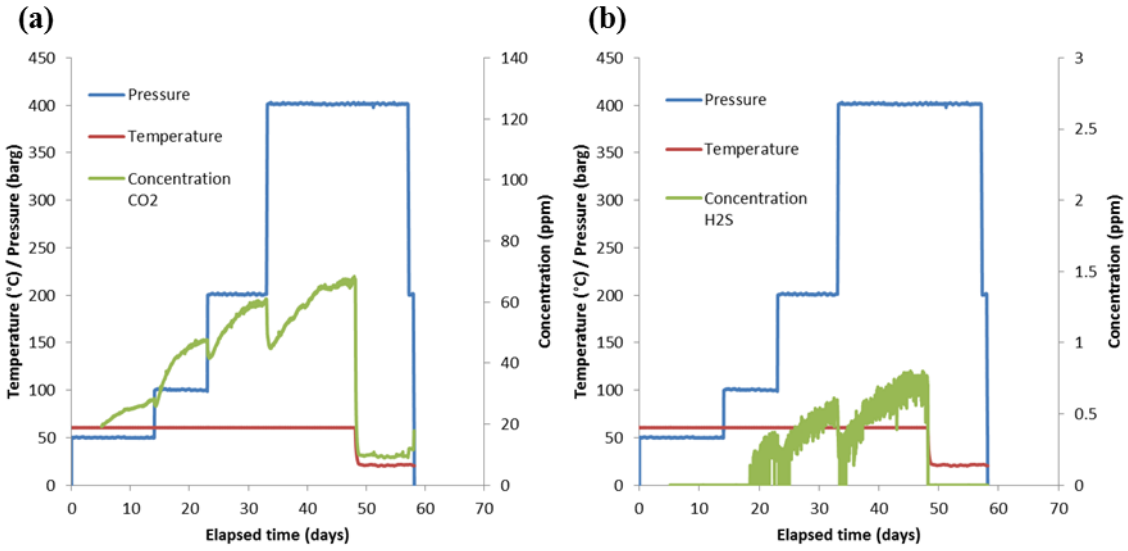

Figure C13. Laminate B. Plots of experimental temperature, pressure and sweep gas permeant concentration against experimental time for (a) CO_2 and (b) H_2S.

Laminate C:

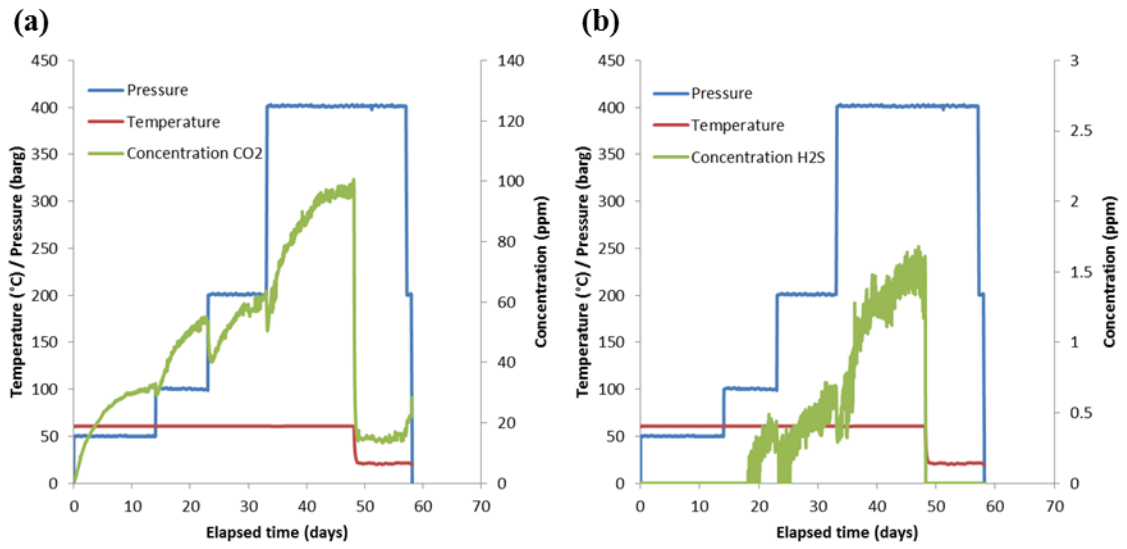

Figure B14. Laminate C. Plots of experimental temperature, pressure and sweep gas permeant concentration against experimental time for (a) CO_2 and (b) H_2S.

Laminate htGO25:

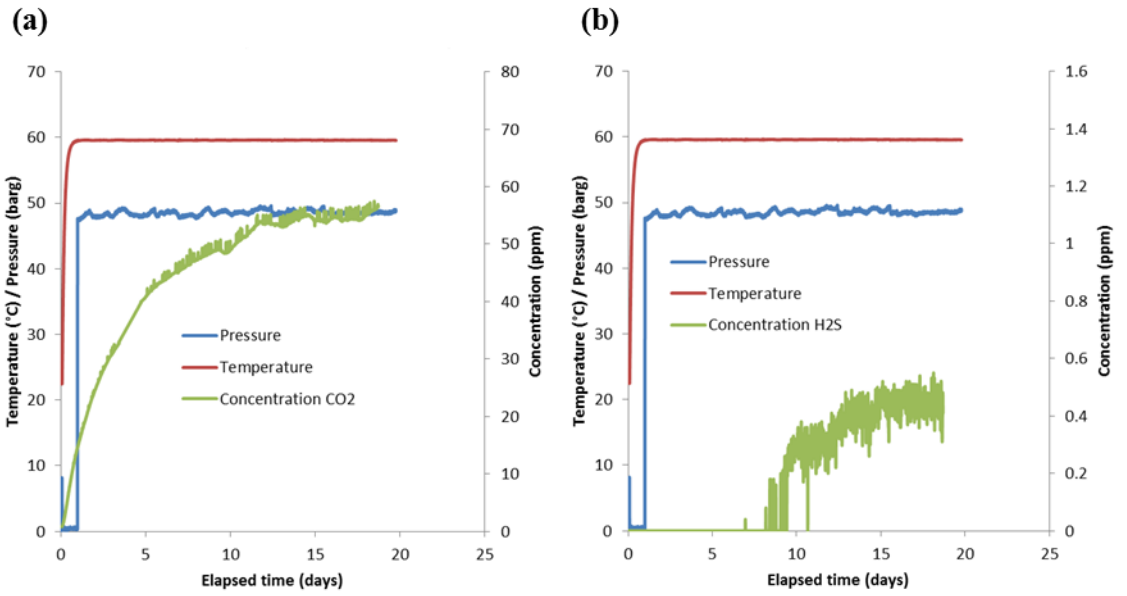

Figure B15. Laminate htGO25. Plots of experimental temperature, pressure and sweep gas permeant concentration against experimental time for (a) CO_2 and (b) H_2S.

0 wt% sandwich:

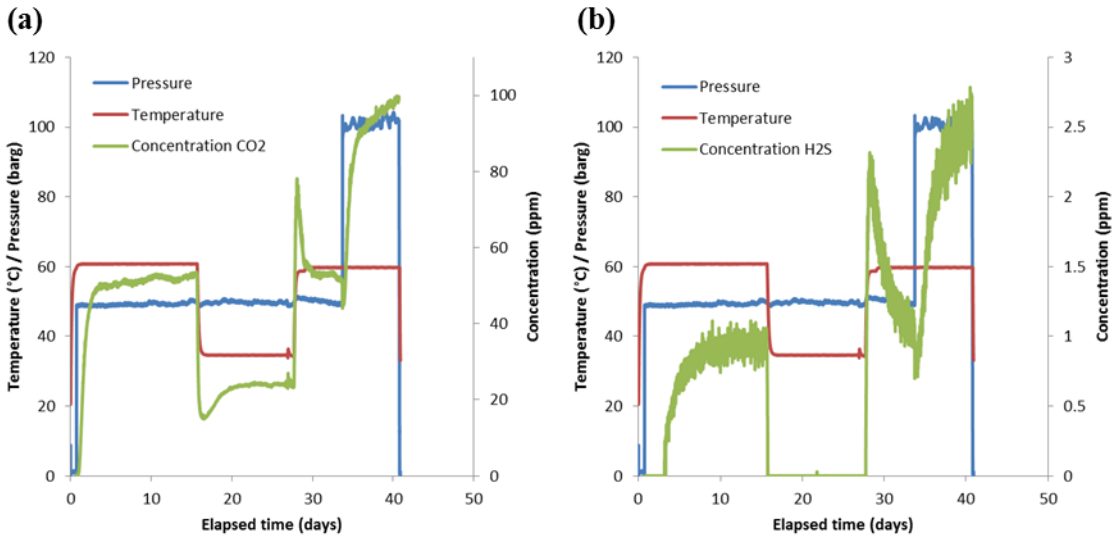

Figure B16. 0 wt% sandwich. Plots of experimental temperature, pressure and sweep gas permeant concentration against experimental time for (a) CO_2 and (b) H_2S.

1 wt% sandwich:

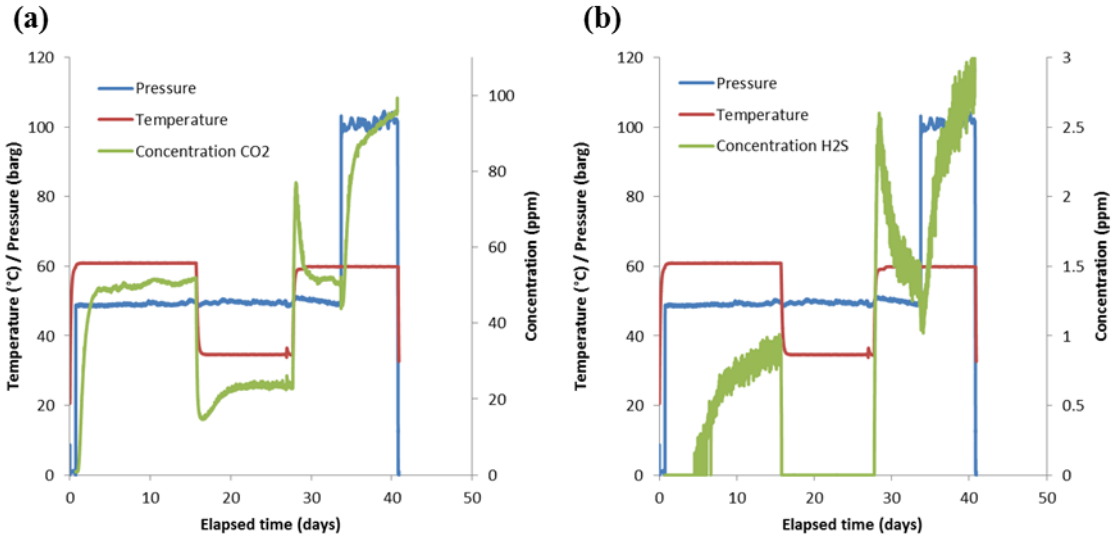

Figure B17. 1 wt% sandwich. Plots of experimental temperature, pressure and sweep gas permeant concentration against experimental time for (a) CO_2 and (b) H_2S.

Plaque control:

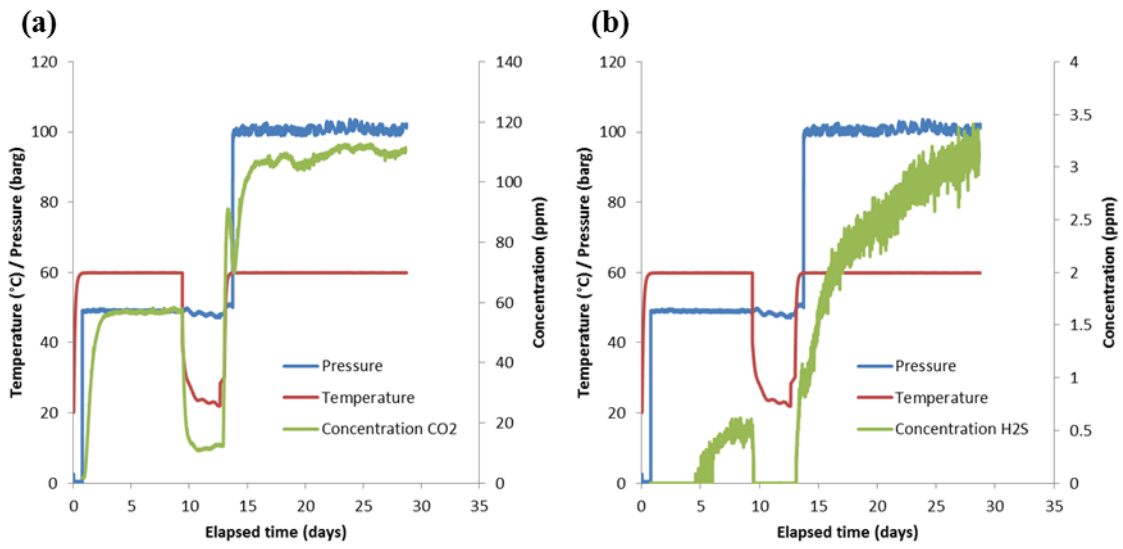

Figure B18. Plaque control. Plots of experimental temperature, pressure and sweep gas permeant concentration against experimental time for (a) CO_2 and (b) H_2S.

Plaque CVD:

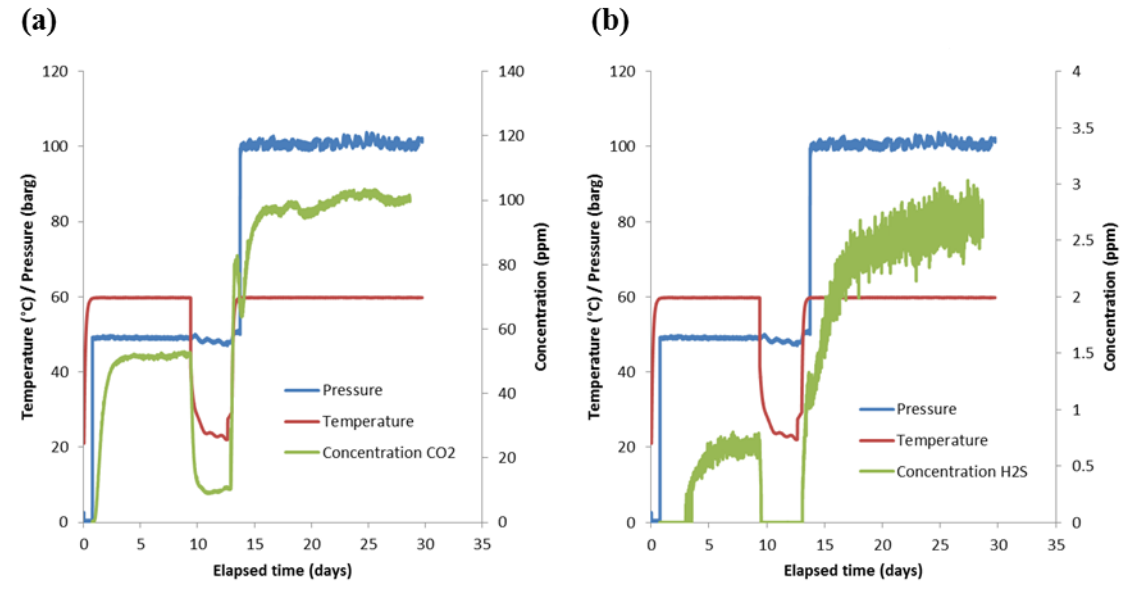

Figure B19. Plaque CVD. Plots of experimental temperature, pressure and sweep gas permeant concentration against experimental time for (a) CO_2 and (b) H_2S.

APPENDIX C

In this appendix, the values of P_f are displayed for all tested samples in Table C1 – Table C5.

Table C1. Melt blended averaged transport coefficients calculated using component fugacity as the driving force in favour of partial pressure.

Sample	Transport Coefficient	5 MPa 60 °C	5 MPa 35 °C	10 MPa 60 °C
PA0	P_{CO2} (10^{-16} mol m^{-1} s^{-1} Pa^{-1})	6.12	3.05	6.96
	D_{CO2} (10^{-12} m^2 s^{-1})	5.44	N/A	11.3
	S_{CO2} (10^{-4} mol m^{-3} Pa^{-1})	1.13	N/A	0.616
PA1	P_{CO2} (10^{-16} mol m^{-1} s^{-1} Pa^{-1})	6.39	3.26	6.78
	D_{CO2} (10^{-12} m^2 s^{-1})	5.49	N/A	12.5
	S_{CO2} (10^{-4} mol m^{-3} Pa^{-1})	1.16	N/A	0.543
PA0	P_{H2S} (10^{-16} mol m^{-1} s^{-1} Pa^{-1})	7.71	0	13.6
	D_{H2S} (10^{-12} m^2 s^{-1})	1.38	N/A	5.45
	S_{H2S} (10^{-4} mol m^{-3} Pa^{-1})	5.60	N/A	2.50
PA1	P_{H2S} (10^{-16} mol m^{-1} s^{-1} Pa^{-1})	7.81	0	15.4
	D_{H2S} (10^{-12} m^2 s^{-1})	1.21	N/A	6.32
	S_{H2S} (10^{-4} mol m^{-3} Pa^{-1})	6.46	N/A	2.43

Table C2. CVD and control BMNO averaged transport coefficients calculated using component fugacity as the driving force in favour of partial pressure.

Sample	Transport Coefficient	0.2 MPa 60 °C	5 MPa 60 °C	10 MPa 60 °C
CVD	P_{CO2} (10^{-16} mol m^{-1} s^{-1} Pa^{-1})	N/A	7.14	8.41
	D_{CO2} (10^{-12} m^2 s^{-1})	N/A	7.56	22.4
	S_{CO2} (10^{-4} mol m^{-3} Pa^{-1})	N/A	0.943	0.375
BMNO	P_{CO2} (10^{-16} mol m^{-1} s^{-1} Pa^{-1})	N/A	7.39	9.32
	D_{CO2} (10^{-12} m^2 s^{-1})	N/A	8.72	22.2
	S_{CO2} (10^{-4} mol m^{-3} Pa^{-1})	N/A	0.847	0.420
CVD	P_{H2S} (10^{-16} mol m^{-1} s^{-1} Pa^{-1})	11.3	5.27	17.0
	D_{H2S} (10^{-12} m^2 s^{-1})	1.49	2.05	7.15
	S_{H2S} (10^{-4} mol m^{-3} Pa^{-1})	7.63	2.57	2.37
BMNO	P_{H2S} (10^{-16} mol m^{-1} s^{-1} Pa^{-1})	13.1	5.58	19.4
	D_{H2S} (10^{-12} m^2 s^{-1})	1.53	2.12	3.77
	S_{H2S} (10^{-4} mol m^{-3} Pa^{-1})	8.57	2.63	5.14

Table C3. Laminate samples low pressure pure H_2S transport coefficients calculated using component fugacity as the driving force in favour of partial pressure.

Sample	Transport Coefficient	0.2 MPa 60 °C
Laminate 25E	P_{H2S} (10^{-16} mol m^{-1} s^{-1} Pa^{-1})	N/A
	D_{H2S} (10^{-12} m^2 s^{-1})	N/A
	S_{H2S} (10^{-4} mol m^{-3} Pa^{-1})	N/A
Laminate 25F	P_{H2S} (10^{-16} mol m^{-1} s^{-1} Pa^{-1})	N/A
	D_{H2S} (10^{-12} m^2 s^{-1})	N/A
	S_{H2S} (10^{-4} mol m^{-3} Pa^{-1})	N/A
Laminate 15E	P_{H2S} (10^{-16} mol m^{-1} s^{-1} Pa^{-1})	11.3
	D_{H2S} (10^{-12} m^2 s^{-1})	1.49
	S_{H2S} (10^{-4} mol m^{-3} Pa^{-1})	7.63
Laminate 15F	P_{H2S} (10^{-16} mol m^{-1} s^{-1} Pa^{-1})	13.1
	D_{H2S} (10^{-12} m^2 s^{-1})	1.53
	S_{H2S} (10^{-4} mol m^{-3} Pa^{-1})	8.57
Laminate control E	P_{H2S} (10^{-16} mol m^{-1} s^{-1} Pa^{-1})	11.3
	D_{H2S} (10^{-12} m^2 s^{-1})	1.49
	S_{H2S} (10^{-4} mol m^{-3} Pa^{-1})	7.63
Laminate control F	P_{H2S} (10^{-16} mol m^{-1} s^{-1} Pa^{-1})	11.4
	D_{H2S} (10^{-12} m^2 s^{-1})	1.34
	S_{H2S} (10^{-4} mol m^{-3} Pa^{-1})	8.49

Table C4. Consecutive high pressure transport coefficients calculated using component fugacity as the driving force in favour of partial pressure for Laminates A, B, C and Control D.

Sample	Transport Coefficient	5 MPa 60 °C	10 MPa 60 °C	20 MPa 60 °C	40 MPa 60 °C	40 MPa 21 °C
Laminate A	P_{CO2} (10^{-16} mol m^{-1} s^{-1} Pa^{-1})	0.626	0.726	0.612	0.433	0.103
	D_{CO2} (10^{-12} m^2 s^{-1})	4.43	14.8	17.7	19.2	N/A
	S_{CO2} (10^{-4} mol m^{-3} Pa^{-1})	0.141	0.0491	0.0346	0.0226	N/A
Laminate B	P_{CO2} (10^{-16} mol m^{-1} s^{-1} Pa^{-1})	3.08	3.34	3.22	2.31	0.0631
	D_{CO2} (10^{-12} m^2 s^{-1})	N/A	10.6	11.3	10.5	N/A
	S_{CO2} (10^{-4} mol m^{-3} Pa^{-1})	N/A	0.315	0.285	0.220	N/A
Laminate C	P_{CO2} (10^{-16} mol m^{-1} s^{-1} Pa^{-1})	3.69	3.75	3.11	3.54	0.980
	D_{CO2} (10^{-12} m^2 s^{-1})	2.31	9.45	16.7	5.80	N/A
	S_{CO2} (10^{-4} mol m^{-3} Pa^{-1})	1.60	0.397	0.186	0.611	N/A
Control D	P_{CO2} (10^{-16} mol m^{-1} s^{-1} Pa^{-1})	7.83	9.76	9.98	7.96	1.79
	D_{CO2} (10^{-12} m^2 s^{-1})	5.30	18.0	21.5	20.4	N/A
	S_{CO2} (10^{-4} mol m^{-3} Pa^{-1})	1.44	0.542	0.464	0.390	N/A
Laminate A	P_{H2S} (10^{-16} mol m^{-1} s^{-1} Pa^{-1})	7.73	15.1	16.5	14.4	0
	D_{H2S} (10^{-12} m^2 s^{-1})	N/A	5.96	19.2	11.6	0
	S_{H2S} (10^{-4} mol m^{-3} Pa^{-1})	N/A	2.53	0.862	1.24	N/A
Laminate B	P_{H2S} (10^{-16} mol m^{-1} s^{-1} Pa^{-1})	0	1.55	2.23	2.31	0
	D_{H2S} (10^{-12} m^2 s^{-1})	0	1.08	4.22	2.71	0
	S_{H2S} (10^{-4} mol m^{-3} Pa^{-1})	N/A	1.44	0.53	0.852	N/A
Laminate C	P_{H2S} (10^{-16} mol m^{-1} s^{-1} Pa^{-1})	0	2.01	2.51	5.01	0
	D_{H2S} (10^{-12} m^2 s^{-1})	0	1.15	3.20	3.03	0
	S_{H2S} (10^{-4} mol m^{-3} Pa^{-1})	N/A	1.74	0.783	1.65	N/A
Control D	P_{H2S} (10^{-16} mol m^{-1} s^{-1} Pa^{-1})	7.45	15.1	16.5	14.4	0
	D_{H2S} (10^{-12} m^2 s^{-1})	1.31	5.96	19.2	11.6	0
	S_{H2S} (10^{-4} mol m^{-3} Pa^{-1})	5.60	2.53	0.862	1.24	N/A

Table C5. Transport coefficients calculated using component fugacity as the driving force in favour of partial pressure for Laminate htGO25 and Laminate Control.

Sample	Transport Coefficient	5 MPa 60 °C
Laminate htGO25	P_{CO2} (10^{-16} mol m^{-1} s^{-1} Pa^{-1})	6.07
	D_{CO2} (10^{-12} m^2 s^{-1})	2.74
	S_{CO2} (10^{-4} mol m^{-3} Pa^{-1})	2.22
Laminate Control	P_{CO2} (10^{-16} mol m^{-1} s^{-1} Pa^{-1})	7.83
	D_{CO2} (10^{-12} m^2 s^{-1})	5.30
	S_{CO2} (10^{-4} mol m^{-3} Pa^{-1})	1.44
Laminate htGO25	P_{H2S} (10^{-16} mol m^{-1} s^{-1} Pa^{-1})	2.69
	D_{H2S} (10^{-12} m^2 s^{-1})	0.719
	S_{H2S} (10^{-4} mol m^{-3} Pa^{-1})	3.74
Laminate Control	P_{H2S} (10^{-16} mol m^{-1} s^{-1} Pa^{-1})	7.45
	D_{H2S} (10^{-12} m^2 s^{-1})	1.31
	S_{H2S} (10^{-4} mol m^{-3} Pa^{-1})	5.60

APPENDIX D

Sample CVD3 was a CVD graphene coated BMNO PA11 sample that was permeability tested with 0.2 MPa pure H_2S. Once tested, optical microscope images were taken of the surface crystals that could be clearly seen. The crystals appeared to be weakly bound as the crystals were lost following sample storage.

21 microscope images of a cuboid shaped sulphur crystal are shown in Figure D1, Figure D2 and Figure D3. The focal plane of the microscope was moved 5 μm down from above the crystal of interest in order to build up a series of microscope images documenting the 3D shape of the crystal. The total crystal height was approximately 105 μm (21 × 5 μm).

32 microscope images of a flower-like sulphur crystal are shown in Figure D4, Figure D5, Figure D6 and Figure D7. The focal plane of the microscope was moved 5 μm down from above the crystal of interest in order to build up a series of microscope images documenting the 3D shape of the crystal. The total crystal height was approximately 160 μm (32 × 5 μm).

It is interesting that the crystals under low pressure 0.2 MPa H_2S grow vertically out from the surface, rather than parallel to the CVD graphene surface as observed in the main text for CVD1 and CVD2.

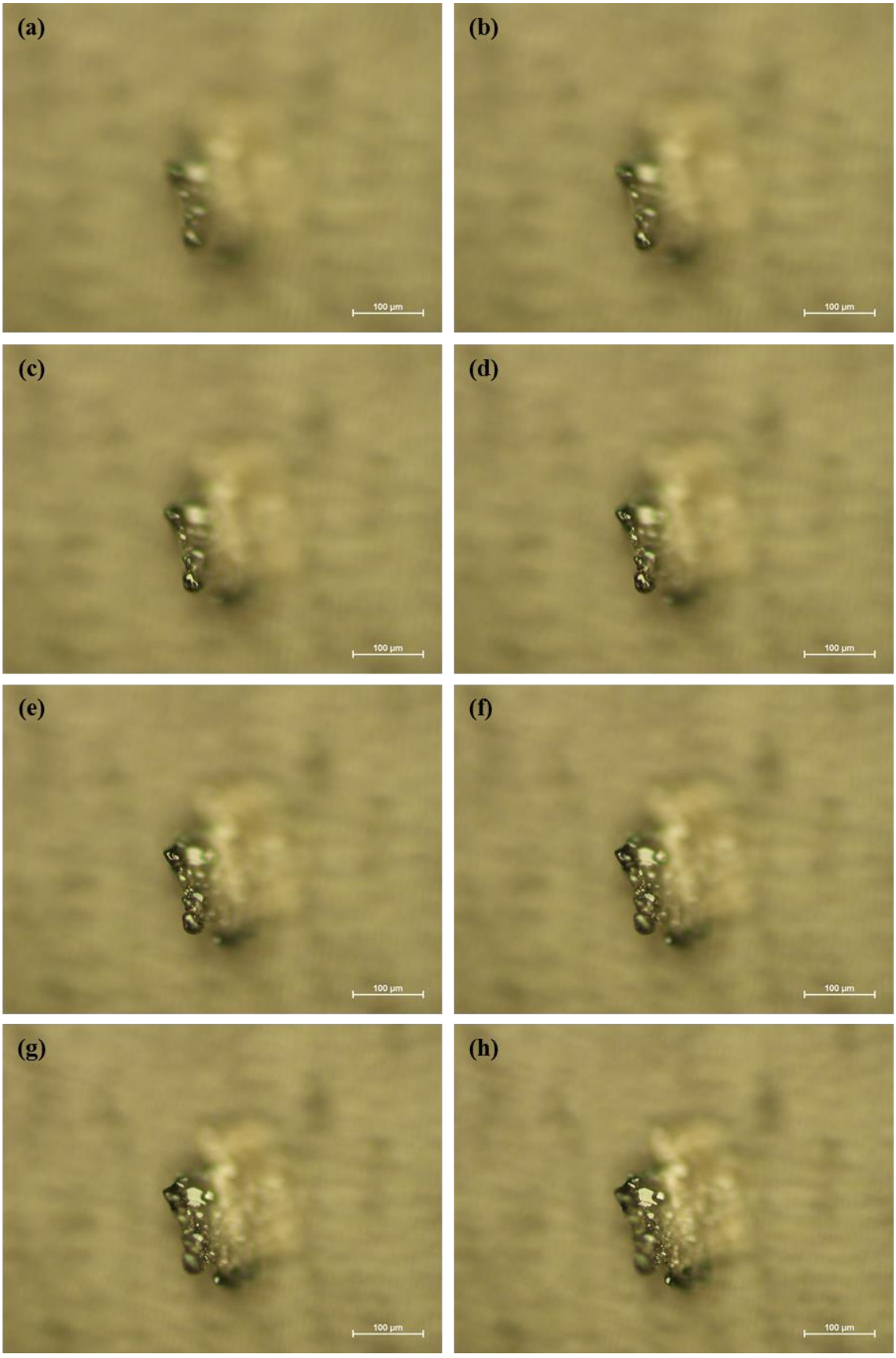

Figure D1. (a) – (h) Images taken at every 5 µm as focal plane is moved down from above the 3D sulphur crystal.

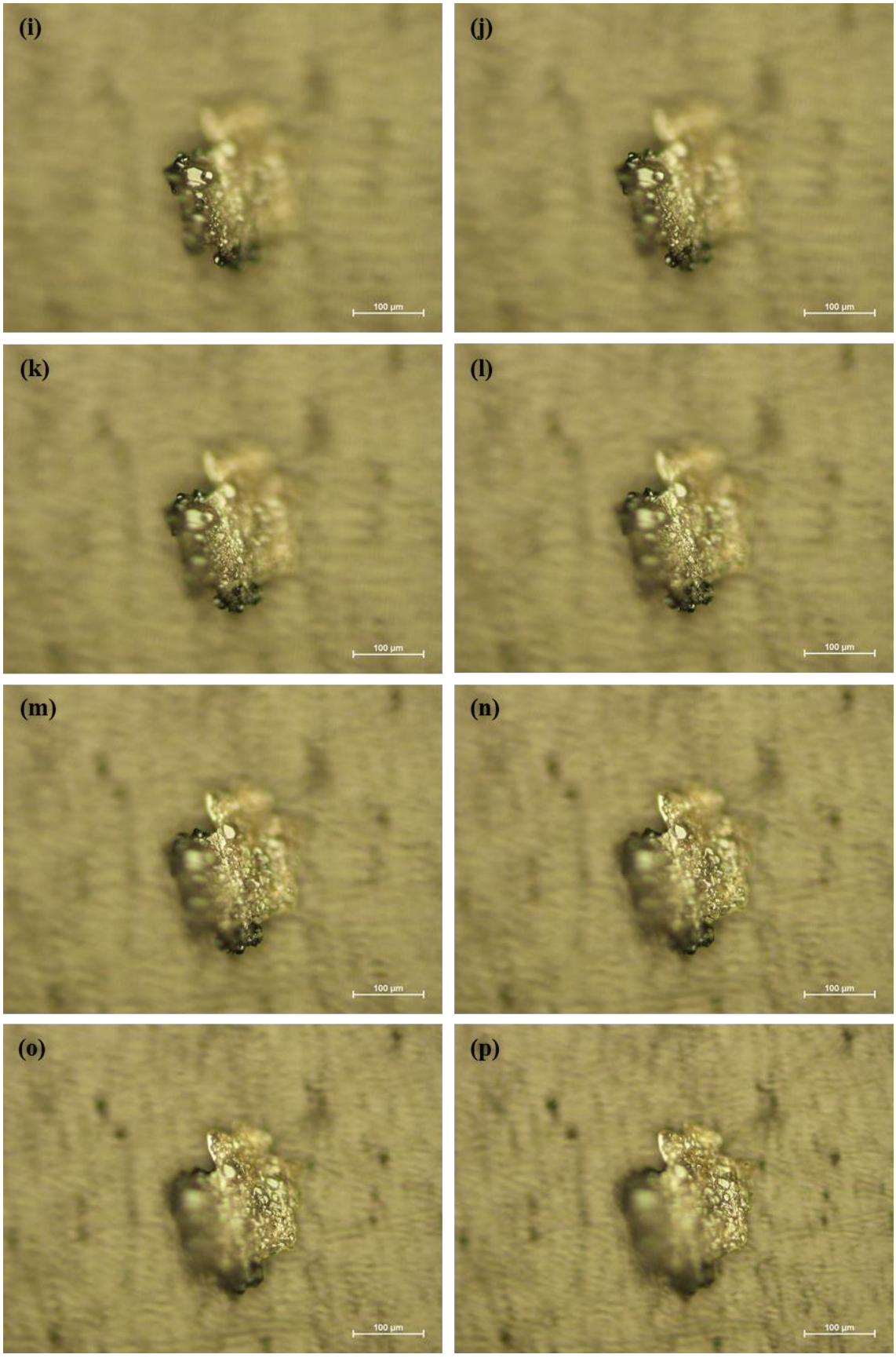

Figure D2. Continuation of Figure D1 (i) – (p) consecutively moving the focal plane down 5 µm.

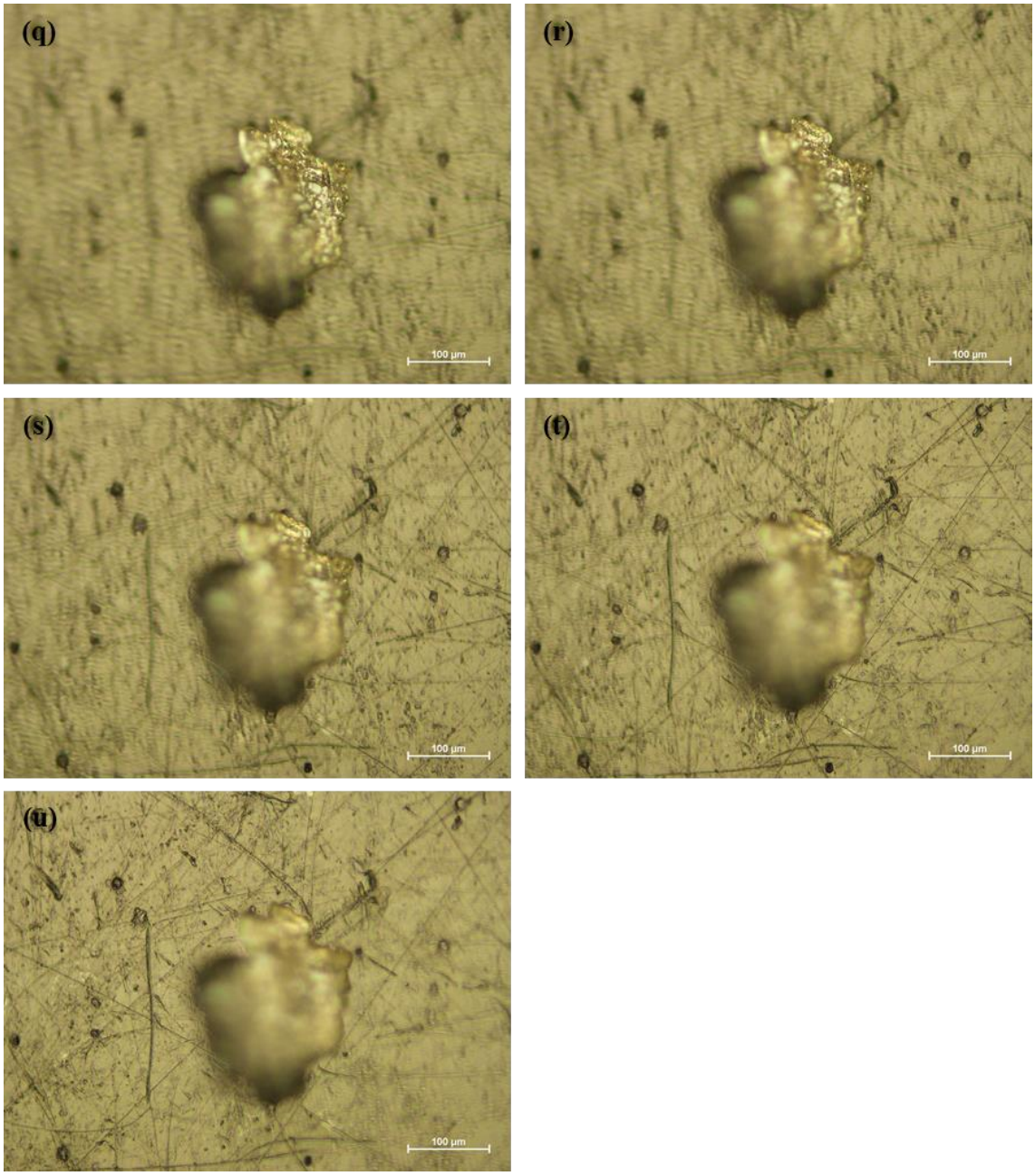

Figure D3. Continuation of Figure D2 (q) – (u) consecutively moving the focal plane down 5 µm until the polymer surface is in focus.

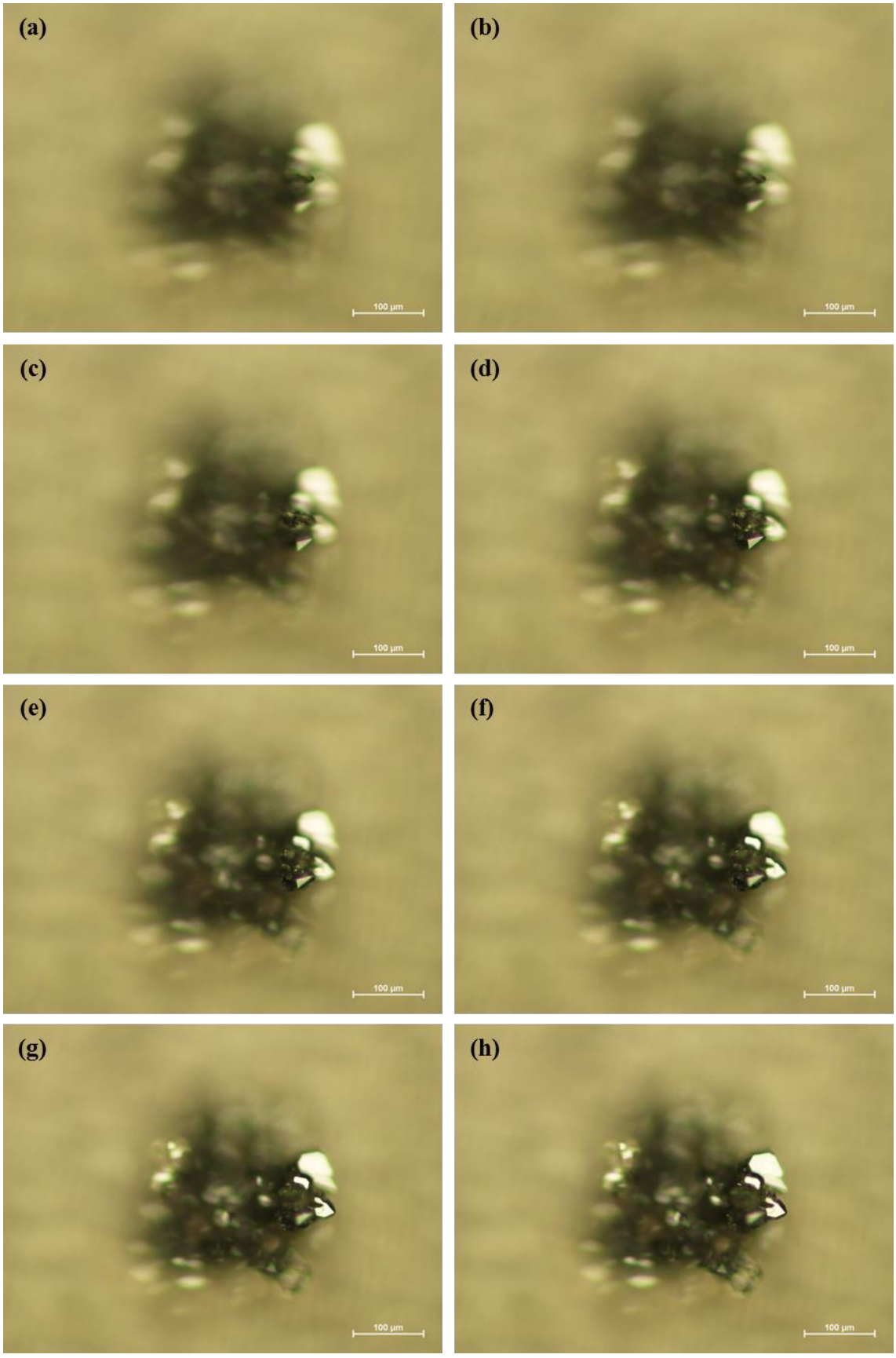

Figure D4. (a) – (h) Images of the flower shaped sulphur crystal every 5 µm down towards the PA11 surface, starting above the crystal top.

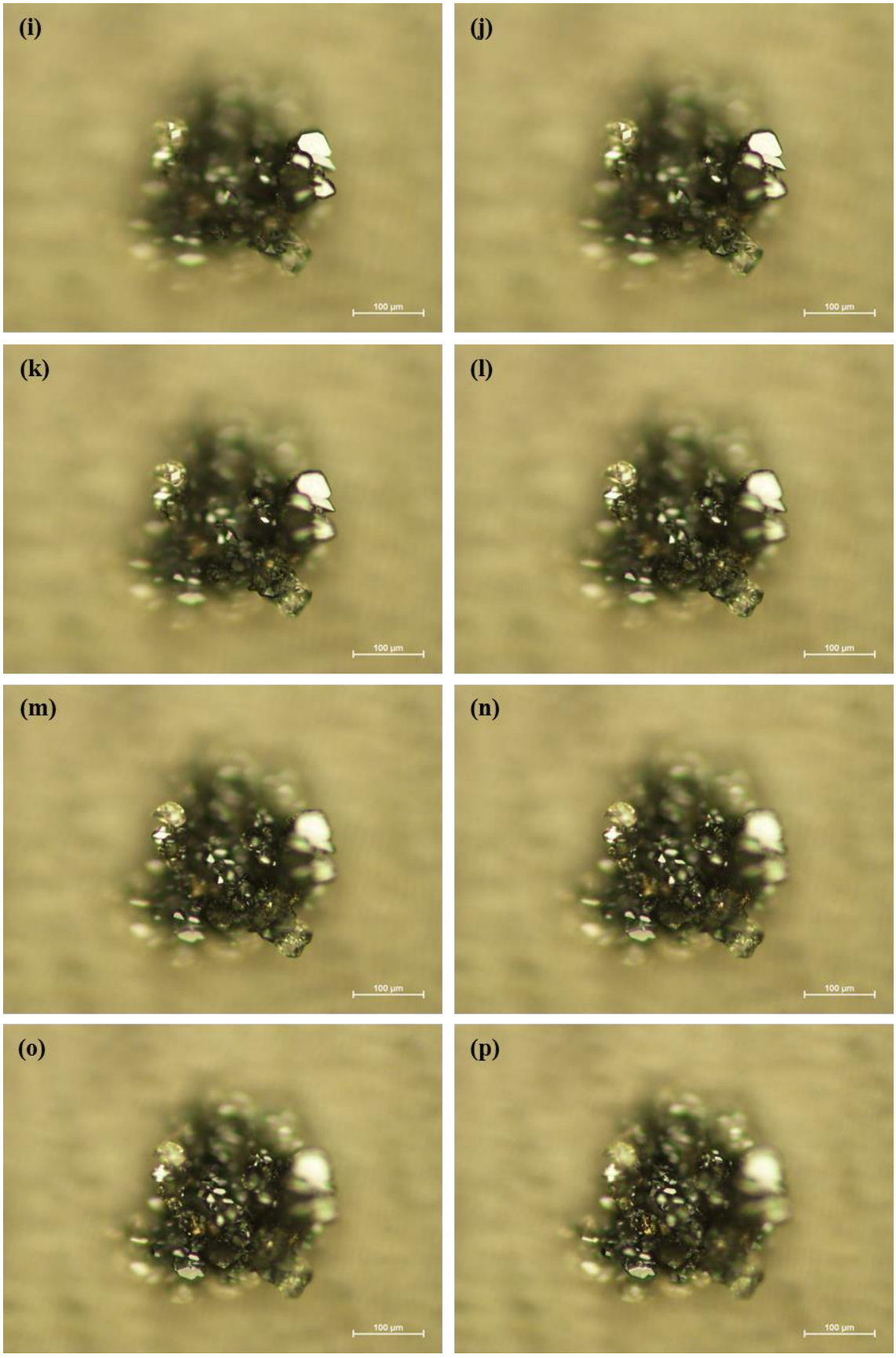

Figure D5. Continuation of Figure D4 (i) – (p) consecutively moving the focal plane down 5 µm.

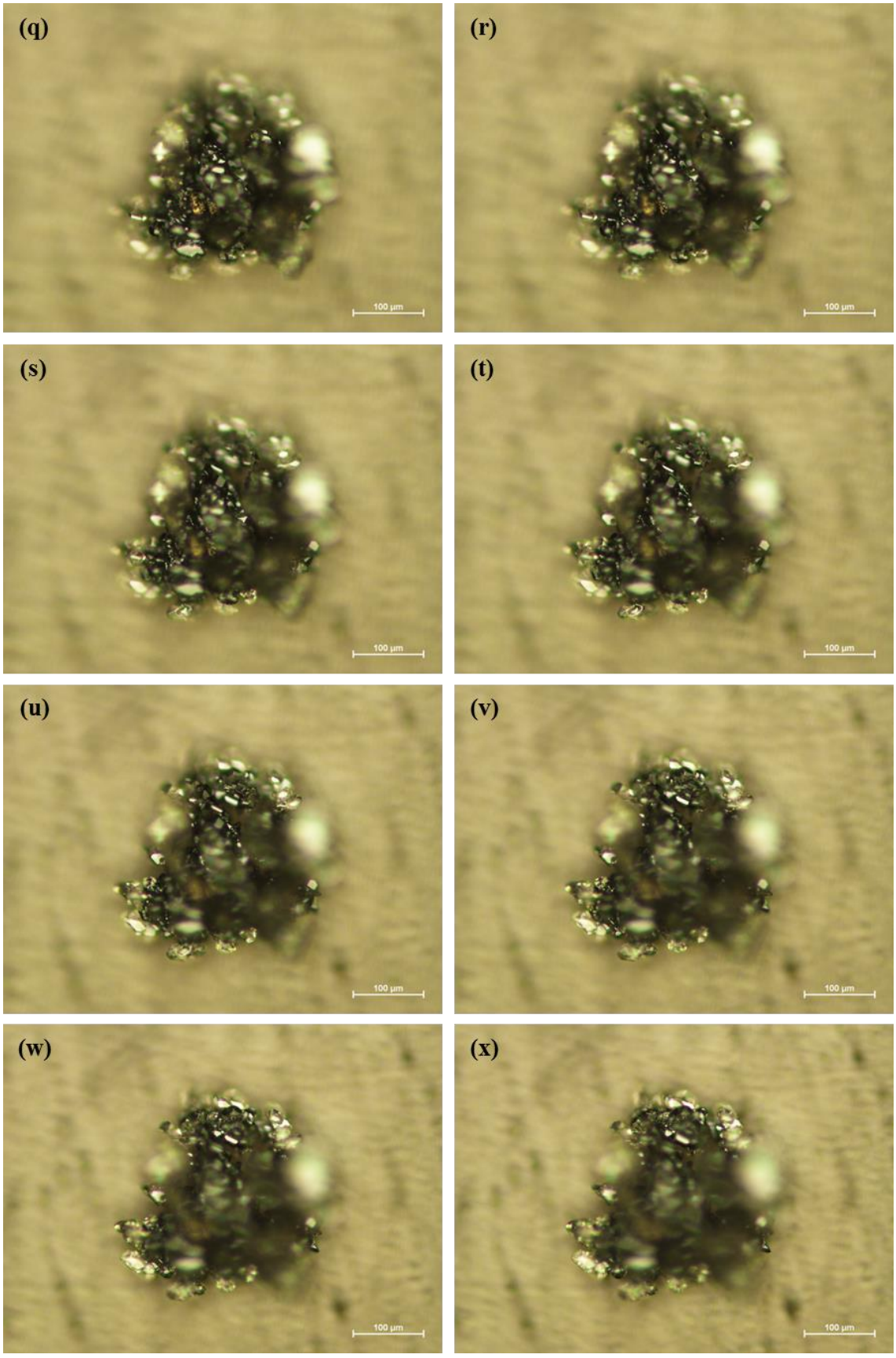

Figure D6. Continuation of Figure D5 (q) – (x) consecutively moving the focal plane down 5 µm.

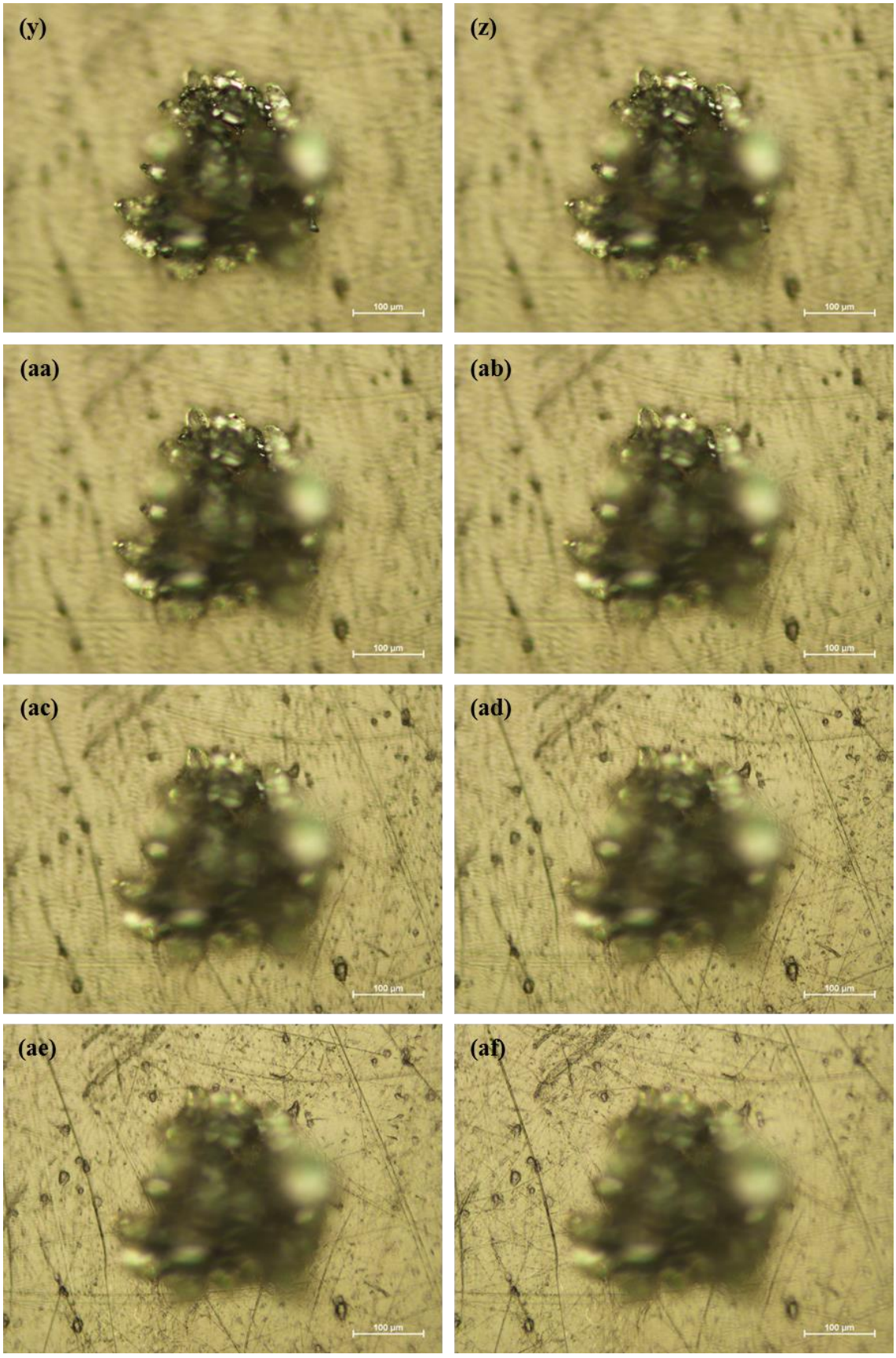

Figure D7. Continuation of Figure D6 (y) – (af) consecutively moving the focal plane down 5 µm until the PA11 surface was in focus.